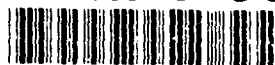Gas Dynamics Laboratory
Department of Mechanical and
Industrial Engineering
University of Illinois at
Urbana-Champaign
Urbana, IL 61801

AD-A271 037

UILU-ENG 93-4019

FINAL TECHNICAL REPORT

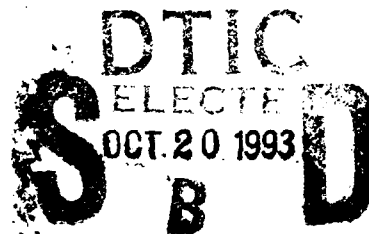## Fluid Dynamic Mechanisms and Interactions within Separated Flows

J. C. Dutton and A. L. Addy

DTIC
ELECTE
OCT. 20 1993
S
B
D

August 1993

93-25174

93 10 19 195

REPORT DOCUMENTATION PAGE

Form Approved
OMB No 0704-0188

1. AGENCY USE ONLY (Leave blank)	2. REPORT DATE 9 August 1993	3. REPORT TYPE AND DATES COVERED Final 11 Dec 89 - 20 May 93

4. TITLE AND SUBTITLE

Fluid Dynamic Mechanisms and Interactions Within Separated Flows

5. FUNDING NUMBERS

DAAL03-90-G-0021

6. AUTHOR(S)

J. C. Dutton and A. L. Addy

7. PERFORMING ORGANIZATION NAME(S) AND ADDRESS(ES)

Department of Mechanical and Industrial Engineering
University of Illinois at Urbana-Champaign
1206 West Green Street
Urbana, Illinois 61801

8. PERFORMING ORGANIZATION REPORT NUMBER

9. SPONSORING / MONITORING AGENCY NAME(S) AND ADDRESS(ES)

U.S. Army Research Office
P. O. Box 12211
Research Triangle Park, NC 27709-2211

10. SPONSORING / MONITORING AGENCY REPORT NUMBER

ARO 27558.14-EG

11. SUPPLEMENTARY NOTES

The view, opinions and/or findings contained in this report are those of the author(s) and should not be construed as an official Department of the Army position, policy, or decision, unless so designated by other documentation.

12a. DISTRIBUTION / AVAILABILITY STATEMENT

Approved for public release; distribution unlimited.

12b. DISTRIBUTION CODE

13. ABSTRACT (Maximum 200 words)

The significant results of a joint research effort investigating the fundamental fluid dynamic mechanisms and interactions within high-speed separated flows are presented in detail. The results have been obtained through primary emphasis on experimental investigations of missile and projectile base flow-related configurations. The objectives of the research program focus on understanding the component mechanisms and interactions which establish and maintain high-speed separated flow regions.

The experimental efforts have considered the development and use of state-of-the-art laser Doppler velocimeter (LDV) and particle image velocimeter (PIV) systems for experiments with axisymmetric and planar, two-dimensional models in subsonic and supersonic flows. The LDV experiments have yielded high quality, well documented mean and turbulence velocity data for a variety of high-speed separated flows including the near-wake region behind a cylindrical afterbody in supersonic flow. The PIV experiments have studied the effect of a base cavity in a two-dimensional, subsonic base flow and the mechanism of drag reduction for this configuration. Another experimental study has considered the interaction occurring when a supersonic stream is separated by means of a second stream impinging the first at an angle (plume-induced separation). The results of these various studies have been carefully documented in a series of journal articles, conference proceedings papers, and theses. The full text of the papers and thesis abstracts are included as appendices of this report.

14. SUBJECT TERMS

separated flow   transonic flow   particle image velocimetry
base flow   supersonic flow
subsonic flow   laser Doppler velocimetry

15. NUMBER OF PAGES 212

16. PRICE CODE

17. SECURITY CLASSIFICATION OF REPORT UNCLASSIFIED	18. SECURITY CLASSIFICATION OF THIS PAGE UNCLASSIFIED	19. SECURITY CLASSIFICATION OF ABSTRACT UNCLASSIFIED	20. LIMITATION OF ABSTRACT UL

FLUID DYNAMIC MECHANISMS AND INTERACTIONS WITHIN SEPARATED FLOWS

Final Technical Report

by

J. C. Dutton[*]

A. L. Addy[**]

August 1993

Supported by

---

[*]   Professor of Mechanical Engineering

[**]   Professor and Head of Mechanical Engineering

ABSTRACT

The significant results of a joint research effort investigating the fundamental fluid dynamic mechanisms and interactions within high-speed separated flows are presented in detail. The results have been obtained through primary emphasis on experimental investigations of missile and projectile base flow-related configurations. The objectives of the research program focus on understanding the component mechanisms and interactions which establish and maintain high-speed separated flow regions.

The experimental efforts have considered the development and use of state-of-the-art laser Doppler velocimeter (LDV) and particle image velocimeter (PIV) systems for experiments with axisymmetric and planar, two-dimensional models in subsonic and supersonic flows. The LDV experiments have yielded high quality, well documented mean and turbulence velocity data for a variety of high-speed separated flows including the near-wake region behind a cylindrical afterbody in supersonic flow. The PIV experiments have studied the effect of a base cavity in a two-dimensional, subsonic base flow and the mechanism of drag reduction for this configuration. Another experimental study has considered the interaction occurring when a supersonic stream is separated by means of a second stream impinging the first at an angle (plume-induced separation). The results of these various studies have been carefully documented in a series of journal articles, conference proceedings papers, and theses. The full text of the papers and thesis abstracts are included as appendices of this report.

TABLE OF CONTENTS

I. INTRODUCTION

A. PROBLEM STATEMENT

This report describes an ongoing research effort funded by the U.S. Army Research Office to investigate the fundamental fluid dynamic mechanisms and interactions within high-speed separated flows with particular attention paid to the projectile and missile base flow problem. The overall effort has concentrated on detailed experimental investigations aimed at gaining a more insightful understanding of the fundamental fluid dynamic mechanisms existing in the near-wake flowfield. The investigations of separated flow problems have been focused on missile and projectile afterbody and base flows and on the interactions between the base and body flows.

Professors J. C. Dutton and A. L. Addy and their graduate students at the University of Illinois at Urbana–Champaign have conducted this series of experiments on two–dimensional and axisymmetric base flow configurations utilizing a number of diagnostic techniques. These include: schlieren and shadowgraph photography, surface streakline visualization, mean and fluctuating pressure measurements, two-component laser Doppler velocimeter (LDV) measurements, and particle image velocimeter (PIV) measurements. This information concerning the mean and fluctuating characteristics of the flowfields in and around the embedded separated flow regions have been used to characterize base flows at both subsonic and supersonic speeds.

The purpose of this final technical report is to collect and present, in their entirety or by summary and reference, the research findings for the near-wake base flow problem and related problems that have been investigated under the research sponsorship of the U.S. Army Research Office through Grant Number DAAL03–90–G–0021. The Technical Monitor for this research has been Dr. Thomas L. Doligalski, Chief, Fluid Dynamics Branch, Engineering and Environmental Sciences Division. The authors of this report and their graduate student researchers are deeply indebted to Dr. Doligalski for his support and technical comments and suggestions during the course of these studies. The research group is also indebted to Dr. Robert E. Singleton, Director,

Engineering and Environmental Sciences Division, for his long-term interest and support of this research program.

In all cases, where the experimental efforts have yielded significant or new results, the information has been presented at professional meetings and/or published in the archival literature by the individual researchers. This final report highlights this work and includes copies of the appropriate publications for completeness. In the case of master's and doctoral degree theses, which are generally quite long and detailed, a summary of the theses is provided and the appropriate reference to the full document is given. In most cases, the conference and/or archival publications are based upon the detailed work reported in these theses.

B. FINAL TECHNICAL REPORT ORGANIZATION

The overall organization of this report details the major accomplishments of the research group during the three-year period of ARO sponsorship. Each research investigation is described in brief detail and the associated published literature is included in an appendix. The inclusion of a copy of the published literature is intended to ease the burden on the reader for obtaining symposium proceedings and other publications which tend to be difficult to obtain.

The relatively brief "text" of this final technical report has been outlined and organized to provide quick reference to a particular topic of interest. Most of the research results have been made available through organized meetings and publications of the American Institute of Aeronautics and Astronautics (AIAA). In those instances when a detailed paper is available, only a brief description is given and the reader is referred to the appropriate appendix for further details.

After the summary of research results, the next two sections of the report provide lists of several administrative quantities related to the current research grant. These include the journal articles published, conference proceedings papers, graduate student theses, faculty and graduate student participants, and advanced degrees earned.

Once the research topics and administrative matters have been discussed and listed, the continuing and future research activities of the group are described. The strong commitment of this research group towards developing an understanding of the base flow problem is evidenced by the

2

multi-year development and assembly of advanced experimental equipment that will provide well-documented data for the ongoing analytical and computational work of other researchers. Although this final technical report summarizes our current three-year effort, our research group is continuing to investigate the base flow problem and anticipates further significant contributions to the understanding of the fundamental mechanisms and interactions within high-speed separated flows. These ongoing and future research activities are described briefly in the last section of the report.

II. SUMMARY OF RESULTS

This section summarizes the results of the ongoing research program concerned with fluid dynamic mechanisms and interactions occurring in high-speed separated flows. In each section below, the most important results are abstracted from the journal articles, conference proceedings papers, and graduate student theses that have been completed under the support of this research grant.

A.1 EFFECTS OF A BASE CAVITY ON SUBSONIC NEAR-WAKE FLOW

An experimental investigation has been conducted to study the effects of a base cavity on the near-wake flowfield of a slender, two-dimensional body in the subsonic speed range. Three base configurations were investigated and compared: a blunt base, a shallow rectangular cavity base of depth equal to one-half the base height, and a deep rectangular cavity base of depth equal to one base height. Each configuration was studied at three freestream Mach numbers ranging from the low to high subsonic range. Schlieren photographs revealed that the basic qualitative structure of the vortex street was unmodified by the presence of a base cavity. However, the vortex street was weakened by the base cavity apparently due to the enhanced fluid mixing occurring at the entrance of the cavity. The weaker vortex street yielded higher pressures in the near wake for the cavity bases, increases in the base pressure coefficients on the order of 10-14%, and increases in the shedding frequencies on the order of 4-6% relative to the blunt-based configuration. The majority of the observed changes occurred in going from the blunt base to the shallow cavity base.

The complete text of this paper may be found in Appendix A.1.

A.2 TWO-STREAM, SUPERSONIC, WAKE FLOWFIELD BEHIND A THICK BASE, PART I: GENERAL FEATURES

An experimental investigation of the complex interaction region generated by the separation of two supersonic streams past a finite-thickness base has been conducted in a two-dimensional wind tunnel. The data were obtained using schlieren photography, pressure measurements, and two-component laser Doppler velocimeter measurements. The shear-layer mixing regions are characterized by initially constant-pressure mixing, by an evolution of velocity profiles from

4

truncated boundary-layer shapes to wakelike profiles farther downstream, and by relatively high levels of turbulence. The separated flow region is characterized by large reverse flow velocities and strong interactions with the low-velocity regions of both shear layers. Turbulence intensities and kinematic Reynolds stresses are strongly affected by the separation process at the base and increase greatly in the latter portions of the two shear layers and in the recompression region. Recovery of the mean velocity field in the redeveloping wake occurs quickly, while the turbulence field remains perturbed to the furthest streamwise location investigated.

The complete text of this paper may be found in Appendix A.2.

A.3 APPLICATION OF PARTICLE IMAGE VELOCIMETRY IN HIGH-SPEED SEPARATED FLOWS

A particle image velocimetry (PIV) system has been developed for use in high-speed separated air flows. The complete system was developed to improve the spatial resolution and accuracy of the PIV technique as applied in high-speed compressible flows and is the first to incorporate both birefringent image shifting and submicron seed particles for analysis of separated flowfields. The system has been proven in preliminary experiments using a simple low-speed round jet flow and has been validated for accuracy with both known displacement simulated PIV photographs and with uniform flow experiments at Mach 0.5 (170 m/s) for comparison with pressure and laser Doppler velocimeter data. PIV data have also been obtained in the separated wake region behind a two-dimensional base model in a Mach 0.4 freestream flow (135-220 m/s) with resolution of velocity in 1.0-mm^2 regions, revealing features of the von Kármán vortex street wake and underlying small-scale turbulence.

The complete text of this paper may be found in Appendix A.3.

A.4 AN INVESTIGATION OF LDV VELOCITY BIAS CORRECTION TECHNIQUES FOR HIGH-SPEED SEPARATED FLOWS

An experimental study of the effects of velocity bias in single realization laser Doppler velocimetry measurements in a high-speed, separated flow environment is reported. The objective of the study is to determine a post-facto correction method which reduces velocity bias *after* individual realization data have been obtained. Data are presented for five velocity bias correction

schemes: inverse velocity magnitude weighting, interarrival time weighting, sample and hold weighting, residence time weighting, and the velocity-data rate correlation method. These data were compared to a reference measurement (saturable detector sampling scheme); the results show that the interarrival time weighting method compares favorably with the refernce measurement under the present conditions.

The complete text of this paper may be found in Appendix A.4.

A.5 SUPERSONIC BASE FLOW EXPERIMENTS IN THE NEAR-WAKE OF A CYLINDRICAL AFTERBODY

The near-wake of a circular cylinder aligned with a uniform Mach 2.5 flow has been experimentally investigated in a wind tunnel designed solely for this purpose. Mean static pressure measurements were used to assess the radial dependence of the base pressure and the mean pressure field approaching separation. In addition, two-component laser Doppler velocimeter (LDV) measurements were obtained throughout the near-wake including the large separated region downstream of the base. The primary objective of the research was to gain a better understanding of the complex fluid dynamic processes found in supersonic base flowfields including separation, shear layer development, reattachment along the axis of symmetry, and subsequent development of the wake. Results indicate relatively large reverse velocities and uniform turbulence intensity levels in the separated region. The separated shear layer is characterized by high turbulence levels with a strong peak in the inner, subsonic region which eventually decays through reattachment as the wake develops. A global maximum in turbulent kinetic energy and Reynolds shear stress is found upstream of the reattachment point which is in contrast to data from the reattachment of a supersonic shear layer onto a solid wall.

The complete text of this paper may be found in Appendix A.5.

A.6 EXPERIMENTAL INVESTIGATION OF AN EMBEDDED SEPARATED FLOW REGION BETWEEN TWO SUPERSONIC STREAMS

The complex interaction region generated by the separation of two supersonic streams past a finite-thickness base occurs frequently in high-speed flight and is characteristic of the aft-end flowfield of a powered missile. An experimental investigation was conducted in which a flowfield

6

of this type was modeled in a two-dimensional wind tunnel. The data was obtained using schlieren photography, pressure measurements, and two-component laser Doppler velocimeter (LDV) measurements. The shear layer mixing regions were characterized by initially constant-pressure mixing, by an evolution of velocity profiles from truncated boundary layer shapes to wake-like profiles farther downstream, and by relatively high levels of turbulence. The separated flow region was characterized by large negative velocities and strong interactions with the low-velocity regions of both shear layers. Turbulence intensities and kinematic Reynolds stresses were increased greatly in the latter portions of the two shear layers and in the recompression region. Recovery of the mean velocity field in the redeveloping wake occurred quickly, while the turbulence field remained perturbed to the furthest streamwise location.

The complete text of this paper may be found in Appendix A.6.

A.7 AN EXPERIMENTAL INVESTIGATION OF AXISYMMETRIC POWER-OFF BASE FLOW PHENOMENA

An experimental program has been conducted to study the flowfield behind a blunt-based body of revolution embedded in a supersonic freestream. The experiments have been conducted in a newly-designed axisymmetric wind tunnel facility at a nominal approach Mach number of 2.5. A cylindrical sting aligned with the axis of the wind tunnel provided the physical model for the study. Qualitative flowfield information was obtained with spark-schlieren photography and surface oil visualization. Mean wall static pressure measurements were made across the base and along the sting parallel to the wind tunnel axis. Nineteen pressure taps were concentrated across the base to properly assess the dependence of local base pressure on radial location. The sting boundary layer profile and nozzle exit flow uniformity were measured by a one-component laser Doppler velocimetry (LDV) system. The base pressure measurements indicate only a small dependence on radial location. Interference waves generated at the junction of the nozzle exit and test section were found to have a large effect on the base pressure profile at certain operating conditions but could be eliminated by proper operation of the tunnel.

The complete text of this paper may be found in Appendix A.7.

A.8 DESIGN OF A PARTICLE IMAGE VELOCIMETER FOR HIGH SPEED FLOWS

A particle image velocimetry (PIV) system has been developed for use as a non-intrusive laser diagnostic tool to complement laser Doppler velocimetry (LDV) in high speed (transonic and supersonic) wind tunnel studies. The PIV system is capable of extracting instantaneous two-dimensional velocity maps within a flow by recording double images of seed particles on photographic film and then examining the local displacement of particle images to determine velocity vectors. The image acquisition system uses two high power pulsed Nd:YAG lasers focused into a thin light sheet to illuminate seed particles for recording on either 35 mm or 4" x 5" format film, with control of seeders, lasers, and the camera shutter performed by a Macintosh II computer. Interrogation of the double-exposed photographs to extract velocity information is done on an image processing system based on a 50 MHz Macintosh workstation, a HeNe laser for illumination, automated positioners to handle the film, and a CCD array camera. The design of the acquisition system, including special considerations for PIV in high speed flows, is discussed. The theory and design of the interrogation system are also described. Finally, results from the cases used to validate and demonstrate the PIV system are presented.

The complete text of this paper may be found in Appendix A.8.

A.9 DEVELOPMENT AND APPLICATION OF A PARTICLE IMAGE VELOCIMETER FOR HIGH SPEED FLOWS

A particle image velocimetry (PIV) system has been developed for use in high-speed separated air flows. The image acquisition system uses two 550 mJ/pulse Nd:YAG lasers and is fully controlled by a host Macintosh computer. The interrogation system is also Macintosh-based and performs interrogations at approximately 2.3 sec/spot and 4.0 sec/spot when using the Young's fringe and autocorrelation methods, respectively. The system has been proven in preliminary experiments using known-displacement simulated PIV photographs and a simple axisymmetric jet flow. Further results have been obtained in a transonic wind tunnel operating at Mach 0.4 to 0.5 (135 m/s to 170 m/s). PIV experiments were done with an empty test section to provide uniform flow data for comparison with pressure and LDV data, then with a two-

8

dimensional base model, revealing features of the von Kármán vortex street wake and underlying small scale turbulence.

The complete text of this paper may be found in Appendix A.9.

A.10 A PLUME-INDUCED BOUNDARY LAYER SEPARATION EXPERIMENT

The current paper describes an experimental investigation of a plume-induced boundary layer separation (PIBLS) flowfield produced by the interaction between two nonparallel, supersonic streams in the presence of a finite thickness base. The purpose of the study is to gain a better understanding of the extent to which the fluid dynamic mechanisms and interactions present in the PIBLS flowfield influence the turbulence properties of the flow. A two-stream, supersonic wind tunnel, incorporating a two-dimensional planar geometry and operating in the blowdown mode, was specifically designed to produce a PIBLS flowfield. Preliminary experiments have demonstrated that the wind tunnel is capable of producing a wide range of PIBLS flowfields by simply regulating the stagnation pressure of the lower stream (jet flow) relative to the upper stream (freestream flow). One PIBLS flowfield has been chosen in which to conduct a detailed set of measurements. This flowfield has its separation point located about $6\delta_0$ upstream of the base corner. A detailed study of this PIBLS flowfield is underway using schlieren photography and shadowgraph pictures, surface streakline visualization, surface static pressure measurements, and two-component, coincident LDV measurements.

Unfortunately, the separation shock wave associated with the PIBLS flowfields is unsteady. The streamwise extent of the unsteadiness was estimated from schlieren observation to be on the order of several boundary layer thicknesses. This unsteadiness poses a problem when making LDV measurements because it is impossible to distinguish between velocity fluctuations caused by the turbulent eddies and velocity fluctuations caused by the gross movement of the separated region. Fortunately, this problem is not insurmountable. A conditional sampling technique for acquiring and analyzing the LDV data is currently under development using surface static pressure measurements taken from fast-response pressure transducers as a means of tracking the separation shock wave motion. This technique effectively reduces the length scale of the

unsteadiness by eliminating from the data analysis any LDV measurements that are recorded when the shock wave is outside the region confined between the two pressure transducers.

The complete text of this paper may be found in Appendix A.10.

A.11 STUDY OF THE NEAR-WAKE STRUCTURE OF A SUBSONIC BASE CAVITY FLOWFIELD USING PIV

A new particle image velocimetry (PIV) system has been used to study the near-wake structure of a two-dimensional base in subsonic flow in order to determine the fluid dynamic mechanisms of observed base drag reduction in the presence of a base cavity. Experiments were done over a range of freestream Mach numbers up to 0.8, including local flowfield velocities over 300 m/s. Effects of the base cavity on the von Kármán vortex street wake were found to be related to the expansion and diffusion of vortices near the cavity, although the effects are of small magnitude and no significant change in the vortex formation location or path was observed. The base cavity effects are also less significant at higher freestream velocities due to the formation of vortices further downstream from the base. The base cavity drag reduction was found to be mainly due to the displacement of the base surface to a location upstream of the low-pressure wake vortices, with only a slight modification in the vortex street itself.

The complete text of this paper may be found in Appendix A.11.

A.12 AN EXPERIMENTAL INVESTIGATION OF THE SUPERSONIC AXISYMMETRIC BASE FLOW BEHIND A CYLINDRICAL AFTERBODY

An experimental investigation has been conducted to study the flowfield behind a blunt-based circular cylinder aligned with a supersonic freestream. The experiments have been conducted in a newly designed axisymmetric wind tunnel facility at a nominal approach Mach number of 2.5. A cylindrical sting aligned with the axis of the wind tunnel provided the physical support for the bases and afterbodies. Qualitative flowfield information was obtained with spark-schlieren photography and surface oil visualization. Mean wall static pressure measurements were made across the base and along the sting parallel to the wind tunnel axis. A two-component laser Doppler velocimeter (LDV) system was used to document the mean and turbulent velocity fields near the shear layer reattachment point. In addition, the nozzle approach flowfield including the

10

sting boundary layer profile was measured with a one-component LDV configuration. The base pressure measurements indicated only a small dependence on radial location with an average base pressure coefficient of -0.102. Interference waves generated at the junction of the nozzle exit and test section were found to have a large effect on the base pressure profile at certain operating conditions but could be eliminated by proper operation of the tunnel. The shear layer reattachment point was found to lie 1.4 base diameters downstream of the base plane. The entire region surrounding the reattachment point was characterized by large turbulence intensities and steep radial velocity gradients.

The complete manuscript of this thesis is available from the authors of this report.

A.13 DESIGN AND VALIDATION OF AN INTERROGATION SYSTEM FOR PARTICLE IMAGE VELOCIMETRY

A particle image velocimetry (PIV) system has been developed for use as a non-intrusive laser diagnostic tool to complement laser Doppler velocimetry (LDV) in high speed (transonic and supersonic) wind tunnel studies. The PIV system is capable of extracting instantaneous two-dimensional velocity maps within a flow by recording double images of seed particles on photographic film and then examining the local displacement of particle images to determine velocity vectors. The image acquisition system uses two high power pulsed Nd:YAG lasers focused into a thin light sheet to illuminate seed particles for recording on either 35 mm or 4" x 5" format film, with control of seeders, lasers, and the camera shutter performed by a Macintosh II computer. Interrogation of the double-exposed photographs to extract velocity information is done on an image processing system based on a 50 MHz Macintosh workstation, a HeNe laser film illumination source, automated positioners to handle the film, and a CCD array camera. The design of the acquisition system, including special considerations for PIV in high speed flows, is discussed. The theory and design of the interrogation system is described in detail. Finally, results from the cases used to validate and demonstrate the PIV system are presented.

The complete manuscript of this thesis is available from the authors of this report.

A.14 DEVELOPMENT AND APPLICATION OF PARTICLE IMAGE VELOCIMETRY IN HIGH-SPEED SEPARATED FLOW: TWO-DIMENSIONAL BASE CAVITIES

A new particle image velocimetry (PIV) system has been developed to obtain two-dimensional instantaneous velocity data over a planar region in high-speed separated flows for the quantitative analysis of turbulent and unsteady flow structures. This PIV system is the first of its type to incorporate sub-micron seed particles and birefringent image shifting for the resolution of flow velocity in separated regions. The system was also developed with improved in-plane spatial resolution over previous high-speed flow PIV applications by using a 1.0 mm^2 interrogation region (in flowfield dimensions) for each independent velocity measurement. The system has been proven in preliminary experiments using a simple low-speed round jet flow and has been validated for accuracy with both known-displacement simulated PIV photographs and uniform flow experiments at Mach 0.5 (170 m/s) for comparison to pressure and laser Doppler velocimeter (LDV) data.

The PIV system was also used in a study of the near-wake structure of a two-dimensional base in subsonic flow. This application was chosen in order to determine the fluid dynamic mechanism of the observed base drag reduction in the presence of a base cavity. Experiments were done over a range of freestream Mach numbers up to 0.8, including local flowfield velocities up to 300 m/s. Effects of the base cavity on the von Kármán vortex street wake were found to be related to the expansion and diffusion of vortices near the cavity, although the effects are of small magnitude and no significant change of the vortex formation location or path was observed. The base cavity effects are also less significant at higher freestream velocities due to the formation of vortices further downstream from the base. The base cavity drag reduction was found to be mainly due to the displacement of the base surface to a location upstream of the low-pressure wake vortices, with only a slight modification in the vortex street itself.

The complete manuscript of this thesis is available from the authors of this report.

12

A.15 AN EXPERIMENTAL INVESTIGATION OF SUPERSONIC AXISYMMETRIC BASE FLOWS INCLUDING THE EFFECTS OF AFTERBODY BOATTAILING

An experimental investigation of the near-wake flowfield downstream of blunt-based axisymmetric bodies in supersonic flow has been conducted. Using a blowdown-type wind tunnel designed specifically for this purpose, experiments were conducted at a nominal approach Mach number of 2.5 and a unit Reynolds number of 51 (10^6) per meter. Two different axisymmetric afterbodies were examined in the study: a circular cylinder was used as a baseline configuration, and a conical boattailed afterbody with a boattail angle of five degrees and a boattail length of one afterbody radius was used to investigate the effects of afterbody boattailing on the fluid dynamic processes in the near-wake. Neither afterbody contained a central jet so that the base flowfield in unpowered, supersonic flight was simulated. The primary objective of the research program was to enhance the understanding of the fluid dynamic processes inherent to axisymmetric base flows by obtaining and analyzing detailed, non-intrusive experimental data including flow visualization photographs, static pressure measurements, and mean velocity and turbulence data throughout the near-wake. Of special significance in the current research is the detailed turbulence information obtained with laser Doppler velocimetry (LDV) since these data are virtually nonexistent in supersonic base flows and provide new insight into the physics of these complex flows. In addition, the present data form a substantial data base which can be used to advance and improve theoretical and numerical base flow modeling techniques.

The static pressure measurements on the base and afterbody of each model indicate a relatively constant pressure across the base with the addition of the boattail resulting in a decrease in the base drag coefficient of 16% from the baseline cylindrical afterbody. The net afterbody drag coefficient (boattail + base contributions) was reduced by 21% which shows the usefulness of afterbody boattailing as a practical method to reduce afterbody drag in supersonic, axisymmetric flow. The mean velocity and turbulence fields in the near-wake of each afterbody were investigated with LDV. In general, the near-wake flowfield can be characterized by large turbulence levels in the separated shear layer, relatively large reverse velocities in the recirculation

13

region, and gradual recompression/realignment processes as the shear layer converges on the axis of symmetry. The shear layer development was found to be dependent on the conditions immediately downstream of the base corner separation point (upstream history effect). Furthermore, the centered expansion at the base corner reduced the turbulence levels in the outer region of the shear layer relative to the approach boundary layer but enhanced the mixing and entrainment along the fluid-fluid interface between the shear layer and the recirculating region which results in large turbulence levels along the inner edge of the shear layer. The shear layer growth rate is initially large due to substantial mass entrainment from the recirculation region near the inner edge, but further downstream, a self-similar state is reached where growth rates are significantly reduced. In general, the effects of afterbody boattailing on the near-wake flowfield include a weaker expansion at the base corner separation point (less distortion of the shear layer and reduced turbulence production near the inner edge), reduced turbulence intensity and Reynolds shear stress levels throughout the near-wake (reduced mass entrainment along the length of the shear layer resulting in a higher base pressure), and a mean velocity field which is qualitatively similar to that of the cylindrical afterbody.

The complete manuscript of this thesis is available from the authors of this report.

III. LIST OF PUBLICATIONS

A substantial number of journal articles, conference proceedings papers, and graduate student theses have reported the results of this research effort. The following is a list of those publications.

A. JOURNAL ARTICLES

Kruiswyk, R. W. and Dutton, J. C., "Effects of a Base Cavity on Subsonic Near-Wake Flow," _AIAA Journal_, Vol. 28, No. 11, November 1990, pp. 1885-1893.

Amatucci, V. A., Dutton, J. C., Kuntz, D. W., and Addy, A. L., "Two-Stream, Supersonic, Wake Flowfield Behind a Thick Base, Part I: General Features," _AIAA Journal_, Vol. 30, No. 8, August 1992, pp. 2039-2046.

Molezzi, M. J. and Dutton, J. C., "Application of Particle Image Velocimetry in High-Speed Separated Flows," _AIAA Journal_, Vol. 31, No. 3, March 1993, pp. 438-446.

Herrin, J. L. and Dutton, J. C., "An Investigation of LDV Velocity Bias Correction Techniques for High-Speed Separated Flows," accepted for publication in _Experiments in Fluids_.

Herrin, J. L. and Dutton, J. C., "Supersonic Base Flow Experiments in the Near-Wake of a Cylindrical Afterbody," accepted for publication in the _AIAA Journal_.

B. CONFERENCE PROCEEDINGS PAPERS

Amatucci, V. A., Dutton, J. C., Kuntz, D. W., and Addy, A. L., "Experimental Investigation of an Embedded Separated Flow Region Between Two Supersonic Streams," AIAA Paper No. 90-0707, presented at the _28th AIAA Aerospace Sciences Meeting_, Reno, Nevada, January 1990.

Herrin, J. L., "An Experimental Investigation of Axisymmetric Power-Off Base Flow Phenomena," paper presented at the _AIAA Student Regional Conference_, Purdue University, West Lafayette, Indiana, March 1991.

Rosner, R. A., "Design of a Particle Image Velocimeter for High Speed Flows," paper presented at the _AIAA Student Regional Conference_, Purdue University, West Lafayette, Indiana, March 1991; also presented as AIAA Paper No. 92-0259 at the _30th AIAA Aerospace Sciences Meeting_, Reno, Nevada, January 1992.

Molezzi, M. J. and Dutton, J. C., "Development and Application of a Particle Image Velocimeter for High Speed Flows," AIAA Paper No. 92-0004, presented at the _30th AIAA Aerospace Sciences Meeting_, Reno, Nevada, January 1992.

Shaw, R. J. and Dutton, J. C., "A Plume-Induced Boundary Layer Separation Experiment," paper presented at the 77th Semi-Annual Supersonic Tunnel Association Meeting, University of Notre Dame, Notre Dame, Indiana, April 1992.

Herrin, J. L. and Dutton, J. C., "Supersonic Base Flow Experiments in the Near-Wake of a Cylindrical Afterbody," AIAA Paper No. 93-2924, presented at the 24th AIAA Fluid Dynamics Meeting, Orlando, Florida, July 1993.

Molezzi, M. J. and Dutton, J. C., "Study of the Near-Wake Structure of a Subsonic Base Cavity Flowfield Using PIV," AIAA Paper No. 93-3040, presented at the 24th AIAA Fluid Dynamics Meeting, Orlando, Florida, July 1993.

C. THESES

Herrin, J. L., "An Experimental Investigation of the Supersonic Axisymmetric Base Flow Behind a Cylindrical Afterbody," M.S. Thesis, Department of Mechanical and Industrial Engineering, University of Illinois at Urbana-Champaign, May 1991.

Rosner, R. A., "Design and Validation of an Interrogation System for Particle Image Velocimetry," M.S. Thesis, Department of Mechanical and Industrial Engineering, University of Illinois at Urbana-Champaign, May 1991.

Molezzi, M. J., "Development and Application of Particle Image Velocimetry in High-Speed Separated Flow: Two-Dimensional Base Cavities," Ph.D. Thesis, Department of Mechanical and Industrial Engineering, University of Illinois at Urbana-Champaign, April 1993.

Herrin, J. L., "An Experimental Investigation of Supersonic Axisymmetric Base Flows Including the Effects of Afterbody Boattailing," Ph.D. Thesis, Department of Mechanical and Industrial Engineering, University of Illinois at Urbana-Champaign, July 1993.

IV. LIST OF PARTICIPATING SCIENTIFIC PERSONNEL
AND ADVANCED DEGREES EARNED

Following are lists of the faculty and graduate student scientific personnel who have contributed to this research effort and the graduate degrees that have been earned in conjunction with this project.

A. FACULTY

A. L. Addy
Co-Principal Investigator
Professor and Head of Mechanical Engineering

J. C. Dutton
Co-Principal Investigator
Professor of Mechanical Engineering

B. GRADUATE STUDENTS

J. L. Herrin	T. Mathur
M.S. 1991	M. S. 1990
Ph.D. 1993	Ph.D. Candidate
M. J. Molezzi	R. A. Rosner
M.S. 1988	B.S. 1989
Ph.D. 1993	M.S. 1991
R. J. Shaw	
M.S. 1986	
Ph.D. Candidate	

C. ADVANCED DEGREES EARNED

J. L. Herrin	R. A. Rosner
M.S., May 1991	M.S., May 1991
M. J. Molezzi	J. L. Herrin
Ph.D., April 1993	Ph.D., July 1993

V. CONTINUING AND FUTURE RESEARCH ACTIVITIES

As a result of continued funding by the U.S. Army Research Office, the investigation reported on herein will be continued for an additional three-year period. Future studies will build on our experience over the last several years of experimentally investigating several fundamental high-speed separated flow configurations that have particular relevance to projectile and missile base flows. As discussed in this report, flowfields studied in the past include the near-wake region of a cylindrical afterbody, plume-induced boundary layer separation, and near-wake flowfield modifications due to the presence of a base cavity. The previous measurements included conventional schlieren and shadowgraph photography, surface streakline visualization, mean and fluctuating static pressure measurements, with major emphasis on two-component, coincident laser Doppler velocimetry (LDV) and particle image velocimetry (PIV) measurements. In addition to pointwise measurements, the ongoing work will emphasize the further development and implementation of planar diagnostic techniques, such as Mie scattering light sheet visualization and PIV, in order to address such questions as the existence and role of large-scale turbulent structures in these flows, mechanisms of entrainment, mixing, reattachment, and redevelopment, the instantaneous structure of these flowfields, etc. Brief descriptions of the specific experimental studies to be conducted in the ongoing research program are given below.

The continuing experimental research effort consists of three interrelated projects whose overall goal is to quantify and better understand the complex features and interactions that occur in separated high-speed flows. The results of these studies will be of substantial benefit to the U.S. Army in a number of applications, most directly for improved prediction and design of the flight characteristics of projectiles and missiles through a better understanding of the features of the separated base flow region of these devices.

In the first project, two commonly used drag reduction techniques for supersonic axisymmetric base flows will be investigated, boattailing and base bleed. Detailed mean and turbulent velocity measurements will be obtained in the near-wake regions for each case using laser

Doppler velocimetry. Emphasis will be placed on determining the statistical description of the initial shear layer formation process at separation, the growth and development of the shear layer, the flow patterns occurring in the separated region, the recompression/reattachment phenomena near the rear stagnation point, and the redevelopment of the trailing wake. The effects of boattailing and base bleed on these processes will also be examined by comparison to data for a blunt base cylindrical afterbody that are currently being obtained.

The objective of the second project is to augment the pointwise statistical description of the velocity field obtained from LDV with temporally and spatially resolved planar visualization and measurement studies. The techniques to be used are planar laser sheet visualization (Mie scattering) and particle image velocimetry. The experiments will be conducted in the near-wake of a cylindrical afterbody in supersonic flow both with and without base bleed. The purpose of these experiments is to visualize and quantify the time-resolved planar structure of supersonic base flows, in particular the existence, dominance, and evolution of large scale turbulent structures in these flows. Study of these structures is of importance because of their influence in determining entrainment and mixing phenomena in shear layers, jets, and wakes.

The third project is focused on the study of plume-induced boundary layer separation, whereby separation of one supersonic stream is caused by impinging it at an angle with a second, such as occurs in powered missile applications. The emphasis in this investigation will also be on using planar measurement methods, Mie scattering and PIV, to determine the instantaneous planar structure of this interaction and the importance and evolution of large scale turbulent structures in it. Major differences between this flow and supersonic flow over a cylindrical afterbody are that the separation occurs under adverse pressure gradient conditions and that it is unsteady. Thus, emphasis will be placed on comparing the turbulence structure between the two cases. In addition, the planar images will be examined for determination of possible causes of the unsteadiness of the plume-induced separation process.

During the first year of the program, LDV measurements for the boattail model will be obtained, ongoing conditionally analyzed LDV measurements of the plume-induced separation

19

interaction will be completed, several facilities and instrumentation modifications and developments will be carried out, and Mie scattering studies of the cylindrical afterbody and plume-induced separation experiment will be started. During the second year, several additional facilities upgrades will be completed, the Mie scattering visualization studies of the cylindrical afterbody, base bleed, and plume-induced separation experiments will be conducted, and PIV and flow visualization and pressure measurement studies of the plume-induced separation and base bleed experiments, respectively, will be obtained. The final year of the program will be devoted to LDV measurements of the base bleed case, PIV measurements of the cylindrical afterbody case both with and without base bleed, and further Mie scattering and PIV studies of plume-induced separation.

By carrying out this integrated series of experimental studies, substantially improved understanding of high-speed separated base flows will be gained, so that they can be better predicted, controlled, and perhaps even optimized in applications of importance to the U.S. Army and others.

APPENDIX A.1

EFFECTS OF A BASE CAVITY ON SUBSONIC NEAR-WAKE FLOW

by

R. W. Kruiswyk and J. C. Dutton

Effects of Base Cavity on Subsonic Near-Wake Flow

R. W. Kruiswyk and J. C. Dutton

Effects of a Base Cavity on Subsonic Near-Wake Flow

R. W. Kruiswyk* and J. C. Dutton†

University of Illinois at Urbana-Champaign, Urbana, Illinois 61801

An experimental investigation has been conducted to study the effects of a base cavity on the near-wake flowfield of a slender, two-dimensional body in the subsonic speed range. Three base configurations were investigated and compared: a blunt base, a shallow rectangular cavity base of depth equal to one-half the base height, and a deep rectangular cavity base of depth equal to one base height. Each configuration was studied at three freestream Mach numbers ranging from the low to high subsonic range. Schlieren photographs revealed that the basic qualitative structure of the vortex street was unmodified by the presence of a base cavity. However, the vortex street was weakened by the base cavity apparently due to the enhanced fluid mixing occurring at the entrance of the cavity. The weaker vortex street yielded higher pressures in the near wake for the cavity bases, increases in the base pressure coefficients on the order of 10-14%, and increases in the shedding frequencies on the order of 4-6% relative to the blunt-based configuration. The majority of the observed changes occurred in going from the blunt base to the shallow cavity base.

Nomenclature

C_p	= coefficient of pressure, $\equiv (P - P_{ref})/(1/2\rho_{ref}U_{ref}^2)$
d	= cavity depth
f	= frequency
h	= base height
M	= Mach number
P	= pressure
Re	= Reynolds number, $\equiv \rho_{ref}U_{ref}h/\mu_{ref}$
St	= Strouhal number, $\equiv fh/U_{ref}$
U	= freestream velocity
x	= streamwise coordinate measured from the trailing edge plane
u	= absolute viscosity
ρ	= density

Subscripts

base	= base location
ref	= reference location
∞	= freestream conditions

Introduction

THE near wake of a two-dimensional bluff body at subsonic Mach numbers and sufficiently high Reynolds numbers (greater than 50 based on freestream conditions and body thickness) is dominated by the periodic and alternate shedding of vortices known as the von Karman vortex street. When these vortices form near the leeward side or base of the body, the low pressure of the vortex centers is communicated to the base producing a low-base pressure. This combines with the momentum loss associated with the concentrations of vorticity to yield an especially high-base drag. The von Karman vortex street occurs frequently in engineering applica-

tions and has even been observed behind such slender bodies as turbine blades of just 3% thickness ratio.[1] Because the base drag (often the dominant drag component) of both bluff and slender two-dimensional bodies is affected by the strength and proximity of the vortex street, any attempts at base drag reduction must be aimed at weakening the vortex shedding or at displacing the vortex formation position further downstream.

The present investigation focuses on the use of a base cavity as a drag reducing mechanism and on the effect of such a cavity on the near-wake flowfield of a two-dimensional slender body in the subsonic speed range (see Fig. 1). The base cavity has proven effective in reducing drag in several past investigations. However, the precise mechanism of this drag reduction is still unknown. Therefore, the present study is aimed at investigating the interaction between the cavity and the separated flow and the effect of this interaction on the fluid dynamic mechanisms in the near wake. The specific objectives of the investigation are to explain the drag reducing effect of the base cavity, to improve understanding of the phenomena of vortex formation and shedding, and to resolve some of the conflicts that have arisen between the numerical and experimental work on base cavities to date.

Experimental investigations of the base cavity have been conducted by Nash et al.,[2] Pollock,[3] and Clements[4] among others. They have studied cavity depths of from zero to two base heights on slender, two-dimensional bodies. Generally, they have found base drag reductions of 15-20% in the subsonic speed range and no effect into the supersonic speed range. The lack of any effect at supersonic speeds is evidence that the cavity acts on the vortex street since vortex shedding ceases at Mach numbers just beyond 1.0. Clements investigated cavities of various depths and reported base pressure' increases for increasing cavity depths up to 1/2 base height, beyond which no further increases in base pressure were observed. Clements also measured a rise in the Strouhal number (i.e., vortex shedding frequency) for increasing cavity depth up to 1/2 base height. Although Nash et al. hypothesized that the walls of the cavity may constrain the upstream part of the vortices and thus improve wake stability, their schlieren photographs did not appear to show any vortex motion extending into the base cavity.

Two important computational efforts on the effects of base cavities have been carried out by Clements[4] and Rudy.[5] Clements employed an inviscid discrete vortex method, whereas Rudy used an explicit, Navier-Stokes, finite-differ-
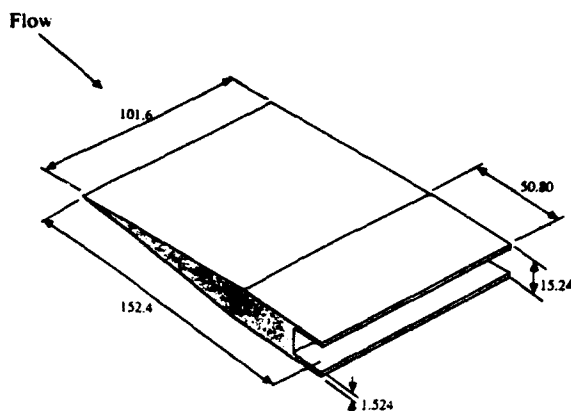
Fig. 1 Schematic of model (dimensions in mm).

Fig. 2 Model configurations under investigation: a) blunt base; b) shallow cavity base, depth = 1/2 base height; c) deep cavity base, depth = 1 base height.

ence scheme at freestream Mach numbers of 0.4 and 0.6 with laminar Reynolds numbers (based on freestream conditions and the base height) of 700 and 962, respectively. Both investigators studied the effects of a rectangular cavity in the base of a slender, two-dimensional body at subsonic speeds. Clements and Rudy both found that the vortices penetrate partially into the cavity for at least a portion of the shedding cycle. Rudy reported that the pressure rises in the low-velocity region between the first vortex and the back of the cavity yielding a higher base pressure for the cavity base as compared to the blunt base. Because of this result, Rudy hypothesized that the drag reducing effect of the base cavity is similar to that of splitter plates and base bleed,[6-11] i.e., it is due to the increased distance between the base of the body and the vortex formation location. Interestingly, both Clements and Rudy computed a continuous decrease in the Strouhal number with increasing cavity depth in direct contrast to the experimental results of Clements. Rudy attributed the decrease in shedding frequency to the increase in interaction between the vortices in the presence of a cavity.

Experimental Setup

Wind-Tunnel Facilities and Model

A previously fabricated two-dimensional transonic wind tunnel was used in this investigation. This tunnel has a 101.6 mm × 101.6 mm test section and was built based on a NASA design by Little and Cubbage.[12] The sidewalls of the tunnel are solid, whereas the upper and lower walls are slotted to relieve the blockage effect of the model and to allow experimentation through the transonic speed range. A pair of round windows may be mounted in the sidewalls to allow visualization of the flow over the aft end of the model and in the near wake. Solid aluminum inserts may also be used in place of the windows for the wake static pressure traverses and shedding frequency measurements described below. The results of tunnel-empty calibrations at Mach numbers from the low subsonic through transonic speed ranges demonstrated that this tunnel produces remarkably uniform flow.

To accomplish the objectives of this study, the two-dimensional model illustrated in Fig. 1 was constructed. The model has a wedge-shaped forebody, a constant 10% thick afterbody, and three interchangeable base geometries (see Fig. 2): a blunt base, a shallow rectangular cavity base with depth equal to one-half the base height, and a deep rectangular cavity base with depth equal to one base height. This model is similar to that used in the experiments of Nash et al.[2] and is identical to the computational geometry used by Rudy,[5] except that Rudy's cavity heights were 90% of the base height, and those of the current experiments were 80% of the base height to ensure structural rigidity of the extended portions of the base.
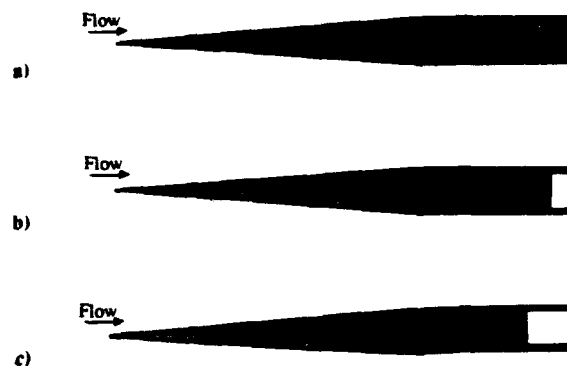
The maximum blockage of the model in the wind tunnel of this study was 15% (see Fig. 1), which is a bit high by transonic tunnel standards. This model size was chosen to be as small as possible to minimize blockage effects while remaining large enough to adequately instrument the base with pressure taps and so that the flowfield could be adequately resolved with the available measurement techniques. In addition, larger than normal interference effects were deemed acceptable in light of the objectives of this investigation to study the physical mechanisms of the flowfield and the trends that the data exhibit with either increasing cavity depth or increasing Mach number. These mechanisms and trends should be accurately reflected in the current measurements even if small errors in the absolute values of the data occur due to interference effects. Also, the basic structure of the vortex street, which is of prime importance here, should not be strongly affected by the blockage of the model. As evidence, El-Sherbiny and Modi[13] found that the lateral and longitudinal spacings of the vortices in the wakes behind inclined flat plates were independent of blockage ratios up to 20%.

Measurement Techniques

Black and white schlieren photography was used to visualize the structure of the vortex streets behind the model and to determine to what degree the vortex motions extended into the cavities. The schlieren system used was a standard Toepler arrangement with the sending and receiving optics located off axis in the familiar "z" pattern and with parabolic mirrors directing the parallel light beam through the test section. A straight knife edge in the cut off plane provided exposure and sensitivity control and was set parallel to the flow direction (i.e., horizontally) to allow visualization of the separating shear layers. The light source was a Xenon model 457 flash lamp with a flash duration of 1.4 μs. Processing of large numbers of photographs was accomplished via a 35 mm format camera and Kodak Panatomic-X (ASA 32) roll film.

Surface oil flow visualization was utilized to ascertain flow directions within the cavities and on the model and to examine the streakline patterns formed on the tunnel sidewalls. A mixture of lampblack and a 90 weight viscous oil was used for this purpose. This mixture was either spread evenly on the surface of interest with a paint brush or applied as discrete dots of oil to yield highly defined surface streakline patterns.

Tuft visualization was used to further examine the air motions within the cavities and to complement the results of the surface flow studies. Short strands of a lightweight white thread were fixed with small dots of rubber cement to the trailing edge of the deep cavity, whereas several others were suspended from the upper cavity wall at depths of 1/3, 1/2, and 2/3 base heights from the entrance.

Base pressure measurements were made to determine the effect of cavity depth on base drag. Fifteen static pressure taps

were distributed across each base so as to reveal any variations in pressure across the span or height of the base. These taps were connected via nylon tubing to a Pressure Systems Incorporated (PSI) model DPT 6400 electronic pressure scanner. The output from the PSI system was directed to an HP-9000 minicomputer for data analysis and storage.

Vortex shedding frequency measurements were made to determine the effect of the cavities on the shedding frequency and to help resolve the previously mentioned conflict between numerical and experimental results. The shedding frequencies were determined from a Fourier analysis of the signal from fast response pressure transducers. The transducers used were Endevco model 8506B-15 piezo-resistive pressure transducers, which have a 2.31 mm face diam and a resonant frequency of 130 kHz. The data from the transducers were collected with a DEC PDP 11/73 microcomputer using a Data Translation model DT2752 high-speed, 12 bit, 8 channel, A/D converter. For each Mach number-base geometry configuration, 50 sets of 4096 data points were collected at a sampling rate of 20 kHz yielding a bandwidth of approximately 4.88 Hz. The time domain pressure data were analog filtered at 80% of the Nyquist rate (i.e., 8000 Hz) to prevent aliasing and were transformed into the frequency domain via a fast Fourier routine utilizing the Hanning window to suppress side-lobe leakage. The data sets were also averaged in the spectral domain to filter out low-level white noise.

Static pressure surveys of the wake were performed in order to define the position of vortex formation for each of the base configurations. This method has been employed in previous investigations by Nash et al.[2] and Roshko,[6] who state that the location of a low-pressure trough in the wake behind a body coincides with the position of vortex formation. Four different 3.175 mm diam static probes were used with the static holes ranging in distances from 3.175 to 12.5 mm from the tip of the probe. Eight exit holes were drilled in the solid sidewall insert at intervals of 7.62 mm (1/2 base height), and in conjunction with the four probes, these gave up to 32 possible pressure measurement locations from the base of the body to a distance of four base heights downstream. Data gathering and reduction followed the same procedures as described previously for the base pressure measurements.

Further details concerning the experimental apparatus, instrumentation, and measurement and data reduction procedures may be found in Ref. 14.

Experimental Results

Experimental Conditions

The experimental results for the three base geometries shown in Fig. 2 were obtained at three different Mach numbers ranging from the low to the high subsonic range to give a total of nine different experimental conditions (see Table 1).

Rather than try to apply a freestream Mach number correction to account for the effects of model blockage, a reference Mach number was specified as measured in the tunnel, i.e., without correction factors, that would be most relevant to the flowfield region of greatest interest, namely the vortex street

and near wake. Thus, the reference Mach number was chosen to be that outside the boundary layer over the aft end of the model just prior to separation. The three values of the reference Mach number shown in Table 1 were chosen to correspond approximately to freestream flows at Mach 0.4, 0.6, and 0.8. The reference of 0.880 was chosen by matching the schlieren photograph at that condition to the schlieren of Nash et al.[2] of a freestream Mach 0.8 flow over the same model geometry in a much larger tunnel with essentially interference-free conditions. The reference of 0.720 was chosen via Rudy's[5] computations, which indicate that at a freestream Mach number of 0.6 the Mach number over the aft end of the body is 0.720. Finally, the reference of 0.485 was chosen by setting the upstream Mach number in the tunnel to 0.4, as it was known that interference effects would be relatively small at the lower Mach number.

The Reynolds numbers listed in the table are based on conditions at the reference location and the base height. Boundary-layer trips (0.25 mm diam hypodermic tubing) were placed at the 10% chord location to fix the transition points. Thus, the boundary layers at separation from the base were turbulent in all cases. The boundary-layer thickness at separation for each case was estimated to be 1.5 mm from enlarged schlieren photographs.

a)

b)

c)

Fig. 3   Schlieren photographs of the near-wake flowfield for the blunt-base configuration: a) $M_{ref} = 0.485$; b) $M_{ref} = 0.720$; c) $M_{ref} = 0.880$.

Table 1   Experimental conditions

Base type	Ref. Mach no.	Ref. Reynolds no., $\times 10^5$
Blunt base	0.485	1.62
	0.720	2.32
	0.880	2.78
Shallow cavity	0.485	1.62
	0.720	2.32
	0.880	2.78
Deep cavity	0.485	1.62
	0.720	2.32
	0.880	2.78

Schlieren Photographs

Schlieren photography was used to visualize the structure of the vortices behind the models and to reveal any qualitative differences that may exist in the near wakes of the flows for the different base configurations and Mach numbers. Figure 3a depicts the flow over the model fitted with the blunt base at a reference Mach number of 0.485 (the screw visible in the photograph was used for focusing purposes and is outside the tunnel). In this case the vortex shed from the upper surface of the body has apparently reached the fully formed condition, whereas the shear layer separating from the lower surface is just beginning to roll up. It is clear from this figure that the vortices form right at the base of the body and that in the fully formed condition, the vortices extend over the majority of the thickness of the base. Figures 3b and 3c show the flowfield over the blunt-based model at reference Mach numbers of 0.720 and 0.880, respectively. The basic features of the near-wake flowfield for these cases are similar to the Mach 0.485 flowfield, except that the vortex street becomes more obscured by turbulence at the higher Mach numbers and at Mach 0.880 pressure waves generated from the vortex shedding are evident at the base of the model. Comparison of these schlieren photographs with Rudy's[5] computed vorticity contour plots for a freestream Mach 0.6 flow over the same blunt-based configuration indicates excellent qualitative agreement for the near-wake structure, particularly in terms of the proximity of the vortex formation location to the base. Some minor differences, such as more rapid diffusion of the vortices in the experiments, may be attributed to the fact that the boundary layers at separation are turbulent in the experiments and laminar in the computations.

Figures 4a and 4b are schlieren photographs of the flow over the model fitted with the shallow cavity base at reference Mach numbers of 0.485 and 0.720, respectively. The basic structure of the vortex street appears unchanged in comparison to the blunt-based configuration just discussed. By comparing schlieren pictures of the flow for the two geometries at

similar points in the shedding cycle, the spacing of the vortices and the spread rate of the vortex street in the early part of the wake appear virtually identical, as though the base cavity does not influence the vortex formation and shedding process at all. However, a closer examination shows that for the cavity base, the vortices may form slightly farther downstream of the trailing-edge plane; whereas this is impossible to confirm from a single still photograph. This point will be discussed further in light of other experimental results to be presented in the sections to follow. The main difference between the various Mach number conditions for the shallow cavity base is again the presence of more turbulence at the higher Mach numbers resulting in greater diffusion of the vortices. Comparison of Rudy's[5] computed vorticity plots with these schlieren photographs for the shallow cavity base shows that the experimental and computational results are not in agreement for this case. The schlieren pictures (including many others not shown here) indicate clearly that the vortices do not extend into the cavity during any portion of the shedding cycle, whereas Rudy's computational results (as well as those of Clements[4]) indicate that the vortices form at least partially within the cavity throughout the shedding cycle. This discrepancy between experiments and computations for base cavity flows was also reported by Clements. Further discussion of this point will follow the presentation of the remainder of the experimental results.

Figures 5a and 5b depict the flow over the model fitted with the deep cavity base at $M_{ref} = 0.485$ and 0.720, respectively. Again the basic structure of the vortex street wake appears unchanged in comparison to the wakes of the two base configurations discussed above. In fact, Figs. 4b and 5b at $M_{ref} = 0.720$ look virtually identical except for the geometry of the base itself. For the deep cavity base, as for the shallow one, it appears that the vortices form slightly further downstream of the trailing-edge plane than they did for the blunt-based configuration. Comparing the schlieren photographs of Fig. 5 with Rudy's[5] constant vorticity lines for the Mach 0.6 computations of the deep cavity configuration indicate the

a)

b)

Fig. 4 Schlieren photographs of the near-wake flowfield for the shallow cavity base configuration: a) $M_{ref} = 0.485$; b) $M_{ref} = 0.720$.

a)

b)

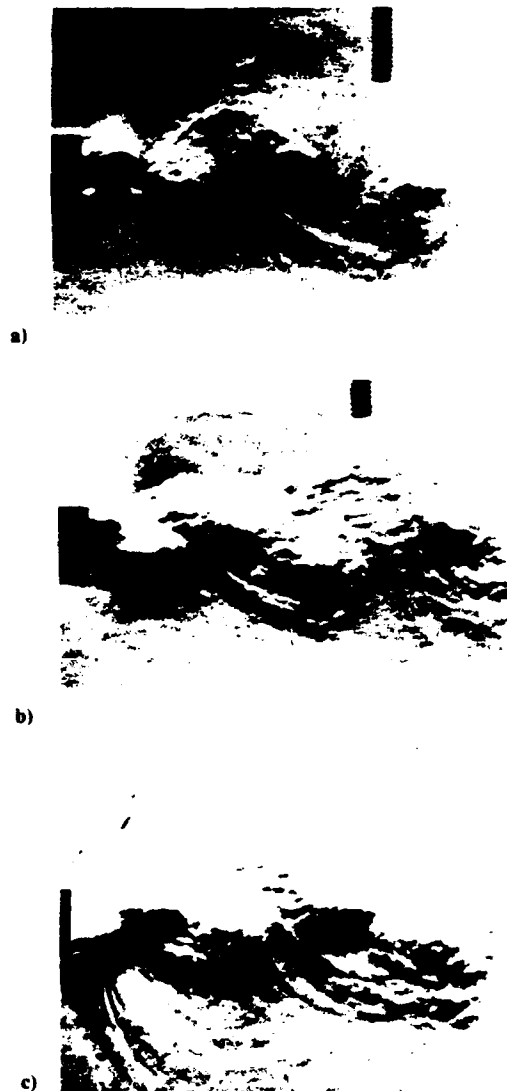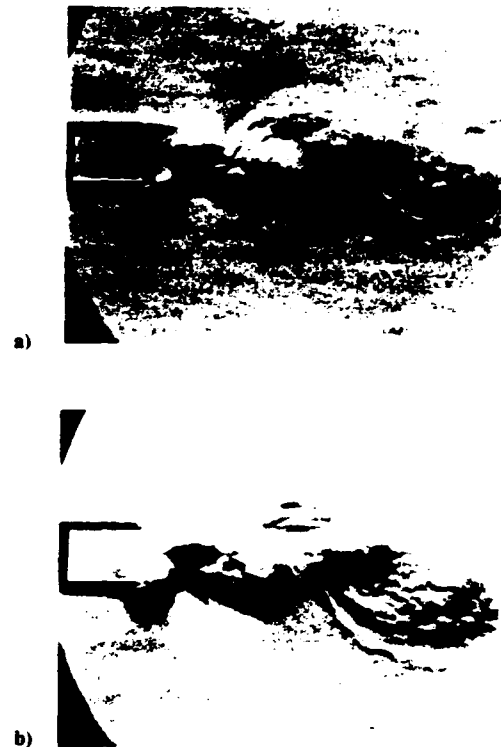Fig. 5 Schlieren photographs of the near-wake flowfield for the deep cavity base configuration: a) $M_{ref} = 0.485$; b) $M_{ref} = 0.720$.
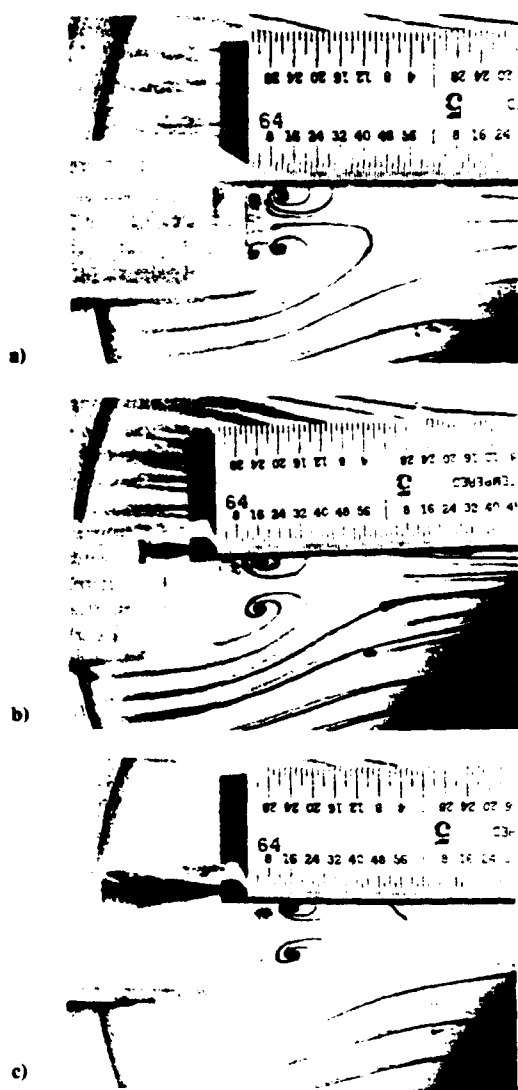
Fig. 6   Oil streak patterns on sidewall for $M_{ref} = 0.485$; a) blunt-base configuration; b) shallow cavity base configuration; c) deep cavity base configuration.

same discrepancy between the computational and experimental results noted above: the schlierent photographs show no vortex motion extending into the cavity whatsoever, whereas the computations show the vortices extending well into the cavity throughout the shedding cycle. As mentioned, this point will be discussed further below.

Surface Oil-Flow Patterns

The surface oil-flow visualization results presented here are intended to answer several important questions regarding the qualitative nature of the flowfield: first, to ascertain that the flow in the tunnel is satisfactorily two dimensional; second, to determine whether any significant fluid motion occurs within the base cavities; and finally, to help determine if the vortices form farther downstream from the trailing-edge plane for the cavity bases in comparison to the blunt-based model, as was hinted at by the schlieren stills.

The oil-flow patterns across the span of the upper surface of all three models and for all three reference Mach numbers indicated that the flow was appropriately two dimensional, i.e., the streaklines were extremely straight and in the streamwise direction with no recirculatory regions even very near the sidewalls. For the blunt-based model, essentially vertical streak patterns on the base were formed from a series of oil dots placed across the span of the base midway between the

upper and lower trailing edges. Apparently, the mean effect of the vortices shed from alternate trailings edges was to push some of the oil to the upper trailing edge and some to the lower trailing edge. The clarity and rapidity with which these streak patterns formed indicates that the vortices do indeed form immediately adjacent to the base for the blunt-based model, as was evident in the schlieren photographs of Fig. 3.

To determine the surface flow patterns on the internal cavity surfaces of the two cavity configurations, oil was spread on all cavity surfaces, and even as discrete dots very near the lip of the cavity. However, no streak patterns were formed on any of these internal cavity surfaces. This indicates that there is no strong vortex motion extending into the cavity and that apparently no significant recirculatory motion occurs in the cavity at all. The specifics of the air motions, if any, in the cavities will be discussed in some of the results to follow.

Figures 6a–6c are reproductions of the near-wake oil streak patterns that were formed on the wind-tunnel sidewalls for each base configuration with a scale placed so as to indicate the distance of the oil "vortices" from the trailing-edge plane. The reference Mach number for these figures is 0.485, although similar patterns were formed for all three reference Mach number conditions. These streak patterns simply represent the time-mean effect of the unsteady vortex street wake phenomenon as determined at the tunnel sidewall. The centers of the vortices of oil that formed on the sidewall are considered to indirectly represent the correct relative position of vortex formation for the three base configurations. In other words, while the absolute position of vortex formation relative to the trailing-edge plane may not be correctly represented due to the time-averaging and sidewall boundary-layer effects, the position of vortex formation for one base geometry relative to the other bases should be approximately correct assuming that these effects influence the oil streaks for all three base configurations approximately equally. These photographs indicate the center of the sidewall oil vortex to be about 3/16 in. (4.76 mm or 0.31 base height) from the trailing edge for the blunt base and about 1/4 in. (6.35 mm or 0.42 base height) for the two cavity bases, a difference of approximately 1/16 in. (1.59 mm). Similar results were found at reference Mach number conditions of 0.720 and 0.880 Therefore, these photographs suggest the qualitative fact that the vortex formation position for the cavity bases is further downstream from the trailing-edge plane relative to that for the blunt-base configuration. Further support for this argument is presented in the section discussing the wake static pressure traverses.

Tuft Visualizations

The fact that the surface oil-flow patterns showed no significant recirculatory flow in the cavity revealed the need for a more sensitive measurement technique to determine if any fluid motion occurs in the cavity. To this end the tuft visualization experiments described earlier were performed with several lightweight tufts attached to the trailing edge of the deep cavity, as well as from the upper cavity wall at several depths from the cavity entrance. The tufts at the trailing-edge plane were extremely active, rotating rapidly back and forth in the streamwise direction in a 75 to 80 deg arc, nearly 45 deg in the downstream direction and roughly 30 to 35 deg back upstream into the cavity. Some spanwise motion was also observed, though to a much lesser extent. This high degree of activity is not unexpected; since the vortices form close to the trailing-edge plane even for the deep cavity; the tufts there are subjected to a rapid periodic pressure variation. For the tufts suspended further back in the cavity, the motion was similar, but the level of activity decreased gradually from the trailing edge to the back of the cavity. These results suggest that the periodic pressure pulses from the shedding vortices set the air in the cavity into a rapid vibratory motion but without any strong net flow direction as would be sensed by the surface oil coatings.

Wake Static Pressure Traverses

The static pressure traverses of the near-wake region, along the centerline of the body and away from the tunnel sidewall boundary layers, were performed to help confirm the apparent observation that the vortices form farther downstream in the presence of a base cavity. Because these measurements were time consuming and because the sidewall surface streaklines indicated similar trends in the vortex formation location for all three reference Mach numbers, these measurements were made at $M_{ref} = 0.485$ only.

The streamwise variation of the near-wake static pressure coefficient $C_p \equiv (P - P_{ref})/(1/2\rho_{ref}U_{ref}^2)$ for the three base geometries is shown in Fig. 7. The plots display the characteristic features of the vortex street wake as described by Nash et al.[2] and Roshko,[6] namely a low-pressure trough in the near wake at the vortex formation position followed by a gradual rise in pressure to an essentially constant value further downstream. This figure shows clearly that the location of vortex formation has indeed been displaced slightly farther downstream from the trailing-edge plane in the presence of a base cavity. In addition, the plots for the shallow cavity base and the deep cavity base overlap each other quite closely except for some data scatter between two and four base heights downstream of the trailing edge. This result agrees with the sidewall oil-flow visualizations and suggests that increasing the cavity depth beyond 1/2 base height has no further effect in pushing the vortex formation position downstream. Examination of Figs. 6 and 7 also shows that both the sidewall oil streak patterns and the wake static pressure traverses indicate a downstream displacement of the vortex formation position of approximately 1/10 base height for the cavity bases relative to the blunt base.
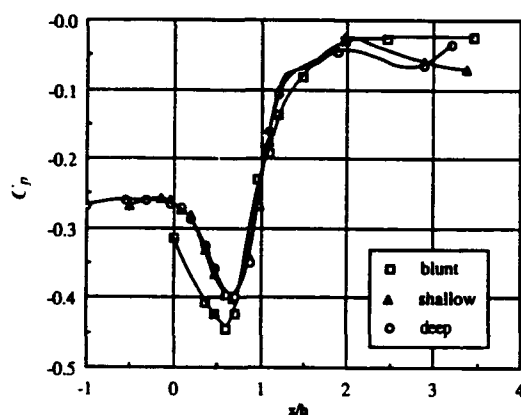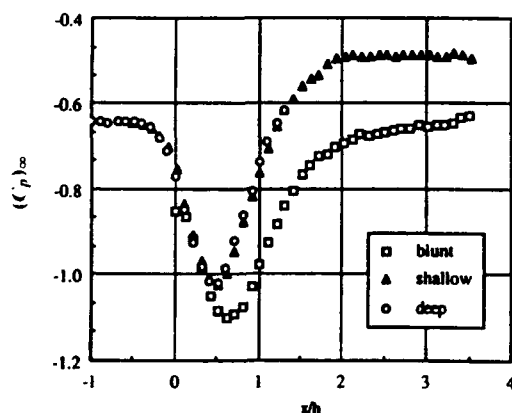
The results in Fig. 7 may be compared to those in Fig. 8, which has been adapted from the computational study of Rudy[5] for a freestream Mach number of 0.4. The curves in Fig. 8 have been obtained by averaging the instantaneous pressures at eight different times in the shedding cycle. Also note that Rudy's pressure coefficient is based on freestream conditions, $(C_p)_\infty \equiv (P - P_\infty)/(1/2\rho_\infty U_\infty^2)$, which is the reason for the discrepancy in the magnitudes of the pressure coefficients in Figs. 7 and 8. However, it is the location of vortex formation and the trends with cavity depth that are of primary interest here. The agreement between the experimental (Fig. 7) and computational (Fig. 8) results for the vortex formation location is excellent for the blunt-based configuration but not for the cavity bases where the computations indicate that the vortex formation position moves upstream. These results then follow the same trends seen earlier in comparing the schlieren photographs of the present study to Rudy's vorticity plots.

The experimental results in Fig. 7 also reveal that the static pressure within the cavities remains essentially constant. This is again in contrast with the computations but confirms the experimental observations made earlier that there is no significant recirculatory motion in the cavities. Note in Fig. 8 that the computations indicate a rapid rise in pressure from the trailing-edge plane to about midway back in the cavities as a result of the vortices extending partially into the cavity. A final observation on the measurements in Fig. 7 is that the cavity bases cause an increase not only in the base-pressure coefficient but also in the values of the pressure coefficient in the near wake within roughly 5/8 base heights of the trailing-edge plane. This point will be considered further in the discussion below.

Base Pressure Measurements

As mentioned, 15 static pressure taps were distributed across the base of each model to determine if any significant transverse or spanwise base pressure variations were present. For most of the Mach number-base geometry configurations, the base pressure distributions were quite uniform, though there was a tendency for the pressures near the sidewalls to be slightly higher than at the midpoint (maximum variations were generally less than 2%). The average of the pressures at the 15 taps was therefore taken as the base pressure for the results to be presented here.

Fig. 7 Near-wake static pressure coefficient at $M_{ref} = 0.485$.

Fig. 8 Near-wake static pressure coefficient at $M_\infty = 0.4$ from Rudy's computations.[5]
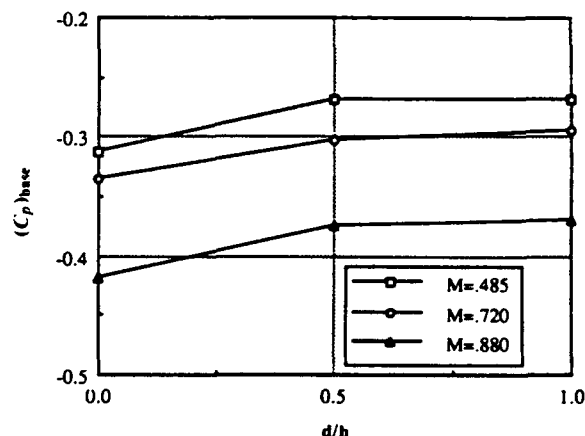

Fig. 9 Base pressure coefficient vs cavity depth and reference Mach number.

Table 2 Base pressure results

Ref. Mach no.	Shallow cavity, %	Deep cavity, %
0.485	+14.1	+14.4
0.720	9.8	11.9
0.880	10.3	11.5

Table 3 Vortex shedding frequency results

Ref. Mach no.	Base type	Shedding frequency, Hz	Strouhal no.
0.485	Blunt	2539.1	0.2375
	Shallow	2705.1	0.2530
	Deep	2690.4	0.2517
0.720	Blunt	3730.5	0.2414
	Shallow	3867.2	0.2502
	Deep	3881.8	0.2511
0.880	Blunt	4379.9	0.2372
	Shallow	4492.2	0.2433
	Deep	4501.9	0.2438

The variation of the base pressure coefficient with cavity depth and reference Mach number is plotted in Fig. 9. The percentage increases in the base pressure coefficient for the cavity bases relative to the blunt base are shown in Table 2. These percentage increases are of the same order as those found by Rudy[5] for his freestream Mach 0.6 case. Figure 9 illustrates quite clearly that the majority of the base pressure increase occurs with a cavity depth equal to 1/2 base height and that increasing the cavity depth to one base height yields only slightly greater drag reducing benefits. This was precisely the conclusion arrived at in the computational results of both Clements[4] and Rudy. Note that although the beneficial effects drop off slightly between reference Mach numbers of 0.485 and 0.720 (see Table 2) there is no significant change between $M_{ref} = 0.720$ and 0.880. It would seem, as reported by Nash et al.,[2] that the base cavity will be effective as long as vortex shedding is present, which means through Mach 1.

Shedding Frequency Measurements

As discussed, the vortex shedding frequencies were determined through a power spectral density analysis of the signal from a fast response piezo-resistive pressure transducer. For all results presented herein, the transducer was located in the tunnel sidewall and downstream of one of the trailing edges. It is realized that the frequency measurements obtained at this location could possibly be distorted by the presence of the sidewall boundary layer. However, comparison of measurements obtained for the blunt-based geometry with the transducer located in the base and in the sidewall showed less than a 4% difference in the value of the shedding frequency. It was felt that this difference was small enough that the more convenient sidewall location could be used. In addition, the fluctuating pressure signal for the cavity bases is stronger at the sidewall location than at the rear cavity wall location.

For all cases, a strong peak in the power spectral density function occurs at the shedding frequency with a second smaller peak apparent at twice the shedding frequency. The relatively broad nature of the peaks in the spectral density plots is at least partly because the vortex street is superimposed on a random turbulent flowfield resulting in the diffusion or feeding of some of the discrete energy (from the vortex shedding) to the continuous (turbulent) portion of the spectra. The shedding frequencies and Strouhal numbers, $St \equiv fh/U_{ref}$, for each of the experimental cases are given in Table 3. Note that these Strouhal numbers are based on the velocity measured at the reference location, i.e., over the aft end of the model just prior to separation.

The Strouhal numbers are plotted vs cavity depth and reference Mach number in Fig. 10. The results of Nash et al.[2] for a similar blunt-based model indicate that for slender, two-dimensional models, the Strouhal number remains constant [at a value based on freestream conditions of $(St)_\infty \equiv fh/U_\infty = 0.25$] from low-subsonic speeds up to a freestream Mach number of about 0.9. The results in Fig. 10 agree reasonably well with this observation except for the drop in Strouhal number that occurs for the two cavity bases at the reference Mach number of 0.880. The reason for this
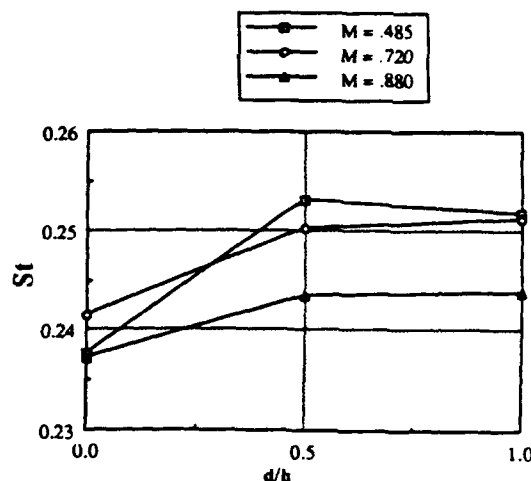

Fig. 10 Strouhal number vs cavity depth and reference Mach number.

drop is unclear. It could be due to the increase in wall interference effects that occurs as the flow approaches Mach 1.0, but that does not explain why a similar decrease did not occur for the blunt-based configuration at the higher Mach number. What is obvious from Fig. 10 is that the effect of the cavity is to increase the shedding frequency, in agreement with the experimental observations of Clements,[4] but again in disagreement with the computational results of both Clements and Rudy.[5] Also, note that the deep cavity again produces virtually no change beyond that which was achieved with the shallower cavity, a trend that has been evident in all of the experimental results presented so far. Further discussion of some of these observations will be given in the following section.

Summary and Discussion

The common thread among all of the experimental results is that increasing the depth of the cavity from 1/2 to 1 base height does not have any significant effect on the parameter being observed; the majority of the changes occur in going from the blunt base to the shallow cavity and may in fact occur for an even shallower cavity, though this was not investigated here. This result was also evident in the computational results of both Rudy[5] and Clements[4] and suggests that, whatever the mechanism is that causes the drag reduction for the cavity bases, it is little affected by depth once the cavity has reached some critical, rather shallow, depth.

It is evident in the schlieren photographs that the basic structure of the vortex street is relatively unmodified by the presence of a base cavity, and that the vortex motions do not extend into the cavity at all. In fact, the vortex formation position is pushed slightly further downstream with a base cavity as compared to a blunt base. This is perhaps somewhat surprising; since the vortices form immediately adjacent to the

base for the blunt geometry, one might expect the vortices to move partially into the cavity when the solid boundary of the blunt base is replaced with the compliant fluid boundary of the cavity base. That this does not occur refutes the hypothesis of Nash et al.[2] that the cavity walls improve wake stability and decrease drag by constraining the upstream part of the vortices.

The fact that the present results show that the vortices do not extend into the cavity also accounts for the discrepancy between the experiments and computations regarding the effect of a base cavity on the shedding frequency. In the computations, the cavity was found to increase the interaction between the vortices and thereby decrease the shedding frequency. (Devices such as splitter plates and base bleed that decrease interaction between the vortices have been found to yield an increase in the shedding frequency.[7-11]) In the experiments, the interaction between the vortices is apparently not facilitated by the presence of the base cavity, and so the shedding frequency does not decrease. The observation that the shedding frequency actually increases with a base cavity may be because the vortices form slightly further downstream in this case so that the distance between the separated shear layers is less at the start of vortex formation. (Fage and Johansen[15] have found that the vortex shedding frequency is inversely proportional to the distance between the separated shear layers). This seems plausible: in Bearman's[7,9] splitter plate and base bleed experiments, the vortex formation position was moved downstream approximately one base height, and the Strouhal number increased by roughly 33%. In this investigation the vortex formation position was moved downstream approximately 1/10 base height due to the cavities and the Strouhal number increased by roughly 4-6%.

The fact that the drag reducing mechanism of the base cavity is different than that of either the splitter plate or base bleed is evidenced by the very different degrees of displacement of the vortex formation position for these geometries relative to a plain blunt-based configuration. For the base cavity, there are no structural or fluid elements to interfere with the interaction between the separating shear layers as for splitter plates and base bleed. The effect of the cavity on the vortex street is apparently of a more subtle nature. The results of the present surface flow experiments seem to refute even Compton's[16] theory that the recirculating flow in the cavity forms a steady co-flowing stream on the inner edges of the separated shear layers thereby decreasing mixing and increasing the base pressure. If any significant recirculating flows were present in the cavity, they would most likely have left some directional indication in the oil coatings, and as reported earlier, this was not found to be the case in the experiments reported herein.

A clue as to what is happening in the near wakes of the cavity configurations comes from the results of the wake static pressure traverses. Figure 7 shows that the cavity base increases not only the base pressure coefficient but also the pressure coefficient in the near wake within roughly 5/8 base heights of the trailing edge. Nash et al.[2] have stated that the value of the pressure coefficient in the low-pressure trough in the wake of a bluff body decreases with an increasing degree of bluffness of the body and hence with increasing strength of the vortex street. In Fig. 7 it is apparent that the low-pressure troughs of the cavity bases do not reach as low a minimum as for the blunt base, and this suggests that the vortex streets of the cavity bases are somewhat weaker than the vortex street of the blunt-based configuration. The weaker vortex street results in the higher pressure at the base and in the near-wake, and the higher pressure, in turn, may then move the vortex formation position to a location slightly further downstream of the trailing edge as compared to the blunt-base geometry.

The question then becomes what causes the weakening of the vortex street; there are no interference elements in the wake, there is no constraint of the upstream part of the vortices by the cavity walls, and there is apparently no

significant steady recirculating flow causing the formation of a co-flowing stream. The only difference between the blunt base and the cavity bases is that the forming vortices see a solid boundary at the trailing-edge plane in the one case and a compliant fluid boundary in the other. It is quite possible that enhanced fluid mixing at the trailing edge of the base cavity causes a greater loss of vorticity than does the solid wall friction at the trailing edge of the blunt base. The tuft experiments have shown that the air at the cavity entrance is in a state of unsteady pulsating motion as it is forced first one way by the vortex shedding from the upper trailing edge and then the other way by the vortex shedding from the lower trailing edge. These unsteady, oscillating air motions could increase the fluid mixing at the trailing-edge plane to such a degree that the forming vortices are weakened. If this is indeed the case, then the shape or geometry of the cavity would seem to be unimportant; the cavity should be effective as long as it is deep enough to completely replace the fluid-solid wall interaction for the blunt base with a purely fluid interaction for the cavity base and as long as the cavity is of such a height to cover the majority of the base. This was, in fact, evident in the results of Pollock,[3] who found that the drag reducing effect of a special cusp cavity, whose shape was chosen on theoretical grounds was essentially identical to that of the simple rectangular cavity of Nash et al.[2] Furthermore, the results reported herein, as well as the experimental results of Clements,[4] have indeed shown cavity depth to be unimportant once the cavity has reached a somewhat shallow, critical depth.

Having discussed several points of disagreement between the present experimental results and the computational results of Rudy[5] and Clements,[4] it is important to reiterate the differences in the relevant flowfield conditions of these investigations in an attempt to explain why these disagreements may exist. One obvious difference is that the computations model a perfectly two-dimensional flowfield although the experiments can never be completely free from three-dimensional effects. In fact, Nash[17] has stated that over no part of the Reynolds number range is the vortex street strictly two dimensional due to the presence of spanwise periodic structures and/or random turbulent fluctuations. Considering the relatively small scale of the wind tunnel used in this investigation, some effects of three dimensionality are inevitable, despite the two-dimensional indications of the surface oil-flow patterns and the base pressure measurements. Apparently, however, the effects of any three dimensionalities are primarily confined to the interactions of the vortices with the base cavities, as the results for the blunt-based model in these experiments showed excellent agreement with the corresponding results from Rudy's computations. The fact that the tufts suspended in the base cavities did show a degree of spanwise as well as streamwise motion lends support to the argument that three-dimensional effects in the base cavity may affect the interactions with the vortices in the near-wake region.

A second major difference between the conditions of the present experiments and the computational results is the Reynolds numbers. For Rudy's[5] computations, the Reynolds numbers based on freestream conditions and base height were 700 for the $M_\infty = 0.4$ condition and 962 for the $M_\infty = 0.6$ case. Furthermore, the boundary layers at separation were laminar. Clements'[4] computations, on the other hand, were inviscid. In the current experiments, the Reynolds numbers based on the reference conditions and base height were between 1.62×10^5 and 2.78×10^5, and the boundary layers at separation were turbulent. In his study of vortex street wakes behind circular cylinders, Roshko[18] observed that the development and characteristics of the vortex street are strongly dependent on where the transition point is located and that very different trends are displayed depending on whether the separating shear layers are laminar or turbulent. Thus, it is quite possible that the behavior of a vortex street in the presence of a base cavity will likewise depend on the state of

the separating boundary layers. Rudy recognized this and suggested that computations be performed at higher Reynolds numbers using appropriate turbulence models in order to better match experimental conditions.

Another point to be considered is that the computations model an unconstrained freestream, whereas the experiments reflect the blockage effects of the wind-tunnel walls. It is recognized that some of the observations reported in the present investigation may have been influenced by wall-interference effects. However, as discussed earlier, it is felt that although wall interference may have somewhat affected the absolute values of the various measured flow parameters, the effects on the basic structure of the vortex street and the trends of the data with increasing Mach number or cavity depth are probably small. Therefore, the blockage effects are probably less likely to be the cause of the observed discrepancies between the computational and experimental results than the three-dimensional and Reynolds number effects discussed above.

A final point to consider is that the cavity geometries for this investigation were not identical in every detail to those used in Rudy's[5] computations; the cavities in the current experiments covered 80% of the base height, whereas Rudy's cavities spanned 90% of the base height. It seems doubtful, however, that this difference could be responsible for the discrepancies reported herein.

Acknowledgments

References

[1]Heinemann. H. J., Lawaczeck, O., and Butefisch. K. A., "Von Karman Vortices and their Frequency Determination in the Wakes of Profiles in the Sub- and Transonic Regimes," *IUTAM Symposium Transsonicum II*, edited by K. Oswatitsch, and D. Rues, Springer Verlag, New York, 1978, pp. 75-82.

[2]Nash. J. F., Quincey, V. G., and Callinan, J., "Experiments on Two-Dimensional Base Flow at Subsonic and Transonic Speeds," ARC R&M No. 3427, Jan. 1963.

[3]Pollock, N., "Some Effects of Base Geometry on Two-Dimensional Base Drag at Subsonic and Transonic Speeds," Australian A.R.L., Aerodynamics Note 316, Oct. 1969.

[4]Clements. R. R., "Computer Models of Separated Flows Behind Two-Dimensional Bluff Bodies," Ph.D. Dissertation. Cambridge Univ., Cambridge. United Kingdom, July 1973.

[5]Rudy, D. H., "A Numerical Study of Unsteady Two-Dimensional Subsonic Compressible Base Flow." Ph.D. Dissertation. Department of Mechanical and Industrial Engineering, Univ. of Illinois at Urbana-Champaign, Urbana, IL, May 1987.

[6]Roshko, A., "On the Drag and Shedding Frequency of Two-Dimensional Bluff Bodies." NACA TN 3169, July 1954.

[7]Bearman. P. W., "Investigation of the Flow Behind a Two-Dimensional Model with a Blunt Trailing Edge and Fitted with Splitter Plates," *Journal of Fluid Mechanics*, Vol. 21, Feb. 1965, pp. 241-255.

[8]Nash, J. F., "A Discussion of Two-Dimensional Turbulent Base Flows," ARC R&M No. 3468, July 1965.

[9]Bearman, P. W., "The Effect of Base Bleed on the Flow Behind a Two-Dimensional Model with a Blunt Trailing Edge." *Aeronautical Quarterly*, Vol. 18, Aug. 1967, pp. 207-224.

[10]Wood, C. J., "The Effect of Base Bleed on a Periodic Wake," *Journal of the Royal Aeronautical Society*, Vol. 68, July 1964, pp. 477-482.

[11]Wood, C. J., "Visualization of an Incompressible Wake with Base Bleed," *Journal of Fluid Mechanics*, Vol. 29, Aug. 1967, pp. 259-272.

[12]Little, B. H., Jr., and Cubbage, J. M., Jr., "The Development of an 8-Inch by 8-Inch Slotted Tunnel for Mach Numbers up to 1.28," NASA TN D-908, Aug. 1961.

[13]El-Sherbiny, S. E., and Modi, V. J., Blockage Effect on Vortex Shedding from Bluff Bodies," *Arabian Journal for Science and Engineering*, Vol. 8, Jan. 1983, pp. 61-66.

[14]Kruiswyk, R. W., and Dutton, J. C., "An Experimental Investigation of the Effects of a Base Cavity on the Near-Wake Flowfield of a Body at Subsonic and Transonic Speeds," Department of Mechanical and Industrial Engineering, Univ. of Illinois at Urbana-Champaign, Rept. No. UILU-ENG-89-4008, May 1989.

[15]Fage, A., and Johansen, F. C., "The Structure of Vortex Sheets," ARC R&M No. 1143, Aug. 1927.

[16]Compton, W. B., "Effect on Base Drag of Recessing the Bases of Conical Afterbodies at Subsonic and Transonic Speeds," NASA TN D-4821, Oct. 1968.

[17]Nash, J. F., "A Review of Research on Two-Dimensional Base Flow," ARC R&M No. 3323, March 1962.

[18]Roshko, A., "On the Development of Turbulent Wakes from Vortex Streets," NACA TN 2913, March 1953.

APPENDIX A.2

TWO-STREAM, SUPERSONIC, WAKE FLOWFIELD BEHIND A THICK BASE, PART I: GENERAL FEATURES

by

V. A. Amatucci, J. C. Dutton, D. W. Kuntz, and A. L. Addy

Two-Stream, Supersonic, Wake Flowfield Behind a Thick Base, Part 1: General Features

V. A. Amatucci, J. C. Dutton, D. W. Kuntz, A. L. Addy

Two-Stream, Supersonic, Wake Flowfield Behind a Thick Base, Part I: General Features

V. A. Amatucci*
Sandia National Laboratories, Albuquerque, New Mexico 87185
J. C. Dutton†
University of Illinois at Urbana-Champaign, Urbana, Illinois 61801
D. W. Kuntz‡
Sandia National Laboratories, Albuquerque, New Mexico 87185
and
A. L. Addy§
University of Illinois at Urbana-Champaign, Urbana, Illinois 61801

An experimental investigation of the complex interaction region generated by the separation of two supersonic streams past a finite-thickness base has been conducted in a two-dimensional wind tunnel. The data were obtained using schlieren photography, pressure measurements, and two-component laser Doppler velocimeter measurements. The shear-layer mixing regions are characterized by initially constant-pressure mixing, by an evolution of velocity profiles from truncated boundary-layer shapes to wakelike profiles farther downstream, and by relatively high levels of turbulence. The separated flow region is characterized by large reverse flow velocities and strong interactions with the low-velocity regions of both shear layers. Turbulence intensities and kinematic Reynolds stresses are strongly affected by the separation process at the base and increase greatly in the latter portions of the two shear layers and in the recompression region. Recovery of the mean velocity field in the redeveloping wake occurs quickly, while the turbulence field remains perturbed to the furthest streamwise location investigated.

Nomenclature

C_f = skin-friction coefficient
H = splitter plate height, 25.4 mm
k = turbulent kinetic energy
M = Mach number
O = origin location for the coordinate system
P = pressure
Re = Reynolds number
Re_δ = Reynolds number based on boundary-layer thickness
Re_θ = Reynolds number based on momentum thickness
u = U-component of the velocity vector
u_τ = friction velocity
v = V-component of the velocity vector
w = width of the wind tunnel test section
X = coordinate parallel to the wind tunnel floor
Y = coordinate perpendicular to the wind tunnel floor
Z = spanwise coordinate
δ = boundary-layer thickness
δ^* = boundary-layer displacement thickness
θ = boundary-layer momentum thickness
λ = wavelength of laser light
ν = kinematic viscosity
Π = wake strength parameter

τ = shear stress
$\langle \rangle$ = root-mean-square quantity

Subscripts
Base = condition immediately behind the splitter plate
e = edge condition
J = inner jet or lower stream condition
w = condition at the wall
1 = condition for the Mach 2.56 stream (upper stream)
2 = condition for the Mach 2.05 stream (lower stream)
∞ = infinity or freestream conditions of the Mach 2.56 stream

Superscripts
‾ = ensemble average
′ = fluctuation from the mean value

Introduction

THE complex interaction region generated by the separation of two supersonic streams past a finite-thickness base occurs frequently in high-speed flight and is characteristic of the aft-end flowfield of a powered missile in the supersonic flight regime. This fluid dynamic flowfield exists in other applications as well, including the flow region at the trailing edge of a blunt airfoil in a supersonic freestream or the initial mixing region of confluent multiple streams in a supersonic combustor. In each of these cases the near-wake region is dominated by strong velocity and density gradients, energetic viscous interactions, and expansion and compression processes covering the full range of gas dynamic regimes.

Research programs through the years have attempted to develop analytical, numerical, and experimental insight into the fluid dynamic processes ongoing in the near-wake region. The usual motivating goal is the development of a predictive capability for base pressure and other flowfield properties over a wide range of flight regimes. The analyses develop a physical flow model of the strong dissipative regions of the

near wake, including interaction with the adjacent inviscid regions, and attempt to find applicability for a variety of Mach number, Reynolds number, and afterbody geometry conditions. The dominant analytical approach has been the Chapman-Korst component model[1,2] in which the turbulent base flowfield is separated into distinct regions and each part is analyzed individually, subject to appropriate assumptions and boundary conditions. The expansion process at the geometric corner, the shear layer mixing process, and the recompression and redevelopment processes (see Fig. 1) are each analyzed as separate components, utilizing empirical formulations as needed. The individual components are then joined together into an overall model of the separated flowfield, allowing for interaction between each component, and a unique solution is determined.

With the advent of more powerful computing facilities during recent years, both thin-layer and full Navier-Stokes computations of high-speed separated base flows have been performed. To date the agreement of these computations with experimental measurements of high-speed separated flowfields has been only moderate.[3] However, by focusing on the issues of grid resolution and alignment, as well as turbulence modeling, improved predictions of these flows have recently been obtained.[4-8] The difficulty in accurately computing these flows is understandable due to their complexity, since they include regions of large flow property gradients in thin shear layers, expansion waves, and shock waves, and also due to the inability of the current generation of turbulence models to adequately treat such effects as large streamline curvature, compressibility (i.e., high Mach-number effects), shear-layer impingement, and the effects on turbulence of the previously mentioned large gradient regions.

To aid in the understanding of the detailed mechanisms of these high-speed flows both with and without regions of significant flow separation, a program of small-scale wind tunnel experiments of simple flow geometries has been conducted at the University of Illinois at Urbana-Champaign. Initial experimental work has examined in detail the shear-layer mixing process[9,10] and the recompression and reattachment processes.[11-13] The measurements presented here take the next step in this progression and add the recirculating region and the wake redevelopment region (see Fig. 1) as focuses of study to obtain experimental data for a unified two-stream near-wake flowfield. The present experimental program has
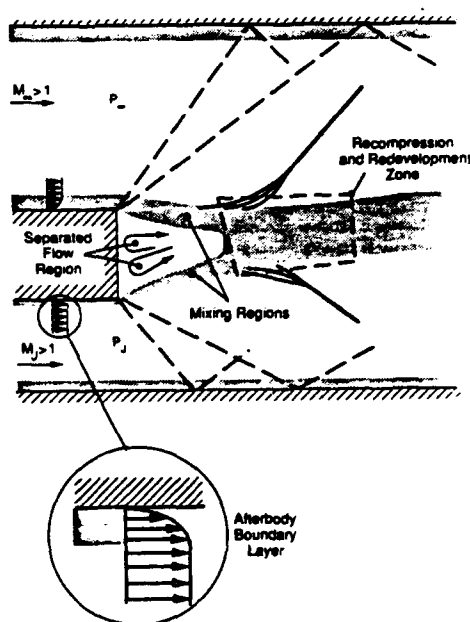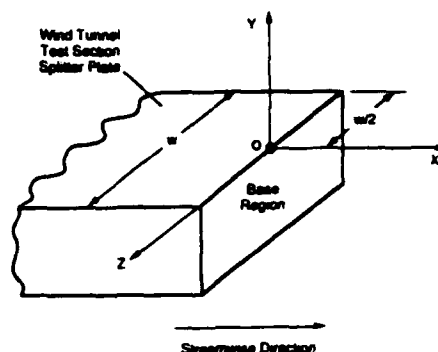

Fig. 2 Schematic of the origin location and coordinate system used for collection and presentation of the near-wake interaction mean and turbulence data.

obtained measurements over the full range of mechanisms exhibited in this flowfield for a well-determined set of incoming flow conditions. The data for these experiments are obtained from schlieren photography, sidewall pressure measurements, and laser Doppler velocimeter (LDV) measurements. The use of a two-color, two-component, frequency-shifted LDV system to measure instantaneous flow velocity, despite its added complexity, has certain special advantages in the near-wake separated flowfield. Most past near-wake interaction experiments have focused on mean velocity values obtained from pressure distribution data gathered by intrusion into the near wake, usually with a single pressure probe or a probe rake. The LDV measurements of the current investigation provide accurate instantaneous velocity data obtained in a nonintrusive way by an instrument requiring no prior calibration.

The primary objective of this experimental investigation of the supersonic, two-stream base flow is to investigate the fundamental fluid dynamic mechanisms existing in the near-wake flowfield with an aim toward better understanding of each individual process and how they interact. Detailed data have been collected in all regions of the near-wake flowfield in order to examine such features as changes in velocity profiles due to the corner expansion process, evolution of the velocity profiles during shear-layer mixing, strength and influence of the recirculating region, and mean and turbulent flowfield changes during the recompression, reattachment, and downstream wake redevelopment processes.

The results and trends of the LDV data obtained for the two-stream interaction flowfield are presented in a series of two articles. This first article presents the background, objectives, and techniques involved in making the velocity measurements in this flowfield, and then gives general trends and features of the mean and turbulence fields for the overall global interaction as they change with downstream distance. In the second paper, detailed data will be shown for each of the *components* of the flowfield, such as the shear-layer mixing regions and the recompression/reattachment region, and trends for each component will be compared to literature specific for that component. The two papers, taken together, will then form a complete picture of the turbulent nature of this near-wake interaction.

Experimental Facilities and Measurement Techniques

Facilities

This investigation of the near-wake interaction utilized the air supply and wind tunnel facilities of the Mechanical Engineering Laboratory at the University of Illinois at Urbana-Champaign for a series of dry, cold air experiments. A two-dimensional wind tunnel test section, shown schematically in Fig. 1, produced two uniform supersonic streams which separated at the geometric corners of a finite-thickness splitter

Fig. 1 Detailed flowfield characteristics generated by the separation of two supersonic streams past a finite-thickness base.

plate and formed a flowfield characteristic of the aft-end of a powered missile, including expansion at the separation points, formation of a recirculating region bounded by two shear-layer mixing regions, recompression and reattachment of the shear layers, and downstream wake redevelopment.

The common upstream plenum chamber provided compressed air at 517 kPa to two separate pipe-and-valve arrangements supplying the two converging-diverging nozzles. These nozzles used the splitter plate as a half-nozzle symmetry plane. The upper stream nozzle produced a uniform exit plane flow 50.8 mm in height, having a Mach number of 2.56, and a splitter plate boundary-layer thickness of 3.35 mm. The lower stream nozzle was shorter in length and produced a uniform exit plane flow 25.4 mm in height, having a Mach number of 2.05, and a splitter plate boundary-layer thickness of 1.46 mm. These two supersonic streams separated past the 25.4-mm-thick base and produced the near-wake interaction flowfield. The test section region was 50.8 mm wide and 101.6 mm in height and was within view of clear glass windows on both sides of the wind tunnel for optical diagnostic access. As illustrated in Fig. 2, the origin for the coordinate system was located on the centerline of the wind tunnel at the upper rear edge of the splitter plate. All features of the near-wake flowfield, including wake redevelopment, occurred within the measurement domain before the mixed flow exited the test section through a constant-area diffuser.

Measurement Techniques

The measurement techniques employed in this investigation included schlieren photography, stagnation and static pressure measurements, and laser Doppler velocimetry. Schlieren photographs obtained with a 1.4-μs spark source were used to characterize the qualitative features of the overall flowfield and to determine spatial locations for LDV measurements. The sidewall static pressure data were collected using an aluminum window insert which replaced one of the glass side windows and had a grid of 370 pressure taps. The pressure levels were measured with a Pressure Systems Incorporated (PSI) digital pressure transmitter system and yielded pressure measurements in all regions of the near-wake interaction including along the shear-layer mixing regions.

The two-component, two-color LDV system was based on Thermal Systems Incorporated (TSI) optical and electronic components and employed a Spectra-Physics 5-W argon ion laser. The green beam ($\lambda = 514.5$ nm) and the most powerful blue beam ($\lambda = 488.0$ nm) were used in the beam splitting and recombination processes which produced the ellipsoidal measurement volumes. The use of a 350-mm focal length transmitting lens with 22-mm beam spacing produced a green measurement volume of 0.183 mm diameter, 6.08 mm length, with 8.53-μm fringe spacing. The blue measurement volume diameter, length, and fringe spacing were 0.179 mm, 5.92 mm, and 8.09 μm, respectively. These fringe spacings, in combination with the 40 MHz frequency shift and orientation of the fringes at $\pm$ 45 deg to the mean flow direction, kept signal frequencies within range of the electronic equipment while moving the fringes at a high enough velocity to reduce fringe bias probabilities and eliminate directional ambiguity. TSI frequency counters, operated in the single-measurement-per-burst mode with high- and low-pass filtering, were used to determine the Doppler shift frequencies of the signals from the photodetectors and to perform validation checks to remove erroneous data. The receiving optics of the LDV system were oriented in a forward scatter mode 10 deg from the optical axis in order to reduce the effective length of the measurement volume to 1.46 mm and to provide optimum signal-to-noise ratio of the scattered laser light. The output from the LDV system's frequency counters was stored in the memory of a DEC PDP 11/73 minicomputer by means of a direct memory access board, and the data were transferred serially to an HP-9000 computer system for reduction, analysis, and plot-

ting. The laser, transmitting optics, and collection optics were mounted on a traversing table which allowed movement in all three coordinate directions with an accuracy of approximately ± 0.1 mm.

Seeding of the flow for the LDV measurements was accomplished by injecting silicone oil droplets (50 cP viscosity) produced by a TSI six-jet atomizer into the stagnation chamber. To address the issues of particle size and flow-following capability (i.e., particle dynamics effects), a series of particle lag experiments was conducted whereby LDV measurements were made across an oblique shock wave produced by a 15-deg compression corner in a Mach 2.0 wind tunnel. Using these measurements, together with a particle relaxation analysis based on the work of Maxwell and Seasholtz[14] and the drag law of Walsh,[15] the silicone oil droplets used in these experiments are estimated to be 1.0 μm in diameter. Droplets of this size have an Eulerian frame of reference frequency response of up to approximately 200 kHz which is adequate for following the turbulent fluctuations of the current near-wake flowfield.

The use of counter-type signal processors to measure individual velocity realizations introduces additional considerations, especially in high-speed flows, due to counter clock resolution, statistical uncertainty, velocity bias, fringe bias and spatial resolution. The $\pm$ 1 ns accuracy of the counter results in a minimum measurable turbulence intensity in the highest speed regions of the flow of 1.37%, with proportionately smaller values in the lower speed regions. To control the uncertainty due to finite sample size, either 2048 or 4096 velocity realizations were generally collected throughout the flowfield. At a confidence level of 95%, the resulting statistical uncertainty in the mean velocity is therefore a maximum of $\pm$ 3% for turbulence intensities less than about 100%, and the statistical uncertainty in the standard deviation is a maximum of approximately $\pm$ 3.1%. For the current low data density measurements,[16] the seed particles generated valid Doppler signals at a rate several orders of magnitude lower than the capability of the processors to sample, resulting in a free running processor condition in which the LDV data is totally velocity biased.[10] To correct for this condition, a two-dimensional inverse velocity magnitude weighting scheme[17] has been employed. As mentioned, the relatively large fringe spacing, use of the 40-MHz frequency shift, and the $\pm$ 45-deg orientation of the fringes to the mean flow direction, greatly reduced the possibility of fringe bias in these experiments. In fact, an implementation of the fringe bias analysis of Buchhave[18] demonstrated that for the vast majority of the measurements the fringe bias correction was less than 3% and, as a result, no such correction has been used in the measurements presented here. Spatial-resolution errors can also occur in high-gradient regions of the flow due to the finite size of the probe volume. Using the analysis of Karpuk and Tiederman,[19] the maximum spatial-resolution error at the location 5 mm downstream

Fig. 3 Schlieren photograph of the two-stream interaction flowfield visible through the sidewall windows of the wind tunnel test section (1.4-μs flash duration).

Table 1 Properties of the Mach 2.56 and Mach 2.05 boundary layers

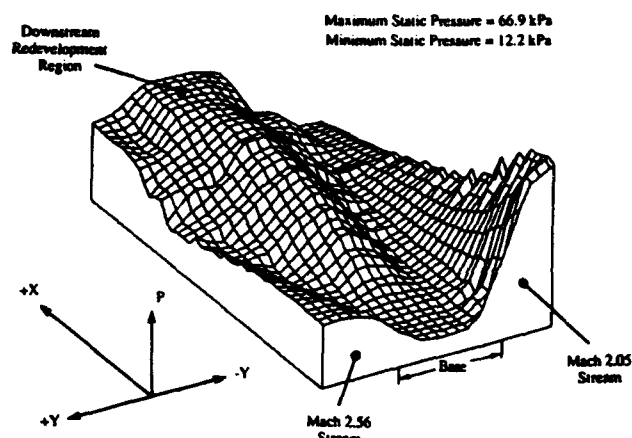| Parameter	Upper stream	Lower stream
Mach number	2.56	2.05
δ, mm	3.35	1.46
δ^*, mm	0.947	0.393
θ, mm	0.220	0.118
Re, m^{-1}	5.12×10^7	6.36×10^7
Re_θ	1.12×10^4	7.48×10^3
Π	0.9216	1.121
u_τ, m/s	25.11	21.45
C_f	0.001597	0.001821

Fig. 4 Three-dimensional surface contour representation of the static pressure levels existing in the near-wake interaction flowfield (viewed from upstream).

from the base is estimated to be ± 2.8% for the mean velocity and ± 4.8% for the turbulence intensity, with much smaller errors in the downstream regions of the near-wake flow.

Further details concerning the equipment and apparatus, measurement methods, and experimental procedures are found in Ref. 20.

Experimental Results and Discussion

Two-Dimensionality of the Flowfield

Past work[21,22] has indicated the tendency for existence of spanwise nonuniformity in flowfields characterized by large embedded separation regions leading to reattachment. To examine these effects in the present flowfield, transverse profiles of velocity were obtained at three spanwise locations: at the midplane ($Z = 0$) and at $Z = \pm 10$ mm from the midplane. In addition, these profiles were obtained at three *streamwise* locations chosen to examine distinctly different regions of the near-wake flowfield: $X = 25$ mm where separate shear layers and recirculation were present, $X = 45$ mm in the recompression and reattachment region, and $X = 100$ mm in the redeveloping downstream wake. The centerline and off-centerline streamwise mean velocity and turbulence intensity profiles show that the central 40% of the test section flowfield was highly two-dimensional in all regions, with the largest deviations occurring in the recirculating region. Once impingement of the two shear layers occurred, the LDV data indicate very little deviation from two-dimensionality at any transverse location. Although regions of slight three-dimensionality do exist, they seem characteristic of the fluid dynamic processes ongoing in those components of the near-wake and are not due to the wind tunnel design or sidewall boundary layers.

Turbulent Boundary Layers

The turbulent boundary-layer characteristics of the two supersonic streams provide the initial conditions for the expansion, mixing, recompression, and redevelopment processes

which occur in the near wake. Detailed LDV measurements were made of the boundary layers which developed on the upper and lower surfaces of the splitter plate at a location 4 mm before geometric separation. Two-component measurements were made to a distance of 0.75 mm from either surface and then one-component measurements completed the survey to a distance within 0.25 mm above either surface. The measured velocity profiles for the upper and lower boundary layers were fit to the generalized velocity profile equation of Sun and Childs[23] using the boundary-layer thickness δ, the friction velocity u_τ, and the wake strength parameter Π as curve-fit coefficients. The important parameters describing the growth and development of the two boundary layers prior to separation are presented in Table 1. The differences in thicknesses between the Mach 2.56 stream ($\delta = 3.35$ mm) and the Mach 2.05 stream ($\delta = 1.46$ mm) were generated intentionally to simulate the ratio of boundary-layer thicknesses typical of powered missile applications. The aim was to simulate zero angle-of-attack configurations while including the effects of strong expansion of the inner propulsive flow. The wake strength parameter, friction velocity, and skin-friction coefficient values are consistent with earlier studies[9,11-13,21,24,25] of compressible turbulent boundary layers.

Global Near-Wake Interaction Flowfield

Schlieren photography has been used to obtain a qualitative view of the component processes existing in the near-wake interaction. The schlieren photograph of Fig. 3 shows well-developed splitter plate boundary layers undergoing strong expansion and turning processes at geometric separation. The two free shear layers generated at separation appear to be initially very thin and to undergo a moderately long constant pressure mixing region before they show any signs of curvature associated with the recompression process prior to impingement. The beginning of the recompression process for each shear layer is marked by the first compression waves which emanate from the slightly supersonic regions of the shear layer and eventually coalesce into the recompression oblique shock wave. One of the more interesting features in this photograph is the apparent large-scale turbulent structures which border the edges of the redevelopment core produced by the impingement of the two free shear layers. These structures are similar to those that occur in high-Reynolds-number free jets and have an effect on the turbulence intensities measured in the redeveloping wake. Similarly, each shear layer shows signs of large-scale structures and intermittency at its edges, especially on the side bounded by the recirculating region.

The arrangement of sidewall static pressure tap locations was designed to obtain detailed pressure surveys of the expansion process, mixing layers, and recompression and redevelop-
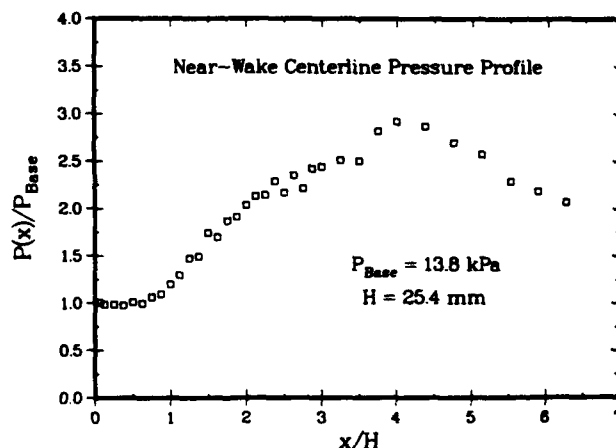
Fig. 5 Centerline pressure profile ($Y/H = -0.5$, $Z = 0$, X variable) for the near-wake interaction region.

ment processes. The three-dimensional contour plot of Fig. 4 shows the static pressure data viewed by an observer located upstream at the base and looking in the streamwise direction. Although no detailed vertical scale is given for the levels of static pressure, a relative indication of the pressure magnitude can be obtained by recognizing that the maximum static pressure in the figure is 66.9 kPa and occurs at the exit of the Mach 2.05 nozzle, while the minimum static pressure of 12.2 kPa occurs in the highly expanded flow region downstream of the Mach 2.05 nozzle and just upstream of the lower recompression shock wave. In a quantitative sense the plot of Fig. 4 shows the strong expansion of the two supersonic streams to the low base pressure "valley" immediately behind the finite-thickness base, the initially constant pressure mixing of the two shear layers, and the gradual but strong pressure rise through the recompression and reattachment regions extending into the downstream wake redevelopment region. The base pressure measured in the region behind the splitter plate was 13.8 kPa.

A profile of the measured static pressure along a centerline extending downstream from the vertical center of the splitter plate is shown in Fig. 5. The static pressure has been nondimensionalized by the average base pressure (13.8 kPa) and the streamwise distance was nondimensionalized by the value of the splitter plate height. The data in Fig. 5 indicate the relatively constant pressure existing in the recirculating region just downstream of the base and the strong pressure rise which occurs during the recompression and impingement process for the two shear layers. Since impingement of the shear layers occurs at approximately $X/H = 1.37$, the data illustrate the initial pressure rise up to reattachment and the substantial increase in pressure existing downstream of that location. The maximum pressure rise level of $P/P_{Base} = 2.92$ (at $X/H = 4.0$) is consistent with other experimental data[11-13] and indicates

the strong mixing and diffusionlike processes occurring in the separated flow region.

The LDV data presented in this paper are intended to give an overview of the mechanisms existing in the near-wake interaction, including a detailed indication of the mean flow and some turbulence quantities. The objective of this overview is to show representative data highlighting the dramatic changes in mean velocity and turbulence quantities in the region immediately behind the splitter plate and in the initial stages of recompression and reattachment. The LDV data presented herein include the "reference" upstream boundary-layer traverses, *every other* vertical traverse from 5.0 mm behind the splitter plate to 40.0 mm downstream, and then *every* measured traverse from $X = 40.0$ to 55.0 mm. In the case of the data presented in Fig. 12, the profiles extend to the farthest downstream location, namely at $X = 160$ mm. The omission of some LDV traverses from the figures for the global interaction was necessary to reduce plot congestion. In the presentation of these results, all of the instantaneous velocity data obtained with the LDV system have been rotated to a coordinate system which aligns the u-component direction parallel to the wind tunnel floor (primary streamwise direction) and the v-component direction perpendicular to the wind-tunnel floor (see Fig. 2).

The mean velocity profiles obtained from the LDV instantaneous data are shown in vector representation in Fig. 6. The vector field plot clearly shows the approach and separation of the two turbulent boundary layers from the upper and lower surfaces of the splitter plate, with the resulting large separated flow region. The shear-layer mixing regions spread with streamwise distance until impingement occurs approximately 1.4 base heights downstream of separation (at $X = 34.9$ mm), where the recirculating region ends (no negative streamwise velocity components are measured) and recovery of the wake

Fig. 6 Mean velocity vector field for the two-stream interaction flowfield showing the near-wake region.
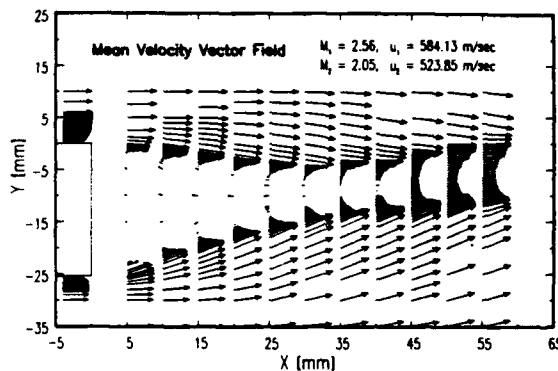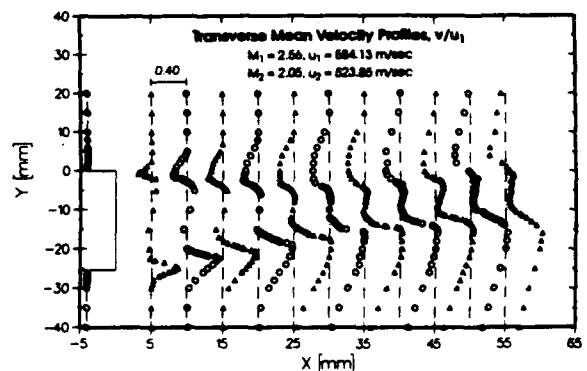

Fig. 8 Transverse mean velocity profiles for the two-stream interaction flowfield showing the near-wake region.
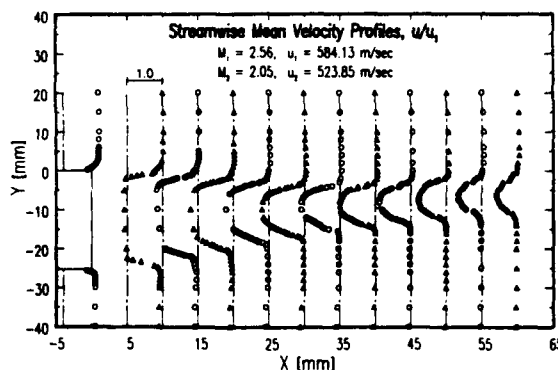

Fig. 7 Streamwise mean velocity profiles for the two-stream interaction flowfield showing the near-wake region.
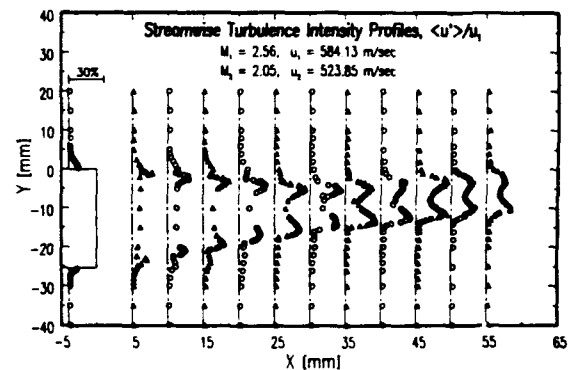

Fig. 9 Streamwise turbulence intensity profiles for the two-stream interaction flowfield showing the near-wake region.

deficit begins. The turbulent mixing which occurs throughout the recompression and reattachment regions quickly effects elimination of the velocity deficit by approximately five base heights downstream of separation, although only part of this process can be seen in Fig. 6.

Examining Fig. 6 in greater detail, the data show that the upper Mach 2.56 flow has a freestream velocity of 584 m/s before separation and expands sharply downward around the corner of the base to a flow angle of approximately −10.6 deg (relative to the freestream). The lower Mach 2.05 freestream moves at a velocity of 524 m/s before separation and then expands upward about the splitter plate corner at an angle of approximately 21.6 deg. Both turbulent boundary layers are fully developed and expand upon geometric separation to a matched base pressure of 13.8 kPa which exists in the recirculating region. The inner jet-to-freestream static pressure ratio $(P_J/P_\infty$ or $P_2/P_1)$ just prior to geometric separation was measured to be 2.14. The mean velocity vectors shown in Fig. 6 illustrate the complex nature of separation past a relatively thick base, and indicate differences from the type of wake developed behind a very thin splitter plate.[26]

The vector representation of the recirculating region in Fig. 6 indicates the existence of two large separation bubbles. The upper separation bubble rotates clockwise while the lower bubble rotates counterclockwise, and relatively large velocity magnitudes exist in this region. Historically posed by Korst[2] as a "dead-air" region, the recirculating region of the near-wake in the present investigation had a maximum negative velocity of 132 m/s at the $X = 22.5$ mm streamwise location. This maximum reverse flow velocity magnitude of $0.23u_1$ is very consistent with the results of Petrie et al.,[9,10] Samimy et al.,[11-13] and Etheridge and Kemp,[27] in the entire range of Mach numbers.

The streamwise mean velocity profiles, nondimensionalized by the edge velocity of the Mach 2.56 stream prior to separa-

tion, are shown in Fig. 7. The dashed line at each X value represents the streamwise location of the traverse and the $u/u_1 = 0$ plane for that set of data. The upstream boundary-layer profiles represent a typical range of u/u_1 beginning at a value of 1.0 in the Mach 2.56 stream and 0.90 in the Mach 2.05 stream $(u_2/u_1 = 0.9)$ and decreasing to zero on the two surfaces of the splitter plate. This series of profiles once again indicates the large negative velocities occurring in the recirculating region and the recovery of the velocity defect with downstream distance. The very fine transverse resolution of the LDV measurement locations yields u-component data which show the spreading of the velocity profiles in each of the shear layers from a very sharp gradient at the $X = 5.0$ mm location to a much broader velocity change for the thickened shear layers at the streamwise stations near recompression and reattachment. The rapid recovery of the mean velocity defect is consistent with the data of Samimy and Addy[13] for a similar two-stream near-wake interaction between Mach 2.07 and Mach 1.50 streams.

The mean velocity field in the transverse direction is shown in Fig. 8 for the range of profiles in the near-wake region. The sign convention illustrated by the data is consistent with the coordinate system defined using Fig. 2; the large positive values of v/u_1 occurring for the lower stream indicate the strong expansion and turning which that region experiences during the mixing process. One noticeable difference between the streamwise and transverse mean velocity profile characteristics for any particular X location is the slower relaxation of the transverse profiles with downstream distance.

The turbulence field, represented in part by the streamwise turbulence intensity profiles of Fig. 9, demonstrates strong enhancement of mixing due to the interaction at the base. The counter clock resolution problem with the LDV system is illustrated in the edge values of $\langle u'\rangle/u_1$ of approximately 2% in the two relatively high-velocity isentropic core flows. The
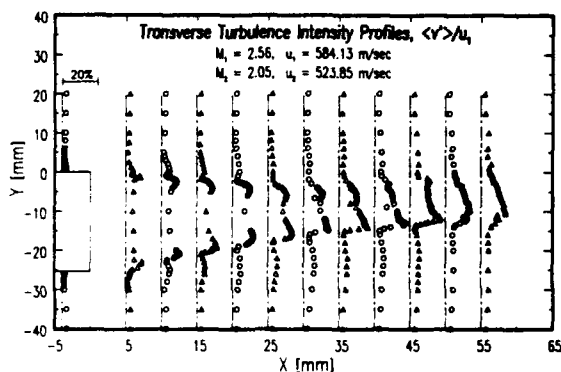
Fig. 10   Transverse turbulence intensity profiles for the two-stream interaction flowfield showing the near-wake region.

Fig. 12   Maximum turbulence intensities and shear stresses for the two-stream interaction flowfield showing the entire streamwise range of measurements.

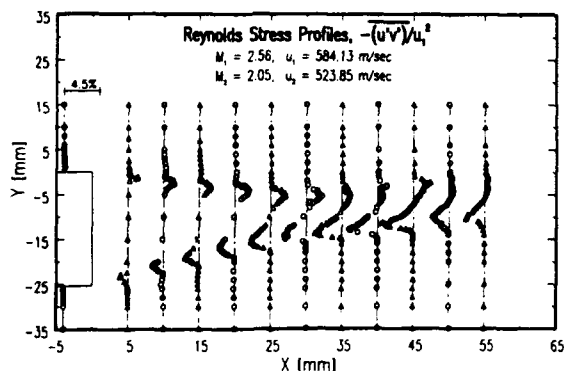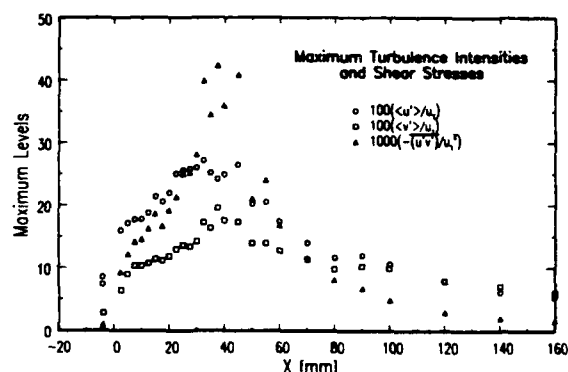Fig. 11   Kinematic Reynolds stress profiles for the two-stream interaction flowfield showing the near-wake region.
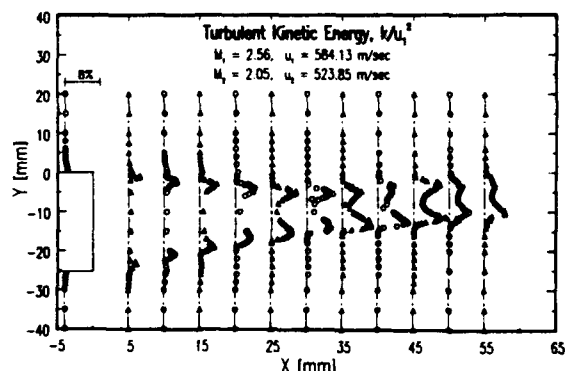

Fig. 13   Turbulent kinetic energy profiles for the two-stream interaction flowfield showing the near-wake region.

striking feature of Fig. 9, however, is the relatively high levels of streamwise turbulence intensity reaching nearly 30% in the latter streamwise stations in the mixing layers and in the recompression and reattachment regions. Despite similarities in the form of the turbulence intensity profiles across either shear layer to those found by Andreopoulos and Bradshaw[28] in an incompressible shear layer behind a flat plate and by Ikawa and Kubota[29] in a supersonic free shear layer, the levels of $\langle u' \rangle / u_1$ are dramatically higher in the present investigation. Although Samimy and Addy's[13] streamwise turbulence intensity levels were slightly lower than those shown in Fig. 9, the trends are similar and indicate strong shear-layer mixing and the highly turbulent nature of the reattachment process.

The transverse turbulence intensity profiles shown in Fig. 10 similarly reflect the strong mixing near recompression and the disturbed nature of the turbulence field even downstream to the last traverse location shown. Fig. 10, now scaled twice as sensitive for a maximum $\langle v' \rangle / u_1$ value of 30% (as compared to the scaling of $\langle u' \rangle / u_1$ in Fig. 9), shows the moderately low levels of transverse turbulence intensity existing in both of the upstream boundary layers in contrast to the high levels of $\langle v' \rangle / u_1$ occurring in the shear layers. The transverse turbulence intensity appears to spread more broadly across the transverse height of the interaction region than the streamwise turbulence intensity does and is similar to results obtained by Kuntz et al.[21] for a Mach 2.94 shock-wave/boundary-layer interaction flowfield.

The data for the kinematic Reynolds stress portion of the turbulent shear stress for the near-wake interaction region are nondimensionalized by the square of the Mach 2.56 edge velocity and plotted in Fig. 11. Initially low levels of Reynolds stress in the splitter plate boundary layers rise to relatively high levels immediately downstream of separation, persist throughout the mixing layer development, and reach maximum values in the recompression and reattachment regions. The Reynolds stresses then tend to decrease sharply after reattachment, very similar to the trends of incompressible reattachment as shown by the data of Chandrsuda and Bradshaw.[30] The lower Mach 2.05 stream's mixing layer appears to be more highly turbulent than the Mach 2.56 stream, and as suggested by Samimy and Addy[13] may be the result of a stronger separation and expansion process for this shear layer, or may be the consequence of a lower convective Mach number.[26] The decrease in Reynolds stress just downstream of reattachment has been explained by restriction of the larger eddies[30] and by bifurcation of the turbulent eddies at reattachment[31,32] resulting in much smaller length scales and lower Reynolds stresses.

The maximum levels of turbulence intensity and shear stresses in the near-wake interaction flowfield are plotted in Fig. 12 for each of the streamwise locations, including the traverses which were omitted previously (those in the range from $X = 2.5$ to 37.5 mm and the range from $X = 60$ to 160 mm). To fit all three quantities on the same ordinate, the streamwise and transverse turbulence intensities are shown in percent while the shear stress levels are actually 10 times the percent value. Since the reattachment of the two mixing layers into a single wake with no reverse velocities occurs at 34.9 mm behind the step, the maximum levels of the quantities plotted in Fig. 12 should peak in that region or slightly downstream. Both the streamwise turbulence intensity $\langle u' \rangle / u_1$ and the transverse turbulence intensity $\langle v' \rangle / u_1$ increase gradually from initially relatively low values in the boundary layers ($X = -4.0$ mm) to reach maximum levels in the general vicinity of reattachment, then decrease with increasing streamwise distance. The kinematic Reynolds stress, which indicates the correlation between the u' and v' fluctuations, tends to peak sharply in the reattachment region near the streamwise location of $X = 34.9$ mm, then decreases rapidly downstream.

The last data plotted for a global view of the near-wake interaction are the turbulent kinetic energy k nondimensionalized by the square of the Mach 2.56 stream edge velocity u_1.

The three-dimensional turbulent kinetic energy, shown in Fig. 13, was obtained by estimating the w-component contribution to be an *average* of the streamwise and transverse variances. Since the turbulent kinetic energy tends to be dominated by the streamwise turbulence intensity, the value of k reaches its peak in the central regions of the mixing layers and maximizes in the recompression and reattachment regions. Research by Lee and Harsha[33,34] indicated that there existed a strong correlation between measurements of turbulent shear stress and turbulent kinetic energy in constant-density mixing flows, and extended to include typical wakelike flows. Their work determined that the shear stress levels were approximately three-tenths of the level of turbulent kinetic energy, with nearly 70% of the cases correlating with proportionality factors between 0.2 and 0.4. The decrease in turbulent kinetic energy with downstream distance in the redevelopment region and the diffusion of k outward with the growth of the redeveloping wake (shown in Fig. 13), when combined with the form of the decay in Reynolds stress as seen in Fig. 11, are trends which appear to verify that such that a correlation exists between those two quantities as observed by researchers[33-36] for wake flows and boundary-layer flows.

Conclusions

The near-wake interaction flowfield generated by the separation of two supersonic streams past a finite-thickness base is characterized by steep velocity gradients, high turbulence intensity levels, and viscous mixing in the presence of an adverse pressure gradient. The shear-layer mixing regions are characterized by constant-pressure mixing along the initial two-thirds of their length, and show an evolution of velocity profiles from truncated forms of the boundary-layer shapes to more wake-like profiles farther downstream. The region of separated flow existing between the two supersonic streams in the near-wake exhibits vigorous recirculation, maximum reverse flow velocity magnitudes reaching $0.23u_1$, and strong turbulent interaction with the low-velocity regions of both shear layers. Peak levels of turbulence intensity and Reynolds stress were measured in the recompression and reattachment regions and decreased rapidly with streamwise distance. The turbulence field in the region of recompression and reattachment is strongly anisotropic. LDV data for the redevelopment of the downstream wake flow showed lower levels of turbulence intensity and kinematic Reynolds stress than other regions of the near-wake interaction, but illustrated the strong preservation of the disturbed turbulence field with even large distances downstream. While recovery of the mean velocity profiles was achieved, much slower recovery of the turbulence field was seen.

Acknowledgments

References

[1]Chapman, D. R., "An Analysis of Base Pressure at Supersonic Velocities and Comparison with Experiment," NACA TN 2137, July 1950.

[2]Korst, H. H., "A Theory for Base Pressures in Transonic and Supersonic Flow," *Journal of Applied Mechanics*, Vol. 23, No. 4, 1956, pp. 593–600.

[3]Petrie, H. L., and Walker, B. J., "Comparison of Experiment and Computation for a Missile Base Region Flowfield with a Centered Propulsive Jet," AIAA Paper 85-1618, July 1985.

[4]Venkatapathy, E., and Lombard, C. K., "Accurate Numerical Simulation of Jet Exhaust Flows with CSCM for Adaptive Overlapping Grids," AIAA Paper 87-0465, Jan. 1987.

[5]Sahu, J., "Computations of Supersonic Flow Over a Missile Afterbody Containing an Exhaust Jet," *Journal of Spacecraft*, Vol. 24, No. 5, 1987, pp. 403–410.

[6]Hoffman, J. J., Birch, S. F., and Hopcraft, R. G., "Navier-Stokes Calculations of Rocket Base Flows," AIAA Paper 87-0466, Jan. 1987.

[7]Childs, R. E., and Caruso, S. C., "On the Accuracy of Turbulent Base Flow Predictions," AIAA Paper 87-1439, Honolulu, HI, June 1987.

[8]Childs, R. E., and Caruso, S. C., "Assessment of Modeling and Discretization Accuracy for High Speed Afterbody Flows," AIAA Paper 89-0531, Reno, NV, Jan. 1989.

[9]Petrie, H. L., Samimy, M., and Addy, A. L., "Compressible Separated Flows," *AIAA Journal*, Vol. 24, No. 12, 1986, pp. 1971–1978.

[10]Petrie, H. L., Samimy, M., and Addy, A. L., "Laser Doppler Velocity Bias in Separated Turbulent Flows," *Experiments in Fluids*, Vol. 6, No. 2, 1988, pp. 80–88.

[11]Samimy, M., Petrie, H. L., and Addy, A. L., "A Study of Compressible Turbulent Reattaching Free Shear Layers," *AIAA Journal*, Vol. 24, No. 2, 1986, pp. 261–267.

[12]Samimy, M., Petrie, H. L., and Addy, A. L., "Reattachment and Redevelopment of Compressible Turbulent Free Shear Layers," *Proceedings of the ASME International Symposium on Laser Anemometry*, ASME FED-Vol. 33, Miami Beach, FL, Nov. 1985, pp. 159–166.

[13]Samimy, M., and Addy, A. L., "Interaction Between Two Compressible, Turbulent Free Shear Layers," *AIAA Journal*, Vol. 24, No. 12, 1986, pp. 1918–1923.

[14]Maxwell, B. R., and Seasholtz, R. G., "Velocity Lag of Solid Particles in Oscillating Gases and in Gases Passing Through Normal Shock Waves," NASA TN D-7490, March 1974.

[15]Walsh, M. J., "Influence of Particle Drag Coefficient on Particle Motion in High-Speed Flow with Typical Laser Velocimeter Applications," NASA TN D-8120, Feb. 1976.

[16]Edwards, R. V., "Report of the Special Panel on Statistical Particle Bias Problems in Laser Anemometry," *Transactions of the ASME: Journal of Fluids Engineering*, Vol. 109, Series I, No. 2, 1987, pp. 89–93.

[17]McLaughlin, D. K., and Tiederman, W. G.. Jr., "Biasing Correction for Individual Realization of Laser Anemometer Measurements in Turbulent Flows," *Physics of Fluids*, Vol. 16, No. 12, 1973, pp. 2082–2088.

[18]Buchhave, P., "Biasing Errors in Individual Particle Measurements with the LDA-Counter Signal Processor," *Proceedings of the LDA-Symposium*, Copenhagen, Denmark, 1975, pp. 258–278.

[19]Karpuk, M. E., and Tiederman, W. G., Jr., "Effect of Finite-Size Probe Volume Upon Laser Doppler Anemometer Measurements," *AIAA Journal*, Vol. 14, No. 8, 1976, pp. 1099–1105.

[20]Amatucci, V. A., "An Experimental Investigation of the Two-Stream, Supersonic, Near-Wake Flowfield Behind a Finite-Thickness Base," Ph.D. Thesis, Dept. of Mechanical and Industrial Engineering, Univ. of Illinois at Urbana-Champaign, Urbana, IL, 1990.

[21]Kuntz, D. W., Amatucci, V. A., and Addy, A. L., "Turbulent Boundary-Layer Properties Downstream of the Shock-Wave/Boundary-Layer Interaction," *AIAA Journal*, Vol. 25, No. 5, 1987, pp. 668–675.

[22]Taghavi, K., "Unsteady Reattachment of Supersonic Flow Past a Backward-Facing Step," M.S. Thesis, Dept. of Mechanical and Industrial Engineering, Univ. of Illinois at Urbana-Champaign, Urbana, IL, 1988.

[23]Sun, C.-C., and Childs, M. E., "A Modified Wall Wake Velocity Profile for Turbulent Compressible Boundary Layers," *Journal of Aircraft*, Vol. 10, No. 6, 1973, pp. 381–383.

[24]Sturek, W. B., and Danberg, J. E., "Supersonic Turbulent Boundary Layer in Adverse Pressure Gradient. Pt. I: The Experiment," *AIAA Journal*, Vol. 10, No. 4, 1972, pp. 475–480.

[25]Sturek, W. B., and Danberg, J. E., "Supersonic Turbulent Boundary Layer in Adverse Pressure Gradient. Pt. II: Data Analysis," *AIAA Journal*, Vol. 10, No. 5, 1972, pp. 630–635.

[26]Papamoschou, D., and Roshko, A., "Observations of Supersonic Free Shear Layers," AIAA Paper 86-0162, Reno, NV, Jan. 1986.

[27]Etheridge, D. W., and Kemp, P. H., "Measurements of Turbulent Flow Downstream of a Rearward-Facing Step," *Journal of Fluid Mechanics*, Vol. 86, Pt. 3, June 1978, pp. 545–566.

[28]Andreopoulos, J., and Bradshaw, P., "Measurements of Interacting Turbulent Shear Layers in the Near Wake of a Flat Plate," *Journal of Fluid Mechanics*, Vol. 100, Pt. 3, Oct. 1980, pp. 639–668.

[29]Ikawa, H., and Kubota, T., "Investigation of Supersonic Turbulent Mixing Layer with Zero Pressure Gradient," *AIAA Journal*, Vol. 13, No. 5, 1975, pp. 566–572.

[30]Chandrsuda, C., and Bradshaw, P., "Turbulence Structure of a Reattaching Mixing Layer," *Journal of Fluid Mechanics*, Vol. 110, Sept. 1981, pp. 171–194.

[31]Bradshaw, P., and Wong, F. Y. F., "The Reattachment and Relaxation of a Turbulent Shear Layer," *Journal of Fluid Mechanics*, Vol. 52, Pt. 1, March 1972, pp. 113–135.

[32]Eaton, J. K., and Johnston, J. P., "A Review of Research on Subsonic Turbulent Flow Reattachment," *AIAA Journal*, Vol. 19, No. 9, 1981, pp. 1093–1100.

[33]Lee, S. C., and Harsha, P. T., "Use of Turbulent Kinetic Energy in Free Mixing Studies," *AIAA Journal*, Vol. 8, No. 6, 1970, pp. 1026–1032.

[34]Harsha, P. T., and Lee, S. C., "Correlation Between Turbulent Shear Stress and Turbulent Kinetic Energy," *AIAA Journal*, Vol. 8, No. 8, 1970, pp. 1508–1510.

[35]Bradshaw, P., Ferriss, D. H., and Atwell, N. P., "Calculation of Boundary-Layer Development Using the Turbulent Energy Equation," *Journal of Fluid Mechanics*, Vol. 28, Pt. 3, May 1967, pp. 593–616.

[36]Bradshaw, P., and Ferriss, D. H., "Calculation of Boundary-Layer Development Using the Turbulent Energy Equation: Compressible Flow on Adiabatic Walls," *Journal of Fluid Mechanics*, Vol. 46, Pt. 1, March 1971, pp. 83–110.

APPENDIX A.3

APPLICATION OF PARTICLE IMAGE VELOCIMETRY IN HIGH-SPEED SEPARATED FLOWS

by

M. J. Molezzi and J. C. Dutton

Application of Particle Image Velocimetry in High-Speed Separated Flows

M. J. Molezzi and J. C. Dutton

Application of Particle Image Velocimetry in High-Speed Separated Flows

M. J. Molezzi* and J. C. Dutton†

University of Illinois at Urbana-Champaign, Urbana, Illinois 61801

A particle image velocimetry (PIV) system has been developed for use in high-speed separated air flows. The complete system was developed to improve the spatial resolution and accuracy of the PIV technique as applied in high-speed compressible flows and is the first to incorporate both birefringent image shifting and submicron seed particles for analysis of separated flowfields. The system has been proven in preliminary experiments using a simple low-speed round jet flow and has been validated for accuracy with both known displacement simulated PIV photographs and with uniform flow experiments at Mach 0.5 (170 m/s) for comparison with pressure and laser Doppler velocimeter data. PIV data have also been obtained in the separated wake region behind a two-dimensional base model in a Mach 0.4 freestream flow (135–220 m/s) with resolution of velocity in 1.0-mm² regions, revealing features of the von Kármán vortex street wake and underlying small-scale turbulence.

Introduction

EXPERIMENTAL investigation of turbulent and compressible flows has become increasingly sophisticated in recent years with the advent of laser based measurement techniques. Among these tools is a relatively new technique called particle image velocimetry (PIV). PIV is performed by illuminating a seeded flowfield with a planar laser sheet that is pulsed at a known time interval, forming two or more images of each seed particle within the light sheet (Fig. 1). After recording these images on film or another medium, image separations and therefore velocities can be determined for the entire plane. Unlike pointwise techniques such as laser Doppler velocimetry (LDV) which provides statistical velocity data on a point-by-point basis, PIV can identify instantaneous flow structures that may be random in nature but important to the overall behavior of the flow. PIV also reveals planar views of three-dimensional flow structures that are smeared by volume integration inherent in techniques such as schlieren photography. Other advantages include the ability to obtain PIV images quickly, allowing shorter run times, larger test sections, and higher Mach numbers.

Although molecular imaging techniques have recently been used for high-speed velocity measurements,[1,2] pioneering work by Kompenhans and Höcker[3,4] and Post et al.[5] have recently extended the particle-based PIV technique to high-speed flows. Despite this initial work, difficulties in seeding and image acquisition have limited the spatial resolution of PIV. One of the most important considerations in PIV for high-speed flow applications is obtaining adequate seed density for successful interrogation at all locations. Since most high-speed wind tunnels are not recirculatory, high seed density can only be obtained by injecting a large mass of seed with the flow. Local seeding in areas of interest can be a solution, but injection may need to be done upstream of flow conditioning devices and nozzles that partially disperse the seed. Difficulty also arises in obtaining sufficient seeding in separated zones of the flow (behind bases, steps, etc.). Experience with both PIV and LDV

shows that seed density in these areas is generally sparse, causing significant data dropout. Another concern is the choice of seed particles that are small enough to follow large velocity gradients while still scattering sufficient light to expose film. The seeding material is further restricted when birefringent image shifting[6] is used to resolve the directional ambiguity of image displacements in high-speed separated flows. Image shifting involves shifting the second image of every particle by a known distance to assure that the direction of image displacement is known over the entire PIV photograph. Birefringent image shifting is done by using vertically and horizontally polarized light for the two illumination pulses, then photographing the flowfield through a birefringent calcite crystal that shifts one polarization of light (and therefore one set of images) by a known distance. This use of polarized light sources requires seed particles which maintain polarization in sidescatter. After image displacements are determined from the photograph, the "shift displacement" is subtracted off to return the actual flowfield displacements (and velocities).

Laser requirements are also a factor in the use of PIV for high-speed flow applications. To illuminate small seed particles, high power in the visible spectrum is a necessity. Kompenhans and Höcker[3,4] have used a Nd:YAG system with 70 mJ/pulse for recording images on 35-mm film, but when necessary, resolution of small-scale velocity fluctuations in high-speed test sections requires the use of large format film to reduce diffraction-limited image sizes and to avoid film grain limitations. The larger film area, in turn, requires much greater illumination. The high laser energy must also be combined with very short pulse duration to prevent image blur which reduces the accuracy of velocity measurements. Typical super-
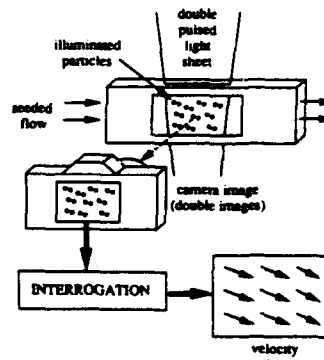
Fig. 1 Principle of PIV.

sonic flow speeds require laser pulse durations on the order of 10 ns or less.

With consideration of the aforementioned factors for PIV application, the present work sets out to advance the capabilities of the PIV technique as applied in high-speed flows. Specifically, the objectives include improvement of the spatial resolution of velocity measurements on a uniform grid to improve detection of small-scale instantaneous structures. The technique is also applied in fully separated flowfields where recirculatory, unsteady, instantaneous structures can dominate the fluid dynamic behavior. These applications involve careful choice of the seeding material and delivery system and the implementation of birefringent image shifting. Finally, the importance of obtaining highly accurate data for quantitative analysis requires careful system validation and determination of data accuracy.

Particle Image Velocimetry Equipment and Operation

Acquisition System

The acquisition system refers to the equipment used to obtain double-exposed particle image photographs of the flowfield of interest. Diagrams of the PIV acquisition system equipment and beam optics are shown in Fig. 2. This system uses two Continuum YG681C-10 Nd:YAG lasers equipped with frequency doubling crystals to provide a maximum output energy of 550 mJ/pulse at a wavelength of 532 nm (green light) with a pulsewidth of 4–6 ns. High-resolution black-and-white films are very sensitive to green wavelengths and the high visibility of the green light also simplifies alignment of the two beams, which is a critical factor in obtaining double exposures of particles in the flow. Two separate lasers are required since a single laser cannot generate two distinct, equal energy pulses in the short time interval required for high-speed flows (typically less than 1 μs). The horizontally and vertically polarized beams of the two lasers are combined by a polarized beam splitter, then shaped by spherical and cylindrical lenses to form a planar beam profile with a waist thickness of 0.4 mm. Beam thickness can be increased by positioning the beam waist either above or below the test section. Beam width at the test section is adjustable up to 125 mm by positioning the 300-mm cylindrical lens. All lenses are made from fused silica substrate and all optics use high-power Nd:YAG coatings to limit beam energy loss to less than 0.25% per surface.

The photographic recording of particle images is done by a camera mounted on the same optical table as the lasers and beam shaping optics. This allows maintenance of the relative position of all optical components for consistent alignment

a)

b)
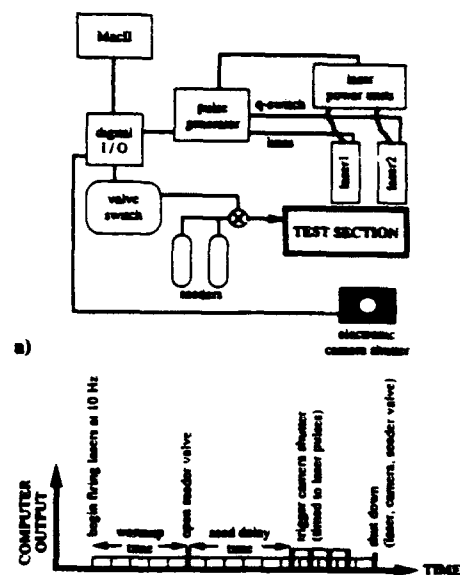
Fig. 3 Acquisition system control: a) equipment schematic; b) timing diagram for automated acquisition of PIV photographs.

and focus. This table is also mounted on vibration-isolated supports to avoid the effects of laboratory vibrations. The system can use a 35 mm, 6×8 cm, or 4×5 in. camera. The 35 mm and 6×8 cm cameras have 100- and 300-mm macro lenses, respectively, and both have auto film wind and an electronic shutter for automated operation. The system has also been used with a modified 4×5 in. camera with a manual shutter and 120-mm macro lens, but since it can take only one frame before reloading, its large format film is most useful when the highest possible resolution of particle images for determination of small-scale turbulent motions is necessary. Flat-field or macro lenses are required to prevent distortion of the field of view at the edges which would induce error in the measurement of particle displacements. Long focal length lenses are used to reduce the solid angle from the lens to the field of view, thereby minimizing parallax. For given flowfield dimensions, longer focal length lenses are required for larger format films to maintain a constant solid angle. In the case of the 4×5 in. camera, a longer focal lens would be desirable, but since none was available the experiments done with this camera used a laser sheet with half the thickness used for other experiments, thereby effectively reducing parallax.

Automation of the system is a key for allowing acquisition of multiple photographs in short run-time test sections, thereby randomly capturing unsteady structures in various stages of development. Control of this system is done by a Macintosh II computer equipped with a digital input/output board and solid state module switches (Fig. 3a). Computer software controls the triggering of the lasers via a Stanford Research pulse generator, an electro-pneumatic valve to release seed into the test section, and the camera shutter. The timing diagram in Fig. 3b indicates the sequence of events controlled by the computer system. Software allows the user to select the warmup time (for laser warmup and wind tunnel adjustment), the seed delay time (to allow seed to propagate from the seeder valve to the test section), and the number of photographs desired. Since the pulse rate of the lasers must be fixed at 10 Hz, conditional sampling of PIV by external events would only be possible for periodic events, in which case software could be implemented to predict from input data when an event would coincide with a laser pulse, factoring in delay times from all inputs and outputs.

Interrogation System

After PIV negatives are obtained and processed for high contrast (to increase signal-to-noise ratio) and contact printed
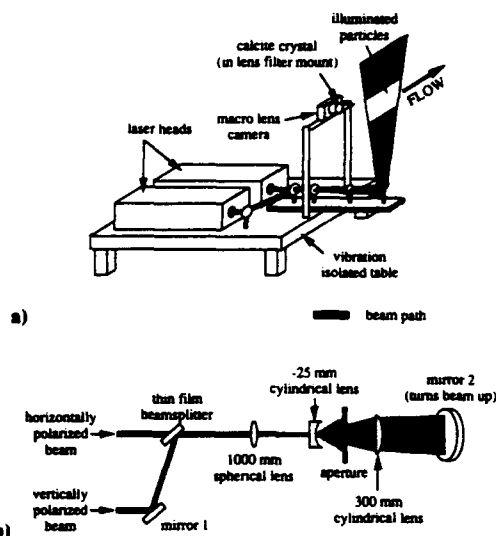

a)

b)

Fig. 2 PIV acquisition system: a) laser and camera equipment for acquiring PIV photographs; b) top view of laser optics for forming planar beam profile.
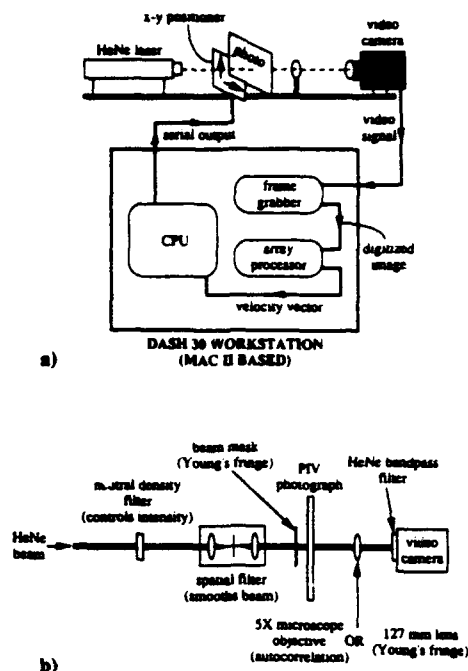
Fig. 4   PIV interrogation system: a) equipment schematic; b) optical components.

onto film to obtain positive images, the photographs are examined using an automated interrogation system controlled by a "Dash 30" modified Macintosh II computer operating at 50 MHz. Diagrams of the interrogation system and the accompanying optics are shown in Figs. 4a and 4b.

Simply explained, the average particle displacement for an interrogation spot is determined from its spatial autocorrelation function, which is derived by performing two two-dimensional Fourier transforms.[7] This is most commonly done by either the "Young's fringe" method where the first transform is done optically and the second is done digitally by fast Fourier transform (FFT), or the "autocorrelation" method where the original interrogation spot is digitized and both transforms are done by digital FFTs. Although the Young's fringe method is faster, the autocorrelation method provides the advantages of easier setup and increased flexibility. Imaging the interrogation spot to the video camera allows control over image focus, image contrast, and interrogation spot size by direct observation. Use of the Young's fringe method requires collimation of the illuminating beam to obtain good interference fringes from the optical transform, beam masking to select the spot size, and the relatively difficult task of determining the "best" fringe pattern by adjustment of optics, beam focus, and beam intensity. The speckle in typical fringe patterns (caused by coherent light interference) makes this task difficult, and if not done well, it can significantly reduce the number of successful interrogations on a given PIV photograph. An additional advantage of the autocorrelation method is that both the original particle images and the autocorrelation output can be digitally recorded for a particular interrogation spot, allowing the user to physically measure the particle displacements and compare to the system output for accuracy. For these reasons and the fact that interrogation time constraints are not particularly important in comparison to other processing tasks, the autocorrelation method is used for the data presented in this paper.

For this system, the completed PIV photograph is mounted between glass plates on a two-dimensional Aerotech positioner system to scan the photograph spot by spot with a fixed 5-mW HeNe illumination beam and optics. The HeNe beam is passed through a neutral density filter to control intensity, then it is spatially filtered to eliminate high-frequency intensity variations that could add noise to the illuminated interrogation

spot. If the Young's fringe method is being used, the beam then passes through a mask to determine the interrogation spot size. After passing through the photograph, an imaging lens is then chosen to obtain either the actual particle images or the far-field diffraction pattern (optical Fourier transform) of the interrogation spot, depending on the interrogation method being used. A 5X microscope objective lens is used to obtain particle images, while a 127-mm plano-convex lens is used to obtain the optical Fourier transform. Finally, the image is received by a Sierra Scientific CCD array video camera with a HeNe bandpass filter to eliminate room light interference. The choice of a HeNe laser is made to ensure uniform illumination by use of the spatial filter, to allow interrogations in normal room light conditions by using the HeNe bandpass filter, and to provide the collimated light source required when Young's fringe interrogations are desired.

The video image is then digitized to a 512×512 pixel array by a Perceptics frame grabber board with 8-bit grayscale (256 gray levels) and is passed to a Mercury MC3200-NU array processor which performs FFTs and other array operations to obtain the two-dimensional autocorrelation of the original image. The array processor uses a centroidal peak-finding routine to locate up to three of the strongest autocorrelation peaks. These peak locations are stored as the most likely image displacements for that interrogation spot and the process is repeated for the next spot.

After the full vector field is determined, postprocessing must be done to refine the data. As a first pass, the vector field is checked by a routine that looks for "bad" vectors that are outside user-specified absolute limits and replaces them with one of the secondary peaks for that location if it is acceptable, or with a default value to indicate a bad measurement. The few remaining spurious velocity vectors are manually removed and replaced with the aforementioned default value. Another automated routine then searches for default values and replaces them with values interpolated from valid neighboring vectors using multiple linear regression. The vector field is then smoothed by convolution with a Gaussian kernel as described by Landreth and Adrian[8] to eliminate random noise in the vector field caused by image imperfections, video noise, and other factors. This is crucial when spatial differentiation is to be performed on the vector field to derive quantities such as vorticity, since any high-frequency random error will be accentuated by differentiation.

Flow Seeding

The choice of a seeding material and delivery system is key to the successful implementation of PIV in high-speed flows. The limitations of particle techniques hinge on production of particles with sufficiently low slip velocity to accurately follow high-velocity gradients in compressible flows. This also affects the ability of seed to be carried into separated flow regions where vortices tend to throw heavy particles out, thereby reducing seed density. The density of seed in areas of interest also places a limitation on the spatial resolution of velocity measurements. An additional factor is the ability of the particles to scatter sufficient light for PIV photographs, which is dependent on particle shape and refractive index. In the development of this system, various seed materials have been examined for slip velocity and optical performance, including atomized water, atomized silicone oil, and monodispersed polystyrene latex (PSL) spheres of various sizes. Each seed type was used for test photographs and all were successfully recorded on film including 0.5- and 1.0-μm-diam monodispersed PSL spheres. The resulting choice for high-speed flow experiments was silicone oil seed generated by a six-jet atomizer made by TSI, Inc. The polydispersed atomized droplets have a mean diameter of 0.8 μm as quoted by TSI and Bloomberg,[9] and show good response to the velocity gradient across an oblique shock wave.[9] PSL spheres of 0.5 and 1.0 μm diameter also respond well to velocity gradients, but cannot be delivered in large enough quantities for PIV requirements.

Test photographs also show good performance of the silicone oil droplets for image exposure intensity and for birefringent image shifting. The seed delivery system used for the transonic wind-tunnel experiments presented here is a localized multiple-tube arrangement described in further detail in the discussion of experimental results.

Spatial Resolution

In a high image density PIV system, each individual velocity vector is determined by the mean particle displacement in the interrogation spot. Therefore, the spatial resolution of a data-set is determined by the interrogation spot size as measured in the flowfield frame of reference. To use a particular spot size, for example 1×1 mm, many requirements must be satisfied. First, the diameter of the particle images must be small enough to measure displacements greater than one image diameter within the spot, since overlapping images cannot be distinguished. Second, the maximum displacement should be less than approximately 25% of the linear dimension of the spot,[7] in this case 250 μm, to insure that a sufficient number of image pairs will appear fully within the spot for successful interrogation. This is accomplished by selecting the proper time delay between laser pulses for a given flowfield photograph. Finally, the particle image density must be high enough to provide a sufficient number of image pairs for successful interrogation in all spots throughout the region of interest. The last of these requirements is typically the most difficult to satisfy and generally governs the choice of spot size, and thus, spatial resolution.

Results

Interrogation System Validation

Validation of the PIV system first involved testing of the interrogation system. As a first check on the accuracy of the autocorrelation output and the associated image processing software, an interrogation was performed on a known uniform dot pattern with a spacing of 133 dots/in. in both the horizontal and vertical directions. The pattern is a commercially produced screen PMT for making copies of photographic prints. The screen was used in place of a PIV photograph on the interrogation system and was interrogated several times at various magnifications, storing both the dot pattern image input and the autocorrelation output. After analysis, peaks in the spatial autocorrelation output were compared to the original dot pattern. The spacing of peaks in the autocorrelation output was found to match the center spacing of the original dot pattern to within 1%. This is expected for a uniform pattern since each dot correlates perfectly with itself, the closest neighbor in each direction, the second closest neighbor, etc.

Table 1 Uniform displacement photograph interrogation results

	Photo 1	Photo 2
$\overline{\Delta x}$,[a] μm	63.515	131.299
$\overline{\Delta y}$,[b] μm	58.523	133.153
$\sigma_{\Delta x}$, μm	2.001	1.166
$\sigma_{\Delta y}$, μm	1.929	2.153
$\sigma_{\Delta x}/d_p$, %	5.72	6.19
$\sigma_{\Delta y}/d_p$, %	5.51	6.15
$\overline{|\Delta X|}$,[c] μm	86.366	187.000
$\overline{|\Delta X|}_{actual}$, μm	87	187
Interrogation spot, mm		0.8×0.8
Increment, mm		0.4
Total spots/photo		10,000
Image pairs/spot		~8
Mean image diameter, d_p, μm		~35

[a] Mean interrogated x displacement.
[b] Mean interrogated y displacement.
[c] $\overline{|\Delta X|} = [(\Delta x)^2 + (\Delta y)^2]^{1/2}$.

Tests were then done with known displacement simulated PIV photographs. The most accurate simulation used photographs of uniformly displaced image pairs. The photographs were made by first printing a randomly spaced dot pattern on an $8\frac{1}{2} \times 11$ in. sheet. A photograph of the unpaired images was then made on 4×5 in. Kodak Technical Pan 4415 film in an enlarger. This unpaired-dot photograph (clear dots on a dark background) was then attached to a translation stage and placed over unexposed film for contact printing. Exposures were made with the unpaired-dot photograph in an initial position and in a second position, displaced by the translation stage, insuring uniform image pair displacements. The resulting paired-dot photograph (dark dot pairs on a clear background) was then contact printed onto film, resulting in the final paired-dot photograph (clear dot pairs on a dark background). Two photographs were made with different displacements. The photographs were examined under a 14X stereo microscope equipped with a measuring reticule marked in 5 μm increments to determine the actual mean displacements of 87 and 187 μm as presented in Table 1. Both photographs started with a pseudo-randomly dispersed pattern of approximately 12.5 image pairs/mm^2, but due to nonuniformity in the pseudo-random dot dispersion, film flatness, film sensitivity, lighting, dust, etc., the image density on the final photographs was reduced and varied throughout the photographs. Image diameters also varied from 20 to 50 μm due to the same photographic effects. This variation in image density, image size, and other effects due to the printing of the images on film creates a good simulation of real PIV photographs, except for the lack of unpaired images which occur in real flowfield photographs due to some particles moving out of the laser sheet between pulses.

Interrogations were made of each photograph at 10,000 locations with the results presented in Table 1. The statistics shown were calculated using only "good" data falling within ± 17 μm of the mean displacement in each direction, which was over 90% of the total for both photographs. The deviation from 100% good data was due to the aforementioned dot dispersion and photographic effects which reduced image density in some areas. Bad vector replacement and smoothing were not done in order to preserve the full error in the interrogation. The photographs were interrogated with the direction of displacement at approximately a 45-deg angle to the horizontal to examine the dependence of error on variations in both the x- and y-displacement magnitudes. The data reveal that the standard deviation of the interrogated displacements is approximately constant at 2 μm for both photographs. This is an expected result since the random error in displacement should be proportional to the particle image diameter and not the magnitude of displacement.[7] Given the mean image diameter d_p of 35 μm, the random error is approximately 6% of d_p. It should be noted that although photographic imperfections and other factors in real PIV photographs may tend to increase this error ratio, the use of vector field smoothing tends to reduce the random error significantly as mentioned in the preceding discussion of the interrogation system. The mean interrogated displacement for photograph 2 is taken as exactly 187 μm since it was used as the reference for determining the pixel-to-μm scaling factor. The mean interrogated displacement for photograph 1 matches the actual displacement to within 1%, which is within the error in the measurement of the actual displacements, showing no evidence of mean bias error.

Low-Speed Round Jet

The full PIV system has been used to examine the flow from a round free jet test stand consisting of a 6 in. long, 1 in. o.d. tube fed by a TSI six-jet atomizer with silicone oil seed and an adjustable dilution air supply as shown in Fig. 5. The jet flows into an $8 \times 10 \times 48$ in. test section exhausted to atmosphere. Image shifted PIV photographs were taken on both 35 mm and 4×5 in. film. Although the jet velocity was relatively low, experiments done with this test stand used the same equipment

and procedures that are used for high-speed flow experiments, including seeding, laser system, birefringent image shifting optics, Kodak Technical Pan film, automated system operation, and high spatial resolution of velocity measurements. The sole differences involve the seeder supply pressure and film formats for the data presented. Reduced seeder pressure (5–10 psig vs 20 psig for high-speed flow experiments) was necessary to avoid damage to the low-speed test section, but the effect of lower pressure and flow rate tends to reduce the mean seed particle size. This is because atomized droplets must rise against gravity to leave the atomizing chamber, and the reduced flowrate carries fewer heavy particles out. The data
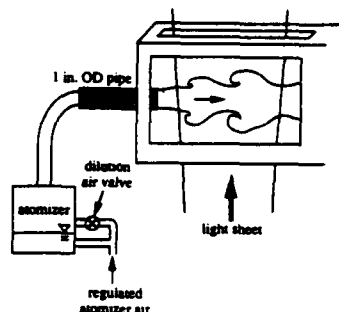
presented for these experiments was also taken on 4 × 5 in. film while subsequent high-speed flow experiments used 35-mm film for convenience, since film grain and image size limitations were found to be acceptable. The main purpose of these low-speed flow experiments was to demonstrate the operation and data analysis capabilities of the system.

Particle image sizes were measured from the photographs for determination of the minimum measurable particle displacement, which must be at least one image diameter to prevent overlap of pairs. Average image diameters were approximately 55 μm for 35-mm photographs and 35 μm for 4 × 5 in. photographs (in the frame of reference of the flowfield). For a projected interrogation spot size of approximately 1 mm^2, for which the maximum measurable displacement is approximately 250 μm (see preceding discussion of spatial resolution), this provides quite sufficient dynamic range, where the dynamic range is the ratio of the maximum to the minimum measurable displacement.

Determination of the mean image diameter also provides the ability to estimate the random error of velocity measurements. Using the information from the validation experiment reported in Table 1, the standard deviation of the random error is expected to be 6% of the mean image diameter, or 3.3 μm for the 35-mm photographs and 2.1 μm for the 4 × 5 in. photographs. With a maximum image displacement of approximately 250 μm (selected by choosing the time delay between laser pulses), the random error is 1.3% or 0.8% of the maxi-

Fig. 5 Round jet test stand used for initial low-speed flow application of PIV system.

Axial Location x (mm)
Measured from Tube Exit   → 2.0 m/s

| Mean Jet Velocity | 2.05 m/s |
| Jet Diameter | 18 mm |
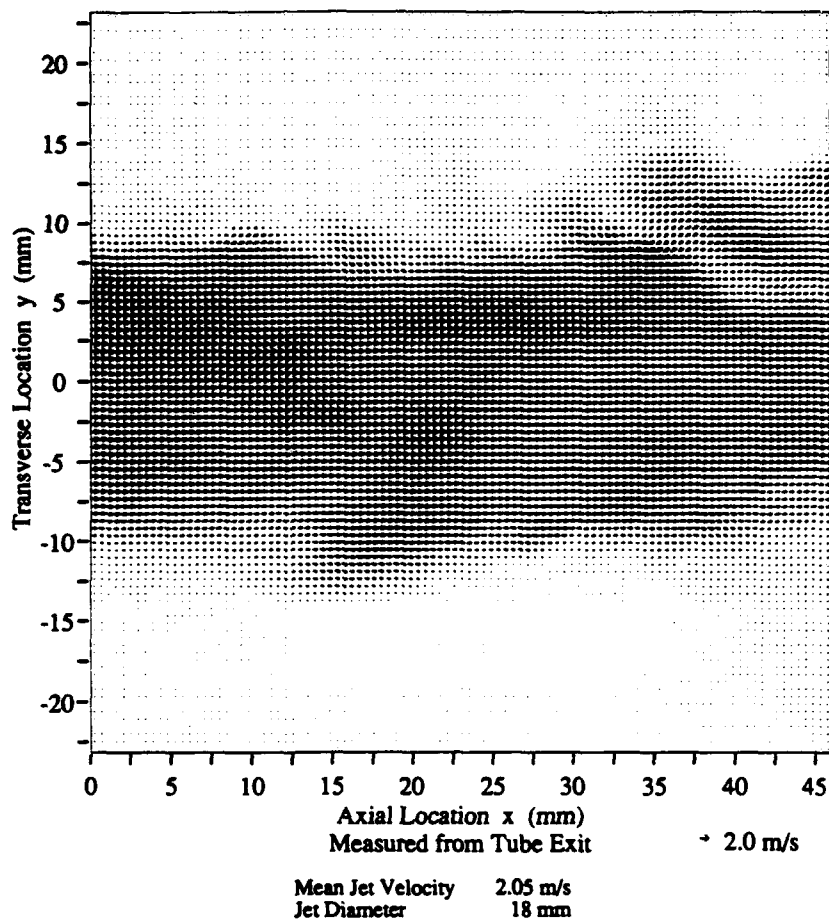
PIV PARAMETERS

Laser Energy	500 mJ/pulse	Magnification	1.08
Laser Sheet Thickness	0.5 mm	Interrogation Method	autocorrelation
Pulse Separation	150 μs	Spot Size (in flowfield)	1.08 mm x 1.08 mm
Image Shift	100 μm transverse	Increment	0.46 mm

Fig. 6 Round jet velocity field: initial application of PIV system in low-speed jet flow.

mum velocity (proportional to image displacement) for 35-mm photographs or 4×5 in. photographs, respectively.

An example PIV photograph of the jet was then interrogated. This photograph was taken using Kodak Technical Pan 4415 4×5 in. film with a 120-mm lens at f 5.6. Other parameters for acquisition and interrogation are shown in Fig. 6. Before a full interrogation was done, the repeatability of the measurements was checked by interrogating a small region of the photograph, then resetting the positioner to its original position and reinterrogating. The results showed perfect agreement of both the first and second peak locations for the entire 4×4 grid of interrogation spots. Only the first two autocorrelation peaks were stored for this interrogation which was done before third peak storage was implemented. Reinterrogation was also done on two 5×5 regions (total of 50 spots) after the full interrogation was completed, involving a positioner travel of more than 25 mm in each direction. This resulted in 28 matches of both the first and second highest autocorrelation peaks, 18 matches of the first peak only, and 4 nonmatches. It should be noted that exact peak locations can vary due to

Fig. 9 Schlieren photograph of flow past a finite thickness base, $M_\infty = 0.4$ (from Ref. 13).

bidirectional positioner error over long travel distances (±10 µm over 7-mm travel) and random electronic noise in video imaging.

Removal and interpolation of bad vectors for the full flowfield showed a success rate for valid vector determination of approximately 94%, which is quite reasonable in comparison to other reported success rates. The final velocity vector plot after subtraction of image shift, interpolation, and smoothing is shown in Fig. 6. The photograph was interrogated over a 46×46 mm area with 0.46-mm increments in each direction, resulting in 10,201 vectors (101 × 101). The interrogation increment is chosen to be approximately half the spot dimension to avoid aliasing of high spatial frequency velocity fluctuations. The full interrogation took 11 h, 18 min or 4.0 s/spot using the autocorrelation method. Interrogations using the Young's fringe method took 2.3 s/spot.

The mean velocity at the tube exit is approximately 2.05 m/s. Examination of Fig. 6 shows typical vortex structures at the edges of the jet with a gradual decrease in the centerline velocity as the jet propagates downstream. A plot of the spatially averaged axial velocity component at each transverse location is shown in Fig. 7. Although this spatial mean is not equivalent to a time average velocity profile due to spreading of the jet over the field of view, it does reveal a general nonuniformity of the flow, implying that the jet is not truly axisymmetric. The higher velocity at the top of the tube was induced by the flow around a bend in the flexible tubing just before the straight section at the jet exit. Although the test flow is not ideal, the ability to reveal such information is part of the purpose of this experiment.

Identification of flow structures can also be done by manipulating the acquired velocity data. The vortex structure in the upper right section of Fig. 6 is shown in Fig. 8a with a portion of the mean axial velocity subtracted and in Fig. 8b by deriving the out-of-plane vorticity $\{\partial v/\partial x - \partial u/\partial y\}$ from central finite differences of the original velocity data. Both reveal the expected dominant positive (counterclockwise) vorticity at the upper edge of the jet and some resulting negative (clockwise) vorticity between structures. The ability to obtain spatially well-resolved velocity data for such analysis allows quantification of turbulent flow structures by determination of vortex strength and position. Similar analysis can be performed with rate-of-strain, volumetric flux, and other derivative and integral quantities important in a particular flowfield to provide information about the nature of complex high-speed flows.
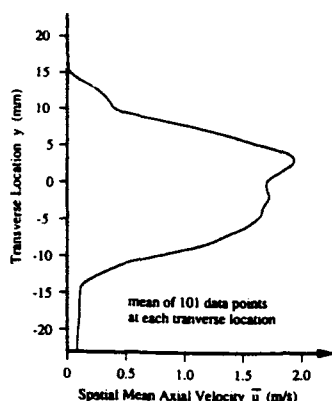

Fig. 7 Round jet spatial mean velocity: mean velocity at each transverse location of Fig. 6.
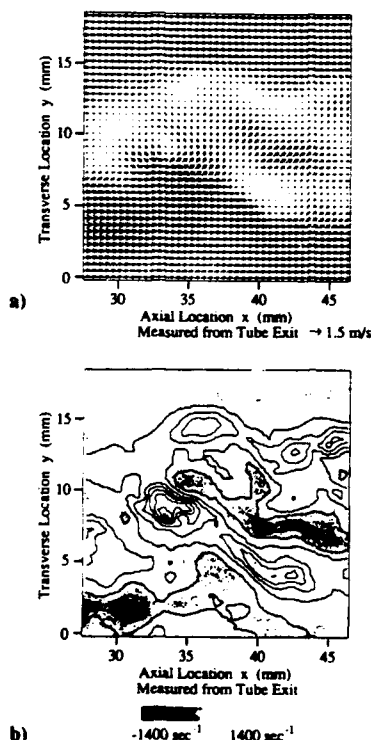

Fig. 8 Enlarged section of round jet: a) velocity field with 0.68-m/s axial velocity subtracted to accent flow structure; b) vorticity field derived from velocity data (grayscale and overlaid contours).

Low-pass and high-pass spatial filtering can also be done[10] to reveal both large- and small-scale structures.

High-Speed Base Flow

Two-dimensional finite thickness bodies in subsonic and transonic flows form a separated flowfield very rich in turbulent structure due to the presence of the well-known von Kármán vortex street wake. The schlieren photograph in Fig. 9 shows the wake behind a blunt base in a Mach 0.4 freestream. The screw visible in the photograph was used for focusing and is outside of the test section. The motivation for studying this flow with PIV stems from both the fact that it exhibits a well-defined instantaneous structure and that the mechanism of the observed base drag reduction in the presence of a base cavity is not completely understood.[11-15] To resolve discrepancies in previous work on this subject and to better define the mechanisms of base cavity drag reduction, PIV experiments are being done to quantify flow structure for various freestream Mach numbers and base configurations.

Modifications have been made to an existing transonic wind tunnel for the use of PIV on two-dimensional base flows (Fig. 10). The previously fabricated tunnel has a 4 × 4 in. test section with solid side walls and slotted upper and lower inner walls to relieve the blockage effect of models in the transonic speed range. To allow visualization past the aft end of base models 6-in.-diam round windows are mounted in both sidewalls. The base model consists of interchangeable afterbodies mounted on a 15.24-mm-thick wedge-shaped forebody, with its upstream edge located approximately 17 in. downstream of the nozzle entrance. The afterbodies include a solid base, a rectangular cavity base with a depth of half the base height, and a rectangular cavity base with a depth of one full base height.

Slot-shaped upper and lower windows have been fabricated and installed in the outer tunnel walls for access with a vertically propagating planar laser sheet for PIV. The sheet passes through the lower window and through one of the streamwise slots of the inner wall to enter the test section. The seed delivery is done by two TSI six-jet atomizers feeding a single ¼-in. o.d. tube that enters the stagnation chamber. This tube leads to a manifold tube that feeds eight smaller tubes directed downstream and oriented in a transverse (vertical) plane aligned with the illuminating laser sheet. The flow then passes through 2-in. long, 3/16-in. cell honeycomb and a 44 × 44 mesh screen with 57% open area to reduce turbulent fluctuations in the supply flow. It should be noted that the screen is cut out in the areas where the seed tubes feed through the honeycomb. This is done because experience with LDV in this laboratory has shown that silicone oil droplets tend to build up on any surface perpendicular to the flow direction, causing large drops to form and burst off, which bias velocity measurements. Flow seeding behind the base is sufficient due to small
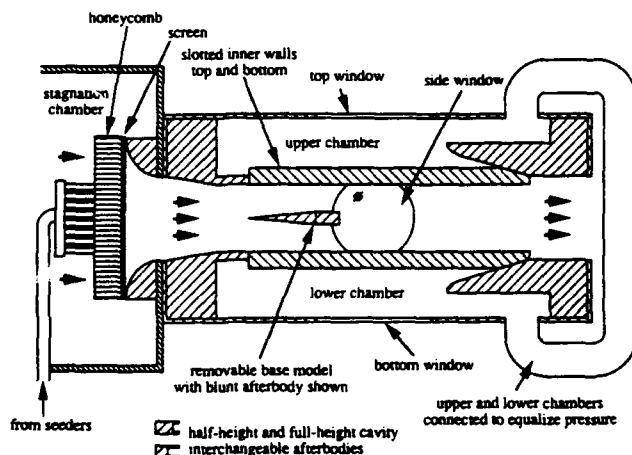

a)

b)

PIV PARAMETERS

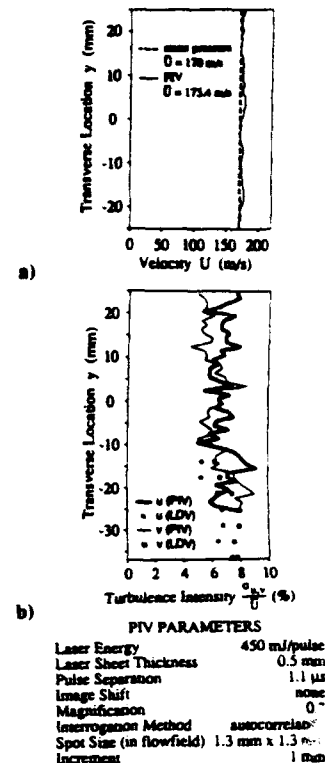|	
Laser Energy	450 mJ/pulse
Laser Sheet Thickness	0.5 mm
Pulse Separation	1.1 μs
Image Shift	none
Magnification	0
Interrogation Method	autocorrelation
Spot Size (in flowfield)	1.3 mm x 1.3 mm
Increment	1 mm

Fig. 11 PIV data validation results from uniform Mach 0.5 flow: a) PIV spatial mean velocity vs temporal mean velocity from pressure data; b) turbulence intensity: PIV spatial data vs LDV temporal data.

seed particle slip velocity allowing the motion of the alternating von Kármán vortex street to carry seed into the wake.

The first experiments in this facility were done without a base model to compare PIV velocity measurements to data obtained with both LDV and static pressure taps. PIV photographs were taken on 35-mm Kodak Technical Pan 2415 film. To facilitate comparison to the time-integrated pressure and LDV measurements of velocity, PIV velocity data from a single photograph were summed along the row at each transverse location to obtain mean velocity components and standard deviations were found to determine turbulence intensities. Given that the flowfield is not evolving in the streamwise direction in this tunnel-empty case, equating spatial statistics to temporal statistics is adequate for a first approximation, although the number of samples available from a single PIV photograph is not sufficient for highly accurate statistics. It should be noted that there were not yet any flow conditioning devices in the wind tunnel when these experiments were done, the effects of which will be discussed in the following paragraphs.

The results for mean velocity from a run at Mach 0.5 are shown in Fig. 11a with the relevant PIV parameters. The PIV data are compared to the mean velocity calculated with pressure data from taps measuring static pressure in the test section and total pressure in the stagnation chamber. Although there are at most only 81 PIV measurements per data point in this plot, the mean velocity at each transverse location varies only slightly from the overall mean of 173.4 m/s, which is within 2% of the mean velocity determined from the pressure measurements.

A more stringent test of the accuracy of PIV lies in the ability to measure velocity fluctuations. To this end, LDV measurements of streamwise and transverse turbulence intensity were made for comparison to the PIV data (Fig. 11b). Because of the spatial constraint of avoiding contact between the LDV laser and the lower wall of the wind tunnel, LDV measurements could only be made up to a transverse location of − 12.5 mm measured from the test section centerline.

Fig. 10 Transonic wind tunnel with slotted-wall test section and two-dimensional base model.

a)

b)

-110,000 sec^{-1} 110,000 sec^{-1} → 220 m/s

PIV PARAMETERS

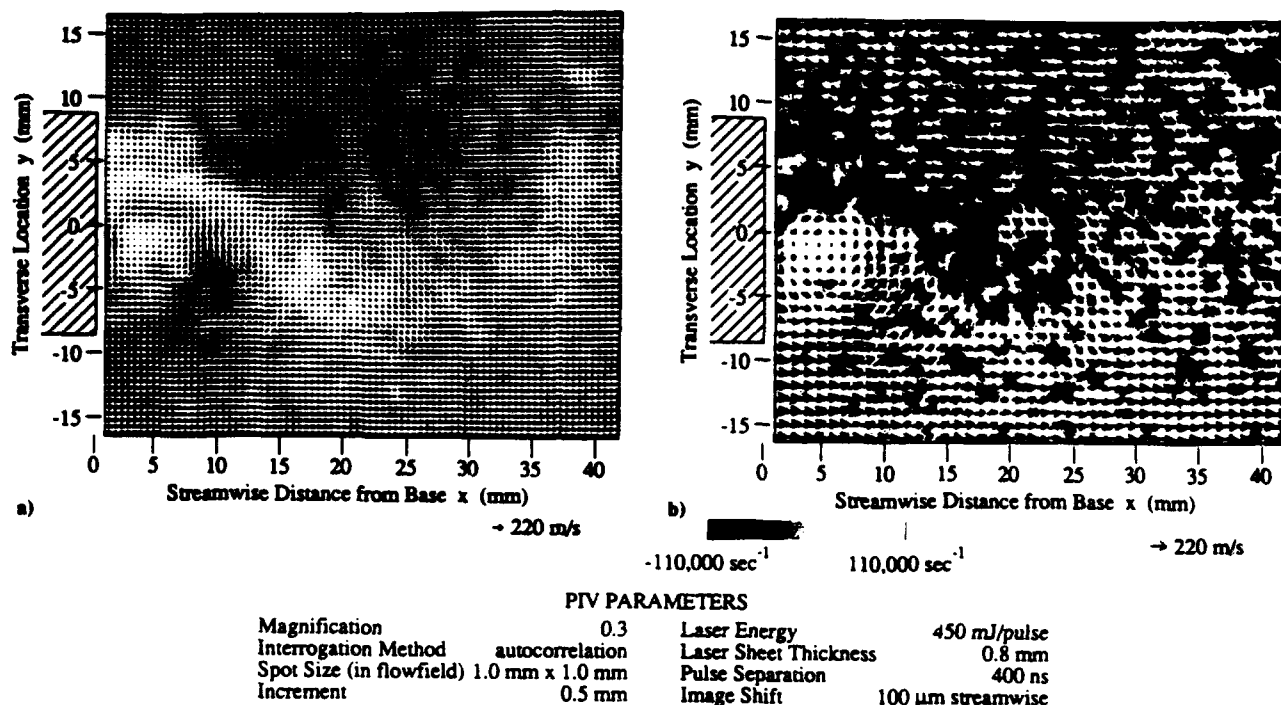|			
Magnification	0.3	Laser Energy	450 mJ/pulse
Interrogation Method	autocorrelation	Laser Sheet Thickness	0.8 mm
Spot Size (in flowfield)	1.0 mm x 1.0 mm	Pulse Separation	400 ns
Increment	0.5 mm	Image Shift	100 μm streamwise

Fig. 12 Two-dimensional base flow PIV results at $M_\infty = 0.4$: a) velocity field with full resolution; b) vorticity (grayscale) with velocity field overlay (reduced resolution for clarity).

Again, a maximum of only 81 PIV measurements was used for the data at each transverse location, but it can be seen from the plot that both the LDV and PIV data vary from 5 to 8% turbulence intensity. Although this data lends some confidence in the accuracy of the PIV data, it revealed undesirable freestream turbulence in the test section without flow conditioning. The aforementioned honeycomb and screen were therefore added to the facility. PIV measurements of turbulence intensity with the flow conditioning devices installed have shown turbulence intensities of 3-5% which, while improved, are still relatively high. Although LDV measurements with flow conditioning have not yet been made due to restrictions on the availability of the LDV system, the high turbulence intensity measured by PIV is quite likely due to turbulence generated downstream of the honeycomb and screen by the velocity gradients between the freestream and the lower velocity seeded jets.

Experiments have most recently been done with a solid base model in a Mach 0.4 freestream. The Mach 0.4 freestream condition is determined by running the test section at a stagnation pressure that results in a Mach 0.4 flow when no model is present. PIV photographs using birefringent image shifting were taken on 35-mm Kodak Technical Pan 2415 film. The mean image diameter for the photos is approximately 40–50 μm in the frame of reference of the flowfield. Using the error data from the validation results presented in Table 1, the random measurement error is expected to be approximately 6% of the mean image diameter, or less than 1.6% of the maximum particle image displacement.

The interpolated and smoothed velocity plot for a region spanning approximately 2.7 base heights downstream of the base edge is shown in Fig. 12a. The location of the base is indicated by the cross-hatched region. The plot includes 5346 vectors (81 × 66) with an increment of 0.5 mm between vectors and a square interrogation spot of 1.0 mm². As with the round jet data, the increment is chosen to be approximately half the interrogation spot dimension to avoid aliasing of high spatial frequency velocity fluctuations. The total interrogation time was 6 h, 15 min or 4.2 s/spot using the autocorrelation method. The success rate for valid vector determination was 80% overall including edge regions where seed density

dropped off, and approximately 90% in the wake region within the upper and lower edges of the base. The presence of interrogated particle images at the vortex centers also indicates that submicron oil droplets are being recorded on film since centripetal acceleration forces all but the smallest particles out of the vortex centers as they travel downstream. Using an estimate from Fig. 12 of the centripetal acceleration in a vortex and using the Stokes flow drag law, the slip velocity of a 1 μm diam silicone oil sphere was found to be approximately 15 m/s, which would carry the particle more than 2 mm away from the vortex center by the time it moves one base height downstream of the base edge. Therefore, the velocity data obtained at the vortex centers must be obtained from submicron particles.

Figure 12a includes all interrogated velocity vectors to indicate the full resolution of the measurements. Although the wake structure is somewhat evident in Fig. 12a, it is accentuated in Fig. 12b which has the velocity vector field overlaid on a grayscale representation of the vorticity. Only every other vector is plotted in Fig. 12b in the interest of clarity. The vorticity plot reveals the fragmentation of the main vortices and the presence of lower intensity small-scale turbulent structures of about 3 mm diameter throughout the flowfield. The source of these structures is presently unknown. They may be due to high freestream turbulence levels, but an estimate of the Taylor microscale for this flowfield using mean velocity gradient data was found to be 2.67 mm, suggesting that the structures may be a secondary feature of the vortex street wake. Additional data is required with reduced freestream turbulence levels and various freestream velocities to make a more definite determination, but the more important fact at this point is that the PIV technique has shown the capability to reveal and quantify flowfield structure not found in previous work.

Conclusion

A complete PIV system has been developed for application in separated high-speed flows. Successful demonstration in both low- and high-speed flow validation experiments along with analysis of known displacement photographs has shown the capability for accurate velocity measurement with the use

of submicron seed particles and birefringent image shifting. Analysis of a high-speed separated flowfield has also been done with a spatial resolution of 1.0 mm^2 per interrogation spot (measured in the flowfield frame of reference). This improvement in the spatial resolution of the PIV technique in compressible flows increases the capability for determination and quantification of small-scale turbulent structures and stands to provide important data for turbulence modeling, numerical simulations, and analysis of complex flowfields.

Future work in the area of subsonic and transonic base flows will concentrate on reduction of freestream turbulence, adjustment of the acquisition system optics for improved performance, and improvement of seeding uniformity, which has been the most challenging problem to this point. The result will be a quantitative analysis of base cavity effects on wake structure for the determination of the fluid dynamic mechanisms governing base cavity drag reduction.

Acknowledgments

References

[1]Miles, R. B., Connors, J. J., Markovitz, E. C., Howard, P. J., and Roth, G. J., "Instantaneous Profiles and Turbulence Statistics of Supersonic Free Shear Layers by Raman Excitation Plus Laser-Induced Electronic Fluorescence (RELIEF) Velocity Tagging of Oxygen," *Experiments in Fluids*, Vol. 8, No. 1–2, 1989, pp. 17–24.

[2]Palmer, J., McMillin, B., and Hanson, R., "Planar Laser-Induced Fluorescence Imaging of Velocity and Temperature in Shock Tunnel Free Jet Flow," AIAA 30th Aerospace Sciences Meeting, AIAA Paper 92-0762, Reno, NV, Jan. 1992.

[3]Kompenhans, J., and Höcker, R., "Application of Particle Image Velocimetry to High Speed Flows," *Von Kármán Institute Lecture Series 1988-06*, Von Kármán Inst., Brussels, Belgium, March 1988, pp. 67–83.

[4]Höcker, R., and Kompenhans, J., "Application of Particle Image Velocimetry to Transonic Flows," *Proceedings, Fifth International Symposium on Applications of Laser Techniques to Fluid Mechanics*, Springer-Verlag, Berlin, 1990, pp. 415–434.

[5]Post, M. E., Goss, L. P., and Brainard, L. F., "Two-Color Particle-Imaging Velocimetry in a Turbine Cascade," AIAA 29th Aerospace Sciences Meeting, AIAA Paper 91-0274, Reno, NV, Jan. 1991.

[6]Landreth, C. C., and Adrian, R. J., "Electrooptical Image Shifting for Particle Image Velocimetry," *Applied Optics*, Vol. 27, No. 20, 1988, pp. 4216–4220.

[7]Adrian, R. J., "Particle-Imaging Techniques for Experimental Fluid Mechanics," *Annual Review of Fluid Mechanics*, Vol. 23, 1991, pp. 261–304.

[8]Landreth, C. C., and Adrian, R. J., "Measurement and Refinement of Velocity Data Using High Image Density Analysis in Particle Image Velocimetry," *Proceedings, Fourth International Symposium on Applications of Laser Anemometry to Fluid Mechanics*, Springer-Verlag, Berlin, July 1988, pp. 485–497.

[9]Bloomberg, J. E., "An Investigation of Particle Dynamics Effects Related to LDV Measurements in Compressible Flows," M.S. Thesis, Dept. of Mechanical and Industrial Engineering, Univ. of Illinois at Urbana-Champaign, Urbana, IL, May 1989.

[10]Reuss, D. L., Adrian, R. J., Landreth, C. C., French, D. T., and Fansler, T. D., "Instantaneous Planar Measurements of Velocity and Large-Scale Vorticity and Strain Rate in an Engine Using Particle-Image Velocimetry," SAE International Congress and Exposition, Paper 890616, Detroit, MI, Feb. 27–March 3, 1989.

[11]Pollock, N., "Some Effects of Base Geometry on Two-Dimensional Base Drag at Subsonic and Transonic Speeds," Australian Aeronautical Research Lab., Aerodynamics Note 316, Melbourne, Australia, Oct. 1969.

[12]Nash, J. F., Quincey, V. G., and Callinan, J., "Experiments on Two-Dimensional Base Flow at Subsonic and Transonic Speeds," Aeronautical Research Council, R&M 3427, England, UK, Jan. 1963.

[13]Kruiswyk, R. W., and Dutton, J. C., "Effects of a Base Cavity on Subsonic Near-Wake Flow," *AIAA Journal*, Vol. 28, No. 11, 1990, pp. 1885–1893.

[14]Rudy, D. H., "A Numerical Study of Unsteady Two-Dimensional Subsonic Compressible Base Flow," Ph.D. Dissertation, Dept. of Mechanical and Industrial Engineering, Univ. of Illinois at Urbana-Champaign, Urbana, IL, April 1987.

[15]Clements, R. R., and Maull, D. J., "The Representation of Sheets of Vorticity by Discrete Vortices," *Progress in Aerospace Science*, Vol. 16, No. 2, 1975, pp. 129–146.

APPENDIX A.4

AN INVESTIGATION OF LDV VELOCITY BIAS CORRECTION TECHNIQUES FOR HIGH-SPEED SEPARATED FLOWS

by

J. L. Herrin and J. C. Dutton

AN INVESTIGATION OF LDV VELOCITY BIAS CORRECTION TECHNIQUES FOR HIGH-SPEED SEPARATED FLOWS

J.L. Herrin and **J.C. Dutton**
Department of Mechanical and Industrial Engineering, University of Illinois at
Urbana-Champaign, Urbana, IL 61801, USA

Abstract

An experimental study of the effects of velocity bias in single realization laser Doppler velocimetry measurements in a high-speed, separated flow environment is reported. The objective of the study is to determine a post-facto correction method which reduces velocity bias *after* individual realization data have been obtained. Data are presented for five velocity bias correction schemes: inverse velocity magnitude weighting, interarrival time weighting, sample and hold weighting, residence time weighting, and the velocity-data rate correlation method. These data were compared to a reference measurement (saturable detector sampling scheme); the results show that the interarrival time weighting method compares favorably with the reference measurement under the present conditions.

1 Introduction

Laser Doppler velocimetry (LDV) has become a popular experimental tool to measure the velocity field in a variety of fluid dynamic environments. Due to its non-intrusive nature and ability to discriminate flow direction, LDV is well-suited for applications involving large regions of flow separation. The current study is part of an experimental program investigating the separated, near-wake flowfield behind a body of revolution immersed in a supersonic freestream. Characterizing the mean and turbulent velocity fields downstream of the base surface with a two-component LDV system, including the large separated region immediately downstream of the base, has been the focus of the research; hence, a detailed investigation of the accuracy of LDV measurements in this flow environment is necessary. The present paper describes an experimental study which examines the effects of velocity bias on LDV data in high-speed, separated flows and compares traditional methods to correct for this bias.

1

When individual realization LDV measurements are made in turbulent flows, a velocity bias caused by the correlation between the data sampling process and the magnitude of the instantaneous velocity exists. McLaughlin and Tiederman (1973) first recognized this bias and showed that its magnitude was proportional to the square of the local turbulence intensity. This result can be used in a qualitative sense to determine if and when the effects of velocity bias are appreciable. In supersonic base flows, turbulence intensities are generally large in the separated shear layer, especially near the point of reattachment (Amatucci et al., 1992). The magnitude of velocity bias present in individual realization data taken in this region can, therefore, be significant.

Several techniques to eliminate the velocity bias have been proposed, and most fall into two general categories: post-facto correction methods and sampling methods. Techniques in the former category generate correction factors for the individual realizations that are used in computing the mean flowfield quantities. The following equation is used to calculate the ensemble-averaged value of the arbitrary velocity statistic x:

$$\langle x \rangle = \frac{\sum_i x_i \, w_i}{\sum_i w_i} \qquad (1)$$

where w is a weighting factor and the summations are taken over the entire ensemble ($w_i \equiv 1$ corresponds to the totally biased, individual realization case). Several forms of the weighting factor have been proposed including the inverse velocity magnitude (McLaughlin and Tiederman, 1973), particle interarrival time (Hoesel and Rodi, 1977), and particle residence time (Buchhave and George, 1978). The second category of techniques to eliminate velocity bias are methods which attempt to reconstruct a time series with the same statistics as that of the turbulent flow. Commonly used methods which fit into this category include the controlled processor (Erdmann and Tropea, 1981), saturable detector (Edwards, 1978), and sample and hold processor (Dimotakis, 1976). While the controlled processor and saturable detector are sampling techniques which utilize only a fraction of the LDV data available, the sample and hold processor reconstructs a time series using the entire data ensemble which makes it attractive for high-speed flow applications with limited wind tunnel run times.

The task of deciding which method best eliminates the effects of velocity bias can be difficult considering the several conflicting recommendations in the literature. This is especially true in high-speed flow applications where only limited experimental verification of velocity bias effects exists (e.g., Petrie et al., 1988). Differences between high-speed and low-speed flows which can have significant effects on velocity bias include flow time scales, seed particle concentrations, and compressibility effects. In addition, another important constraint on choosing a velocity bias correction method for high-speed flows can be the limited run time of conventional blowdown-type wind tunnels. Typical wind tunnel run times and relatively sparse seed densities generally preclude the use of sampling methods to correct for velocity bias in high-speed flows. Hence, a post-facto correction method (Equation 1), which can be used with the entire data ensemble to reduce the effects of velocity bias *after* data acquisition has been completed, is desired.

In the present study, an objective comparison of the different correction methods for velocity bias is made. The main motivation of the research is to determine experimentally which post-facto correction methods are best suited for high-speed, separated flow applications with typical seed concentrations and turbulence intensity levels. In addition, obtaining experimental data concerning the effects of velocity bias on mean velocities, turbulence intensities, and the Reynolds shear stress in high-speed, separated flow will add to the current understanding of the problem in this flow environment.

2 Experimental Apparatus

The experiments described herein were conducted in a blowdown-type wind tunnel located in the Gas Dynamics Laboratory at the University of Illinois. As previously mentioned, this wind tunnel is being used to study the supersonic, axisymmetric base flow problem. A schematic diagram showing the general features of the near-wake behind a circular cylinder (verified by schlieren photography in the present case) is shown in Fig. 1. As the turbulent boundary layer separates from the afterbody, a free shear layer is formed which separates the outer inviscid flow from the recirculation region immediately behind the base. The shear layer undergoes a recompression-

3

realignment process to satisfy the symmetry condition, and a wake develops downstream of the rear stagnation point.

Two-component LDV data have been acquired throughout the near-wake; however, the detailed velocity bias study presented herein will consider only one representative traverse across the shear layer. The location of the traverse (shown in Fig. 1) is at a downstream distance of $x/R = 1.6$ from the base plane where R is the radius of the afterbody (R = 31.75 mm). The LDV data obtained at this location contain several attributes commonly found in high-speed separated flows, including large variations in mean velocity (+605 m/s in the freestream to -160 m/s along the centerline) and large turbulent fluctuations (local turbulence intensities of up to 400%). Due to the relatively large data ensembles required to obtain the reference measurements (saturable detector scheme) in the present experiments, twenty wind tunnel blowdowns were required to obtain the entire traverse of LDV data.

The LDV system employed was a TSI Inc. two-component unit with conventional optics and Bragg cell frequency shifting (40 MHz) to eliminate fringe blindness and discriminate flow direction. The LDV measurement volume was approximately 120 μm in diameter and 700 μm in length with a nominal fringe spacing of 10.5 μm. Doppler frequencies were measured with a TSI Inc. IFA-750 autocorrelation processor which was completely integrated with a Gateway 2000 486-33 personal computer for automated data acquisition. Use of the IFA-750 in the present experiments provided measurements of the interarrival time and the particle residence time with each velocity measurement. Seed particles were generated by a conventional six-jet atomizer filled with silicone oil which has been shown (Bloomberg, 1989) to produce mean particle diameters of 0.8 μm. The effective Stokes number at the measurement location was approximately 0.15 which was sufficiently small to avoid any significant particle lag effects.

3 Experimental Technique

In order to make an objective comparison between different velocity bias correction techniques, it is necessary to establish a reference measurement. Once the reference is established, different post-facto correction techniques are applied to the same raw data ensembles as used in the

4

reference data. Subsequently, a simple side-by-side comparison of the results obtained with different correction techniques to the reference is performed in order to investigate the effects of velocity bias in the current flow environment. In the sections that follow, the reference measurement will be described and the five post-facto correction schemes to be examined will be discussed.

3.1 Reference Measurement

Establishing a reference measurement for LDV data in high-speed, separated flows has been the primary problem in identifying the effects of velocity bias under these conditions. Hot-wire anemometry, a useful tool in attached flows with relatively low turbulence levels, cannot be used accurately in high-speed separated flows due to its intrusive nature and unreliability at high turbulence intensity levels. In the current study, the saturable detector sampling technique is used as the reference measurement. A description of the technique and a discussion of its applicability to the present measurements are presented below.

The saturable detector scheme is shown in Fig. 2. During data acquisition, the detector is disabled for a period T_s after a measurement is recorded, thus introducing a dead time in the acquisition process when no measurements are possible. In practice, most individual realization systems are saturable detectors with small T_s such that nearly every particle crossing occurs while the processor is enabled. The saturable detector has been used successfully by a number of researchers to minimize the effects of velocity bias in low-speed flows (Stevenson et al., 1982; Adams and Eaton, 1985; Craig et al., 1986).

The saturable detector scheme belongs to the general class of sampling techniques known as controlled processors. These techniques can remove the dependence of sampling rate on flow velocity and, therefore, provide unbiased LDV data. It has been established (Edwards and Jensen, 1983; Gould et al., 1989; Winter et al., 1991) that the success of controlled processors in eliminating velocity bias effects is dependent on the relative magnitudes of three time scales: the local integral time scale of the flow (T_u), the LDV measurement time scale (T_m), and the controlled processor sampling time scale (T_s). In this context, the integral time scale of the flow describes the

5

"persistence" time of the energy-containing turbulent eddies; the measurement time scale is merely the inverse of the mean data rate. For an LDV system with high integral scale data densities ($T_u/T_m \gg 1$), several authors (Gould et al., 1989; Winter et al., 1991; Tummers et al., 1992) have suggested that the following two criteria must be met in order for a controlled processor to produce bias-free results:

$$T_s/T_m \geq 5 \quad \text{and} \quad T_u/T_m \geq 5 \tag{2}$$

In the current study, the integral time scale of the flow was estimated from the results of Gaviglio et al. (1977) who used hot-wire anemometry to measure values of approximately $T_u = 2$ μs in a similar supersonic, axisymmetric base flow experiment. This value is also approximately equal to the shear layer eddy rollover time (b/ΔU) calculated using the current conditions. The measurement time scale is dependent on the signal-to-noise ratio of the Doppler signal, the LDV processor capabilities, and the seed concentration in the flow. Mean coincident data rates ranged from 3000-10000 samples per second in the present experiments, yielding an average measurement time scale of approximately $T_m = 150$ μs. The sampling time scale T_s was varied experimentally from 0.1-10 times the measurement time scale.

A comparison of the relative time scales (with $T_s = 10 T_m$) indicates that $T_s/T_u \approx 750$ which approaches the definition of the one-shot processor ($T_s/T_u \rightarrow \infty$) as given by Erdmann and Tropea (1981,1984). These authors showed analytically that the one-shot processor was capable of eliminating the effects of velocity bias as the integral scale data density, T_u/T_m, approaches zero. In the current study, $T_u/T_m \approx 0.01$ which, according to the results of Erdmann and Tropea (1981, 1984), seems to justify the use of the saturable detector scheme as a means to reduce velocity bias in this case. Note that the present conditions are far different from those established for bias-free sampling in the high data density case (Equation 2). Several authors have cast doubt on the conclusions of Erdmann and Tropea (1981,1984) for one-shot processors (Edwards and Jensen, 1983; Edwards, 1987; Winter et al., 1991) suggesting that, instead of eliminating the velocity bias at very low data densities, the one-shot processor approaches the totally biased individual realization case. The large discrepancy between these results must be resolved by experimental means; however, to the authors'

6

knowledge, no experimental data at the very low data densities of the present experiment have been obtained previously.

The saturable detector scheme in the present case was implemented in software by processing relatively large data sets (20,000-25,000 realizations per ensemble) with various sampling time scales, T_s. The dependence of the mean velocities, turbulence intensities, and Reynolds shear stress on the normalized sample interval, T_s/T_m, was investigated by altering (in software) the value of T_s starting at very small values to simulate the totally biased individual realization case and increasing until $T_s/T_m \approx 10$. Figure 3 is a plot of the mean axial velocity, axial root-mean-square (rms) velocity fluctuation, and Reynolds shear stress as a function of the normalized sample interval at a location near the inner edge of the shear layer where the local turbulence intensity is approximately 138%. This plot is representative of the results obtained throughout the regions of large turbulence intensity in the shear layer (i.e., regions where velocity bias effects should be largest) and are similar to the ones shown by Stevenson et al. (1982) and Craig et al. (1986). As Fig. 3 indicates, all three velocity statistics are dependent on the normalized sample interval for $T_s/T_m < 5$ and reach constant values (indicated by the * subscript) at larger normalized sample intervals. This trend has also been observed by Winter et al. (1991) and Tummers et al. (1992) who point out that, although the asymptotic behavior at large T_s/T_m indicates a *reduction* in velocity bias, it does not by itself guarantee the total *elimination* of velocity bias unless $T_u/T_m \gtrsim 5$ (i.e., high data density case). In the present case, the constant values for $T_s/T_m > 5$ differ from those of the individual realization case ($T_s/T_m \rightarrow 0$) which suggests that the saturable detector does indeed reduce velocity bias in this low data density environment, in agreement with the findings of Winter et al. (1991) and Tummers et al. (1992). Therefore, it is believed that the data obtained using the saturable detector scheme and $T_s/T_m > 5$ can be used as a reference for comparison with post-facto correction methods.

3.2 Post-Facto Correction Methods

A brief review of the five post-facto correction methods that are compared in this paper will now be presented. Along with identification of the velocity bias problem, McLaughlin and

7

Tiederman (1973) also provided the first velocity bias correction method: the inverse velocity magnitude correction. In the nomenclature of Equation 1,

$$w_i = |V_i|^{-1} \tag{3}$$

where V_i is the velocity magnitude of the ith realization. This correction method was originally derived for incompressible, one-dimensional flows but has been used significantly in a wide variety of fluid dynamic environments (e.g., Amatucci et al., 1992; Abu-Hijleh and Samimy, 1989). Oftentimes, a direct measurement of the total velocity vector is not possible so that assumptions must be made concerning the contributions from any unmeasured components. Nakayama (1985) and Petrie et al. (1988) suggest methods to estimate the third component of velocity in a two-component LDV data set. The effects of the three-dimensional correction, however, were shown to be significant only when both measured mean velocity components were negligible. In the present case, either the axial or radial mean velocity was always significant such that a three-dimensional correction was not necessary.

Weighting each velocity realization with the particle residence time in the LDV measurement volume, $w_i = \tau_t$, has also been suggested as a method to correct for the effects of velocity bias (Hoesel and Rodi, 1977; Buchhave and George, 1978). This method is founded on the inverse relationship between particle residence time and velocity. The performance of residence time weighting should be independent of the number of components measured but degrades as velocity magnitudes increase due to hardware accuracy and resolution limitations of the residence time measurement. Residence time weighting is the most difficult of the five post-facto correction methods to implement in practice due to the difficulties in making accurate measurements of τ_t.

Barnett and Bentley (1974) concluded that weighting the individual velocity realizations by the interarrival time between successive particles was a viable method to remove any velocity bias effects. That is, $w_i = t_i - t_{i-1}$ where t_i is the absolute time of arrival for particle i. Barnett and Bentley (1974) also suggested that long time delays relative to the characteristic time of the turbulent fluctuations (i.e., $T_s/T_u \gg 1$) destroy any correlation between instantaneous velocity and sampling rate. As previously mentioned, this hypothesis has still not been adequately investigated for high-

8

speed separated flows. A variation on the interarrival time weighting method is the sample and hold technique (Dimotakis, 1976; Adrian and Yao, 1987) which weights the individual realizations by w_i = t_{i+1} - t_i. Although Winter et al. (1991) suggested that the interarrival time weighting and sample and hold weighting methods should yield the same results at all data densities, they will both be investigated and compared in the present experiments.

The last velocity bias correction method that will be investigated is the velocity-data rate correlation method described by Meyers (1988). Using this technique, the persistence time of the flow and the correlation coefficient between the instantaneous velocity and data acquisition rate are estimated from individual realization LDV measurements. The LDV data ensemble is subsequently sampled once during each persistence period of the flow to yield a new ensemble of statistically independent measurements. To correct for velocity bias effects, the sampled data are normalized by the average number of LDV realizations following a sampled velocity within an average persistence interval. This technique is actually a mix between sampling and correction techniques, but since it can be applied after data acquisition to any ensemble of individual realization LDV data, it is a feasible correction technique for high-speed flow applications with limited wind tunnel run times.

4 Results

In order to document the effects of velocity bias at different locations across the shear layer, the reference data (saturable detector) are compared to the unweighted individual realization data in Fig. 4. The velocity bias effects on the mean axial velocity (Fig. 4a) follow the expected trend with mean velocities from the individual realization case being consistently higher than the reference data in the high turbulence intensity regions of the shear layer (near $r/R = 0.5$). In the outer freestream flow, the velocity bias is negligible as expected. Note that as the mean axial velocity changes sign entering the recirculation region, the velocity bias acts to increase the magnitude of the reversed velocity. At the $U = 0$ location, the effects of velocity bias are negligible due to the symmetry of the velocity histogram about the origin and the competing effects from positive and negative realizations (Adams and Eaton, 1985). The mean radial velocity component (V_r) in the shear layer was also

9

affected by velocity bias in a manner similar to the mean axial velocity with the magnitudes of the individual realization data generally exceeding the reference values.

The effects of velocity bias on the axial rms velocity fluctuation (σ_u) and Reynolds shear stress ($<u'v_r'>$) are shown in Figs. 4b and 4c, respectively. Note that a *global* definition of turbulence intensity (σ_u/U_∞) is used in Fig. 4b instead of the typical *local* definition (σ_u/U) to isolate the effects of velocity bias on the rms velocity fluctuation alone. As is typical of separated shear layers, a strong peak in the turbulence intensity and shear stress exists where intense turbulent mixing and energy exchange dominate the flow. In the present case, the peak values occur relatively near the $U = 0$ location such that velocity bias effects do not distort the magnitudes of the local maxima. However, the effects of velocity bias are significant in the regions of the shear layer where the mean velocity is moderate and turbulence intensity is large (e.g., $r/R \approx 0.55$). Velocity bias tends to decrease the magnitudes of both the turbulence intensity and shear stress independent of the direction of the local mean velocity. In addition, velocity bias effects in the separated region are reduced compared to those in the outer part of the shear layer even though local turbulence intensities are similar. The radial rms velocity fluctuation (σ_{Vr}) was also determined and exhibited trends similar to those shown in Fig. 4b for the axial component. The differences between the saturable detector and individual realization data once again suggest the ability of the sampling method to reduce velocity bias effects in agreement with the findings of Winter et al. (1991) and Tummers et al. (1992).

The same raw data ensembles that were processed in software using the saturable detector scheme were also processed with the different post-facto correction techniques discussed above. A comparison of the results obtained with each correction technique will now be presented. Figure 5 shows the reference mean axial velocity profile along with the data from the five post-facto correction methods (in this and subsequent figures, the comparison between the five correction methods is shown on two separate plots for clarity). As shown in Fig. 5a, the inverse velocity magnitude weighting factor tends to overcorrect (in comparison to the reference data) for the effects of velocity bias both above and below the $U = 0$ location in the shear layer. This may be due, in part,

10

to the three-dimensional nature of the flow as well as non-uniform seeding effects. The interarrival time weighting, sample and hold weighting, and velocity-data rate correlation methods all compare favorably with the reference measurement whenever $U > 0$, but in the recirculation region, the interarrival time weighting is superior. In general, the residence time weighting factor tends to overcorrect the data in comparison to the reference measurement across the entire traverse although to a lesser degree than the inverse velocity magnitude technique. All five post-facto correction techniques yield similar results in regions of the flow where velocity bias effects are negligible such as the freestream and $U = 0$ locations.

As Fig. 4 indicates, the effects of velocity bias are not limited to the mean velocity, but are quite important in accurately determining the turbulence moments as well. Figure 6 is a plot of the axial turbulence intensity profile as determined by the reference measurement and the five post-facto correction methods. The differences in performance of each correction technique become more evident here, with the profile significantly distorted by the inverse velocity magnitude and residence time weighting methods. A translation of the peak turbulence intensity location radially outward is a result of both of these methods, and turbulence intensity values vary considerably from the reference data across the shear layer. As in the mean velocity, the interarrival time and sample and hold weighted turbulence intensity distributions agree quite well with the reference data. The velocity-data rate correlation method also agrees with the reference data throughout most of the profile; however, the profile becomes distorted near the peak turbulence intensity location. A similar comparison was also done for the radial turbulence intensity with each correction method behaving in a similar manner as that indicated in Fig. 6.

A comparison of the Reynolds shear stress profiles as calculated by the five post-facto correction methods is shown in Fig. 7. Again, the differences between methods are significantly more apparent than in the mean velocity. Much like in the turbulence intensity, the inverse velocity magnitude correction significantly distorts the form of the shear stress profile and yields a peak magnitude that is reduced from the reference measurement. The interarrival time weighting closely follows the reference data throughout the entire profile. The sample and hold weighting method also

11

agrees reasonably well with the reference measurement throughout most of the profile. The residence time weighted profile exhibits a peak which is displaced outward from the actual peak location and shear stress values which differ significantly from the reference data in the high turbulence intensity region of the traverse. Also, the velocity-data rate correlation method yields a peak shear stress value which is 10% larger in magnitude than the reference value, although most of the profile agrees well with the reference data.

In addition to comparing the respective profiles of mean velocity, turbulence intensity, and shear stress from each correction method, a measure of the agreement of each technique with the reference can be made by summing the differences between the corrected data and the reference data across the entire profile. The rms difference for each correction method is calculated by the following equation:

$$\text{rms difference} = \sqrt{\frac{\sum_{i} (x_j - X_j)^2}{N}} \tag{4}$$

where x is any mean or turbulence statistic (e.g., U or $<u'v_r'>$), X is the reference value of x at location j, and N is the number of measurement locations across the traverse. Figure 8 shows the rms differences for the mean velocities, turbulence intensities, and Reynolds shear stress. In this figure, each rms difference is normalized by the maximum reference value of the statistic for the entire traverse in order to show the sensitivity of each statistic to velocity bias correction methods. Figure 8 clearly indicates that the interarrival time weighting method provides the best agreement with the reference in the present experiments. Agreement between the saturable detector scheme at $T_s/T_m > 5$ (reference technique) and the interarrival time weighting method has also been found in several previous velocity bias investigations at higher integral scale data densities (Adams and Eaton, 1985; Loseke and Gould, 1991; Winter et al., 1991). As expected, the sample and hold weighting technique provides results which are nearly equal to those of the interarrival time weighting method (Winter et al., 1991). On the other hand, the inverse velocity magnitude and residence time weighting methods produce mean and turbulence statistics that are in significant disagreement with the reference data. The sensitivity of the turbulence statistics (particularly the

12

Reynolds shear stress) and radial mean velocity to the effects of velocity bias are clearly shown. The quantity which is generally used to demonstrate velocity bias effects, the mean streamwise velocity, is the least sensitive to the various correction methods, which may account for the large discrepancies in the literature as to the superior correction method for a particular flow environment.

5 Discussion

As the previous results indicate, choosing an adequate velocity bias correction method can have a large effect on the accuracy of mean velocities and turbulence statistics obtained with individual realization LDV systems. Use of a post-facto correction technique is generally necessary in supersonic, blowdown-type wind tunnels due to limited wind tunnel run times. In the high-speed, separated flow environment of the present study, the interarrival time weighting method has been shown to agree closely with the reference saturable detector method which reduces velocity bias. In a similar velocity bias study in a low-speed (20 m/s) separated flow with comparable turbulence intensities, Loseke and Gould (1991) also showed that the interarrival time weighting method can reduce velocity bias as long as Bragg cell bias (Meyers and Clemmons, 1978) is non-existent. The IFA-750 signal processor used in the present experiments ensures a single measurement for each Doppler burst using a burst centering procedure, thus eliminating any bias due to the Bragg cell frequency shifter. A brief summary of some of the important experimental aspects which may have contributed to the performance of each post-facto correction technique examined here will be presented below.

The inverse velocity magnitude weighting factor was shown to be unreliable throughout the middle region of the shear layer where turbulence intensities are large. This conclusion was also reached by Hoesel and Rodi (1977) and other authors who stated that this method is restricted to low turbulence intensity environments. In addition, the effects of compressibility may cause erroneous results using this method since the rate at which particles cross the measurement volume is proportional to the mass flux (ρV) which, for compressible flows, can be significantly different than the dependence on velocity (volume flux) alone. Lastly, the effects of non-uniform seeding, which was undoubtedly present in the current experiments due to the role of large scale turbulent structures

13

in particle entrainment and transport, can cause additional errors in velocity bias correction by the inverse velocity magnitude technique.

The main problem encountered when implementing the residence time weighting scheme for velocity bias correction is the resolution and accuracy of the residence time measurement. In the IFA-750 processor, the residence time measurement is made with a resolution of 32 ns which, for many flow applications, may be sufficient. However, in high-speed flows the large instantaneous velocities and the small measurement volume dimensions which are necessary for adequate spatial resolution combine to make particle residence times very small. For example, in the present experiments freestream velocities as high as 605 m/s were measured with a measurement volume diameter of 120 μm which yields a particle residence time of 198 ns. In turn, this results in a worst-case residence time uncertainty due to measurement resolution of ±16%. In addition, the residence time measurement is user-dependent since the start and end of a Doppler burst are determined by a threshold level which is set by the user. The combination of these effects makes the residence time weighting technique difficult to implement accurately in high-speed flows.

The interarrival time weighting method was shown to be reliable in reducing velocity bias in the present high-speed, separated flow. Figure 9 shows representative velocity histograms from the inner edge of the shear layer generated with uncorrected individual realization data and the same data after interarrival time weighting. The bias toward higher velocity magnitudes, clearly present in the unweighted data, appears to be corrected by the interarrival time weighting (i.e., the corrected histogram is normally distributed). Of course, when implementing the interarrival time method, an accurate technique to measure the time-between-data (tbd) must be used. In the present experiments, an absolute time stamp with 1 μs resolution was output with each velocity realization, such that the tbd was determined by differencing successive time stamps. Therefore, the uncertainty due to resolution of the tbd measurement was constant for each realization in the ensemble, as opposed to typical counter-type processors which yield tbd measurements with varying resolutions, thereby causing error accumulation throughout the ensemble. Of course, the previous comments regarding

14

the implementation of the interarrival time weighting method also directly apply to the sample and hold weighting technique.

The present results suggest that the concept of the velocity-data rate correlation method in low data density environments must be altered from its original form (Meyers, 1988). The calculated persistence time, which is an important part of the debiasing scheme, must differ from the integral time scale of the flow (as defined in the original version of this method) in the low data density case since $T_m \gg T_u$. Although Tummers et al. (1992) suggested that the use of this method was restricted to cases involving high data densities, the present investigation revealed that it was capable of detecting the velocity bias in low data density environments. Figure 10 is a typical velocity-data rate correlation histogram generated with data from the inner edge of the shear layer which shows the dependence of the data rate on the total velocity. Note that in the central region of the histogram where most of the realizations occur, the data rate dependence is almost linear as suggested by McLaughlin and Tiederman (1973). In the present investigation, the calculated correlation coefficient between velocity and data rate varied from approximately zero in the freestream to a peak value of 0.29 near the inner edge of the shear layer (r/R = 0.35). The magnitudes of the correlation coefficient are similar to those measured by Tummers et al. (1992) in a low-speed wake flow. The correlation coefficient was found to be a reliable indicator of the degree of velocity bias present at any spatial location.

Acknowledgment

References

Abu-Hijleh, B.; Samimy, M. 1989: An experimental study of a reattaching supersonic shear layer. AIAA Paper 89-1801, presented at the AIAA 27th Aerospace Sciences Meeting, Reno, Nevada

Adams, E.W.; Eaton, J.K. 1985: An LDA study of the backward-facing step flow, including the effects of velocity bias. Int. Symp. on Laser Anemometry, New York, ASME FED Vol. 33, pp. 255-264

Adrian, R.J.; Yao, C.S. 1987: Power spectra of fluid velocities measured by laser Doppler velocimetry. Exp. Fluids 5, 17-28

Amatucci, V.A.; Dutton, J.C.; Kuntz, D.W.; Addy, A.L. 1992: Two-stream, supersonic, wake flowfield behind a thick base, part I: general features. AIAA J. 30, 2039-2046

Barnett, D.O.; Bentley, H.T., III 1974: Statistical bias of individual realization laser velocimeters. Proc. 2nd Int. Workshop on Laser Velocimetry, Vol. 1, Purdue University, pp. 428-444

Bloomberg, J.E. 1989: An investigation of particle dynamics effects related to LDV measurements in compressible flows. M.S. Thesis, University of Illinois at Urbana-Champaign, Department of Mechanical and Industrial Engineering

Buchhave, P.; George, W.K., Jr. 1978: Bias corrections in turbulence measurements by the laser Doppler anemometer. Presented at the 3rd Int. Workshop on Laser Velocimetry, Purdue University, pp. 110-119

Craig, R.R.; Nejad, A.S.; Hahn, E.Y.; Schwartzkopf, K.G. 1986: Approach for obtaining unbiased laser Doppler velocimetry data in highly turbulent flows. J. Prop. and Power 2, 541-545

Dimotakis, P.E. 1976: Single scattering particle laser Doppler measurements of turbulence. AGARD CP-193

Edwards, R.V. 1978: How real are particle bias errors. Proc. 3rd Int. Workshop on Laser Velocimetry, Purdue University, pp. 79-85

Edwards, R.V.; Jensen, A.S. 1983: Particle-sampling statistics in laser anemometers: sample-and-hold systems and saturable systems. J. Fluid Mech. 133, 397-411

Edwards, R.V. 1987: Report of the special panel on statistical particle bias problems in laser anemometry. ASME Trans.: J. Fluids Eng. 109, 89-93

Erdmann, J.C.; Tropea, C.D. 1981: Turbulence-induced statistical bias in laser anemometry. Proc. 7th Symp. on Turbulence, University of Missouri-Rolla, pp. 129-138

Erdmann, J.C.; Tropea, C.D. 1984: Statistical bias of the velocity distribution function in laser anemometry. Proc. Int. Symp. on Applications of Laser Doppler Anemometry to Fluid Mechanics, Lisbon, Portugal, pp. 393-403

Gaviglio, J.; Dussauge, J.P.; Debieve, J.F.; Favre, A. 1977: Behavior of a turbulent flow strongly out of equilibrium at supersonic speeds. Phys. Fluids 20, 179-192

Gould, R.D.; Stevenson, W.H.; Thompson, H.D. 1989: Parametric study of statistical bias in laser Doppler velocimetry. AIAA J. 27, 1140-1142

Hoesel, W.; Rodi, W. 1977: New biasing elimination method for laser Doppler velocimetry counter processing. Rev. Sci. Instr. 48, 910-919

Loseke, K.W.; Gould, R.D. 1991: A comparison of velocity bias correction techniques in laser Doppler velocimetry. Proc. ASME Fluid Measurement and Instrumentation Forum, FED-Vol. 108, pp. 63-68

McLaughlin, D.K.; Tiederman, W.G. 1973: Biasing correction for individual realization of laser anemometer measurements in turbulent flows. Phys. Fluids 16, 2082-2088

Meyers, J.F. 1988: Laser velocimeter data acquisition and real time processing using a microcomputer. Presented at the 4th Int. Symp. on Applications of Laser Anemometry to Fluid Mechanics, Lisbon, Portugal

Meyers, J.F.; Clemmons, J.I., Jr. 1978: Processing laser velocimeter high-speed burst counter data. Proc. 3rd Int. Workshop on Laser Velocimetry, Purdue University, pp. 300-313

Nakayama, A. 1985: Measurements of separating boundary layer and wake of an airfoil using laser Doppler velocimetry. AIAA Paper 85-0181, presented at the AIAA 23rd Aerospace Sciences Meeting, Reno, Nevada

Petrie, H.L.; Samimy, M.; Addy, A.L. 1988: Laser Doppler velocity bias in separated turbulent flows. Exp. Fluids 6, 80-88

Stevenson, W.H.; Thompson, H.D.; Roesler, T.C. 1982: Direct measurement of laser velocimeter bias errors in a turbulent flow. AIAA J. 20, 1720-1723

Tummers, M.J.; Absil, L.H.J.; Passchier, D.M. 1992: An experimental investigation of velocity bias in a turbulent flow. Presented at the 6th Int. Symp. on Applications of Laser Techniques to Fluid Mechanics, Lisbon, Portugal

Winter, A.R.; Graham, L.J.W.; Bremhorst, K. 1991: Velocity bias associated with laser Doppler anemometer controlled processors. ASME Trans.: J. Fluids Eng. 113, 250-255
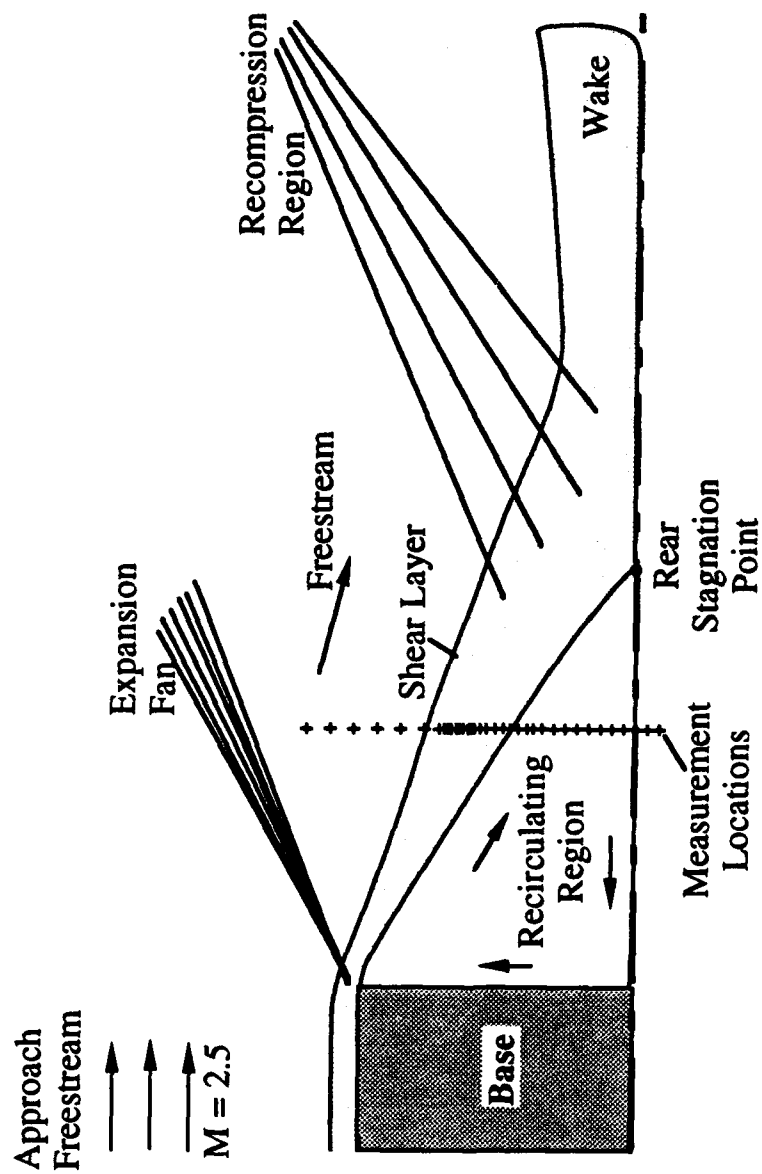
Fig. 1   Schematic Diagram of Supersonic, Axisymmetric Base Flowfield
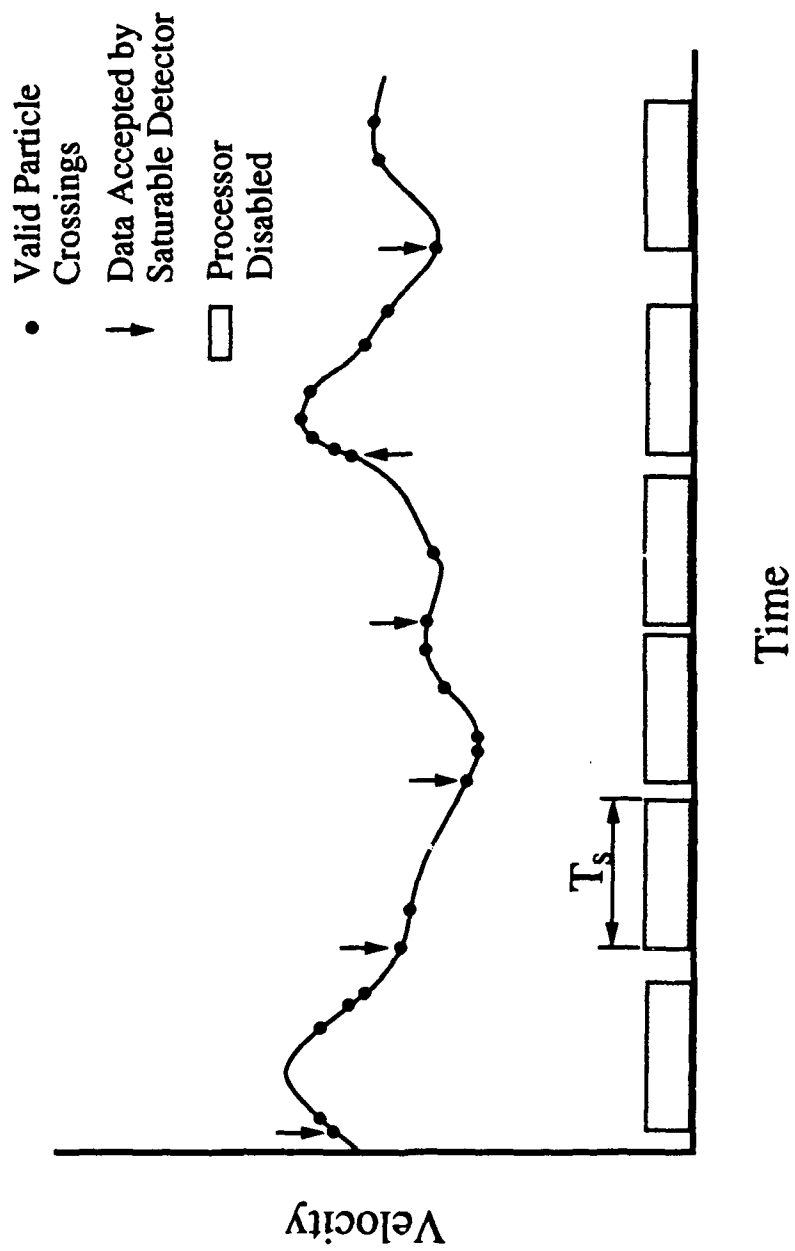
Fig. 2   Sampling Procedure of the Saturable Detector (after Edwards, 1987)
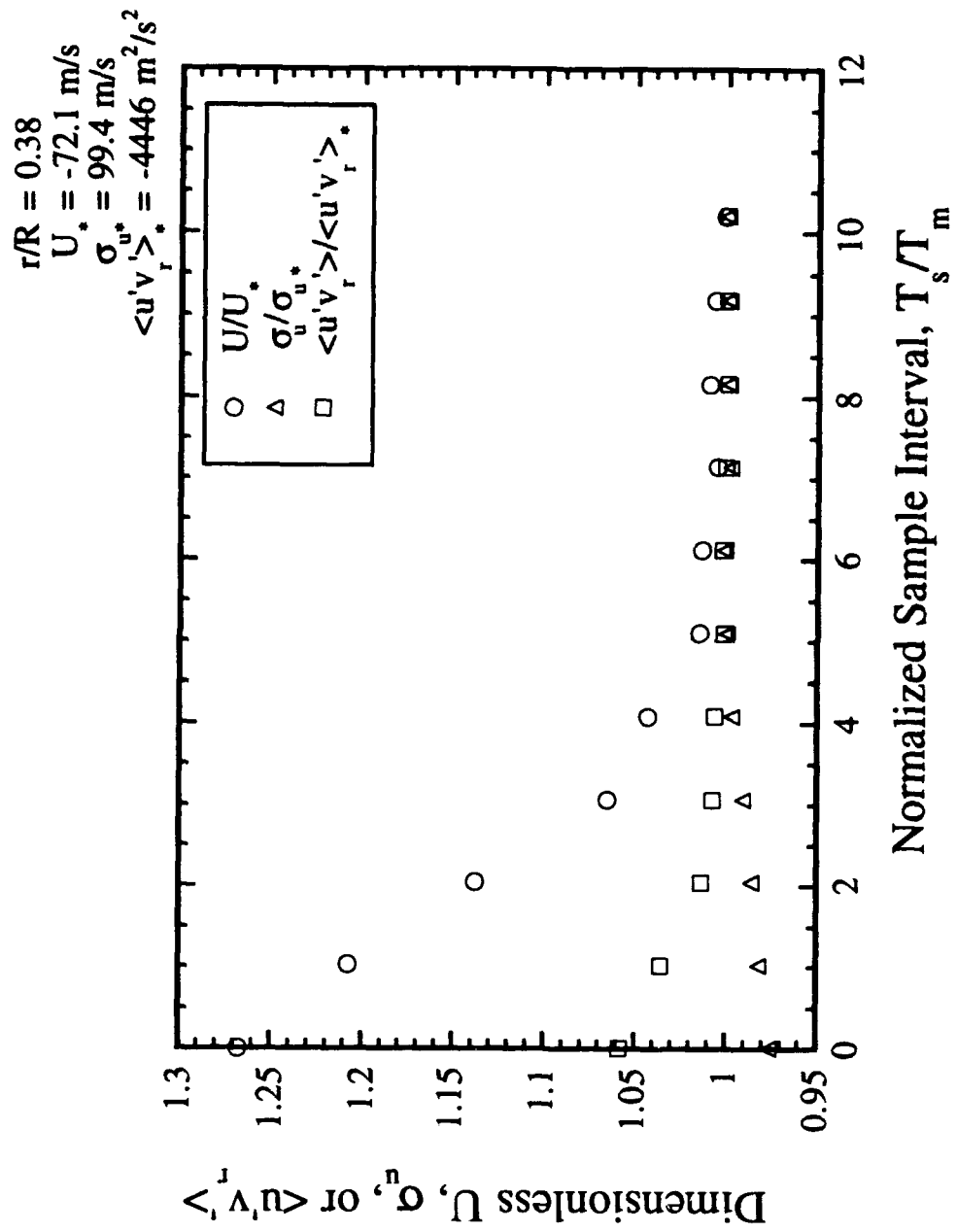
Fig. 3   Dependence of Mean Axial Velocity, Axial RMS Velocity Fluctuation, and Reynolds Shear Stress on T_s/T_m
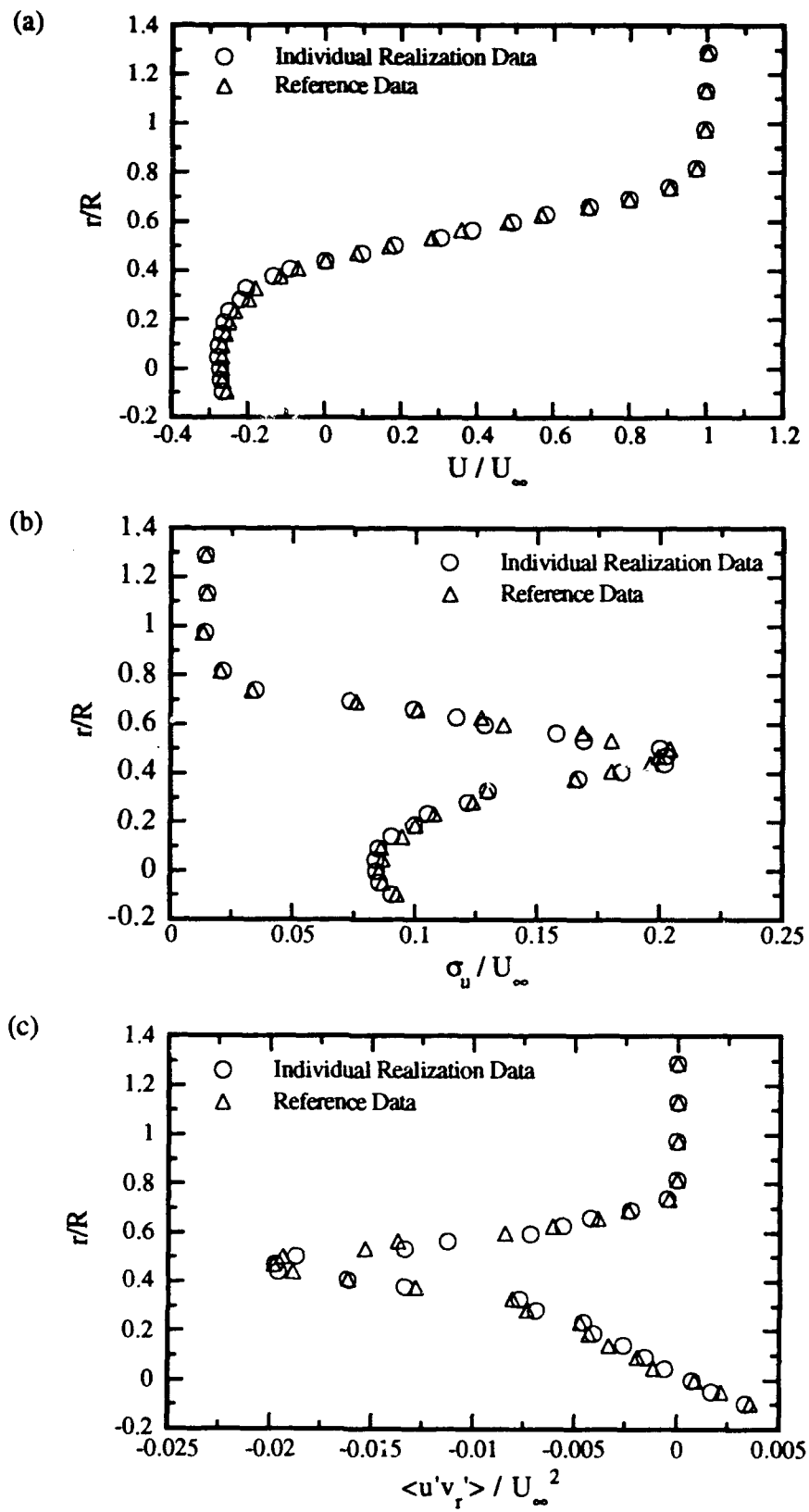
Fig. 4   Comparison of Reference Data to Individual Realization Data: (a) Mean Axial Velocity, (b) Axial RMS Velocity Fluctuation, (c) Reynolds Shear Stress
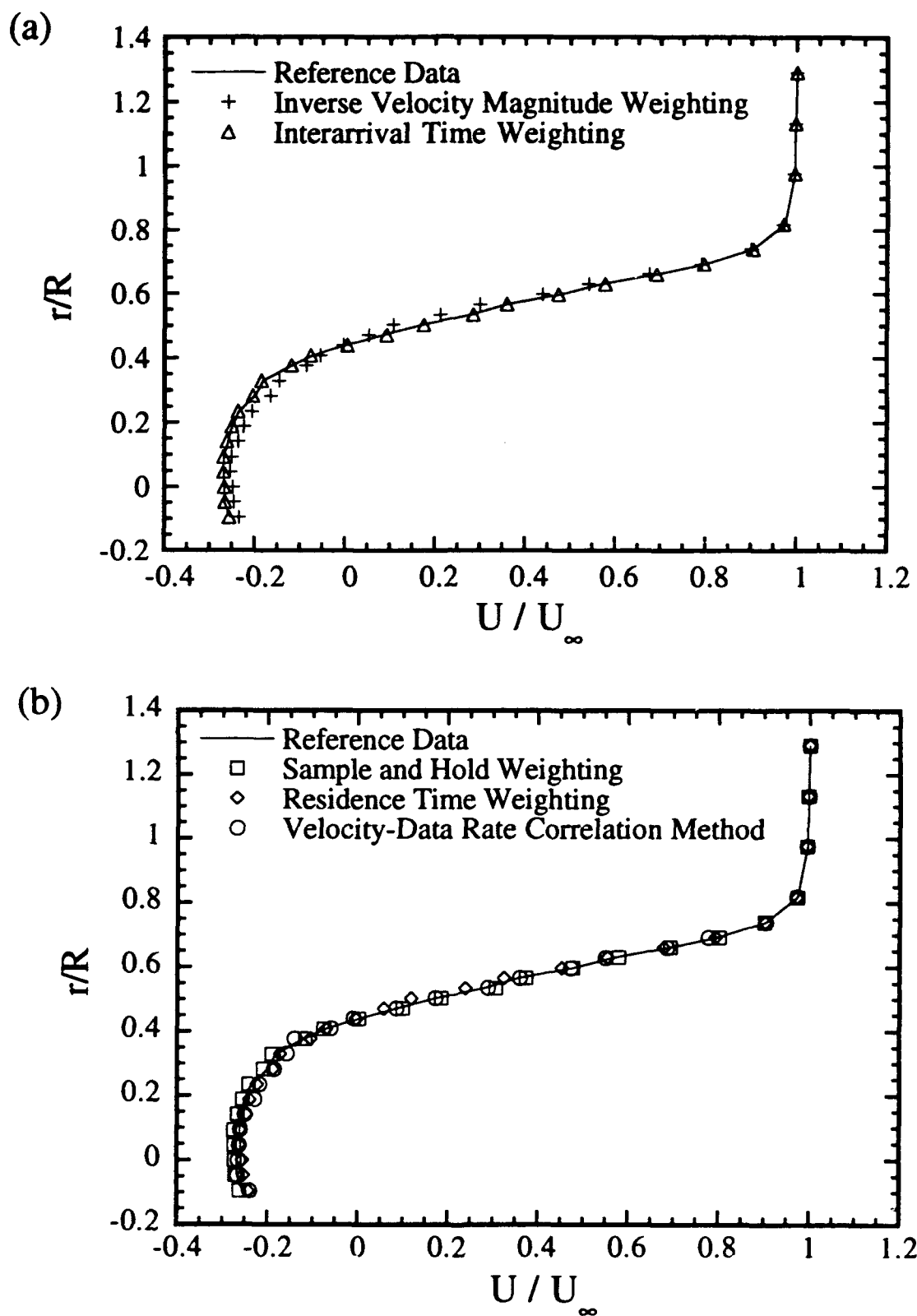
Fig. 5   Comparison of Post-Facto Correction Methods with Reference Data for
Mean Axial Velocity: (a) Inverse Velocity Magnitude and Interarrival
Time Weightings, (b) Sample and Hold Weighting, Residence Time
Weighting, and Velocity-Data Rate Correlation Method

Fig. 6 Comparison of Post-Facto Correction Methods with Reference Data for Axial RMS Velocity Fluctuation: (a) Inverse Velocity Magnitude and Interarrival Time Weightings, (b) Sample and Hold Weighting, Residence Time Weighting, and Velocity-Data Rate Correlation Method

Fig. 7   Comparison of Post-Facto Correction Methods with Reference Data for
Reynolds Shear Stress: (a) Inverse Velocity Magnitude and Interarrival
Time Weightings, (b) Sample and Hold Weighting, Residence Time
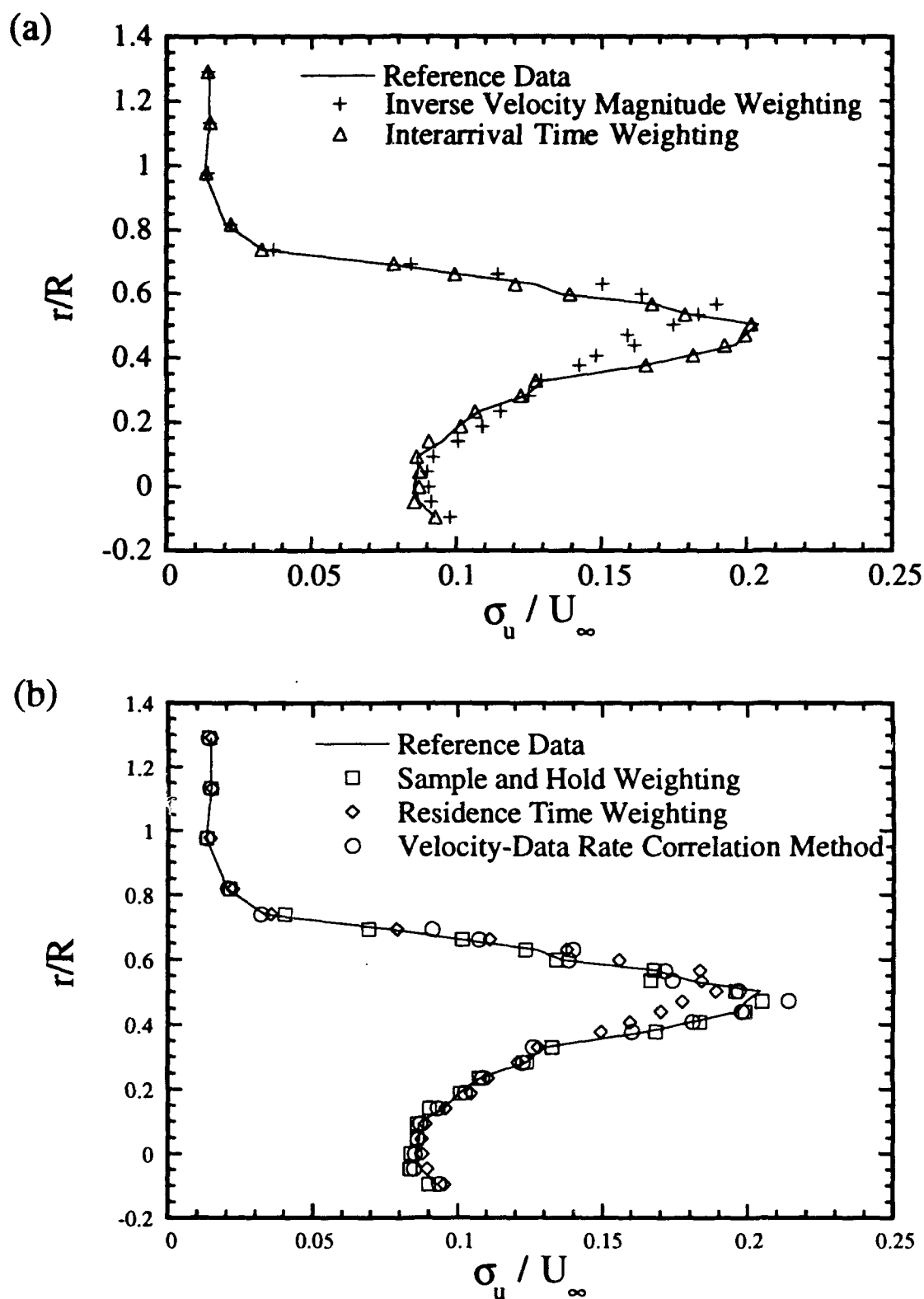Weighting, and Velocity-Data Rate Correlation Method
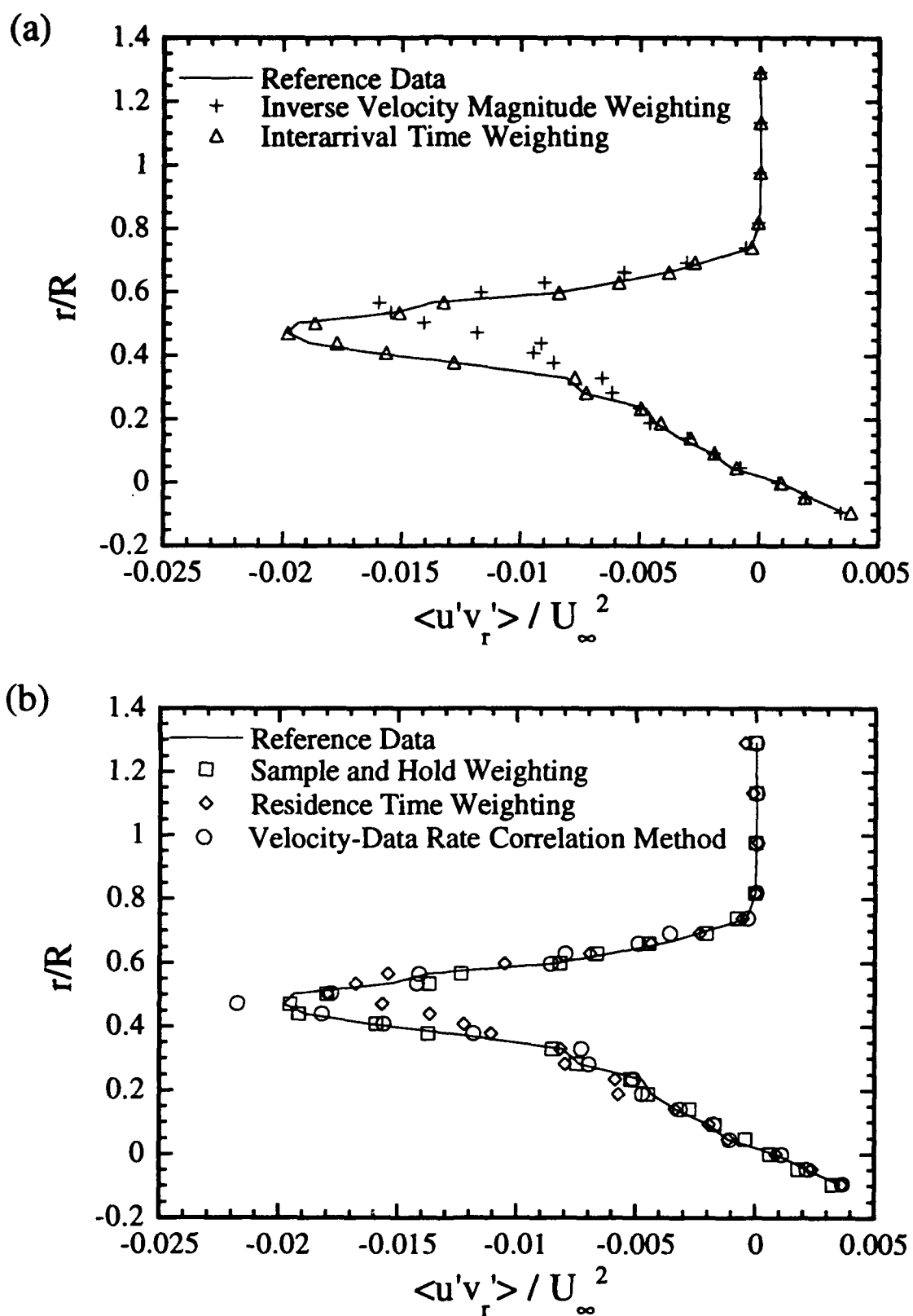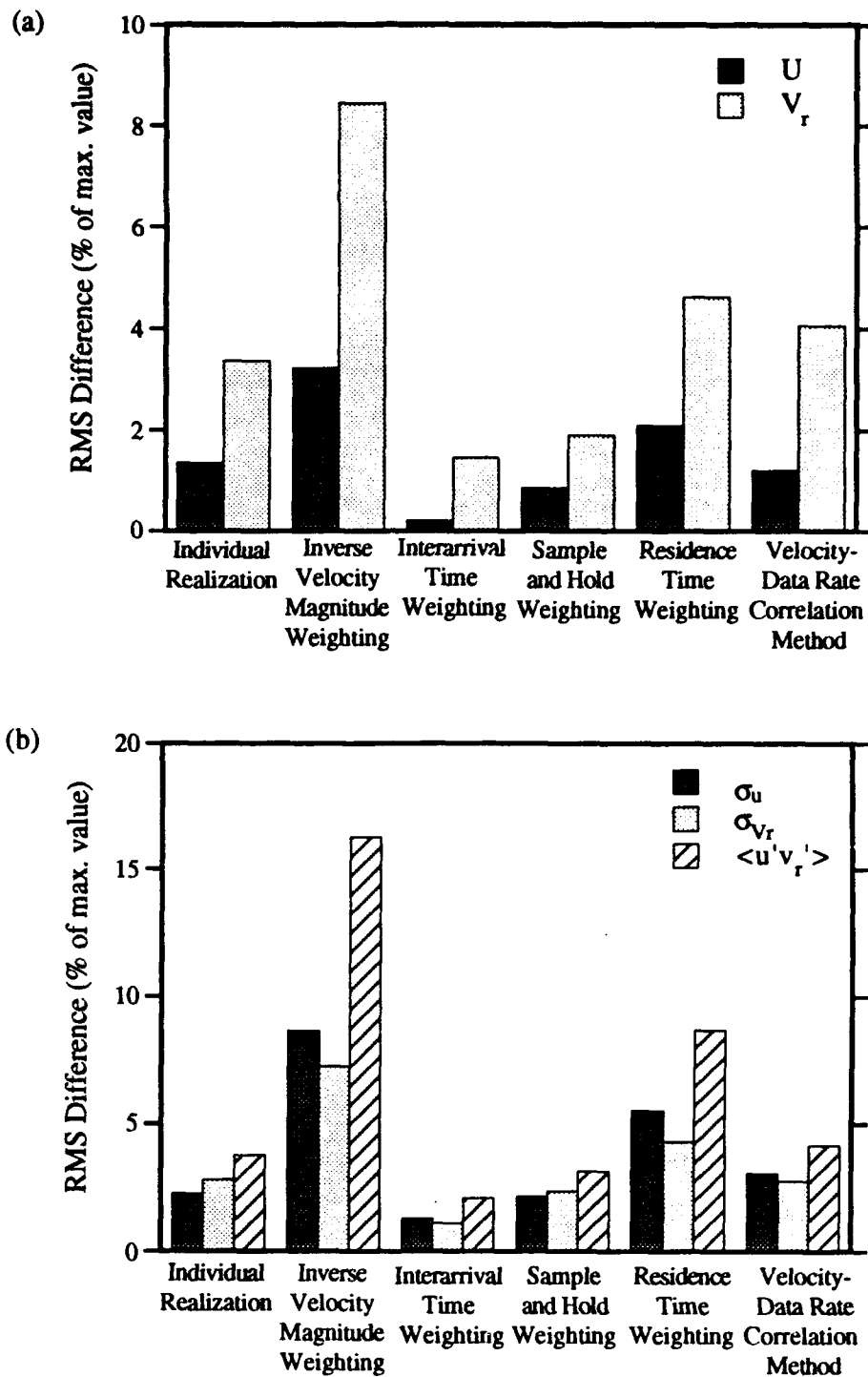
Fig. 8   RMS Differences Across Entire Profile: (a) Mean Velocities (b) Turbulence Quantities
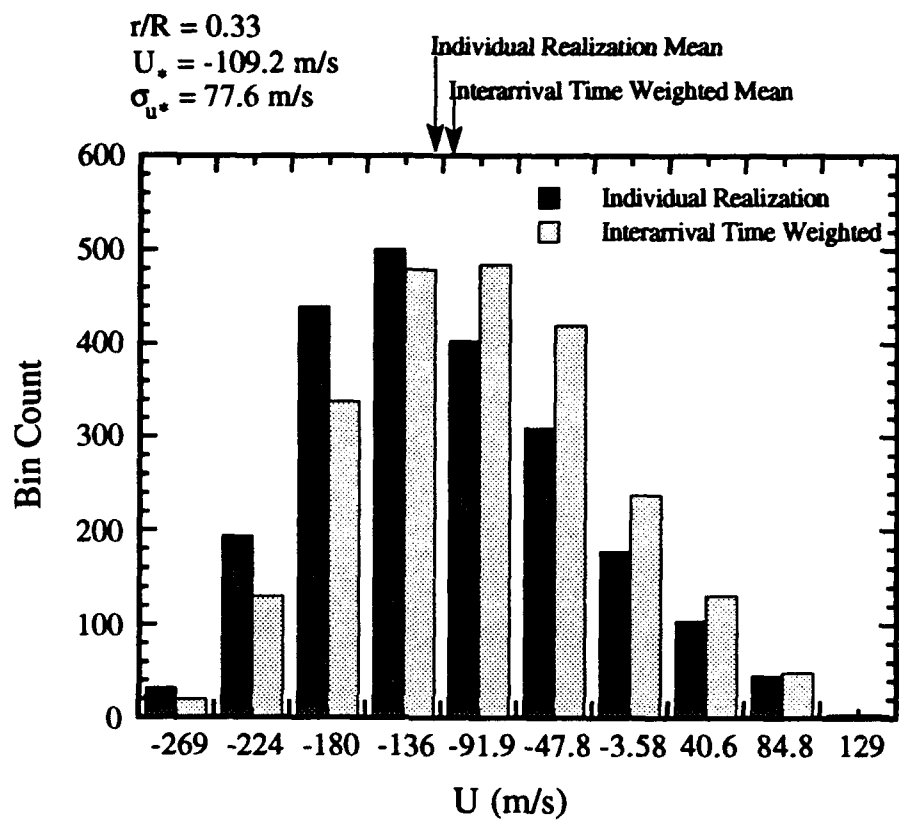
Fig. 9   Effect of Velocity Bias Correction on Shape of Velocity Histogram
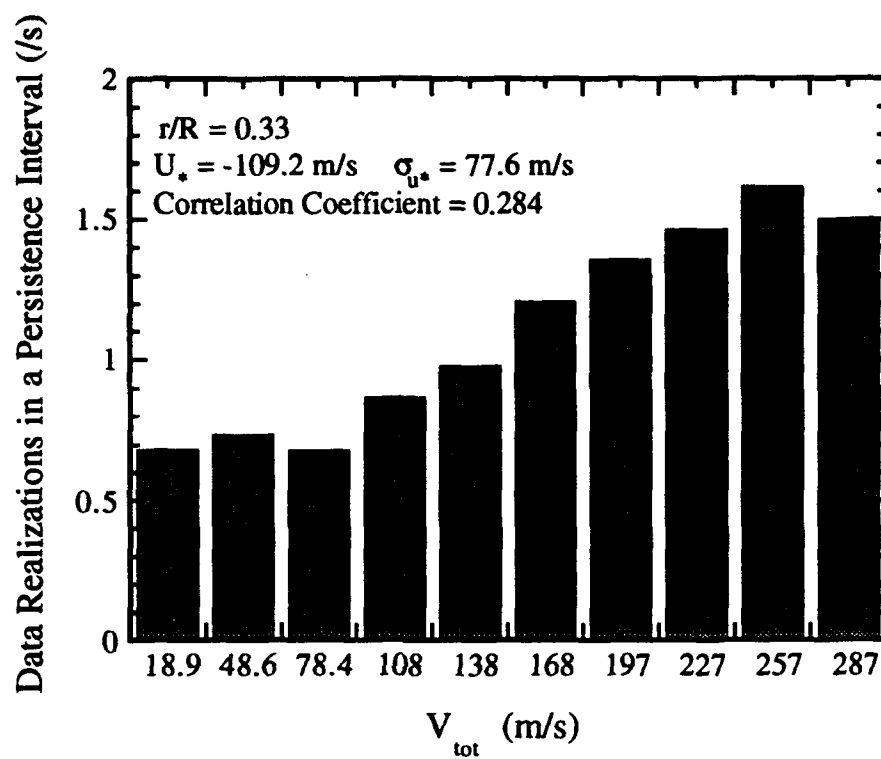
Fig. 10   Example of Velocity-Data Rate Correlation Plot

APPENDIX A.5

SUPERSONIC BASE FLOW EXPERIMENTS IN THE NEAR-WAKE OF A CYLINDRICAL AFTERBODY

by

J. L. Herrin and J. C. Dutton

AIAA 93-2924

Supersonic Base Flow Experiments in the Near-Wake of a Cylindrical Afterbody

J.L. Herrin and J.C. Dutton
University of Illinois at Urbana-Champaign
Urbana, Illinois

AIAA 24th
Fluid Dynamics Conference
July 6-9, 1993 / Orlando, FL

SUPERSONIC BASE FLOW EXPERIMENTS IN THE NEAR-WAKE
OF A CYLINDRICAL AFTERBODY

J.L. Herrin[*] and J.C. Dutton[**]
University of Illinois at Urbana-Champaign
Urbana, Illinois

Abstract

The near-wake of a circular cylinder aligned with a uniform Mach 2.5 flow has been experimentally investigated in a wind tunnel designed solely for this purpose. Mean static pressure measurements were used to assess the radial dependence of the base pressure and the mean pressure field approaching separation. In addition, two-component laser Doppler velocimeter (LDV) measurements were obtained throughout the near-wake including the large separated region downstream of the base. The primary objective of the research was to gain a better understanding of the complex fluid dynamic processes found in supersonic base flowfields including separation, shear layer development, reattachment along the axis of symmetry, and subsequent development of the wake. Results indicate relatively large reverse velocities and uniform turbulence intensity levels in the separated region. The separated shear layer is characterized by high turbulence levels with a strong peak in the inner, subsonic region which eventually decays through reattachment as the wake develops. A global maximum in turbulent kinetic energy and Reynolds shear stress is found upstream of the reattachment point which is in contrast to data from the reattachment of a supersonic shear layer onto a solid wall.

Nomenclature

C_f = skin friction coefficient
C_p = dimensionless pressure coefficient
H = compressible shape factor, δ^*/θ
M = Mach number
k = turbulent kinetic energy
P = pressure
P_k = production of k
r = radial coordinate
R = base radius
S = location of reattachment point
t = tangential coordinate
u_τ = friction velocity
U = mean axial velocity
V_r = mean radial velocity
V_t = mean tangential velocity
x = axial coordinate
y = vertical distance, r-R
γ = ratio of specific heats

δ = boundary layer thickness
δ^* = displacement thickness
θ = momentum thickness
ν_w = kinematic viscosity at wall
Π = wake strength parameter
σ = root-mean-square value
$<>$ = ensemble-averaged value
$(\,)'$ = fluctuating value

Subscripts
1 = condition at nozzle exit
base = condition at base
u = axial component
v_r = radial component
v_t = tangential component

Introduction

The low pressures that act in the base region of bodies of revolution in supersonic flight can cause significant amounts of drag[1]. For this reason, practical methods such as boattailing, base bleed, and base burning have been developed in order to increase the base pressure on aerodynamic vehicles such as missiles, rockets, and projectiles. In order to further enhance vehicle performance, however, a more complete understanding of the complex fluid dynamic processes that occur in base flowfields is necessary. Past experimental efforts have provided an adequate description of the overall flowfield structure and some parametric trends, but very little detailed quantitative data exists, especially for supersonic flows. In fact, a comprehensive survey of the available experimental data on axisymmetric base flows was recently undertaken by GARTEUR Action Group AG09[2]. After an exhaustive search, the group concluded that no accurate, well-documented experimental data existed for the near-wake flowfield in supersonic, axisymmetric flow. Reliable turbulence information in the base region is especially scarce which presents a problem in validating numerical predictions of these flowfields (see Refs. 3-5). Clearly, the practical importance of increasing the understanding of axisymmetric base flowfields lies in the ability to someday control the near-wake flow interactions such that base drag can be reduced and vehicle stability and control can be enhanced.

A schematic diagram of the mean flowfield structure in the near-wake of a cylindrical afterbody aligned with a supersonic flow is shown in Fig. 1. The supersonic afterbody freestream flow undergoes a strong expansion centered at the base corner as the turbulent boundary layer separates geometrically from the body. A free shear layer is formed which separates

---

[*] Graduate Research Assistant, Department of Mechanical and Industrial Engineering, Student Member AIAA

[**] Professor, Department of Mechanical and Industrial Engineering, Associate Fellow AIAA

the outer inviscid flow from a relatively large recirculation region immediately downstream of the base. The intense turbulent mixing and energy exchange that characterize the free shear layer are important in determining the flowfield properties throughout the near-wake including the recirculation region. As the free shear layer approaches the axis of symmetry, a recompression process occurs which eventually realigns the flowfield with the axis. A rear stagnation point, where the mean velocity vanishes, is located on the centerline and separates the recirculation region from the wake which develops downstream.

The early theoretical model for turbulent base flows developed by Korst[6] prompted several experimental investigations which attempted to gather the empirical information necessary to complete the theory[7-10]. However, many experimental problems, including improper model mounting, probe interference effects, and lack of flowfield symmetry, hampered these efforts which resulted in data of questionable accuracy. These experimental difficulties stem primarily from the axisymmetric geometry of the body as well as the sensitivity of the separated region downstream of the base to wind tunnel interference effects[11]. Perhaps the most comprehensive previous study of supersonic power-off base flows was undertaken by Gaviglio et al.[12] using a hot-wire anemometer. The overall inviscid flow structure and downstream wake properties were determined; however, the recirculation region directly behind the base was not investigated due to possible probe interference effects which limits the utility of the data. Neale et al.[13] investigated the mean velocity field behind a circular cylinder with a pitot-static probe but, again, bypassed the separated region. Clearly, accurate experimental measurements in the recirculation region downstream of the base require non-intrusive diagnostic techniques. Laser Doppler velocimetry (LDV) is a non-intrusive velocity measurement tool well-suited for such flows. Delery[14] used LDV to successfully document the near-wake of a subsonic, axisymmetric base flowfield. Detailed mean velocity and turbulence data were gathered throughout the near-wake and provide a good data base for the subsonic case. Amatucci et al.[15] made similar LDV measurements in a supersonic, two-stream flowfield with a two-dimensional base that modeled the power-on case; however, the effects of the more practical axisymmetric configuration were not investigated. Heltsley et al.[16] used LDV to investigate the flowfield downstream of a transonic, axisymmetric, power-on base flow but encountered experimental problems throughout the measurements.

In the current study, experiments were conducted to document the entire near-wake flowfield structure behind a cylindrical afterbody immersed in a supersonic flow. Detailed LDV measurements were made in order to obtain a better understanding of the fluid dynamic processes throughout the near-wake including separation, shear layer growth and development, reattachment, and wake redevelopment.

To the authors' knowledge, these data also provide the first detailed investigation of the mean and turbulent velocity fields inside the recirculation region in a supersonic base flow. In addition, the data provided herein will aid both analytical and numerical modelers of supersonic, axisymmetric base flows.

Experimental Facility and Instrumentation

Wind Tunnel Facility

The experiments were conducted in a supersonic, blowdown-type wind tunnel designed solely for the study of axisymmetric base flows. Figure 2 is a schematic diagram of the axisymmetric wind tunnel facility which is located in the University of Illinois Gas Dynamics Laboratory. Dry, compressed air passes from the stagnation chamber through a flow conditioning module consisting of screens and honeycomb (used to dampen any large scale disturbances generated in the air supply process and to minimize freestream turbulence levels) and finally to the converging-diverging supply nozzle. The pressure and temperature in the stagnation chamber were consistently maintained at 515 ± 2.8 kPa and 294 ± 3 K, respectively. The nozzle takes an annular shape due to the central sting which supports the base model from upstream to prevent any interference with the near-wake flowfield. The cylindrical afterbody used in the present experiments is 63.5 mm in diameter and is attached by internal threads to the sting. Physical supports for the sting are located outside the rear of the stagnation chamber and inside the wind tunnel at the flow conditioning module. The sting supports are of sufficient rigidity such that sting vibration due to flowfield fluctuations was negligible. The nominal design Mach number and unit Reynolds number at the nozzle exit are 2.5 and 52 (10^6) per meter, respectively.

Proper centering of the afterbody/base within the nozzle is critical in obtaining axisymmetric flow in the near-wake. In these experiments, custom-designed wind tunnel adjusting blocks were used to adjust the relative position between the sting and nozzle until an axisymmetric flow was obtained. Oil-streak visualization performed on the base was used effectively to examine the sting/nozzle alignment and was found to be a very sensitive indicator of the symmetry of the near-wake flowfield. Micrometer measurements at the nozzle exit indicated a maximum afterbody misalignment of 0.13 mm from the physical nozzle centerline.

Experimental Methods

Conventional schlieren and shadowgraph photography were used to investigate the qualitative structure of the near-wake flowfield. The photographs were of only moderate quality due to the axisymmetric nature of the flow, but they were used successfully to confirm the flowfield structure shown in Figure 1 and to determine a proper operating condition that eliminated any wind tunnel interference effects.

2

Mean static pressure measurements were made at several locations on the base and afterbody surfaces using a Pressure Systems Inc. digital pressure transmitter (DPT 6400-T). Nineteen pressure taps (0.64 mm in diameter) were located symmetrically across the base at radial intervals of 3.18 mm. Along the afterbody, two sets of diametrically-opposed pressure taps (0.64 mm in diameter) were located starting 2.38 mm upstream of the base corner with each tap separated axially by 3.18 mm and a total of five taps in each set. In addition to the afterbody pressure taps, total pressure and temperature probes were mounted in the stagnation chamber.

The focus of this investigation involved the implementation of a two-component LDV system for measuring the near-wake velocity field. Artificial seed particles were generated by a TSI Inc. six-jet atomizer filled with 50 cp silicone oil. The droplets were injected into the flow upstream of the facility nozzle to avoid disturbing the flowfield with the injection process. In previous experiments with the same seeding apparatus, Bloomberg[17] deduced a mean droplet diameter of 0.8 μm and showed mean particle relaxation distances of approximately 2 mm downstream of an oblique shock wave generated by a 15 degree compression corner in a Mach 2.6 flow. The maximum velocity gradients in the present experiments (near boundary layer separation) are significantly weaker than for the oblique shock in Bloomberg's work; however, to ensure negligible particle lag in the current experiments, no data are presented within the first 5 mm downstream of the base corner separation point. In the separated shear layer, the Stokes number for this seeding configuration is estimated to be 0.15 which Samimy and Lele[18] have shown yields root-mean-square slip velocities (difference in velocity between the particle and the local fluid element) of approximately 1.5%.

The LDV measurement volume used in these experiments was 120 μm in diameter and had a fringe spacing of approximately 10.3 μm. A 20° off-axis, forward-scatter receiving optics configuration was used to reduce the effective measurement volume length to 0.70 mm. Bragg cells were used in each component to frequency shift one of the beams 40 MHz against the mean flow direction in order to discriminate reversed velocities. In addition, the two orthogonal fringe patterns were rotated to ±45 degrees relative to the wind tunnel axis to reduce fringe blindness. To measure accurately the Doppler frequencies in this demanding flow, a TSI IFA-750 autocorrelation processor was used. Data were gathered from the processor by a Gateway 2000 486-33 personal computer where further processing and analysis were performed. Positioning of the LDV measurement volume throughout the near-wake flowfield was accomplished using a three-axis, computer-controlled traversing table with a positioning resolution of 0.75 μm.

The LDV measurement locations were concentrated in the regions of high velocity gradients including the approach boundary layer, separated shear layer, developing wake, and also near the reattachment point. Radial traverses were completed at 21 axial stations throughout the near-wake with approximately 30 spatial locations per traverse. In addition, an axial traverse along the model centerline was performed to show the development of the centerline mean velocity and turbulence intensities. During each radial traverse, three or four locations below the axis of symmetry were measured to check the symmetry of the flow. In all cases, the measured wake centerline (defined as the location where $<u'v_r'> = 0$) was within 2 mm of the geometric model centerline. Approximately 4000 instantaneous velocity realizations were gathered at each spatial location and probability density functions (pdfs) of each velocity component were calculated. The pdfs generally resembled a Gaussian profile except near the inner edge of the shear layer (near U = 0) where bimodal peaks in each pdf consistently occurred. The bimodal pdfs most likely indicate the presence of large-scale structures on the inner edge of the shear layer which play an important role in the entrainment of fluid from the recirculation region. The effects of velocity bias on the LDV data were accounted for by weighting each velocity realization with the interarrival time between realizations[19].

With the current two-component LDV arrangement, both the horizontal and vertical components of velocity were measured. In two-dimensional flows, this generally allows direct measurement of the streamwise and transverse velocities, but no measurement of the spanwise component. In the current axisymmetric flow, by using the same LDV configuration and making measurements independently in both the horizontal and vertical planes which pass through the axis of symmetry, all three mean and rms velocities have been measured. In addition, the axial-radial $<u'v_r'>$ and axial-tangertial $<u'v_t'>$ Reynolds shear stresses have been directly measured. An error analysis including the uncertainties associated with velocity biasing, fringe biasing, velocity gradient biasing, finite ensemble size, processor resolution, optical misalignment, and fringe spacing determination has been completed. The estimated *worst-case* uncertainty in the mean velocity measurements is 1.2% of U_1 and, in the rms velocity fluctuations, 2.3% of U_1, where U_1 is the freestream velocity just prior to separation.

Results

Pressure Measurements

Static pressure measurements along the afterbody were used to assess the uniformity of the nozzle exit flow as well as any upstream influence of the separation process. As expected, the pressure field approaching the base corner was relatively uniform and takes a value consistent with an isentropically expanded Mach 2.44 flow. No upstream influence from the base corner separation was evident in the data.

Pressure measurements have also been made at nineteen locations on the base in order to assess the radial distribution of the mean static pressure. Figure

3

3 shows the dimensionless base pressure coefficient at each location, defined as:

$$C_{Pbase} = \frac{2\left(\frac{P_{base}}{P_1} - 1\right)}{\gamma M_1^2}$$ (1)

where P is the static pressure, M the Mach number, and the subscript 1 denotes conditions at the nozzle exit. The pressure is shown to be relatively constant across the base (note the expanded vertical scale) with a slight increase toward larger radii where the maximum pressure measured was 3.9% higher than the pressure at the center of the base. Similar base pressure profiles were observed by Reid and Hastings[8] for a cylindrical afterbody in a Mach 2.0 flow with a maximum rise in pressure of approximately 3% across the base. An area-weighted average of the current data across the base was performed to determine an average base pressure coefficient of -0.102.

Flowfield Velocity Measurements

Approach Flow Measurements

The boundary layer approaching the base corner separation point was measured at three axial stations upstream of the base. Figure 4 is a plot of the boundary layer profile obtained 1 mm upstream of the base corner along with a curve fit by Sun and Childs[20] for compressible, turbulent boundary layers. The boundary layer properties derived from the curve fit are also shown in Figure 4. The values for the dimensionless properties (H, Π, and C_f) are typical of those found in equilibrium, compressible, turbulent boundary layers[21]. In order to determine the integral properties, the mean density profile through the boundary layer was determined using the ideal gas equation of state and the assumptions of negligible radial pressure gradient, adiabatic wall, and a recovery factor of 0.89 as suggested by Kays and Crawford[22]. The freestream Mach number across the nozzle exit was measured by LDV to be 2.46 ± 1% (the corresponding approach velocity was U_1 = 567 m/s). Also, measured freestream turbulence intensities in the approach flow were less than 1%.

Centerline Measurements

The LDV measurements along the model centerline were taken in 5 mm increments from the base to the end of the viewing window in the test section. A plot of the mean axial velocity along the model centerline is shown in Fig. 5. The origin of the cylindrical coordinate system has been arbitrarily set at the center of the base with all axial distances positive downstream. The axial location where the data crosses the U = 0 line clearly defines the rear stagnation point, S, since the other two measured velocity components are negligible along the centerline; this occurs at x/R = 2.65. The maximum reversed velocity occurs at x/R = 1.5 and takes a value of approximately 27% of the approach freestream velocity. In a similar experiment using LDV in subsonic flow (Mach 0.85) behind a circular cylinder, Delery[14] found the rear stagnation

point located at 3.06 base radii downstream and a maximum reversed velocity of approximately 30% of the local freestream value and located at x/R = 1.8. It is interesting to note that for both the supersonic and subsonic cases, the maximum reversed velocity occurs at a location approximately 57% of the distance from the base to the reattachment point. Merz et al.[23] found that for all Mach numbers from 0.1-0.9, the maximum reversed velocity was 35-40% of the freestream velocity and occurred at a distance 60% of the length to reattachment. The degree of wake redevelopment in the present experiments is indicated in Fig. 5 by the maximum positive centerline velocity which takes the value of 57% of the approach velocity (M = 1.05) at the furthest downstream station.

Near-Wake Mean Velocity Measurements

The mean velocity vector field in the near-wake is shown in Fig. 6. In this and subsequent figures, the vertical axis has been expanded by 42% compared to the horizontal axis in order to more clearly show the features of the flowfield (the axial-to-radial aspect ratio of the actual LDV measurement grid is 4.27:1). In order to place the experimental data on a uniform grid for the vectors shown in Fig. 6, a simple linear interpolation in both x and r between the unequally spaced data was completed. The velocity vectors show clearly the dominance of the axial velocity on the overall mean velocity field. The turning of the mean flow through the base corner expansion fan, the relatively low-speed recirculation region, and the realignment of the mean flow with the axis downstream of reattachment (S) are clearly shown.

A contour plot of the Mach number distribution throughout the near-wake is shown in Fig. 7. The steep velocity gradients through the initial portion of the shear layer are clearly evident in the figure. The spreading of the contour lines further downstream is indicative of the growth of the shear layer prior to reattachment and, also, the wake development downstream. Note that the flow along the axis reaccelerates to sonic velocity at approximately five base radii downstream which is similar to the measurements of Neale et al.[13] in a Mach 3 base flowfield where the sonic point was located at x/R = 5.1. The maximum Mach number of the reversed flow is 0.48 and is located on the centerline at approximately x/R = 1.5. The gradual recompression of the outer flow is indicated by the decreasing Mach number contours in the upper right of the figure.

The mean radial velocity contours are shown in Fig. 8. The small values relative to the mean axial approach velocity once again show the dominance of the axial velocity in the near-wake flowfield. The closely spaced contours emanating from the base corner mark the turning of the mean flow through the expansion fan. As the outer inviscid flow approaches the axis of symmetry, the radial velocity continues to increase in magnitude, due to the axisymmetric effect, to a peak value of 22% of the mean approach velocity

4

at a location approximately two base radii downstream. The location of flowfield realignment with the axis of symmetry appears to depend on whether the flow is supersonic or subsonic. The realignment process in the outer flow is shown in the upper right of Fig. 8 by the contour lines of decreasing magnitude and the relatively uniform flow region downstream of the last contour. However, closer to the axis of symmetry, a much slower realignment of the subsonic inner flow occurs, such that the mean radial velocity is appreciable out to $x/R = 4.5$. The mean tangential (swirl) velocity was also directly measured with the LDV system, and as expected, the magnitudes were negligible compared to the other two components.

Near-Wake Turbulence Measurements

The root-mean-square fluctuation velocities were directly measured in all three coordinate directions and will be presented in the form of turbulence intensities, σ/U_1. Figure 9 shows the axial turbulence intensity contours throughout the near-wake. The large increase in turbulent fluctuations from the outer freestream to the values in the shear layer and wake are apparent. A peak axial rms velocity fluctuation of 22% of the mean approach velocity occurs at a location 83% of the axial distance from the base to reattachment. Upstream of reattachment at any axial station, the radial location of the maximum axial turbulence intensity lies in the subsonic region of the shear layer. In contrast, Amatucci et al.[15] found peak levels of turbulence intensity near the sonic line in a two-dimensional, two-stream base flow. Throughout the recirculation region in the current study, the axial turbulence intensity is relatively constant except very close to the base where it is attenuated. Further downstream as the shear layer transforms into a wake, the overall level of turbulent fluctuations diminishes and a well-defined peak in the axial turbulence intensity profiles is no longer discernible.

Contours of constant radial turbulence intensity are shown in Fig. 10. The general trends follow closely those of the axial turbulence intensity, but the overall fluctuation levels are smaller. The peak radial velocity fluctuation is 15.6% of U_1 and occurs at roughly the same location as the peak axial fluctuation. The recirculation region contains a greater variation in radial turbulence intensity than axial turbulence intensity with a steady increase from the base to the reattachment point (not including the base effects at $x/R<0.5$). The turbulence relaxation beyond reattachment is fairly slow with a uniform radial turbulence intensity across the inner portion of the wake as it develops.

The tangential turbulence intensity represents fluctuations from the mean swirl velocity which, as mentioned above, is negligible for axisymmetric flows. Figure 11 is a plot showing the tangential turbulence intensity throughout the near-wake. The overall level of fluctuations in the tangential direction is reduced compared to the axial turbulence intensity and is generally smaller than the radial fluctuations. The peak value of the tangential velocity fluctuations is 13.5% of U_1 and occurs near the shear layer reattachment point at $x/R = 2.65$. The greatest variation in tangential turbulence intensity occurs at the outer edges of the shear layer and wake, and the radial profiles do not exhibit the sharp peaks evident in the axial and radial turbulence intensities.

The ratio of the turbulence intensity contributions from each component gives a relative indication of the anisotropy in the normal stress field. In the current flow, the axial turbulence intensity dominates with peak values approximately 30-50% higher than the peak radial fluctuations and 60-70% higher than the peak tangential fluctuations in the shear layer where anisotropy is largest. The relative ordering of the peak turbulence intensity magnitudes (axial-radial-tangential) found in the current base flow experiments can be contrasted with the recent data from Gruber and Dutton[24] for a two-dimensional, compressible, constant pressure mixing layer. In their study, the magnitude of the spanwise component of turbulence intensity exceeded the contribution from the transverse component by approximately 20% in the peak intensity region of the shear layer, probably due to the three-dimensional nature of the large scale structures in the planar, compressible mixing layer. In axisymmetric flow, the tendency of the structures to grow asymmetrically (in the tangential direction) is most likely dampened by the more stringent axisymmetric conditions imposed by the mean flowfield. In incompressible, constant pressure mixing layers, the spanwise component of turbulence intensity has been shown to be approximately equal to the transverse turbulence intensity[25].

An important turbulence quantity often used to describe the overall level of turbulent fluctuations is the turbulent kinetic energy defined as:

$$k = \frac{1}{2}(\sigma_u^2 + \sigma_{v_r}^2 + \sigma_{v_t}^2) \qquad (2)$$

In these experiments, all three mean square fluctuations (normal stresses) have been directly measured. Figure 12 is a plot of the turbulent kinetic energy as measured throughout the near-wake. Since the axial turbulence fluctuation levels dominate the flowfield, the contours of turbulent kinetic energy appear relatively similar to those of the axial turbulence intensity (Fig. 9). The turbulent kinetic energy grows rapidly after separation as the shear layer grows. Prior to reattachment, however, a maximum is reached and a subsequent decay to the relatively constant values in the wake occurs. Again, the sharp peaks in turbulent kinetic energy radial profiles occurring in the shear layer are nonexistent in the wake further downstream. In the recirculation region, the level of turbulent kinetic energy is reduced by the lack of turbulence production due to small mean velocity gradients. The maximum turbulent kinetic energy measured in the near-wake was 4.4% of U_1^2 and occurred at $x/R = 2.2$, or somewhat upstream of reattachment.

In the current experiments, both the axial-radial ($<u'v_r>$) and axial-tangential ($<u'v_t>$) Reynolds shear stresses have been measured directly. As expected, the axial-radial shear stress dominates the axial-tangential stress which is negligible throughout the near-wake. Figure 13 is a plot showing the axial-radial shear stress distribution downstream of the base. The shear stress peaks in the shear layer upstream of reattachment in approximately the same location as the peak in turbulent kinetic energy. Abu-Hijleh and Samimy[26] used LDV to investigate a supersonic shear layer reattaching onto a wall and found peak values of turbulent kinetic energy and Reynolds stress *downstream* of the reattachment location. The difference in the locations for the peak turbulence quantities between these experiments may possibly be attributed to the differences between solid wall and compliant surface reattachment.

The production of turbulent kinetic energy, defined as follows:

$$P_k = -<u_i'u_j'>\frac{\partial U_i}{\partial x_j} \qquad (3)$$

provides a measure of the amount of kinetic energy transferred from the mean flow to the turbulence field. Investigating the distribution of P_k throughout the near-wake provides insight into the structure of the turbulence field as well as establishing the role of turbulence production in different regions of the flow. In axisymmetric flow, only four of the nine production terms are non-zero which leaves the following expression for P_k:

$$P_k = -\sigma_u^2\frac{\partial U}{\partial x} - <u'v_r>(\frac{\partial U}{\partial r} + \frac{\partial V_r}{\partial x}) - \sigma_{vr}^2\frac{\partial V_r}{\partial r} \qquad (4)$$

which is plotted in Fig. 14 (to avoid clutter, only a reference contour label is shown; all other contours are equally spaced with values increasing by 0.02). Strong turbulence production is seen to occur immediately downstream of the separation point on the inner edge of the shear layer. This is not surprising as the mean velocity gradients are very large in this region. As the shear layer develops, the mean velocity gradients decrease but the Reynolds stresses increase (Figs. 9-13) such that the total production remains significant up to the reattachment point. Downstream of reattachment, however, the Reynolds stresses and mean velocity gradients both decrease rapidly resulting in a diminished level of turbulence production.

Since the total production of turbulent kinetic energy is merely the sum of the production terms for each Reynolds normal stress, separating the total production expression into its individual components yields:

$$P_k = P_u + P_{vr} + P_{vt} \qquad (5)$$

where the individual production terms for each Reynolds normal stress are

$$P_u = -\sigma_u^2\frac{\partial U}{\partial x} - <u'v_r>\frac{\partial U}{\partial r} \qquad (6)$$

$$P_{vr} = -\sigma_{vr}^2\frac{\partial V_r}{\partial r} - <u'v_r>\frac{\partial V_r}{\partial x} \qquad (7)$$

$$P_{vt} = 0 \qquad (8)$$

From the current experiments, the relative magnitudes of each term indicate that $P_u \gg P_{vr} > P_{vt}$. Consequently, the majority of the energy exchange between the mean flow and the turbulence field occurs through the axial component of the Reynolds normal stress. The radial and tangential components, on the other hand, must receive their kinetic energy from other sources such as pressure-velocity interactions or momentum transport by turbulent velocity fluctuations. Therefore, the relative ordering of the Reynolds normal stresses ($\sigma_u^2 > \sigma_{vr}^2 > \sigma_{vt}^2$) is consistent with the amount of turbulence production that each component receives from the mean flow.

Summary and Conclusions

The turbulent near-wake of a circular cylinder aligned with a supersonic flow has been investigated using non-intrusive measurement techniques. The main objective of these experiments is to increase the understanding of the complex fluid dynamic phenomena that occur in supersonic base flowfields by the use of detailed quantitative data gathered throughout the near-wake. Specifically, afterbody and base pressure distributions, mean velocities, turbulence intensities, and Reynolds shear stresses have been obtained; these data have been tabularized on a floppy disk which is available from the authors. As a result of data analysis, the following conclusions concerning the near-wake flowfield can be made:

(1) The mean static pressure profile across the base is relatively uniform with an average base pressure coefficient of -0.102.

(2) The maximum reverse velocity along the wake centerline reached 27% of the mean approach velocity, or Mach 0.48, and occurs approximately 57% of the distance from the base to the reattachment point (located at $x/R = 2.65$). Along the centerline, the axial and radial turbulence intensities peak near the reattachment point and decay as the wake develops downstream.

(3) The recirculating flow is generally characterized by small mean velocity gradients and relatively uniform turbulence intensities.

(4) The separated shear layer is found to contain steep radial velocity gradients and sharp peaks in turbulence intensity in the subsonic region. Beyond reattachment, the sharp peaks decay toward nearly uniform turbulence intensities across the redeveloping wake.

(5) Peak values of turbulent kinetic energy and axial-radial shear stress are located in the subsonic region of the shear layer upstream of reattachment. This is in contrast to earlier results on compressible shear layer reattachment onto a solid surface which indicate peak levels at or downstream of the reattachment point. The production of turbulent kinetic energy peaks immediately downstream of separation along the inner edge of the shear layer.

6

References

[1] Rollstin, L., "Measurement of Inflight Base Pressure on an Artillery-Fired Projectile," AIAA Paper 87-2427, 1987.

[2] Delery, J., and Wagner, B., "Results of Garteur Action Group AG09 on Flow Past Missile Afterbodies," *Proceedings of the AGARD/FDP Symposium on Missile Aerodynamics*, Friedrichshafen, Germany, 1990.

[3] Peace, A.J., "Turbulent Flow Predictions for Afterbody/Nozzle Geometries Including Base Effects," *Journal of Propulsion and Power*, Vol. 7, No. 3, 1991, pp. 396-403.

[4] Sahu, J., "Supersonic Flow Over Cylindrical Afterbodies with Base Bleed," AIAA Paper 86-0487, 1986.

[5] Wilmoth, R.G., and Putnam, L.E., "Subsonic/Transonic Prediction Capabilities for Nozzle/Afterbody Configurations," AIAA Paper 84-0192, 1984.

[6] Korst, H.H., "A Theory for Base Pressures in Transonic and Supersonic Flow," *Journal of Applied Mechanics*, Vol. 23, No. 4, 1956, pp. 593-600.

[7] Zumwalt, G.W., "Analytical and Experimental Study of Axially-Symmetric Supersonic Base Pressure Problem," Ph.D. Thesis, Department of Mechanical Engineering, University of Illinois at Urbana-Champaign, 1959.

[8] Reid, J., and Hastings, R.C., "Experiments on the Axi-Symmetric Flow Over Afterbodies and Bases at M=2.0," Royal Aircraft Establishment, R.A.E. Report Aero. 2628, Farnborough, England, 1959.

[9] Badrinarayanan, M.A., "An Experimental Investigation of Base Flows at Supersonic Speeds," *Journal of the Royal Aeronautical Society*, Vol. 65, July 1961, pp. 475-482.

[10] Demetriades, A., "Mean-Flow Measurements in an Axisymmetric Compressible Wake," *AIAA Journal*, Vol. 6, No. 3, 1968, pp. 432-439.

[11] Hawkins, R., and Trevett, E., "Changes in the Flow at the Base of a Bluff Body Due to a Disturbance in its Wake," AGARD Report 539, 1966.

[12] Gaviglio, J., Dussauge, J.P., Debieve, J.F., and Favre, A., "Behavior of a Turbulent Flow Strongly Out of Equilibrium at Supersonic Speeds," *Physics of Fluids*, Vol. 20, No. 10, 1977, pp. 179-192.

[13] Neale, D.H., Hubbartt, J.E., Strahle, W.C., and Wilson, W.W., "Effects of External Compression on an Axisymmetric Turbulent Near Wake," *AIAA Journal*, Vol. 16, No. 9, 1978, pp. 940-947.

[14] Delery, J., "ONERA Research on Afterbody Viscid/Inviscid Interaction with Special Emphasis on Base Flows," *Proceedings of the Symposium on Rocket/Plume Fluid Dynamic Interactions*, University of Texas at Austin, 1983.

[15] Amatucci, V.A., Dutton, J.C., Kuntz, D.W., and Addy, A.L., "Two-Stream, Supersonic, Wake Flowfield Behind a Thick Base, Part I: General Features," *AIAA Journal*, Vol. 30, No. 8, 1992, pp. 2039-2046.

[16] Helmsley, F.L., Walker, B.J., and Nichols, R.H., "Transonic Nozzle-Afterbody Flow Field Measurements Using a Laser Doppler Velocimeter," AGARD CP-348, 1983.

[17] Bloomberg, J.E., "An Investigation of Particle Dynamics Effects Related to LDV Measurements in Compressible Flows," M.S. Thesis, Department of Mechanical and Industrial Engineering, University of Illinois at Urbana-Champaign, 1989.

[18] Samimy, M., and Lele, S.K., "Motion of Particles with Inertia in a Compressible Free Shear Layer," *Physics of Fluids* - A, Vol. 3, No. 8, 1991, pp. 1915-1923.

[19] Herrin, J.L., and Dutton, J.C., "An Investigation of LDV Velocity Bias Correction Techniques for High-Speed Separated Flows," *Experiments in Fluids*, to be published, 1993.

[20] Sun, C.C., and Childs, M.E., "A Modified Wall Wake Velocity Profile for Turbulent Compressible Boundary Layers," *Journal of Aircraft*, Vol. 10, No. 6, 1973, pp. 381-383.

[21] Fernholz, H.E., and Finley, P.J., "A Critical Commentary on Mean Flow Data for Two-Dimensional Compressible Turbulent Boundary Layers," AGARDograph No. 253, 1980.

[22] Kays, W.M., and Crawford, M.E., "The Turbulent Boundary Layer for a Gas with Variable Properties," *Convective Heat and Mass Transfer*, 2nd ed., McGraw-Hill, New York, 1980, pp. 305-309.

[23] Merz, R.A., Page, R.H., and Przirembel, C.E.G., "Subsonic Axisymmetric Near-Wake Studies," *AIAA Journal*, Vol. 16, No. 7, 1978, pp. 656-662.

[24] Gruber, M.R., Messersmith, N.L., and Dutton, J.C., "The Three-Dimensional Velocity Field in a Compressible Mixing Layer," *AIAA Journal*, to be published, 1993.

[25] Bell, J.H., and Mehta, R.D., "Interaction of a Streamwise Vortex with a Turbulent Mixing Layer," *Physics of Fluids*, Vol. 2, No. 11, 1990, pp. 2011-2023.

[26] Abu-Hijleh, B., and Samimy, M., "An Experimental Study of a Reattaching Supersonic Shear Layer," AIAA Paper 89-1801, 1989.
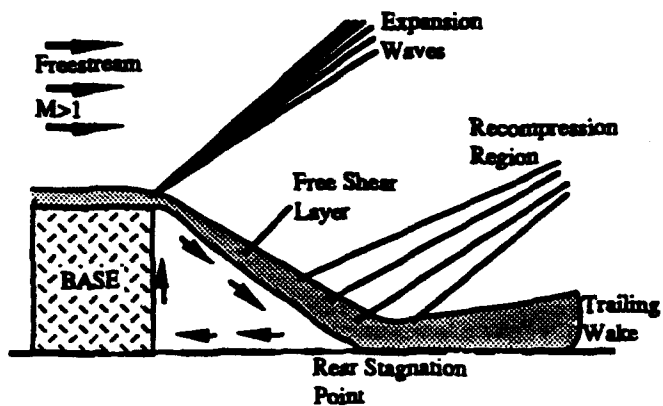
7

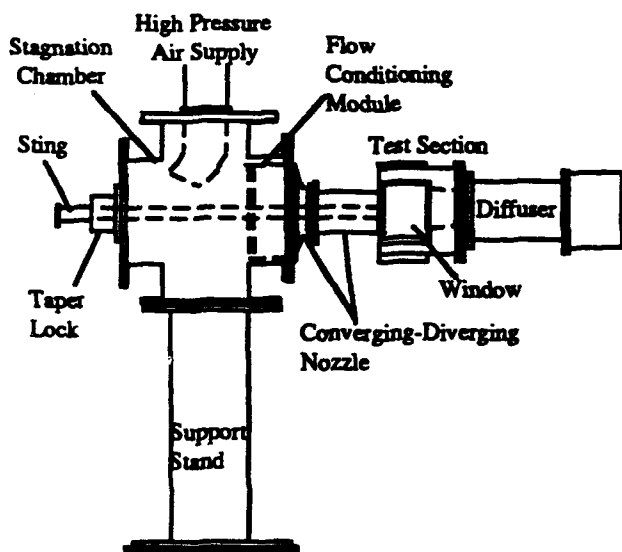Fig. 1   Supersonic, Axisymmetric Base Flow Schematic

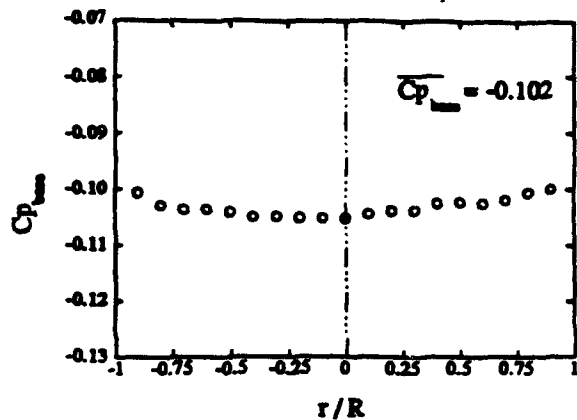Fig. 2   Schematic Diagram of Axisymmetric Wind Tunnel
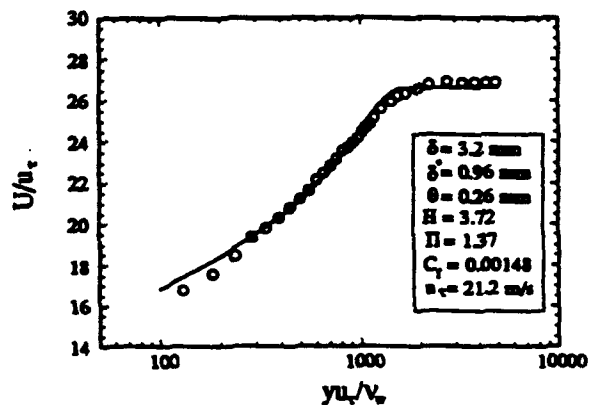

Fig. 3   Base Pressure Profile

Fig. 4   Sun and Childs[20] Curve Fit of Afterbody Boundary Layer Upstream of Base Corner
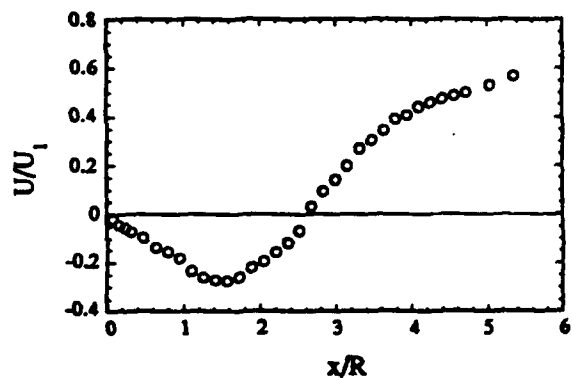

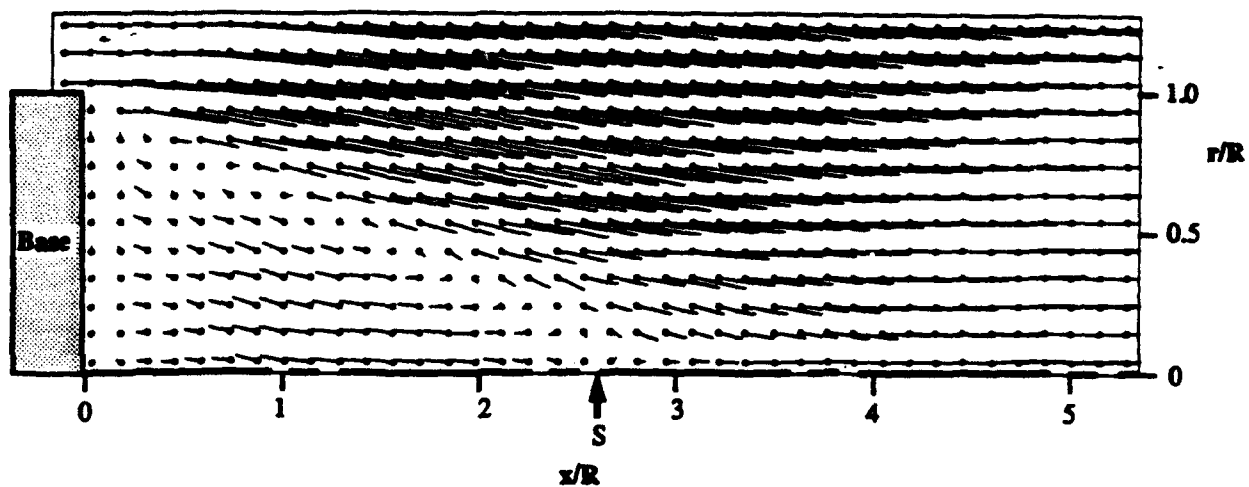Fig. 5   Mean Axial Velocity Along Model Centerline

Fig. 6   Mean Velocity Vector Field Throughout Near-Wake
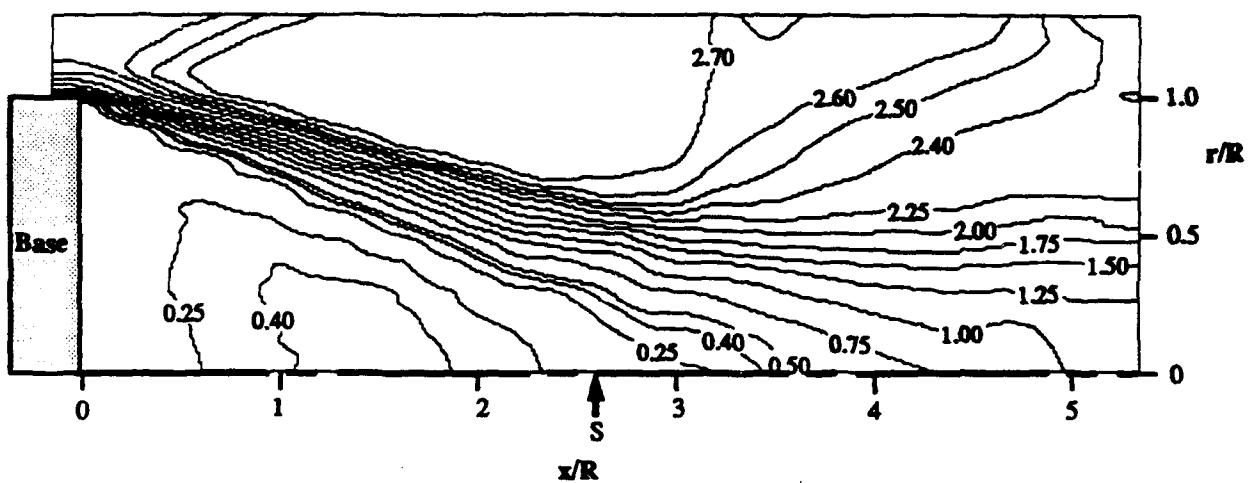
Fig. 7   Mach Number Contours
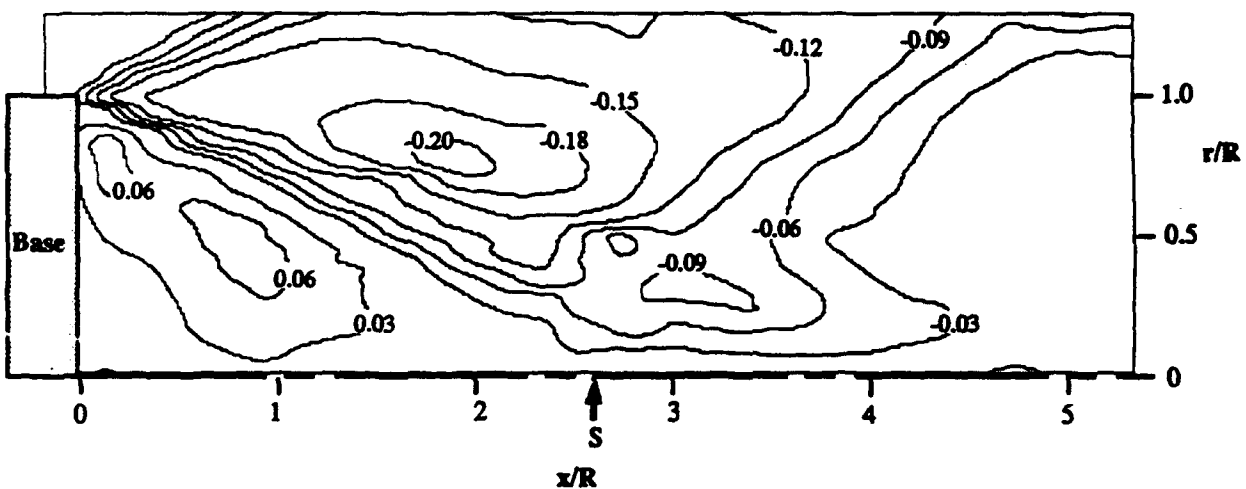
Fig. 8   Mean Radial Velocity Contours - V_r / U_1

9
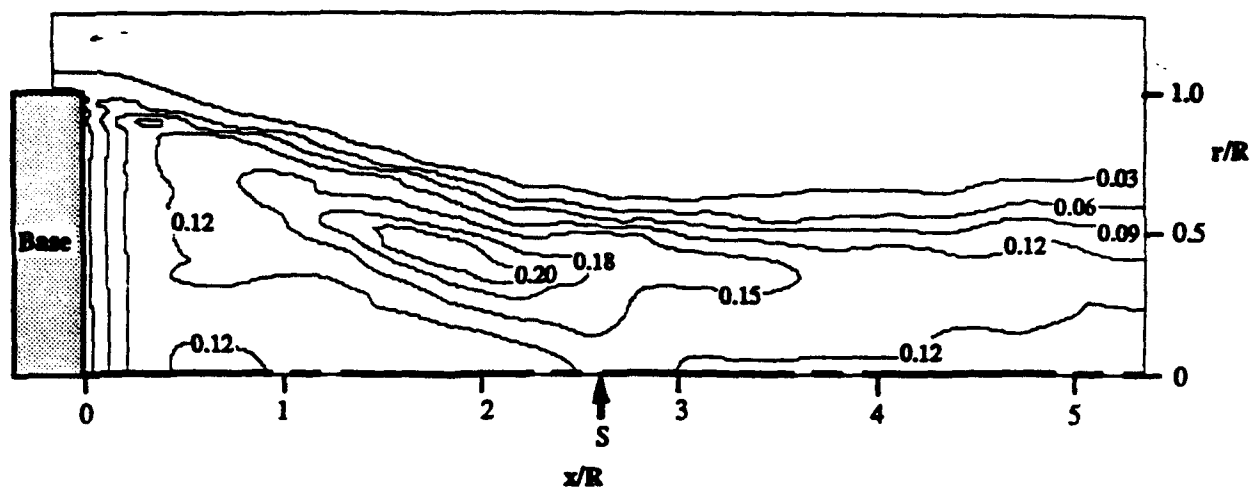
Fig. 9   Axial Turbulence Intensity Contours - σ_u / U_1
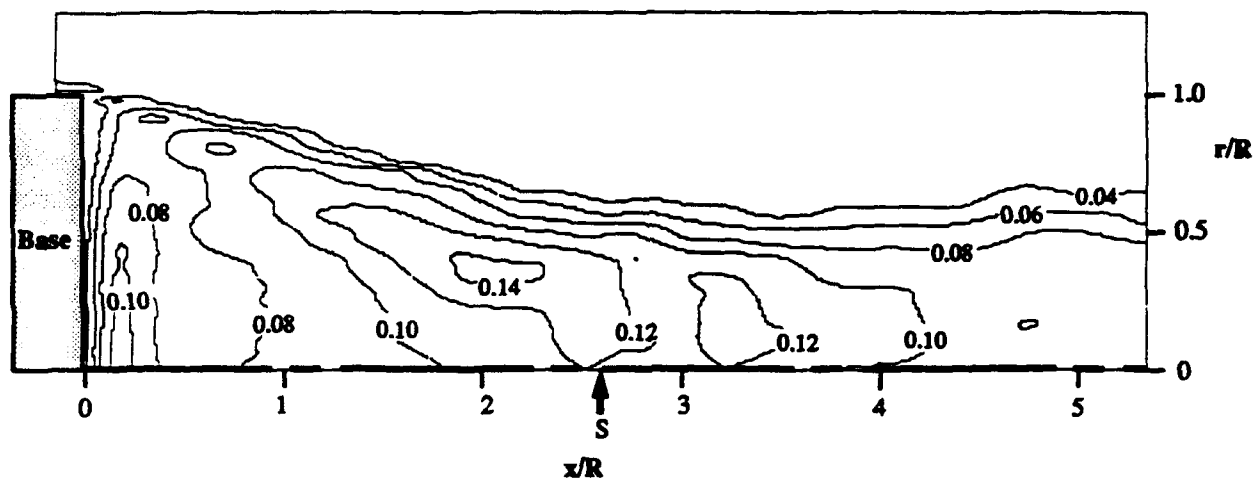
Fig. 10   Radial Turbulence Intensity Contours - σ_{V_r} / U_1
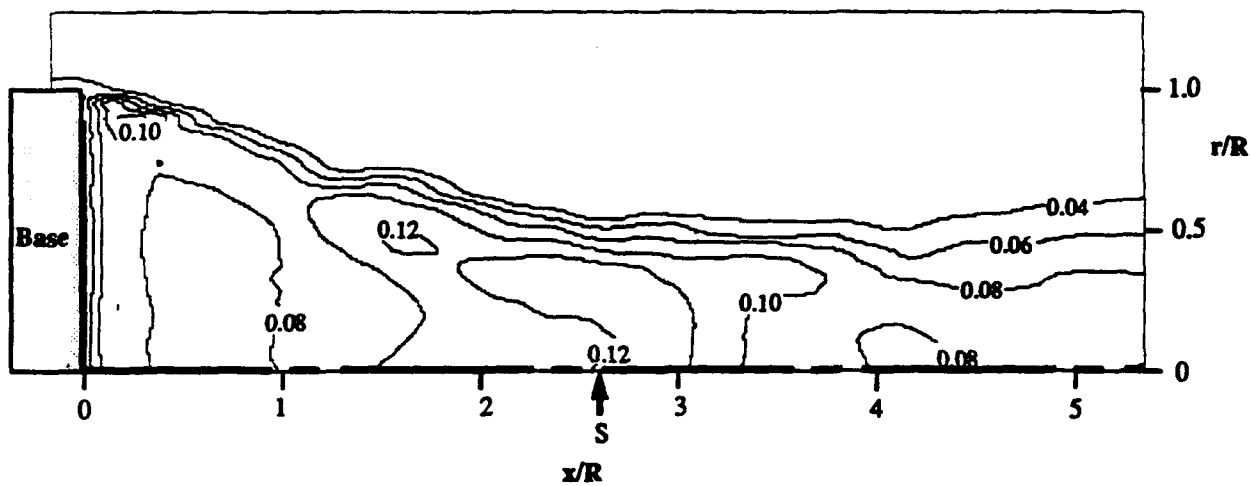
Fig. 11   Tangential Turbulence Intensity Contours - σ_{V_t} / U_1

10
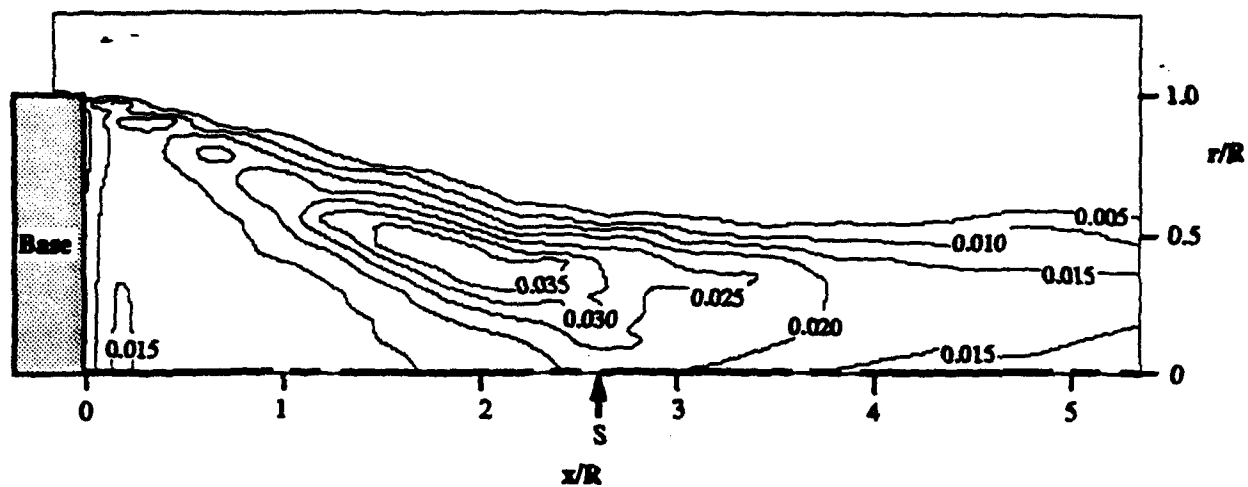
Fig. 12   Turbulent Kinetic Energy Contours - k / U_1^2
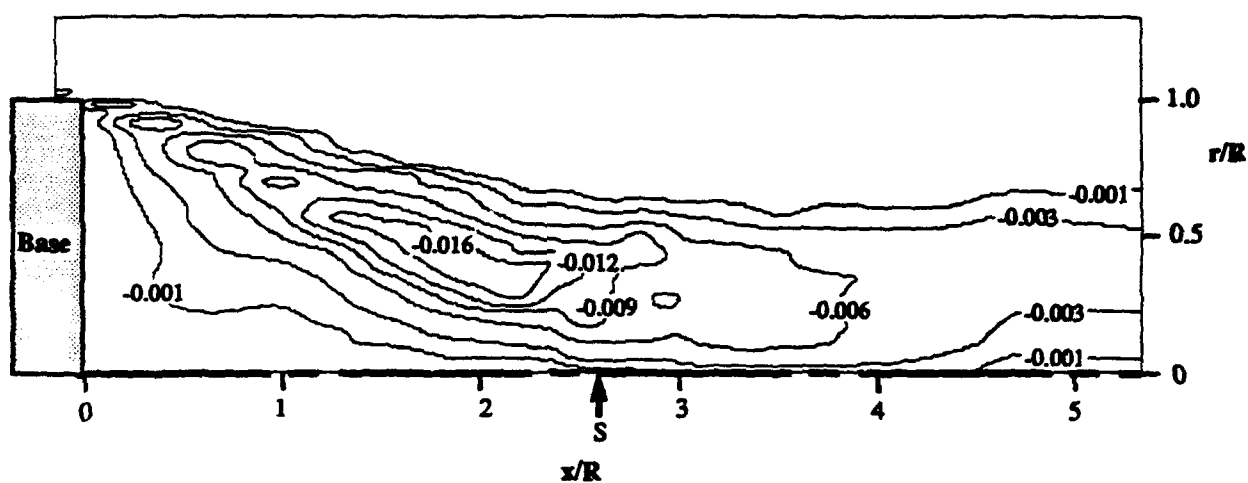
Fig. 13   Reynolds Shear Stress Contours - $<u'v_r'> / U_1^2$
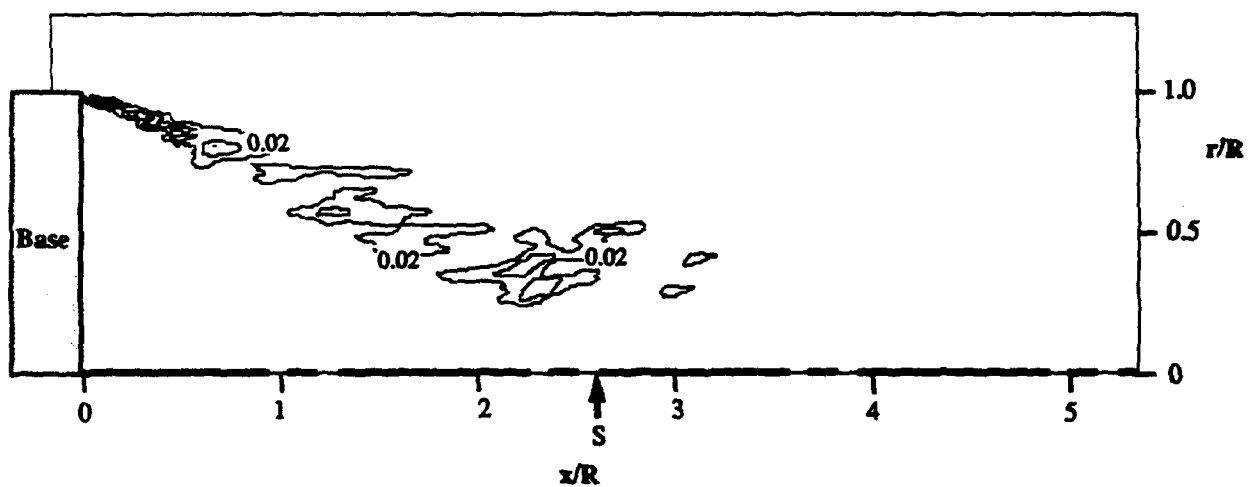
Fig. 14   Turbulence Production Contours - $P_k \cdot R / U_1^3$

11

APPENDIX A.6

EXPERIMENTAL INVESTIGATION OF AN EMBEDDED SEPARATED FLOW REGION BETWEEN TWO SUPERSONIC STREAMS

AIAA Paper No. 90-0707

Presented at the 28th AIAA Aerospace Sciences Meeting

Reno, Nevada

January 1990

by

V. A. Amatucci, J. C. Dutton, D. W. Kuntz, and A. L. Addy

AIAA-90-0707

EXPERIMENTAL INVESTIGATION OF AN EMBEDDED SEPARATED FLOW REGION BETWEEN TWO SUPERSONIC STREAMS

V. A. Amatucci, Sandia National Laboratories, Albuquerque, New Mexico

J. C. Dutton, University of Illinois at Urbana-Champaign, Urbana, Illinois

D. W. Kuntz, Sandia National Laboratories, Albuquerque, New Mexico

A. L. Addy, University of Illinois at Urbana-Champaign, Urbana, Illinois

28th Aerospace Sciences Meeting
January 8-11, 1990/Reno, Nevada

EXPERIMENTAL INVESTIGATION OF AN EMBEDDED SEPARATED FLOW REGION BETWEEN TWO SUPERSONIC STREAMS

V. A. Amanucci[†], J. C. Dutton[*], D. W. Kuntz[‡], and A. L. Addy[¶]

Abstract

The complex interaction region generated by the separation of two supersonic streams past a finite-thickness base occurs frequently in high-speed flight and is characteristic of the aft-end flowfield of a powered missile. An experimental investigation was conducted in which a flowfield of this type was modeled in a two-dimensional wind tunnel. The data was obtained using Schlieren photography, pressure measurements, and two-component laser Doppler velocimeter (LDV) measurements. The shear layer mixing regions were characterized by initially constant-pressure mixing, by an evolution of velocity profiles from truncated boundary layer shapes to wake-like profiles farther downstream, and by relatively high levels of turbulence. The separated flow region was characterized by large negative velocities and strong interactions with the low-velocity regions of both shear layers. Turbulence intensities and kinematic Reynolds stresses were increased greatly in the latter portions of the two shear layers and in the recompression region. Recovery of the mean velocity field in the redeveloping wake occurred quickly, while the turbulence field remained perturbed to the furthest streamwise location.

Nomenclature

C_f	Skin friction coefficient
M	Mach number
P	Pressure
Re	Reynolds number
Re_δ	Reynolds number based on boundary layer thickness
Re_θ	Reynolds number based on momentum thickness
u	U-component of the velocity vector
u^*	Generalized velocity (see Reference 29)
u_τ	Friction velocity
v	V-component of the velocity vector
X	Coordinate parallel to the wind tunnel floor
Y	Coordinate perpendicular to the wind tunnel floor
Y^+	Wall-wake coordinate, $Y^+ = Yu_\tau/\nu_w$
Z	Spanwise coordinate
δ	Boundary layer thickness
δ^*	Boundary layer displacement thickness
θ	Boundary layer momentum thickness
λ	Wavelength of laser light
ν	Kinematic viscosity
Π	Wake strength parameter
τ	Shear stress
$< >$	Root-mean-square quantity

Subscripts

e	Edge condition
J	Inner jet or lower stream condition
w	Condition at the wall
0	Location where zero velocity occurs
0.5	Location where $u/u_e = 0.5$
0.99	Location where $u/u_e = 0.99$
1	Condition for the Mach 2.56 stream
2	Condition for the Mach 2.05 stream
∞	Infinity or freestream conditions

Superscripts

‾	Ensemble average
'	Fluctuation from the mean value

Introduction

The complex interaction region generated by the separation of two supersonic streams past a finite-thickness base occurs frequently in high-speed flight and is characteristic of the aft-end flowfield of a powered missile in the supersonic flight regime. This fluid dynamic flowfield exists in other applications as well, including the flow region at the trailing edge of a blunt airfoil in a supersonic freestream or the initial mixing region of confluent multiple streams in a supersonic combustor. In each of these cases the near-wake region is dominated by strong velocity and density gradients, energetic viscous interactions, and expansion and compression processes covering the full range of gas dynamic regimes.

Research programs through the years have attempted to develop analytical, numerical, and experimental insight into the fluid dynamic processes ongoing in the near-wake region. The usual motivating goal is the development of a predictive capability for base pressure and other flowfield properties over a wide range of flight regimes. The analyses develop a physical flow model of the strong dissipative regions of the near-wake, including interaction with the adjacent inviscid regions, and attempt to find applicability for a variety of Mach number, Reynolds number, and afterbody geometry conditions. The dominant analytical approach has been the Chapman-Korst component model [1-4] in which the turbulent base flowfield is separated into distinct regions and each part is analyzed individually, subject to appropriate assumptions and boundary conditions. The expansion process at the geometric corner, the shear layer mixing process, and the recompression and redevelopment processes (see Figure 1) are each analyzed as separate components, utilizing empirical formulations as needed. The individual components are then joined together into an overall model of the separated flowfield, allowing for interaction between each component, and a unique solution is determined.

With the advent of more powerful computing facilities during recent years, both thin-layer and full Navier-Stokes computations of high-speed separated base flows have been performed. To date the agreement of these computations with experimental measurements of high-speed separated flowfields has been only moderate [5]. However, by focusing on the

[†] Senior Member of Technical Staff, Sandia National Laboratories, Albuquerque, NM, Student Member AIAA.

[*] Associate Professor, Department of Mechanical and Industrial Engineering, University of Illinois at Urbana-Champaign, Urbana, IL, Member AIAA.

[‡] Senior Member of Technical Staff, Sandia National Laboratories, Albuquerque, NM, Senior Member AIAA.

[¶] Professor and Head, Department of Mechanical and Industrial Engineering, University of Illinois at Urbana-Champaign, Urbana, IL, Associate Fellow AIAA.

issues of grid resolution and alignment, as well as turbulence modeling, improved predictions of these flows have recently been obtained [6-10]. The difficulty in accurately computing these flows is understandable due to their complexity, since they include regions of large flow property gradients in thin shear layers, expansion waves, and shock waves, and also due to the inability of the current generation of turbulence models to adequately treat such effects as large streamline curvature, compressibility (i.e., high Mach number effects), shear layer impingement, and the effects on turbulence of the previously mentioned large gradient regions.

To aid in the understanding of the detailed mechanisms of these high-speed flows both with and without regions of significant flow separation, a program of small-scale wind tunnel experiments of simple flow geometries has been conducted at the University of Illinois at Urbana-Champaign. Initial experimental work has examined in detail the shear layer mixing process [11-13] and the recompression and reattachment processes [14-17]. The measurements presented in this paper take the next step in this progression and add the recirculating region and the wake redevelopment region (see Figure 1) as focuses of study to obtain experimental data for a unified two-stream near-wake flowfield. The present experimental program has obtained measurements over the full range of mechanisms exhibited in this flowfield for a well-determined set of incoming flow conditions. The data for these experiments are obtained from Schlieren photography, sidewall pressure measurements, and laser Doppler velocimeter (LDV) measurements. The use of a two-color, two-component, frequency shifted LDV to measure instantaneous flow velocity, despite its added complexity, has certain special advantages in the near-wake separated flowfield. Most past near-wake interaction experiments, e.g. References 18 through 20, have focused on mean velocity values obtained from pressure distribution data gathered by intrusion into the near-wake, usually with a single pressure probe or a probe rake. The LDV measurements of the current investigation provide accurate instantaneous velocity data obtained in a nonintrusive way by an instrument requiring no prior calibration.

The primary objective of this experimental investigation of the supersonic, two-stream base flow is to investigate the fundamental fluid dynamic mechanisms existing in the near-wake flowfield with an aim toward better understanding of each individual process and how they interact. Detailed data have been collected in all regions of the near-wake flowfield in order to examine such features as changes in velocity profiles due to the corner expansion process, evolution of the velocity profiles during shear layer mixing, strength and influence of the recirculating region, and mean and turbulent flowfield changes during the recompression, reattachment, and downstream wake redevelopment processes.

Experimental Facilities and Measurement Techniques

Facilities

This investigation of the near-wake interaction utilized the air supply and wind tunnel facilities of the Mechanical Engineering Laboratory at the University of Illinois at Urbana-Champaign for a series of dry, cold air experiments. A two-dimensional wind tunnel test section, shown schematically in Figure 1, produced two uniform supersonic streams which separated at the geometric corners of a finite-thickness splitter plate and formed a flowfield characteristic of the aft-end of a powered missile, including expansion at the separation points, formation of a recirculating region bounded by two shear layer mixing regions, recompression and reattachment of the shear layers, and downstream wake redevelopment.

The common upstream plenum chamber provided compressed air at 517 kPa to two separate pipe-and-valve arrangements supplying the two converging-diverging nozzles. These nozzles used the splitter plate as a half-nozzle symmetry plane. The upper stream nozzle produced a uniform exit plane flow 50.8 mm in height, having a Mach number of 2.56, and a splitter plate boundary layer thickness of 3.35 mm. The lower stream nozzle was shorter in length and produced a uniform exit plane flow 25.4 mm in height, having a Mach number of 2.05, and a splitter plate boundary layer thickness of 1.46 mm. These two supersonic streams separated past the 25.4 mm finite-thickness base and produced the near-wake interaction flowfield. The test section region was 50.8 mm wide and 101.6 mm in height and was within view of clear glass windows on both sides of the wind tunnel for optical diagnostic access. All features of the near-wake flowfield, including wake redevelopment, occurred within the measurement domain before the mixed flow exited the test section through a constant-area diffuser.

Measurement Techniques

The measurement techniques employed in this investigation included Schlieren photography, stagnation and static pressure measurements, and laser Doppler velocimetry. Schlieren photographs obtained with a 1.4 microsecond spark source were used to characterize the qualitative features of the overall flowfield and to determine spatial locations for LDV measurements. The sidewall static pressure data was collected using an aluminum window insert which replaced one of the glass side windows and had a grid of 370 pressure taps. The pressure levels were measured with a Pressure Systems Incorporated (PSI) digital pressure transmitter system and yielded pressure measurements in all regions of the near-wake interaction including along the shear layer mixing regions.

The two-component, two-color LDV system was based on Thermal Systems Incorporated (TSI) optical and electronic components and employed a Spectra-Physics 5-watt argon ion laser. The green beam (λ=514.5 nm) and the most powerful blue beam (λ=488.0 nm) were used in the beam splitting and recombination processes which produced the ellipsoidal measurement volumes. The use of a 350 mm focal length transmitting lens with 22 mm beam spacing produced a green measurement volume of 0.183 mm diameter, 6.08 mm length, with 8.53 μm fringe spacing. The blue measurement volume diameter, length, and fringe spacing were 0.179 mm, 5.92 mm, and 8.09 μm, respectively. These fringe spacings, in combination with the 40 MHz frequency shift and orientation of the fringes at ±45° to the mean flow direction, kept signal frequencies within range of the electronic equipment while moving the fringes at a high enough velocity to reduce fringe bias probabilities and eliminate directional ambiguity. TSI frequency counters, operated in the single-measurement-per-burst mode with high- and low-pass filtering, were used to determine the Doppler shift frequencies of the signals from the photodetectors and to perform validation checks to remove erroneous data. The receiving optics of the LDV system were oriented in a forward scatter mode 10 degrees from the optical axis in order to reduce the effective length of the measurement volume to 1.46 mm and to provide optimum signal-to-noise ratio of the scattered laser light. The output from the LDV system's frequency counters was stored in the memory of a DEC PDP 11/73 minicomputer by means of a direct memory access board, and the data was transferred serially to an HP-9000 computer system for reduction, analysis, and plotting. The laser, transmitting optics, and collection optics were mounted on a traversing table which allowed movement in all three coordinate directions with an accuracy of approximately ±0.1 mm.

Seeding of the flow for the LDV measurements was accomplished by injecting 50 cP silicone oil droplets produced by a TSI six-jet atomizer into the stagnation chamber. To address the issues of particle size and flow-following ability

2

(i.e., particle dynamics effects), a series of particle lag experiments was conducted whereby LDV measurements were made across an oblique shock wave produced by a 15° compression corner in a Mach 2.0 wind tunnel. Using these measurements, together with a particle relaxation analysis based on the work of Maxwell and Seasholtz [21] and the drag law of Walsh [22], the silicone oil droplets used in these experiments are estimated to be 1.0 μm in diameter. Droplets of this size have an Eulerian frame frequency response of up to approximately 200 kHz which is adequate for following the turbulent fluctuations of the current near-wake flowfield.

The use of counter-type signal processors to measure individual velocity realizations introduces additional considerations, especially in high-speed flows, due to counter clock resolution, statistical uncertainty, velocity bias, fringe bias, and spatial resolution. The ±1 nanosecond accuracy of the counters results in a minimum measurable turbulence intensity in the highest speed regions of the flow of 1.37%, with proportionately smaller values in the lower speed regions. In order to control the uncertainty due to finite sample size, either 2048 or 4096 velocity realizations were generally collected throughout the flowfield. At a confidence level of 95%, the resulting statistical uncertainty in the mean velocity is therefore a maximum of ±3% for turbulence intensities less than about 100%, and the statistical uncertainty in the standard deviation is a maximum of approximately ±3.1%. For the current low data density measurements, the seed particles generated valid Doppler signals at a rate several orders of magnitude lower than the capability of the pro essors to sample, resulting in a free running processor condition in which the LDV data is totally velocity biased [13]. In order to correct for this condition, a two-dimensional inverse velocity magnitude weighting scheme [23] has been employed. As previously mentioned, the relatively large fringe spacing, use of the 40 MHz frequency shift, and the ±45° orientation of the fringes to the mean flow direction, greatly reduced the possibility of fringe bias in these experiments. In fact, an implementation of the fringe bias analysis of Buchhave [24] demonstrated that for the vast majority of the measurements the fringe bias correction was less than 3% and, as a result, no such correction has been used in the measurements presented here. Spatial resolution errors can occur in high gradient regions of the flow due to the finite size of the probe volume. Using the analysis of Karpuk and Tiederman [25], the maximum spatial resolution error at the location 5 mm downstream from the base is estimated to be ±2.8% for the mean velocity and ±4.8% for the turbulence intensity, with much smaller errors in the downstream regions of the near-wake flow.

Further details concerning the equipment and apparatus, measurement methods, and experimental procedures may be found in Reference 26.

Experimental Results and Discussion

Two-Dimensionality of the Flowfield

Past work [11, 27, 28] has indicated the tendency for existence of spanwise nonuniformity in flowfields characterized by large embedded separation regions leading to reattachment. To examine these effects in the present flowfield, transverse profiles of velocity were obtained at three spanwise locations: at the midplane (Z=0) and at Z=±10 mm from the midplane. In addition, these profiles were obtained at three streamwise locations chosen to examine distinctly different regions of the near-wake: X=25 mm where separate shear layers and recirculation were present, X=45 mm in the recompression and reattachment region, and X=100 mm in the redeveloping wake. The streamwise mean velocity and turbulence intensity data show that the central 40% of the test section flowfield was highly two-dimensional in all regions with the largest deviations

occurring in the recirculating region. Once impingement of the two shear layers occurred, the LDV data indicate very little deviation from two-dimensionality at any transverse location. Although regions of slight three-dimensionality do exist, they seem characteristic of the fluid dynamic processes ongoing in those components of the near-wake and are not due to the wind tunnel design or sidewall boundary layers.

Turbulent Boundary Layers

The turbulent boundary layer characteristics of the two supersonic streams provide the initial conditions for the expansion, mixing, recompression, and redevelopment processes which occur in the near-wake. Detailed LDV measurements were made of the boundary layers which developed on the upper and lower surfaces of the splitter plate at a location 4 mm before geometric separation. Two-component measurements were made to a distance of 0.75 mm from either surface and then one-component measurements completed the survey to a distance within 0.25 mm above either surface. The measured velocity profiles for the upper and lower boundary layers were fit to the generalized velocity profile equation of Sun and Childs [29] using the boundary layer thickness, δ, the friction velocity, u_τ, and the wake strength parameter, Π, as curve fit coefficients. The important parameters describing the growth and development of the two boundary layers prior to separation are presented in Table 1. The differences in thicknesses between the Mach 2.56 stream (δ=3.35 mm) and the Mach 2.05 stream (δ=1.46 mm) were generated intentionally to simulate the ratio of boundary layer thicknesses typical to powered missile applications. The wake strength parameter, friction velocity, and skin friction coefficient values are consistent with earlier studies [11, 14, 27, 30, 31] of compressible turbulent boundary layers.

The measured mean velocity profiles for the Mach 2.56 and Mach 2.05 boundary layers are presented in Figure 2 in wall-wake coordinates together with the least squares curve fits generated from the Sun and Childs [29] analysis. These data indicate relatively similar profiles for both boundary layers despite considerably different upstream "histories" of their growth and development. The relatively small thickness of each boundary layer is illustrated by the lack of LDV data (due to spatial resolution restrictions) below a value of Y^+ of approximately 100 (Y/δ of approximately 0.08). Measurements of the streamwise turbulence intensity and kinematic Reynolds stress for these two boundary layers have also been compared to similar measurements of other workers obtained by both LDV [11, 14, 27, 32] and hot-wire anemometry [33, 34]. In general, the agreement among these various turbulent boundary layer measurements is very good. Small discrepancies that occur between the LDV data and the hot-wire data are likely due to LDV counter clock resolution problems in the outer, high-speed regions of the boundary layer, and due to inaccuracies in calibration of the hot-wires near and below the sonic line in the inner, low-speed regions of the boundary layer.

Global Near-Wake Interaction Flowfield

Schlieren photography has been used to obtain a qualitative view of the component processes existing in the near-wake interaction. The Schlieren photograph of Figure 3 shows well-developed splitter plate boundary layers undergoing strong expansion and turning processes at geometric separation. The two free shear layers generated at separation appear to be initially very thin and to undergo a moderately long constant pressure mixing region before they show any signs of curvature associated with the recompression process prior to impingement. The beginning of the recompression process for each shear layer is marked by the first compression waves which emanate from the slightly supersonic regions of the shear layer and eventually coalesce into the recompression oblique shock wave. One of the more interesting features in this

3

photograph is the apparent large-scale turbulent structures which border the edges of the redevelopment core produced by the impingement of the two free shear layers. These structures are similar to those that occur in high Reynolds number free jets and have an effect on the turbulence intensities measured in the redeveloping wake. Similarly, each shear layer shows signs of large-scale structures and intermittency at its edges, especially on the side bounded by the recirculating region.

The arrangement of sidewall static pressure tap locations was designed to obtain detailed pressure surveys of the expansion process, mixing layers, and recompression and redevelopment processes. The three-dimensional contour plot of Figure 4 shows the static pressure data viewed by an observer located upstream at the base and looking in the streamwise direction. Although no detailed vertical scale is given for the levels of static pressure, a relative indication of the pressure magnitude can be obtained by recognizing that the maximum static pressure in the figure is 66.9 kPa and occurs at the exit of the Mach 2.05 nozzle, while the minimum static pressure of 12.2 kPa occurs in the highly expanded flow region downstream of the Mach 2.05 nozzle and just upstream of the lower recompression shock wave. In a quantitative sense the plot of Figure 4 shows the strong expansion of the two supersonic streams to the low pressure "valley" immediately behind the finite-thickness base, the initially constant pressure mixing of the two shear layers, and the gradual but strong pressure rise through the recompression and reattachment regions extending into the downstream wake redevelopment region.

The series of LDV data presented in this section is intended to give an overv... of the mechanisms existing in the near-wake interaction, including a detailed indication of the mean flow and some turbulence quantities. The objective of this overview is to show representative data highlighting the dramatic changes in mean velocity and turbulence quantities in the region immediately behind the splitter plate and in the initial stages of recompression and reattachment. The LDV data presented in this section include the "reference" upstream boundary layer traverses, *every other* vertical traverse from 5.0 mm behind the splitter plate to 40.0 mm downstream, and then *every* measured traverse from X = 40.0 mm to X = 55.0 mm. The omission of some LDV traverses from the figures discussed in this section was necessary to reduce plot congestion. In this section, all of the instantaneous velocity data obtained with the LDV system have been rotated to a coordinate system which aligns the u-component direction parallel to the wind tunnel floor (primary streamwise direction) and the v-component direction perpendicular to the wind tunnel floor.

The mean velocity profiles obtained from the LDV instantaneous data are shown in vector representation in Figure 5. The vector field plot clearly shows the approach and separation of the two turbulent boundary layers from the upper and lower surfaces of the splitter plate, with the resulting large separated flow region. The shear layer mixing regions spread with streamwise distance until impingement occurs approximately 1.4 base heights downstream of separation (at X = 34.9 mm), where the recirculating region ends (no negative streamwise velocity components are measured) and recovery of the wake deficit begins. The turbulent mixing which occurs throughout the recompression and reattachment regions quickly effects elimination of the velocity deficit by approximately 5 base heights downstream of separation, although only part of this process can be seen in Figure 5.

Examining Figure 5 in detail, the data show that the upper Mach 2.56 flow has a freestream velocity of 584.13 m/sec before separation and expands sharply downward around the corner of the base to a flow angle of approximately -10.6 degrees. The lower Mach 2.05

freestream moves at a velocity of 523.85 m/sec before separation and then expands upward about the splitter plate corner at an angle of approximately 21.6 degrees. Both turbulent boundary layers are fully developed and expand upon geometric separation to a matched base pressure of 13.8 kPa which exists in the recirculating region. The mean velocity vectors shown in Figure 5 illustrate the complex nature of separation past a relatively thick base, and indicate differences from the type of wake developed behind a very thin splitter plate [35, 36].

The vector representation of the recirculating region in Figure 5 indicates the existence of two large separation bubbles. The upper separation bubble rotates clockwise while the lower bubble rotates counterclockwise, and relatively large velocity magnitudes exist in this region. Historically posed by Korst [3] as a "dead-air" region, the recirculating region of the near-wake in the present investigation had a maximum negative velocity of 132.01 m/sec at the X = 22.5 mm streamwise location. This maximum negative velocity magnitude of 0.23 u_1 is very consistent with the results of Petrie [11], Samimy [14], Etheridge and Kemp [37], and Delery [38] in the entire range of Mach numbers.

The streamwise mean velocity profiles, nondimensionalized by the edge velocity of the Mach 2.56 stream prior to separation, are shown in Figure 6. The dashed line at each X value represents the streamwise location of the traverse and the $u/u_1 = 0$ plane for that set of data. The upstream boundary layer profiles represent a typical range of u/u_1 beginning at a value of 1.0 in the Mach 2.56 stream and 0.90 in the Mach 2.05 stream ($u_2/u_1 = 0.9$) and decreasing to zero on the two surfaces of the splitter plate. This series of profiles once again indicates the large negative velocities occurring in the recirculating region and the recovery of the velocity defect with downstream distance. The fine transverse resolution of the LDV measurement locations yields u-component data which show the spreading of the velocity profiles in each of the shear layers from a very sharp gradient at the X = 5.0 mm location to a much broader velocity change at the streamwise stations near recompression and reattachment. The rapid recovery of the mean velocity defect is consistent with the data of Samimy and Addy [17] for a similar two-stream near-wake interaction between Mach 2.07 and Mach 1.50 streams.

The turbulence field, represented in part by the streamwise turbulence intensity profiles of Figure 7, demonstrates strong enhancement of mixing due to the interaction at the base. The counter clock resolution problem with the LDV system is illustrated in the edge values of $<u'>/u_1$ of approximately 2 percent in the two relatively high-velocity isentropic core flows. The striking feature of Figure 7, however, is the relatively high levels of streamwise turbulence intensity reaching nearly 30 percent in the latter streamwise stations in the mixing layers and in the recompression and reattachment regions. Despite similarities in the form of the turbulence intensity profiles across either shear layer to those found by Andreopoulos and Bradshaw [39] in an incompressible shear layer behind a flat plate and by Ikawa and Kubota [40] in a supersonic free shear layer, the levels of $<u'>/u_1$ are dramatically higher in the present investigation. While Samimy and Addy's [17] streamwise turbulence intensity levels were slightly lower than those shown in Figure 7, the trends are similar and indicate strong shear layer mixing and the highly turbulent nature of the reattachment process.

The transverse turbulence intensity profiles shown in Figure 8 similarly reflect the strong mixing near recompression and the disturbed nature of the turbulence field even downstream to the last traverse location shown. Figure 8, now scaled for a maximum $<v'>/u_1$ value of 20 percent, shows the moderately low levels of transverse turbulence intensity existing in both of the upstream boundary layers in contrast to the high

4

levels of $<v'>/u_1$ occurring in the shear layers. The transverse turbulence intensity appears to spread more broadly across the transverse height of the interaction region than the streamwise turbulence intensity does and is similar to results obtained by Kuntz [27] for a Mach 2.94 shock-wave/boundary-layer interaction flowfield.

The turbulence intensity ratio or anisotropy ratio, $<u'>/<v'>$, is a measure of the type of turbulence field existing in the near-wake interaction. In an isotropic turbulence field, where the streamwise and transverse turbulence intensities vary in equal amounts, $<u'>/<v'>$ is equal to unity everywhere. Thus the profiles shown in Figure 9 give an indication of the anisotropic nature of the near-wake interaction flowfield, and where enhancement of the turbulence structure occurs. The strong anisotropy existing in the lower portions of the splitter plate boundary layers is seen to be redistributed by the corner expansion process reducing the ratio from a value of approximately 4 to less than 3. These levels of anisotropy are consistent with the mixing/reattachment studies of Petrie [11] and Samimy [14], and the shock-wave/boundary-layer interaction studies of Kuntz [27] and Ardonceau [41] in supersonic flowfields.

The data for the kinematic Reynolds stress portion of the turbulent shear stress for the near-wake interaction region are nondimensionalized by the square of the Mach 2.56 edge velocity and plotted in Figure 10. Initially low levels of Reynolds stress in the splitter plate boundary layers rise to relatively high levels immediately downstream of separation, persist throughout the mixing layer development, and reach maximum values in the recompression and reattachment regions. The Reynolds stresses then tend to decrease sharply after reattachment, very similar to the trends of incompressible reattachment as shown by the data of Chandrsuda and Bradshaw [42] . The lower Mach 2.05 stream's mixing layer appears to be more highly turbulent than the Mach 2.56 stream, and as suggested by Samimy and Addy [17] may be the result of a stronger separation and expansion process, or may be the consequence of a lower convective Mach number [36]. The decrease in Reynolds stress just downstream of reattachment has been explained by restriction of the larger eddies [42] and by bifurcation of the turbulent eddies at reattachment [43, 44] resulting in much smaller length scales and lower Reynolds stresses.

Shear Layer Mixing Regions

The primary analysis in the Korst model [2-4] of the near-wake interaction flowfield is the prediction of the development and evolution of velocity profiles in the mixing region formed when the turbulent boundary layer flow separates past the base. In general, the shear layer mixing region is characterized by relatively large velocity gradients, strong entrainment rates, and an evolution of velocity profile shapes from those resembling truncated boundary layer profiles to more wake-like distributions further downstream. In the limiting case where the upstream boundary layer thickness is zero, the velocity distributions across the width of the shear layer mixing region exhibit the shape of an error function profile.

The qualitative features of the shear layers produced in the near-wake of the finite-thickness base are identified and explained using the Schlieren photograph of Figure 3. As detailed earlier, the shear layers are produced when the two turbulent boundary layers generated on the splitter plate surfaces adjacent to the Mach 2.56 and Mach 2.05 streams undergo geometric separation at their respective corners of the base. The 3.35 mm thick turbulent boundary layer for the Mach 2.56 stream (see Table 1 for statistics of both turbulent boundary layers) separates from the base and expands about the corner to produce a free shear layer turned downward at

approximately 10.6 degrees. Similarly, the turbulent boundary layer on the surface of the splitter plate adjacent to the Mach 2.05 stream undergoes separation at the base corner and after the expansion process is turned upward at approximately 21.6 degrees. The turning and expansion processes for the two streams adjust their nozzle exit plane static pressure and Mach number to levels consistent with the 13.8 kPa pressure level existing in the recirculating flow region. As a consequence, the initial "edge" Mach number for both mixing layers is approximately 3.02, consistent with Prandtl-Meyer expansion predictions for two streams originating from nearly the same stagnation conditions and expanding to the identical static pressure level.

The detailed view provided in Figure 3 of the two shear layers illustrates features consistent with earlier findings for supersonic mixing layers and worthy of greater attention. In particular, large-scale turbulent structures appear at the high-velocity edges of each shear layer along their entire length. The Schlieren photograph also illustrates the dominant influence of the separated flow region (and the resulting reverse flow velocities) as the low-velocity "inner" boundary of each shear layer, and the relatively short lengths available for shear layer mixing before the turning and recompression of the shear layers begin prior to impingement.

The velocity data obtained with the LDV system was analyzed using coordinate rotations which aligned the u-component direction approximately along the predominant direction of each shear layer. The streamwise traverses from immediately downstream of the base ($X = 2.5$ mm) to the first streamwise traverse at which no reverse flow vectors occur ($X = 35.0$ mm) are included in this range covered as the shear layer mixing component of the base region model. All of the data for the upper Mach 2.56 shear layer was coordinate rotated to a u-component direction of -10.6 degrees (from the horizontal) while the lower Mach 2.05 shear layer data was rotated to a u-component direction of +21.6 degrees.

The profiles used for determination of self-similarity of the mean and turbulent fields are shown in Figures 11 and 12. The optimum scheme for plotting of the mixing layer profiles was found to be a dimensionless position parameter which incorporated the half-velocity location and the shear layer width. For each streamwise traverse the value chosen for the local edge velocity was determined from the LDV data by finding the location on the high-velocity side of each shear layer which represented not just a local plateau level of mean velocity but also the point where there was a significantly increased value of turbulence intensity. Once this edge velocity value was selected, calculations were performed to determine the Y-locations where the velocity was reduced by 1 percent and 50 percent, and also where zero u-component velocity occurred. The nondimensionalizing position parameter was then defined to be $(Y - Y_{0.5})/(Y_{0.99} - Y_0)$, and the mean velocity and turbulence intensity in the appropriate u-component directions were divided by the local edge velocity value.

The data in Figures 11 and 12 illustrate the results of this analysis and seem to confirm quite strongly Birch and Eggers' [45] contention that relative similarity in the mean velocity profiles is not by itself an indication of the fully developed nature of a shear layer, and the turbulent field may still lack similarity. The data for the Mach 2.56 shear layer are plotted in Figures 11 and 12 beginning with the $X = 10.0$ mm traverse location through to the last streamwise location where the two shear layers appear to remain individual entities. The traverses at $X = 2.5$ mm, 5.0 mm, and 7.5 mm were eliminated from Figures 11 and 12 since their profiles were expected to be far from self-similarity and there was less plot congestion as a result.

5

The mean velocity profiles for the Mach 2.56 shear layer illustrate relatively good similarity in the central regions despite the slightly crude method for determining the edge velocity (see Figure 11), but relatively strong deviations from similarity occur at both the low-velocity and high-velocity edges of the mixing region. These deviations are most certainly due to variation of the recirculating flow velocity which forms the "low-velocity" side boundary, while the high-velocity end data is influenced by the presence of the coalescing recompression shock waves and their effects upon the velocity ratio with streamwise distance. The turbulence intensity data for the Mach 2.56 shear layer, shown in Figure 12, more clearly illustrate the non-similarity of the turbulent field not only by the large amount of scatter in the data but by exhibiting only a mild trend for increasing maximum turbulence intensity levels for increasing streamwise distance. The turbulence intensity data of Figure 12 show slow progression towards the similarity needed for so-called fully developed mixing.

Recompression and Reattachment Processes

Since the initial development of a comprehensive turbulent base flow analysis by Korst [3], the recompression and reattachment processes in the near-wake interaction have often been viewed as the most significant components of the entire base flowfield and perhaps the least well understood. Despite large velocity gradients and turbulence intensities existing *throughout* the near-wake region, *peak* levels of turbulence consistently occur in the vicinity of shear layer recompression and reattachment. The recompression and reattachment processes are the focus of numerous research efforts still today, and detailed data are needed.

The recompression process begins as the two free shear layers reach the end of constant pressure mixing and begin to readjust to the downstream flow direction and pressure level. Each shear layer experiences increasing levels of static pressure, increasing levels of turbulence intensity, and the formation of multiple compression waves which coalesce into the traditional single oblique shock wave associated with the turning of a supersonic flow. Near the impingement location of the two shear layers, consistent with the analysis of Korst [3], fluid elements which contain sufficient mechanical energy to overcome the recompression pressure rise will continue downstream, while those fluid elements below this level of mechanical energy will instead be turned back upstream and become part of the recirculating flow region behind the base.

Several qualitative features of the recompression and reattachment processes are evident in the Schlieren photograph of Figure 3. The upper shear layer and the lower shear layer begin gradual turning processes prior to impingement at approximately 1 4 base heights downstream of separation. At this location in the flowfield the first of many compression waves are seen emanating from the low supersonic Mach number regions of each shear layer and extending out into the adjacent high-velocity stream. By approximately 2.8 base heights downstream (X = 70.0 mm), these compression waves have coalesced into a single oblique shock wave for each stream. All of the LDV data for the streamwise traverses presented for the recompression and reattachment processes were collected with the LDV system's measurement volume fringe patterns set at ± 45 degrees to the wind tunnel floor. The acquired data was then rotated 45 degrees to establish the u-component direction *parallel* to the wind tunnel floor and the v-component direction *perpendicular* to the wind tunnel floor.

The streamwise mean velocity profiles, nondimensionalized by the exit plane velocity of the Mach 2.56 stream, are presented for the recompression and reattachment region in Figure 13. The profiles show the vigorous nature of the recirculating flow region, with negative velocities in excess of

20 percent of u_1, and provide a better indication of the end of the recirculation region seen to occur by the X = 35.0 mm traverse location. The velocity profiles in the shear layers are characterized by large gradients in the first few streamwise locations in the recompression region but quickly spread, impinge upon one another, and form profiles very wake-like in nature. The streamwise mean velocity profiles of Figure 13 exhibit a tendency for the lower Mach number stream to experience a more rapid rate of profile development than the higher Mach number stream..

The streamwise turbulence intensity profiles, $<u'>/u_1$, shown in Figure 14, dramatically illustrate the high levels of turbulence which characterize the recompression process for compressible flows. In incompressible reattachment experiments [43, 44] the maximum levels of streamwise turbulence intensity remain below 20 percent. In compressible recompression and reattachment processes, streamwise turbulence intensity levels reach nearly 30 percent based on the Mach 2.56 stream's exit plane velocity, and are even higher when based on local velocity magnitudes. Peak streamwise turbulence intensity levels occur within the shear layers near the sonic lines and are indicative of strongly enhanced mixing which uniformly spreads the turbulence characteristics in a transverse sense by the X = 70.0 mm streamwise traverse location.

Redevelopment of the Downstream Wake Flow

The redeveloping region for the supersonic two-stream interaction defines both the pressure level and flow direction which the flow exiting the recompression and reattachment processes must adjust to and eventually match. The redevelopment process can be viewed as a straightforward adjustment of the severe pressure gradient existing across the viscous wake core to a level consistent with downstream far-field conditions. The redevelopment region, as seen in Figure 3, is dominated by the thickening wake flow which results from the impingement and initial mixing of the two free shear layers. This mixing wake flow appears to have large coherent structures which form the boundaries between the viscous wake core and the adjacent inviscid flows and produce a form of intermittency at these edges.

The redevelopment region has been defined as beginning at the last streamwise measurement location of the recompression/reattachment analysis (at X = 70.0 mm) and continuing downstream to the last traverse location within view of the window in the wind tunnel test section (at X = 160.0 mm). All LDV data have been rotated into a coordinate system which aligns the u-component velocity and fluctuations along the X-axis (wind tunnel floor) and the v-component values along the transverse Y-axis (perpendicular to the wind tunnel floor).

The streamwise mean velocity profiles, u/u_1, are plotted in Figure 15 for the range of the redevelopment region, where the vertical dashed line represents the streamwise location of the measurement traverse and the circle and triangle symbols alternate simply to delineate one location's profile from another. The exaggerated nature of the scale used for plotting is quite evident, and although the profiles exhibit diminishment of the wake deficit with downstream distance, the rate does not compare with the more rapid "filling out" observed for redevelopment after reattachment of a free shear layer onto a solid surface such as seen in the results of Settles, et al. [46], Samimy, et al. [14, 17], and Kuntz [27]. The slower recovery of the wake velocity deficit for the redevelopment region, as seen in Figure 15, still represents significant progression towards uniform flow.

The streamwise turbulence intensity profiles, $<u'>/u_1$, are plotted in Figure 16 and illustrate the strong mixing

6

processes occurring in the initial streamwise locations of the redevelopment region. The first few profiles of the redeveloping wake flow exhibit a rapid change in character from one which retains the individual nature of each shear layer (seen in the "double-peaked" shape of the profiles) to profiles which instead depict a wake flow which is becoming uniformly mixed with a single peak in the profiles. The very slight transverse broadening of the profiles in Figure 16 seems consistent with the nature of the redeveloping wake to remain a strong viscous core surrounded by inviscid regions with minimal interfacial mixing. The final few profiles for $<u'>/u_1$ illustrate the perturbed nature of the turbulence field even at distances far downstream, since plateau streamwise turbulence intensity levels remain at approximately 5-6 percent, comparable to the central regions of a turbulent boundary layer.

The extent of shear work ongoing in the redeveloping wake flow is evident in the trends of the kinematic Reynolds stress term shown in Figure 17. These profiles are essentially zero at the upper and lower vertical extremes and experience positive and negative shear work across the viscous wake flow, with peak levels in the initial few traverses reaching approximately 1.2 percent. Some indication of the role of compressibility on the redeveloping wake flow seems evident in the variation of shear work (with streamwise distance) between the side of the wake which originated from the upper Mach 2.56 stream and the lower side which was energized by the Mach 2.05 stream. This larger shear stress gradient for the lower Mach number stream was also observed by Samimy and Addy [17].

Conclusions

The near-wake interaction flowfield generated by the separation of two supersonic streams past a finite-thickness base was characterized by steep velocity gradients, high turbulence intensity levels, and viscous mixing in the presence of an adverse pressure gradient. The shear layer mixing regions were characterized by constant-pressure mixing along the initial two-thirds of their length, and showed an evolution of velocity profiles from truncated forms of the boundary layer shapes to more wake-like profiles farther downstream. The shear layer profiles appear to achieve relative self-similarity in mean velocity while only approaching self-similarity in the turbulence field. The region of separated flow existing between the two supersonic streams in the near-wake exhibited vigorous recirculation, maximum negative velocity magnitudes reaching $0.23\ u_1$, and strong turbulent interaction with the low-velocity regions of both shear layers. Peak levels of turbulence intensity were measured in the recompression and reattachment regions and decreased rapidly with streamwise distance. The turbulence field in the region of reattachment is strongly anisotropic, reaching turbulence intensity ratio values of approximately 4. LDV data for the redevelopment of the downstream wake flow showed lower levels of turbulence intensity and kinematic Reynolds stress than other regions of the near-wake interaction, but illustrated the strong preservation of the disturbed turbulence field with even large distances downstream. While recovery of the mean velocity profiles was achieved, much slower recovery of the turbulence field was seen.

Acknowledgments

References

1. Chapman, D. R., "An Analysis of Base Pressure at Supersonic Velocities and Comparison with Experiment," NACA TN 2137, July 1950.

2. Korst, H. H., Page, R. H., and Childs, M. E., "A Theory for Base Pressures in Transonic and Supersonic Flows," University of Illinois, ME-TN-392-2, March 1955.

3. Korst, H. H., "A Theory for Base Pressures in Transonic and Supersonic Flow," *Journal of Applied Mechanics*, Vol. 23, December 1956, pp. 593-600.

4. Korst, H. H., Chow, W. L., and Zumwalt, G. W., "Research on Transonic and Supersonic Flow of a Real Fluid at Abrupt Increases in Cross Section (with Special Consideration of Base Drag Problems)," University of Illinois, ME-TR-392-5, December 1959.

5. Petrie, H. L. and Walker, B. J., "Comparison of Experiment and Computation for a Missile Base Region Flowfield with a Centered Propulsive Jet," AIAA Paper No. 85-1618, 1985.

6. Venkatapathy, E. and Lombard, C. K., "Accurate Numerical Simulation of Jet Exhaust Flows with CSCM for Adaptive Overlapping Grids," AIAA Paper No. 87-0465, 1987.

7. Sahu, J., "Computations of Supersonic Flow Over a Missile Afterbody Containing an Exhaust Jet," *Journal of Spacecraft*, Vol. 24, No. 5, September-October 1987, pp. 403-410.

8. Hoffman, J. J., Birch, S. F., and Hopcraft, R. G., "Navier-Stokes Calculations of Rocket Base Flows," AIAA Paper No. 87-0466, 1987.

9. Childs, R. E. and Caruso, S. C., "On the Accuracy of Turbulent Base Flow Predictions," AIAA Paper No. 87-1439, 1987.

10. Childs, R. E. and Caruso, S. C., "Assessment of Modeling and Discretization Accuracy for High Speed Afterbody Flows," AIAA Paper No. 89-0531, 1989.

11. Petrie, H. L., "A Study of Compressible Turbulent Free Shear Layers Using Laser Doppler Velocimetry," Ph.D. Thesis, Department of Mechanical and Industrial Engineering, University of Illinois at Urbana-Champaign, Urbana, Illinois, 1984.

12. Petrie, H. L., Samimy, M., and Addy, A. L., "Compressible Separated Flows," *AIAA Journal*, Vol. 24, No. 12, December 1986, pp. 1971-1978.

13. Petrie, H. L., Samimy, M., and Addy, A. L., "Laser Doppler Velocity Bias in Separated Turbulent Flows," *Experiments in Fluids*, Vol. 6, 1988, pp. 80-88.

14. Samimy, M., "An Experimental Study of Compressible Turbulent Reattaching Free Shear Layers," Ph.D. Thesis, Department of Mechanical and Industrial Engineering, University of Illinois at Urbana-Champaign, Urbana, Illinois, 1984.

15. Samimy, M., Petrie, H. L., and Addy, A. L., "A Study of Compressible Turbulent Reattaching Free Shear Layers," *AIAA Journal*, Vol. 24, No. 2, February 1986, pp. 261-267.

16. Samimy, M., Petrie, H. L., and Addy, A. L., "Reattachment and Redevelopment of Compressible Turbulent Free Shear Layers," *ASME International Symposium on Laser Anemometry*, FED-Vol. 33, November 1985, pp. 159-166.

17. Samimy, M. and Addy, A. L., "Interaction Between Two Compressible, Turbulent Free Shear Layers," *AIAA Journal*, Vol. 24, No. 12, December 1986, pp. 1918-1923.

18. Cortright, E. M., Jr. and Schroeder, A. H., "Investigation at Mach Number 1.91 of Side and Base Pressure Distributions Over Conical Boattails without and with . Flow Issuing from Base," NACA RM E51F26, Septe ber 1951.

19. Fuller, L. and Reid, J., "Experiments on Two-Dimensional Base Flow at M=2.4," Royal Aircraft Establishment Report No. Aero 2569, February 1956.

20. Reid, J. and Hastings, R. C., "The Effect of a Central Jet on the Base Pressure of a Cylindrical Afterbody in a Supersonic Stream," Royal Aircraft Establishment Report No. Aero 2621, December 1959.

21. Maxwell, B. R. and Seasholtz, R. G., "Velocity Lag of Solid Particles in Oscillating Gases and in Gases Passing Through Normal Shock Waves," NASA TN D-7490, March 1974.

22. Walsh, M. J., "Influence of Particle Drag Coefficient on Particle Motion in High-Speed Flow with Typical Laser Velocimeter Applications," NASA TN D-8120, February 1976.

23. McLaughlin, D. K. and Tiederman, W. G., "Biasing Correction for Individual Realization of Laser Anemometer Measurements in Turbulent Flows," *Physics of Fluids*, Vol. 16, No. 12, December 1973, pp. 2082-2088.

24. Buchhave, P., "Biasing Errors in Individual Particle Measurements with the LDA-Counter Signal Processor," Proceedings of the LDA-Symposium, Copenhagen, Denmark, 1975, pp. 258-278.

25. Karpuk, M. E. and Tiederman, W. G., "Effect of Finite-Size Probe Volume Upon Laser Doppler Anemometer Measurements," *AIAA Journal*, Vol. 14, No. 8, August 1976, pp. 1099-1105.

26. Amatucci, V. A., "An Experimental Investigation of the Two-Stream, Supersonic, Near-Wake Flowfield Behind a Finite-Thickness Base," Ph.D. Thesis, Department of Mechanical and Industrial Engineering, University of Illinois at Urbana-Champaign, Urbana, Illinois, 1990.

27. Kuntz, D. W., "An Experimental Investigation of the Shock Wave-Turbulent Boundary Layer Interaction," Ph.D. Thesis, Department of Mechanical and Industrial Engineering, University of Illinois at Urbana-Champaign, Urbana, Illinois, 1985.

28. Taghavi, K., "Unsteady Reattachment of Supersonic Flow Past a Backward-Facing Step," M.S. Thesis, Department of Mechanical and Industrial Engineering, University of Illinois at Urbana-Champaign, Urbana, Illinois, 1988.

29. Sun, C.-C. and Childs, M. E., "A Modified Wall Wake Velocity Profile for Turbulent Compressible Boundary Layers," *Journal of Aircraft*, Vol. 10, No. 6, June 1973, pp. 381-383.

30. Sturek, W. B. and Danberg, J. E., "Supersonic Turbulent Boundary Layer in Adverse Pressure Gradient. Part I: The Experiment," *AIAA Journal*, Vol. 10, No. 4, April 1972, pp. 475-480.

31. Sturek, W. B. and Danberg, J. E., "Supersonic Turbulent Boundary Layer in Adverse Pressure Gradient. Part II: Data Analysis," *AIAA Journal*, Vol. 10, No. 5, May 1972, pp. 630-635.

32. Johnson, D. A., "Turbulence Measurements in a Mach 2.9 Boundary Layer Using Laser Velocimetry," *AIAA Journal*, Vol. 12, No. 5, May 1974, pp. 711-714.

33. Kistler, A. L., "Fluctuation Measurements in a Supersonic Turbulent Boundary Layer," *Physics of Fluids*, Vol. 2, No. 3, May-June 1959, pp. 290-296.

34. Rose, W. C., "Turbulence Measurements in a Compressible Boundary Layer," *AIAA Journal*, Vol. 12, No. 8, August 1974, pp. 1060-1064.

35. Chevray, R. and Kovasznay, L. S. G., "Turbulence Measurements in the Wake of a Thin Flat Plate," *AIAA Journal*, Vol. 7, No. 8, August 1969, pp. 1641-1643.

36. Papamoschou, D. and Roshko, A., "Observations of Supersonic Free Shear Layers," AIAA Paper No. 86-0162, presented at the AIAA 24th Aerospace Sciences Meeting, Reno, Nevada, January 1986.

37. Etheridge, D. W. and Kemp, P. H., "Measurements of Turbulent Flow Downstream of a Rearward-Facing Step," *Journal of Fluid Mechanics*, Vol. 86, Part 3, June 1978, pp. 545-566.

38. Delery, J. M., "ONERA Research on Afterbody Viscid/Inviscid Interaction with Special Emphasis on Base Flows," Proceedings of the Symposium on Rocket/Plume Fluid Dynamic Interactions, Vol. III, Huntsville, Alabama, April 1983.

39. Andreopoulos, J. and Bradshaw, P., "Measurements of Interacting Turbulent Shear Layers in the Near Wake of a Flat Plate," *Journal of Fluid Mechanics*, Vol. 100, Part 3, October 1980, pp. 639-668.

40. Ikawa, H. and Kubota, T., "Investigation of Supersonic Turbulent Mixing Layer with Zero Pressure Gradient," *AIAA Journal*, Vol. 13, No. 5, May 1975, pp. 566-572.

41. Ardonceau, P. L., "The Structure of Turbulence in a Supersonic Shock-Wave/Boundary-Layer Interaction," *AIAA Journal*, Vol. 22, No. 9, September 1984, pp. 1254-1262.

42. Chandrsuda, C. and Bradshaw, P., "Turbulence Structure of a Reattaching Mixing Layer," *Journal of Fluid Mechanics*, Vol. 110, September 1981, pp. 171-194.

43. Bradshaw, P. and Wong, F. Y. F., "The Reattachment and Relaxation of a Turbulent Shear Layer," *Journal of Fluid Mechanics*, Vol. 52, Part 1, March 1972, pp. 113-135.

44. Eaton, J. K. and Johnston, J. P., "A Review of Research on Subsonic Turbulent Flow Reattachment," *AIAA Journal*, Vol. 19, No. 9, September 1981, pp. 1093-1100.

45. Birch, S. F. and Eggers, J. M., "A Critical Review of the Experimental Data for Developed Free Turbulent Shear Layers," NASA SP-321, 1972.

46. Settles, G. S., Williams, D. R., Baca, B. K., and Bogdonoff, S. M., "Reattachment of a Compressible Turbulent Free Shear Layer," *AIAA Journal*, Vol. 20, No. 1, January 1982, pp. 60-67.

Fig. 1   Schematic of the near-wake interaction flowfield.

Parameter	Upper Stream	Lower Stream
Mach Number	2.56	2.05
Reynolds Number Based on Momentum Thickness, Re_θ	1.3×10^4	6.2×10^3
Boundary Layer Thickness, δ [mm]	3.349	1.460
Displacement Thickness, δ^* [mm]	0.947	0.393
Momentum Thickness, θ [mm]	0.219	0.118
Wake Strength Parameter, π	0.921	1.121
Friction Velocity, u_τ [m/se]	25.1	21.4
Skin Friction Coefficient, C_f	0.00160	0.00182

Table 1   Properties of the Mach 2.56 and Mach 2.05 turbulent boundary layers.

Fig. 2   Streamwise velocity profiles plotted in wall-wake law coordinates for the turbulent boundary layers.

9
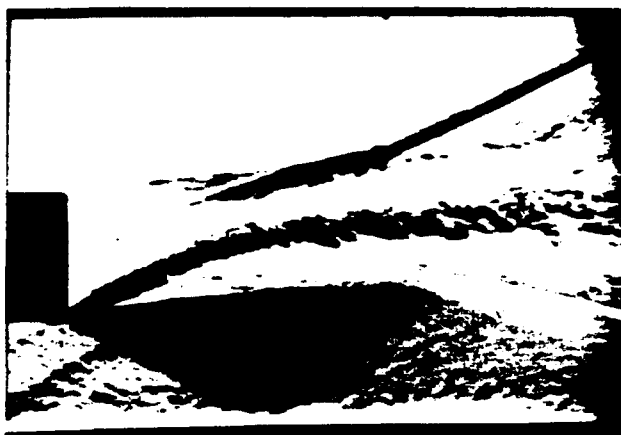
Fig. 3   Schlieren photograph showing the interaction regions
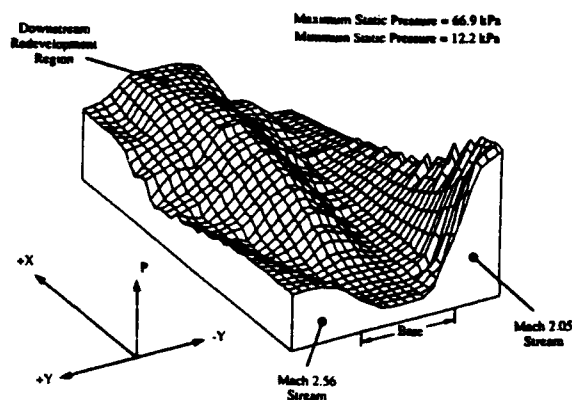   for the near-wake flowfield.

Fig. 6   Streamwise mean velocity profiles for the shear layers
         and the initial part of the recompression region.

Fig. 4   Three-dimensional surface contour representation of
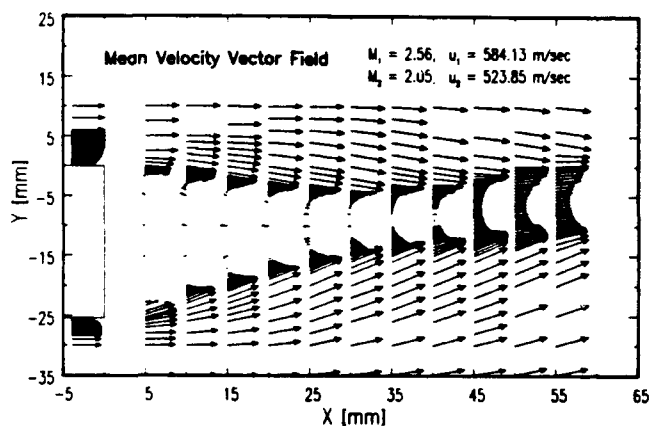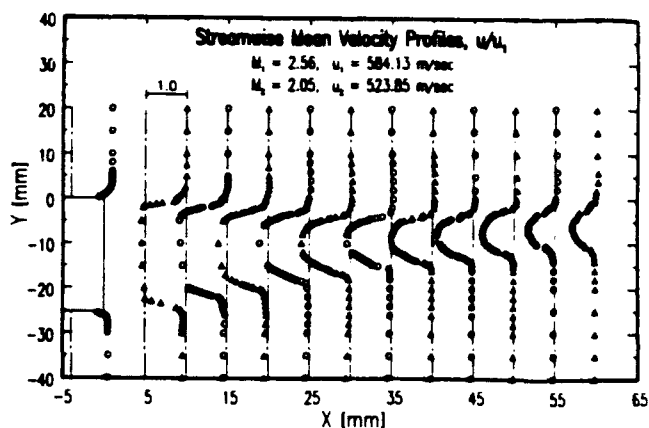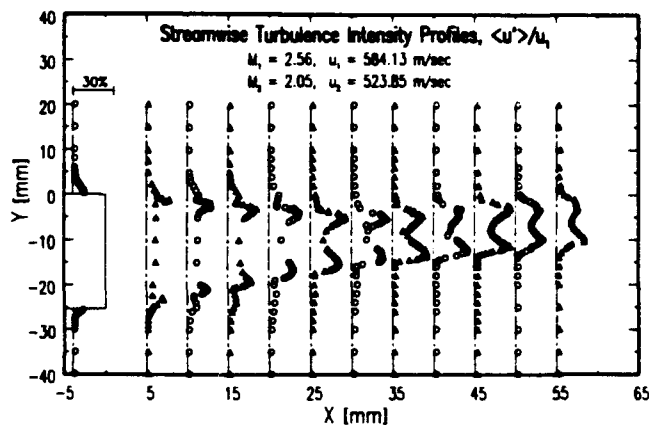   the static pressure field in the near-wake region.

Fig. 7   Streamwise turbulence intensity profiles for the shear
         layers and the initial part of the recompression region.

Fig. 5   Mean velocity vector field for the two-stream
         interaction flowfield.
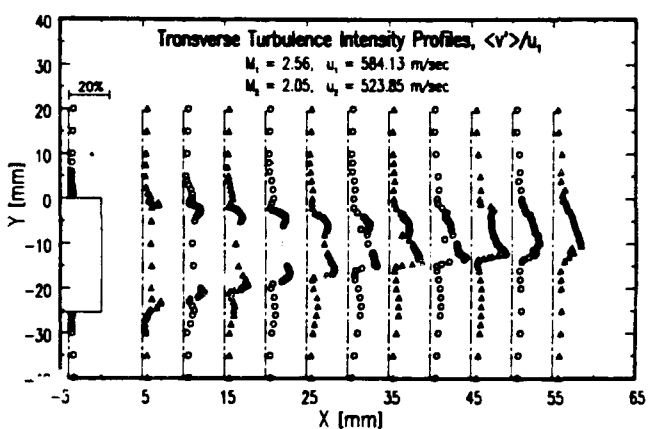
Fig. 8   Transverse turbulence intensity profiles for the shear
         layers and the initial part of the recompression region.
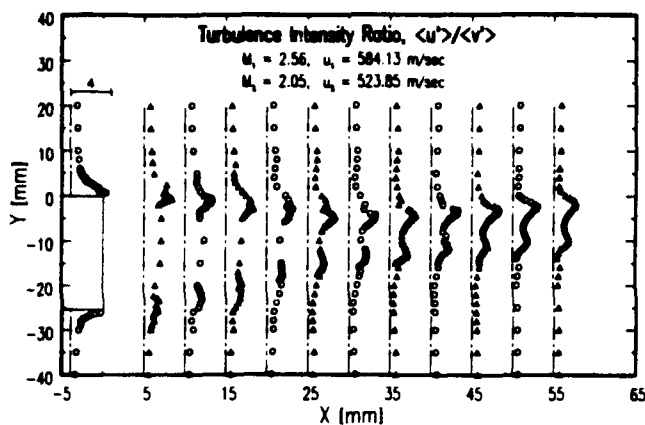
10

Fig. 9   Turbulence intensity ratio profiles for the shear layers
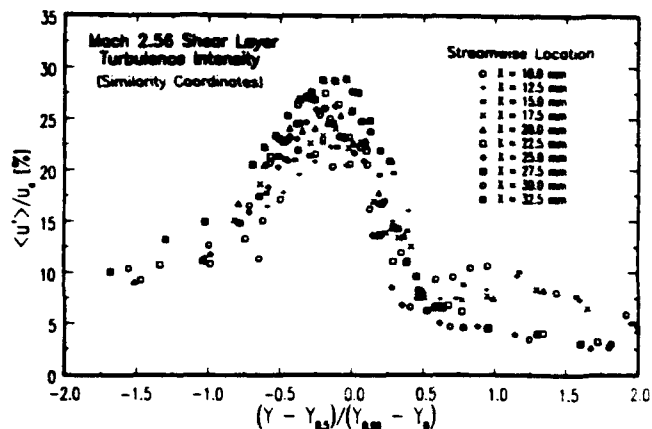and the initial part of the recompression region.

Fig. 12   U-component turbulence intensity profiles for the
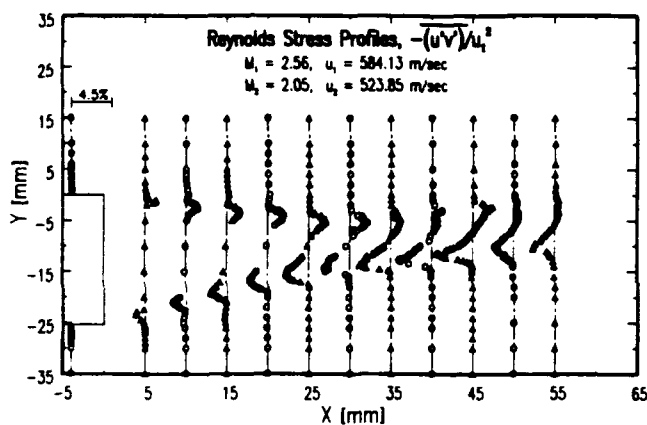upper shear layer plotted in similarity coordinates.

Fig. 10   Kinematic Reynolds stress profiles for the shear
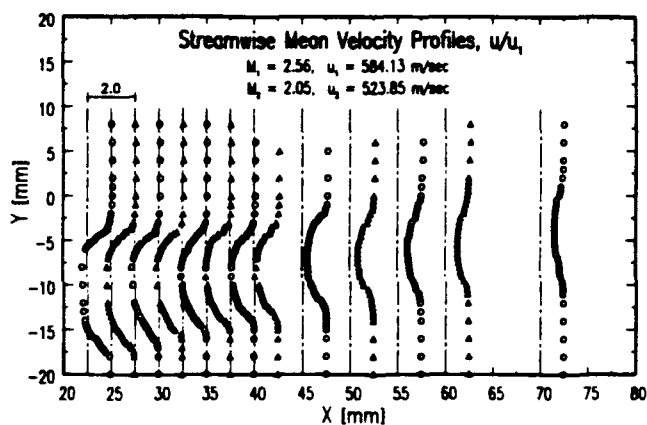layers and the initial part of the recompression region.

Fig. 13   Streamwise mean velocity profiles for the
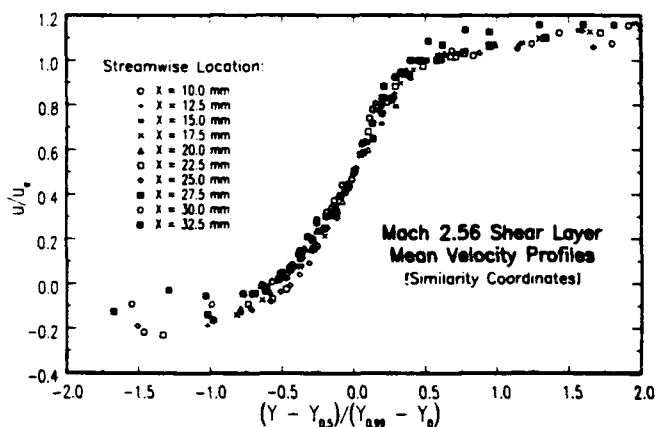recompression and reattachment regions.

Fig. 11   U-component mean velocity profiles for the upper
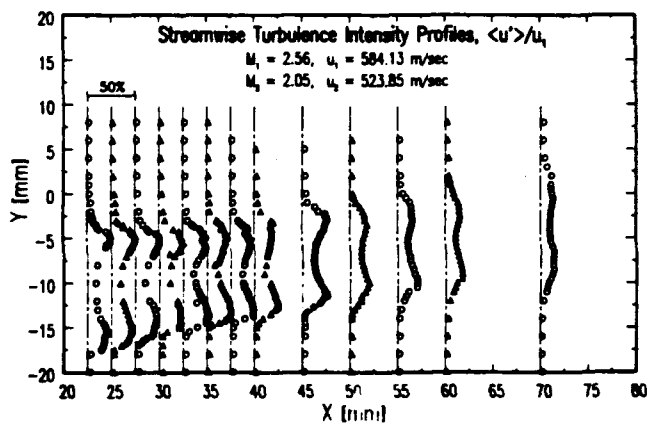shear layer plotted in similarity coordinates.

Fig. 14   Streamwise turbulence intensity profiles for the
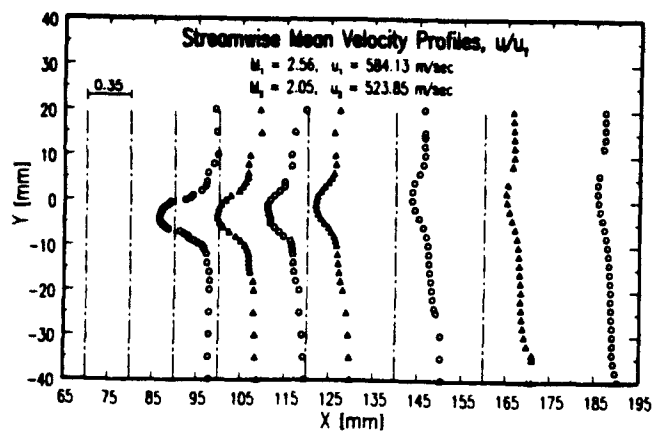recompression and reattachment regions.

11

Fig. 15 Streamwise mean velocity profiles for the downstream redevelopment region.

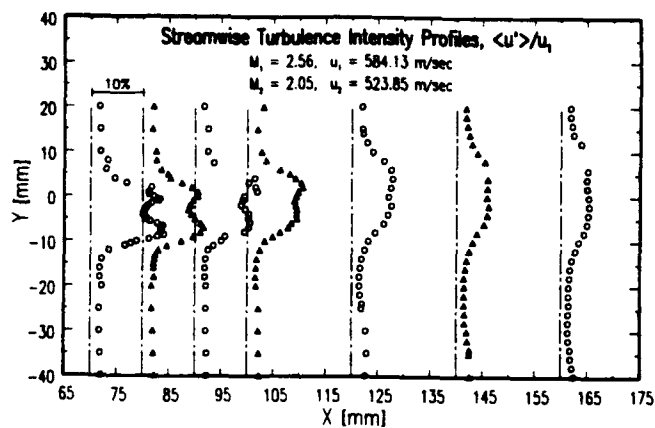Fig. 16 Streamwise turbulence intensity profiles for the downstream redevelopment region.
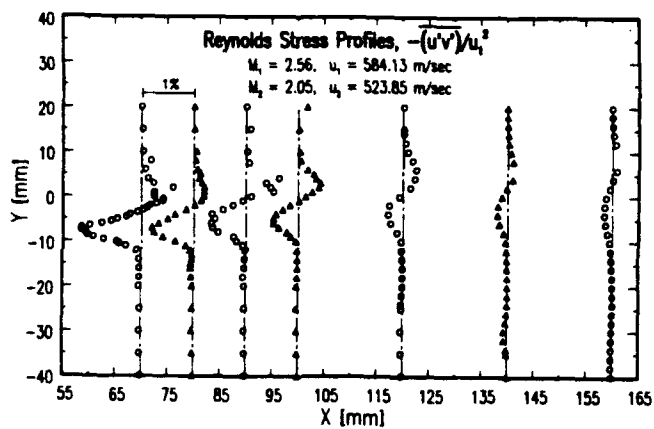
Fig. 17 Kinematic Reynolds stress profiles for the downstream redevelopment region.

APPENDIX A.7

AN EXPERIMENTAL INVESTIGATION OF AXISYMMETRIC POWER-OFF BASE FLOW PHENOMENA

Paper Presented at the AIAA Student Regional Conference

Purdue University

West Lafayette, Indiana

March 1991

by

J. L. Herrin

AN EXPERIMENTAL INVESTIGATION OF AXISYMMETRIC POWER-OFF BASE FLOW PHENOMENA

by

Jeff L. Herrin, Graduate Research Assistant

Department of Mechanical and Industrial Engineering
University of Illinois at Urbana-Champaign
Urbana, Illinois 61801

Supported by

March 1991

Abstract

An experimental program has been conducted to study the flowfield behind a blunt-based body of revolution embedded in a supersonic freestream. The experiments have been conducted in a newly-designed axisymmetric wind tunnel facility at a nominal approach Mach number of 2.5. A cylindrical sting aligned with the axis of the wind tunnel provided the physical model for the study. Qualitative flowfield information was obtained with spark-schlieren photography and surface oil visualization. Mean wall static pressure measurements were made across the base and along the sting parallel to the wind tunnel axis. Nineteen pressure taps were concentrated across the base to properly access the dependence of local base pressure on radial location. The sting boundary layer profile and nozzle exit flow uniformity were measured by a one-component laser Doppler velocimetry (LDV) system. The base pressure measurements indicate only a small dependence on radial location. Interference waves generated at the junction of the nozzle exit and test section were found to have a large effect on the base pressure profile at certain operating conditions but could be eliminated by proper operation of the tunnel.

Nomenclature

C_p dimensionless pressure coefficient, $C_p = \dfrac{2\left(\dfrac{P}{P_\infty} - 1\right)}{\gamma M_\infty^2}$

D base diameter

M Mach number

P static pressure

P_0 total pressure

r radial distance from centerline

R base radius

U axial velocity

X axial distance from nozzle exit, positive downstream

Y vertical distance from sting surface

Greek

δ boundary layer thickness

σ standard deviation of ensemble

Superscripts

$\bullet$ angular degrees

$'$ fluctuation from the mean value

Subscripts

base   referring to blunt base or base plane

cell   test section sudden-expansion region

edge   edge of the boundary layer

exit   nozzle exit plane

matched   matched pressure condition at nozzle exit lip, i.e. $P_{exit} = P_{cell}$

noz   nozzle exit

∞ freestream condition at nozzle exit

AN EXPERIMENTAL INVESTIGATION OF AXISYMMETRIC POWER-OFF BASE FLOW PHENOMENA

Introduction

The pressure which acts on the base of a bluff body traveling through a viscous fluid is known as the base pressure. The fluid separates from the body at or near the base corner setting up a low-speed recirculation region near the base. The pressure in this region is nearly constant and takes a value significantly less than the freestream flow due to the expansion at the corner. This difference in pressure causes an axial component of drag, commonly referred to as base drag, which can account for up to two-thirds of the total drag on a body of revolution [1]. Practical situations where base drag can be significant include missiles, airfoil trailing edges, and nozzle exhaust surfaces.

A general flowfield schematic of supersonic flow over a blunt, axisymmetric body is shown in Figure 1. The approach flow consists of a uniform supersonic flow region and a viscous boundary layer (laminar or turbulent) very near the body of revolution. Near the base corner the flow geometrically separates from the body and a free-shear layer is formed where rapid mixing occurs between the inviscid external stream and the low-speed recirculating flow. The shear layer is concave to the centerline initially but turns outward as the flow approaches the axis of symmetry. Realignment takes place through a recompression region with a rise in pressure to a value above the freestream static pressure due to the axisymmetric nature of the diverging streamlines. This overcompression is the main reason axisymmetric bodies have higher base pressures (lower base drag) than similar two-dimensional bodies. Fluid in the low-speed side of the shear layer is unable to negotiate the adverse pressure gradient imposed during recompression and must reverse direction and return to the base, thus, setting up a relatively low-speed "dead-air region" of recirculating flow. The separated flow region near the base up to recompression is usually referred to as the near wake of the body.

1

In the "power-on" configuration, a central jet is present along the axis of symmetry which greatly reduces the length of the separated flow region. The reduced size of the near wake reduces the problem of wave interference from wind tunnel walls with the sensitive separated flow region. On the other hand, the "power-off" configuration (no central jet) is more succeptible to interference effects but offers more opportunity to accurately resolve the flowfield in the high-gradient regions of the shear layer.

Several researchers have investigated the fundamental problem of axisymmetric base drag. Parametric studies of the effects of Mach number, Reynolds number, and boundary layer thickness on the base pressure have been conducted since the early 1950's [2-6]. Unfortunately, problems such as wind tunnel interference and proper model alignment have plagued base flow researchers and, therefore, make the quality of the subsequent data questionable. Experiments with bodies of revolution have incurred several problems in the proper mounting of the body to avoid interference of the flowfield. In addition, the introduction of instrumentation probes (e.g. pitot-static probes) into the separated flow region has been common, even though it has been shown to disturb the flowfield. Both qualitative and quantitative data has been presented [7-9] which documents the disturbance caused by external waves and probes.

Due to the apparent lack of quality experimental base flow data on bodies of revolution, an axisymmetric base flow program has been undertaken in the University of Illinois Gas Dynamics Laboratory. The objectives of this program include the complete documentation of an interference-free, truly axisymmetric flowfield behind a cylindrical body of revolution embedded in a supersonic freestream. Initially, only the power-off configuration will be investigated. The intent of this research is not to reproduce the parametric studies common in the literature but, rather, to identify the dominant fluid dynamic mechanisms inherent in these complex flows. This will be a large step in devising new base pressure control methods to reduce base drag. Flowfield documentation will include qualitative flow visualization as well as detailed, non-intrusive mapping of the

2

velocity field in the near-wake region. This paper discusses the design of the interference-free, supersonic wind tunnel and the initial experiments in the program which include schlieren photography, surface oil visualization, static pressure measurements, and approach flowfield documentation.

Experimental Apparatus and Preliminary Experiments

The current experimental investigation was conducted in a supersonic, blow-down type wind tunnel designed solely for the study of axisymmetric base flows. A schematic of the basic features of the facility is provided in Figure 2. A hollow sting extends upstream through the stagnation chamber and nozzles to provide a physical mounting surface for the bases under study. For the current investigation, only cylindrical bases (no boattail) were used. Following the advice of Koh [10], the two sting supports were positioned upstream of the nozzle entrance to avoid any support disturbances in the flowfield. The far-upstream support is a Dodge taper lock that closes symmetrically around the sting to aide in its alignment along the axis. As will be discussed later in this report, the taper lock was insufficient as the only means to properly center the sting within the nozzle. Optical access to the flowfield was achieved by two rectangular side plates of optical-quality glass.

The axisymmetric, supersonic nozzle takes on an annular cross section with the central sting in place. The method of characteristics for irrotational, supersonic, axisymmetric flow was used in the nozzle design to design to produce a uniform Mach 2.5 flow with the central sting [11]. Displacement effects due to boundary layer growth on the sting and nozzle surfaces reduce the actual nozzle exit Mach number to 2.46. The freestream Reynolds number based on the base diameter was 10^7. Prior to entrance into the nozzle, the flow passes through a flow conditioning section inserted into the stagnation chamber. The screen-honeycomb-screen combination is used to effectively damp out any large-scale turbulence generated in the air supply to the nozzle.

3

The geometry of the test section is such that the nozzle exit flow undergoes a sudden expansion radially outward as it enters the test section. Figure 3 is a diagram of the junction between the nozzle exit lip and the test section. This location is the most likely cause for any interference with the base flowfield; therefore, several experiments were conducted to investigate methods of reducing or eliminating any interference waves produced by this junction. The location of static pressure taps on both sides of the junction allowed for direct measurement of the pressure differential at the nozzle exit. With the nozzle operating in the overexpanded state, a compression wave is generated at the nozzle exit lip that may or may not intersect the separated flow region downstream of the base. Conversely, an underexpanded nozzle condition causes an expansion wave (fan) at the nozzle exit lip.

To eliminate interference waves, it was necessary to devise a means to make the pressure differential vanish at the operating condition of the tunnel. Sauter [12] describes one such method: mass injection/removal into the separated flow region of the test section in order to raise/lower the pressure. Unfortunately, the existing base flowfield was shown to be adversely affected by the mass transfer causing an open wake downstream of the base. That is to say, the separated "dead-air" region was not closed off by the recompression region and, therefore, extended far downstream of the undisturbed point. After reviewing these previous attempts to equalize the nozzle exit pressures, a passive pressure control method was examined. By varying the pressure in the plenum chamber of the wind tunnel, it was found that the pressure differential at the nozzle exit lip reacted in a linear fashion passing through zero (equal pressures) at some value of stagnation pressure. The pressure differential as a function of stagnation pressure is shown in Figure 4. By operating the wind tunnel at the "matched pressure" condition, any interference waves from the critical nozzle exit-test section junction could be eliminated. The pressure measurements described were well supported by spark-schlieren photographs of the different nozzle operating conditions. Representative photographs are shown in Figure 5

4

for underexpanded, overexpanded and perfectly expanded nozzle exit flow. The interference waves are clearly visible for all cases except the matched pressure case.

The effect of interference waves on the average base pressure was also investigated. Figure 6 presents the non-dimensional base pressure coefficient as a function of the stagnation pressure. As discussed above, different values of P_O correspond to different strengths and types of interference waves from the nozzle exit lip. It is seen that whenever the interference wave is a compression wave (shock wave), the base pressure is altered to higher values, the effect being more pronounced as the shock wave strength increases (i.e. nozzle exit flow more overexpanded). On the other hand, an interference expansion wave $(P_O > P_{matched})$ causes little change in the base pressure. The discrepancy between the two wave types is thought to be only a matter of where the waves intersect the separated base flow region. The composition of the interference wave, in other words, is not necessarily the major factor is determining base pressure dependence.

In a similar study of wind tunnel interference effects behind bodies of revolution, Hawkins and Trevett [9] indicate that any interference wave intersecting the recirculation region upstream of a "critical-interaction point" affected the structure of the flowfield and, consequently, the base pressure. This critical point was found to lie very close to the sonic point of the developing wake for Mach numbers above 1.9 as determined by pitot probe traverses along the centerline. Therefore, in the current study it is suggested that all compression interference waves generated by the nozzle lip intersect the recirculation region upstream of the sonic point. As P_O decreases the compression shock becomes steeper with respect to the wind tunnel axis and, therefore, intersects the base flow region further upstream causing increased interference (higher base pressures). As P_O increases to the matched pressure condition, the shock wave fades into an interference wave of infinitesimal strength and then into an expansion fan at higher stagnation pressures. The leading interference wave of the expansion fan is just the local Mach line determined only by the local flow Mach number. Consequently, the leading interference wave of any nozzle lip

5

expansion fan has a constant angle with respect to the wind tunnel axis and intersects the base flowfield at a fixed location. In the current study, apparently, the intersection point is very near or slightly downstream of the sonic point in the developing wake. From schlieren photographs, this critical interaction distance was measured to be 2.0 base diameters downstream of the base.

Proper centering of the sting within the nozzle is imperative for truly axisymmetric flow behind a blunt base. Unfortunately, this has been a recurring problem in axisymmetric base flow research. Even though careful steps had been taken in the wind tunnel fabrication process of the current study, an additional method to ensure concentricity between the sting and nozzle was found to be necessary. To meet this end, four nozzle adjusting blocks were installed. These blocks allow for the translation of the nozzle and test section vertically or horizontally without changing the position of the upstream-supported sting. The degree of concentricity is checked by applying a mixture of viscous oil and lampblack on the base and then running the wind tunnel at the chosen operating condition. The symmetry of the resulting oil streak pattern is used as an indicator of whether or not the sting is properly centered. If any asymmetry exists in the oil-streak pattern, the position of the nozzle and test section is adjusted and the process is repeated. The oil-streak pattern on the base for a "centered" sting is shown in Figure 7. The trial-and-error centering process has shown the base flow symmetry to be extremely sensitive to the sting position within the nozzle. For example, a nozzle/test section translation of 0.010" can cause a movement in the base symmetry point of up to 1.0". The physical location of the sting relative to the nozzle throat and nozzle exit plane was measured after the most-symmetric oil-streak pattern had been obtained. Interestingly, the sting and nozzle were very concentric at the throat but not at the nozzle exit, even though the oil-streak patterns indicated axisymmetric flow at the base. The uniformity of the transonic flow near the throat is, therefore, thought to be highly dependent on the physical symmetry in that region and can greatly affect the symmetry of the supersonic flowfield exiting the nozzle.

Instrumentation

In addition to the surface oil-streak visualizations described above, schlieren photography, static pressure measurements, and laser Doppler velocimetry were used to document the supersonic, axisymmetric base flowfield. All experimental data was taken with the wind tunnel operating in the matched-pressure condition (i.e. no nozzle exit lip interference) with a sting/nozzle position which yielded a symmetric oil-streak pattern along the base.

Spark-schlieren photographs were taken of the base flowfield using a 1.4 μs duration light source with the knife edge both horizontal and vertical to the flow direction. Schlieren photography relies on the existence of density gradients in the flowfield to bend light rays. The resulting light intensity distribution far away from the wind tunnel is then indicative of the density gradient distribution in the flowfield. The primary advantage of the pulsing light source is the capability to avoid photographic smearing by "freezing" the flow at an instant in time. Photographs were taken for several different operating conditions to investigate the qualitative structure of the flowfield.

Static pressure measurements were taken at various locations on the base and nozzle using a Pressure Systems Inc. Digital Pressure Transmitter (Model 6400-T). Nineteen 0.025" diameter pressure taps were located symmetrically across the base to measure the radial dependence and symmetry of the base pressure. From this data, a local base pressure coefficient was calculated for each pressure tap location. An area average was then performed to yield an average base pressure coefficient which could be compared to base pressure data from previous investigations. In addition to base pressure taps, static pressures were also measured upstream of the base along the sting surface. Five static pressure taps separated by 0.125" were located 180° apart on the sting periphery such that the taps furthest downstream were 0.094" from the base corner. These taps were used to document the static pressure field of the supersonic approach flow. Also, local Mach

7

numbers were calculated assuming isentropic flow from the stagnation chamber pressure. A diagram showing the relative location of the static pressure taps is provided in Figure 8. As described above, eight static pressure taps were placed around the periphery of the nozzle exit and in the test section region to measure the pressure differential at the nozzle exit lip.

The shape of the approach boundary layer was measured by a laser Doppler velocimeter. In order to make measurements close to the sting surface, a one-component arrangement was utilized. Laser Doppler velocimetry (LDV) is a laser-based technique that measures the instantaneous velocity of small particles suspended throughout the flowfield by detecting the Doppler frequency shift of the laser light. A small volume defined by the intersection of two focused laser beams acts as the measurement location for the fluid velocity. As the volume is traversed around the flowfield, a velocity map can be created that intimately describes the flowfield. The non-intrusive nature of LDV offers a significant advantage over other velocity measurement tools. In addition, LDV is capable of discriminating the flow direction which is a necessity in separated flows.

The effective dimensions of the measurement volume and other pertinent data concerning the LDV system are given in Table 1. A schematic diagram of the LDV optical configuration is shown in Figure 9. Since the natural particles existing in the air were too small and few in number to serve as scattering media, an artificial seeding method was necessary. A Thermal Systems Inc. 6-Jet Atomizer with silicone oil as the atomized fluid was used to produce the small particles that were then injected into the flowfield just upstream of the converging nozzle. This combination of atomizer and seeding material has been shown to produce a polydisperse particle size distribution centered at 0.8 μm [13]. Also, recent experiments in the Gas Dynamics Laboratory [14] have shown that particle dynamics effects are minimized when using atomized silicone oil as a seeding media. For this reason, it is believed that in the current investigation the artificial seed accurately

8

follows the flowfield, and velocities of the particles (measured) are the same as the velocity of the local fluid (inferred).

The approach boundary layer was measured with the LDV 8 mm downstream of the nozzle exit along the sting surface. The uniformity of the nozzle exit flow was also determined by traversing the measurement volume vertically across the nozzle exit. In all cases, only the streamwise component of velocity was measured. More than 2000 data samples were gathered at each measurement location and were subsequently reduced into mean and fluctuating velocities by ensemble averaging. A 1-D inverse-velocity bias correction was applied to eliminate any velocity bias in the data. Also, a software filter was used to remove any "bad" data points by specifying a $\pm 5\sigma$ requirement on the ensemble. Since the direction of the flow was almost certainly known prior to taking the data, a method to discriminate flow direction (optical frequency shifting) was not utilized thus simplifying the optical setup. Scattered laser light was collected in an off-axis, forward-scatter configuration located 10° from the transmitted laser beam axis in order to reduce the effective length of the measurement volume. A counter processor converted the scattered light intensity distribution into Doppler frequency by counting the time for 8 cycles of the signal to cross a pre-set threshold. The resolution of the internal counter clock was 10^{-9} seconds.

Results

Schlieren photography was consistently used to grasp the qualitative structure present in the axisymmetric flowfield. Figure 10 is a schlieren photograph of the wind tunnel flowfield at the chosen operating condition for these experiments. Several basic features of the flow are clearly visible including the base corner expansion fan, the merging free-shear layers (actually conical in nature), and the recompression shock system. Also, the separated flow in the expanded test section regions are seen at the top and bottom of the photograph. The base corner expansion waves reflect off these upper and lower shear

9

layers as compression waves which coalesce to form an oblique shock wave directed toward the centerline. This phenomenon is strictly a wind tunnel effect; therefore, the reflected oblique shock wave defines the downstream boundary for any interference-free data taken in the wind tunnel. The lack of detailed clarity in the schlieren photographs was due to the axisymmetric nature of the wind tunnel. Since schlieren photography depends on the bending of light rays across the wind tunnel span, it is ideally suited for two-dimensional flowfields where only streamwise and transverse density gradients are significant. In axisymmetric flows, gradients exist in all Cartesian coordinate directions (x,y,z), so the spanwise integration of light rays results in background smearing and loss of detail in the photographs.

Since base pressure data alone is meaningless, it is important to quantify the approach flow conditions. In the current investigation, LDV traverses across the nozzle exit yielded information on the freestream velocity as well as the boundary layer profile. Figure 11 is a plot showing the variation in Mach number across the nozzle exit assuming isoenergetic flow from the stagnation chamber. The freestream Mach number was very uniform at $M_\infty = 2.46 \pm 1\%$. Again, the slight discrepancy from the design Mach number of 2.5 is due to the displacement effects of the sting and nozzle boundary layers. The freestream Mach number determined by the LDV was verified by static pressure data near the nozzle exit assuming an isentropic expansion through the nozzle. Measured turbulence intensities in the uniform flow region were consistently less than 1% with little variation across the nozzle exit. Hence, the flow conditioning screens and honeycomb upstream of the nozzle entrance were successful in damping out the large-scale turbulence created in the stagnation chamber.

Boundary layer data was obtained 8 mm downstream of the nozzle exit on the central sting. The non-dimensional velocity profile is shown in Figure 12 along with the curve fit of Sun and Childs for compressible, turbulent boundary layers [15]. A least-squares routine was used to provide the "best" fit to the experimental data. The

10

compressible displacement thickness, momentum thickness and shape factor were subsequently calculated by numerical integration assuming an adiabatic wall with a recovery factor of 0.89 [16]. A complete listing of the resulting boundary layer parameters described above is provided in Table 2. The shape of the velocity profile indicate a turbulent boundary layer approached the base. The turbulence intensities throughout the boundary layer are shown in Figure 13. Maximum levels of 10% relative to the freestream velocity were measured very near the wall (Y=0.18mm). Measurements below Y=0.18 mm were not possible due to increased noise levels from laser reflection off the sting surface as well as insufficient seeding.

In addition to documenting the approach velocity field, static pressure measurements were made along the sting surface to quantify the pressure field near the base corner. Figure 14 shows the average pressure field approaching the base plane. Each data point displayed is an average of two pressure taps located the same distance from the base plane but 180° apart on the sting surface. The pressure data reflects the upstream influence of the strong expansion at the base corner. The rise in pressure near the base begins approximately 2.5 boundary layer thicknesses upstream of the base corner. This appears to contradict the classical theory of a decreasing pressure field due to the lower base pressure feeding upstream through the subsonic portion of the boundary layer. The rising-pressure trend in the current investigation is yet unexplained, although it is consistent on both sets of diametrically-opposed pressure taps.

In order to extract meaningful data from the existing wind tunnel, the measured base pressure should be independent of the axial position of the sting. Axial translation of the base into the nozzle should have no effect on the base pressure as long as the base plane still lies in the uniform flow region defined by the characteristic mesh of the supersonic nozzle. By demonstrating the independence of base pressure with sting position, the wind tunnel effects on the base flowfield can be shown to be negligible. The average base pressure normalized by the freestream static pressure is shown in Figure 15 for a variety of

11

axial base positions near the nozzle exit. The experimental data of Lilienthal, et al. [11] from an earlier investigation that used the same nozzle but a different sting is also included for comparison. The maximum deviation in base pressure ratio is approximately 4% of the value at the nozzle exit, so within the axial distances shown in Figure 15, the base pressure is nearly independent of the sting position. The slight increase in pressure as the base is translated into the nozzle may be associated with some asymmetry in the base flow patterns. Base oil-streak patterns were used to center the sting only when the base plane coincided with the nozzle exit plane. Hence, only the flow at the nozzle exit is known to be truly axisymmetric. Nonetheless, the effect of any asymmetry created as the base was pulled into the nozzle had only a small effect on the average base pressure ratio.

Documenting the static pressure profile across the cylindrical base has importance in analytical and computational modelling of these flows. Early theories assumed the entire recirculation region to be of constant pressure, the value being defined by the expansion fan at the corner. For simplicity, the expansion at the corner of a body of revolution was assumed to be two dimensional in order that the well-known Prandtl-Meyer relations could be used. In fact, the corner expansion is not two dimensional but curved due to the axisymmetric nature of the flow. Zumwalt [5] observed from schlieren photographs that the free-shear layer and outer inviscid flow in the base region take a conical shape. For this reason, he abandoned the constant-pressure assumption in the recirculation region in favor of the pressure distribution of a potential flow over a rearward-facing cone. Unfortunately, it is difficult to make pressure measurements in this region without disrupting the flowfield, so no convincing experimental data is available to confirm this theory.

The base pressure profile across the inner 90% of the base is shown in Figure 16. The non-dimensional base pressure coefficient is shown to be relatively independent of base radius and takes an average value of -0.10. Free-flight experimental data of Charters [17] suggests $C_p=-0.11$ at Mach 2.5. The asymmetric increase in C_p on one side of the base may suggest a slight misalignment in sting position at the nozzle exit. Even though

12

the oil-streak pattern was symmetric at this location, it was shown to be extremely sensitive to sting position; consequently, a small, unplanned alteration in position could have occured during the experimental process causing the asymmetry shown in Figure 16. In addition, the pressure differential across the nozzle exit was not entirely symmetric which may suggest interference waves emanating from some local regions around the periphery even though the average pressure differential is near zero. This localized interference would tend to increase the base pressure at the point of intersection with the recirculation region, therefore causing an asymmetry such as is shown in the base pressure profile. Once again, the difficulty in producing an interference-free flowfield that accurately simulates the free-flight conditions has consistently plagued base flow researchers. The effort in the present investigation to fully eliminate any wind tunnel effects has been largely successful, but the data suggests that continued scrutiny as to the origin of these effects must continue throughout the current investigation as well as throughout any base flow investigation in the future.

Conclusions

A list of the major conclusions that can be drawn from the experimental program described in this paper include:

1. Extreme care must be taken to properly center the sting in any axisymmetric wind tunnel experiments. In the current study, nozzle positioning blocks provided good control of relative sting position such that an axisymmetric base flowfield could be produced.

2. Base oil-streak visualization has proven to be an effective method to properly assess the symmetry of the flowfield downstream of the base.

3. Proper physical alignment at the nozzle throat is the controlling factor in creating a axisymmetric flowfield downstream of the nozzle exit.

13

4. Interference waves emanating from the nozzle exit could be effectively eliminated by properly choosing the stagnation pressure in the plenum chamber.

5. The effect of any interference wave intersecting the base flowfield upstream of the critical interaction point in the developing wake was to increase the base pressure. Interference waves intersecting the flow downstream of this point had no effect on the base pressure.

6. Flow conditioning by a screen-honeycomb-screen combination in the stagnation chamber produced a uniform flowfield with freestream turbulence intensities below 1%.

7. The upstream influence of the base corner expansion was to increase the static pressure starting 2.5 boundary layer thicknesses upstream of the base.

8. Non-dimensional base pressures are nearly independent of radial position on the base.

Acknowledgments

References

1. Chapman, D.R., "An Analysis of Base Pressure at Supersonic Velocities and Comparison with Experiments," NACA Report 1051, 1951.

2. Reid, J. and Hastings, R.C., "Experiments on the Axi-Symmetric Flow over Afterbodies and Bases at M=2.0." Report No. Aero 2628, October 1959, Royal Aircraft Establishment, Farnbourough, England.

3. Badrinarayanan, M.A., "An Experimental Investigation of Base Flows at Supersonic Speeds," Journal of the Royal Aeronautical Society, Vol. 65, July 1961, pp. 475-482.

4. Valentine, D.T. and Przirembel, C., "Turbulent Axisymmetric Near-Wake at Mach Four with Base Injection," AIAA Journal, Vol. 8, No. 2, December 1970, pp. 2279-2280.

5. Zumwalt, G.W., "Analytical and Experimental Study of the Axially-Symmetric Supersonic Base Pressure Problem," Ph.D. Thesis, Department of Mechanical and Industrial Engineering, University of Illinois at Urbana-Champaign, 1959.

6. Avidor, J.M. and Schneiderman, A.M., "Experimental Investigation of High Reynolds Number Compressible Axisymmetric Turbulent Wakes," AIAA Journal, Vol. 13, No. 4, April 1975, pp. 485-489.

7. Dayman, B., Jr., "Support Interference Effects on the Supersonic Wake," AIAA Journal, Vol. 1, No. 8, August 1963, pp. 1921-1923.

8. Donaldson, I.S., "The Effect of Sting Supports on the Base Pressure of a Blunt-Based Body in a Supersonic Stream," The Aeronautical Quarterly, Vol. 6, August 1955, pp. 221-229.

9. Hawkins, R. and Trevett, E.G., "Changes in the Flow at the Base of a Bluff Body Due to a Disturbance in its Wake," AGARD Report 539, May 1966.

10. Koh, J.C.Y., "A New Wind Tunnel Technique for Providing Simulation of Flight Base Flow," AIAA-71-268, 1971.

11. Lilienthal, P.F., Brink, D.F. and Addy, A.L., "Experimental Program for the Study of Supersonic and Transonic Axisymmetric Base-Pressure Problems," Department of Mechanical and Industrial Engineering Report, University of Illinois at Urbana-Champaign, Contract No. DA-01-021-AMC-13902(Z), Urbana, Illinois, 1970.

12. Sauter, J.M., "Design of an Axisymmetric Supersonic Wind Tunnel and Experimental Study of Supersonic, Power-off Base Flow Phenomena," M.S. Thesis, Department of Mechanical and Industrial Engineering, University of Illinois at Urbana-Champaign, March 1989.

13. Petrie, H.L., "A Study of Compressible Turbulent Free Shear Layers Using Laser Doppler Velocimetry," Ph.D. Thesis, Department of Mechanical and Industrial Engineering, University of Illinois at Urbana-Champaign, April 1984.

14. Bloomberg, J.E., "An Investigation of Particle Dynamics Effects Related to LDV Measurements in Compressible Flows," M.S. Thesis, Department of Mechanical and Industrial Engineering, University of Illinois at Urbana-Champaign, September 1989.

15. Sun, C.C. and Childs, M.E., "A Modified Wall Wake Velocity Profile for Turbulent Compressible Boundary Layers," AIAA Journal of Aircraft, Vol. 10, No. 6, June 1973, pp. 381-383.

16. Kays, W.M. and Crawford, M.E., "The Turbulent Boundary Layer for a Gas with Variable Properties," Convective Heat and Mass Transfer, 2nd ed., McGraw-Hill, New York, 1980, pp. 305-309.

17. Charters, A.C. and Turetsky, R.A., "Determination of Base Pressure from Free-Flight Data," Report 653, March 1948, Aberdeen Ballistic Research Laboratory.

Table 1   LDV System Technical Data

Laser: Spectra-Physics 5 Watt argon-ion using the green line (514.5nm)

Transmitting Optics: TSI one-component system without optional frequency shifting

Measurement Volume:
    beam diameter = 1.38mm
    beam spacing=22.0mm
    focal length=360.1mm
    fringe spacing=0.00843mm
    measurement volume diameter=0.171mm
    effective length=2.39mm
    number of fringes=20

Receiving Optics: standard TSI receiving module with 250mm focal length receiving lens and 0.25mm pinhole, positioned 10 degrees off the forward scatter axis

Signal Processing: TSI Model 1990B frequency counter requiring 8 fringes for a valid burst

Computer: Digital Equipment Corporation PDP 11/73 with Direct Memory Access (DMA) interface

Seeder: TSI six-jet atomizer running at 75 psi supply pressure

Traversing Table: standard optical breadboard with a DISA electronic drive in two directions and manual positioning in the other (vertical); vertical positioning accuracy of 0.05mm by digitally-coded linear scale

Table 2   Sting Boundary Layer Parameters

Measurement Location: 8 mm downstream of nozzle exit

Boundary Layer Thickness: δ=3.2 mm

Compressible Displacement Thickness: δ^*=0.95 mm

Compressible Momentum Thickness: θ=0.25 mm

Shape Factor: H=3.78

Friction Velocity: u_τ=20.9 m/s

Skin Friction Coefficient: C_f=0.00146
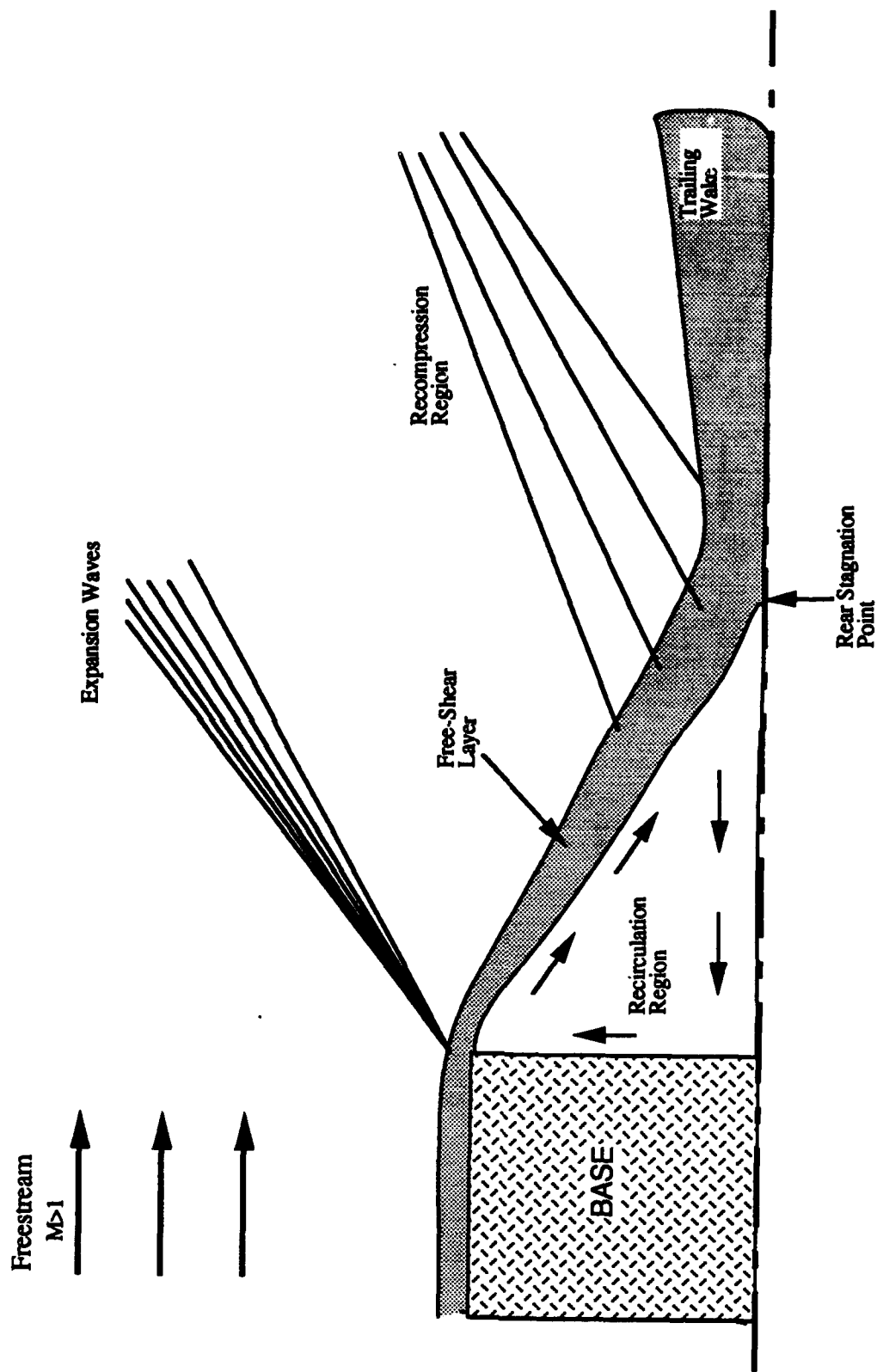
Coefficient of Wake Function: Π=1.41

Figure 1 Diagram of Supersonic Flow over an Axisymmetric Blunt-Based Body
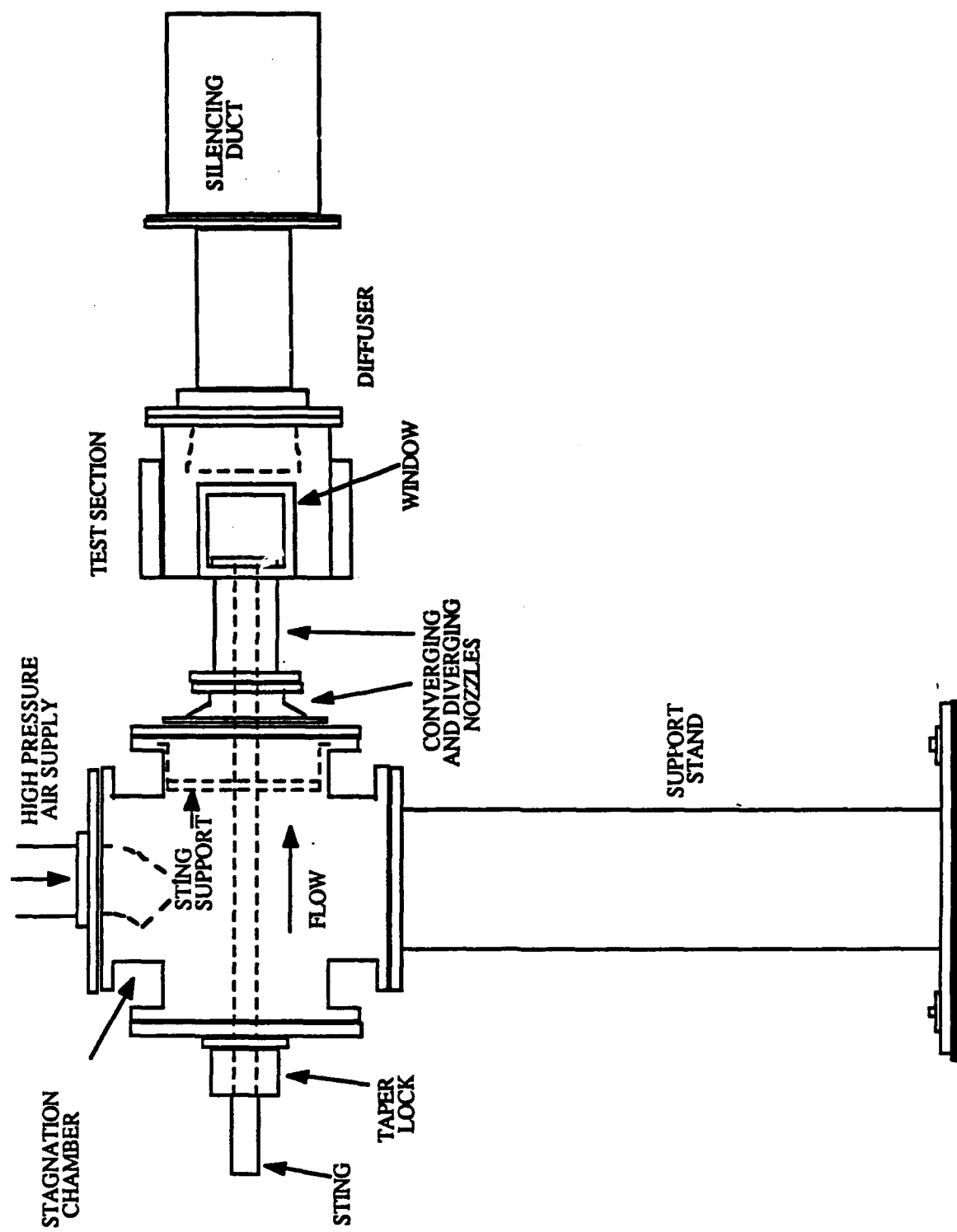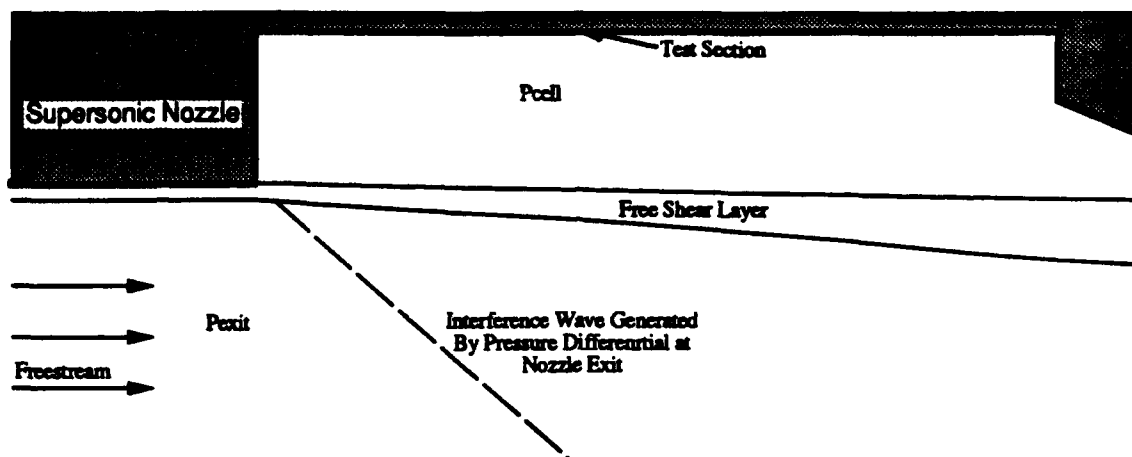
Figure 2 Detailed Sketch of Axisymmetric Wind Tunnel

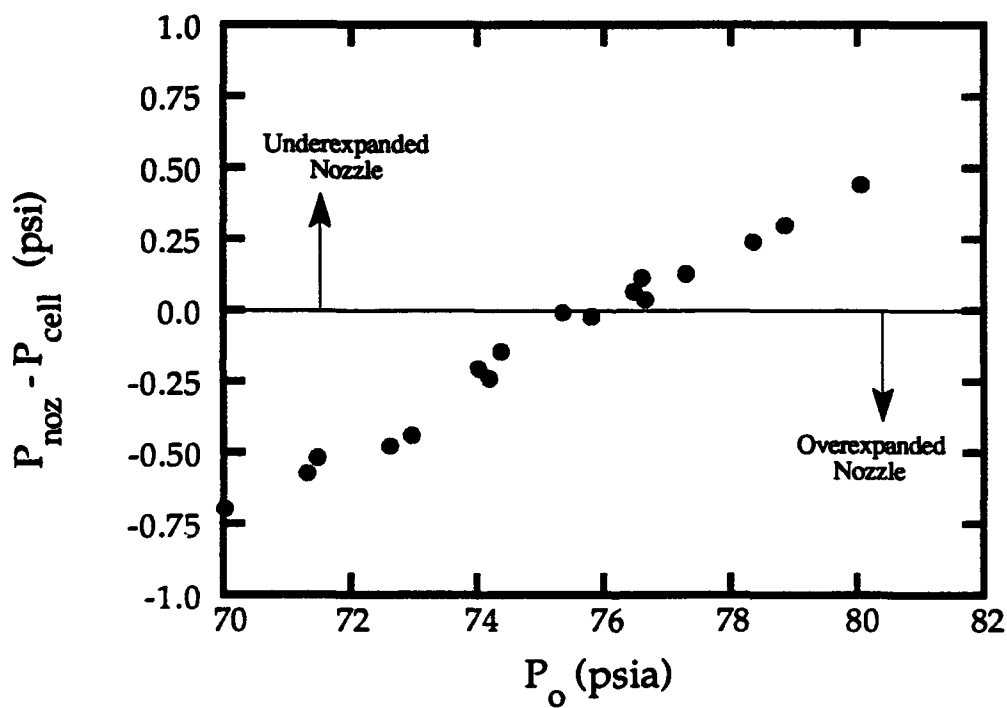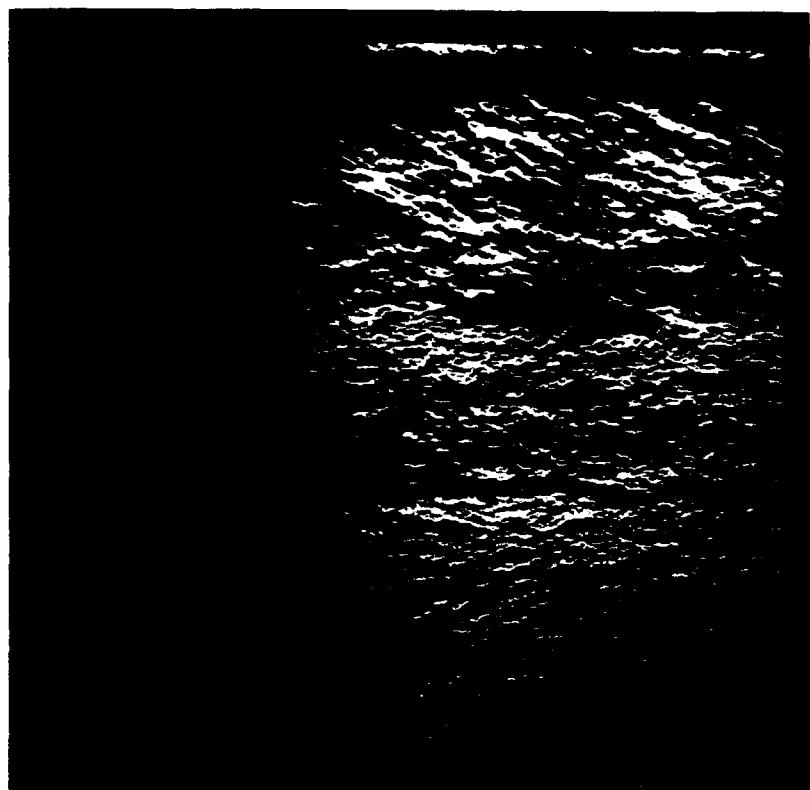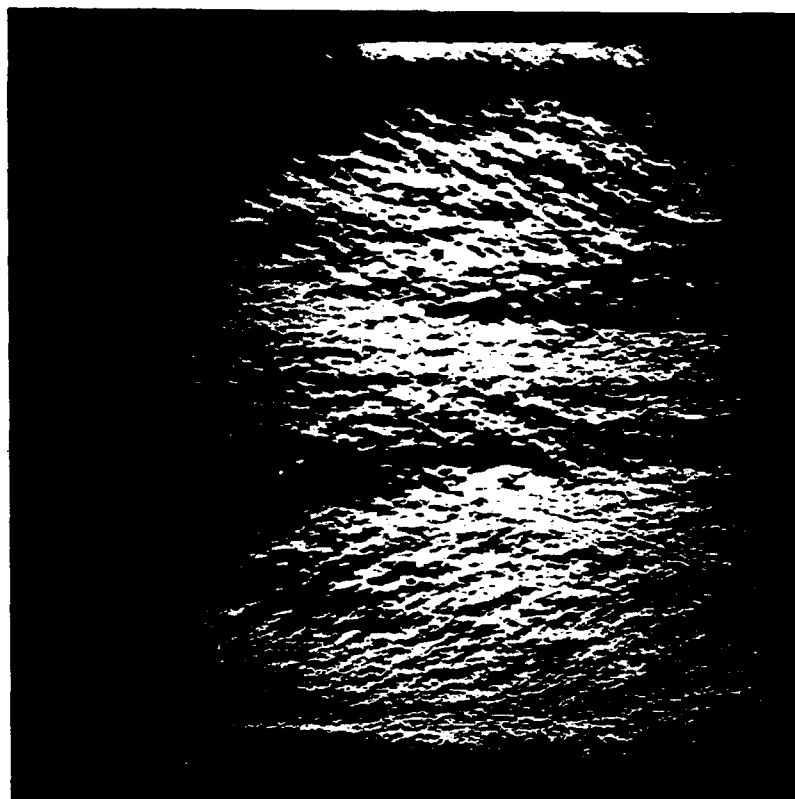**Figure 3**   Sketch of Nozzle Exit - Test Section Junction

Figure 4   Pressure Differential at the Nozzle Exit Lip
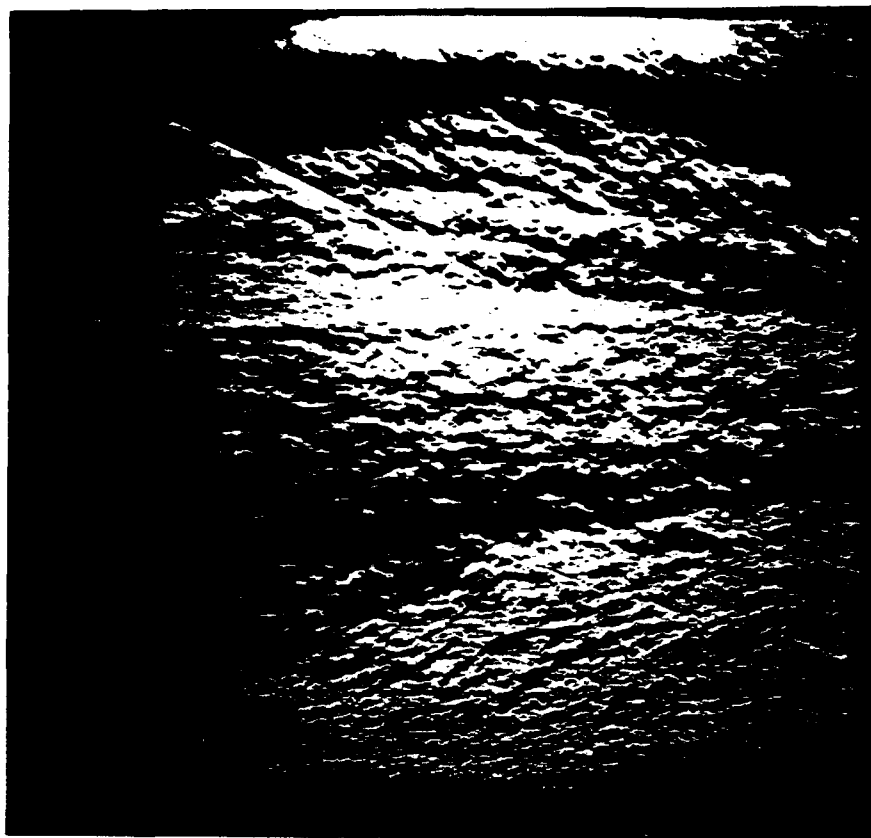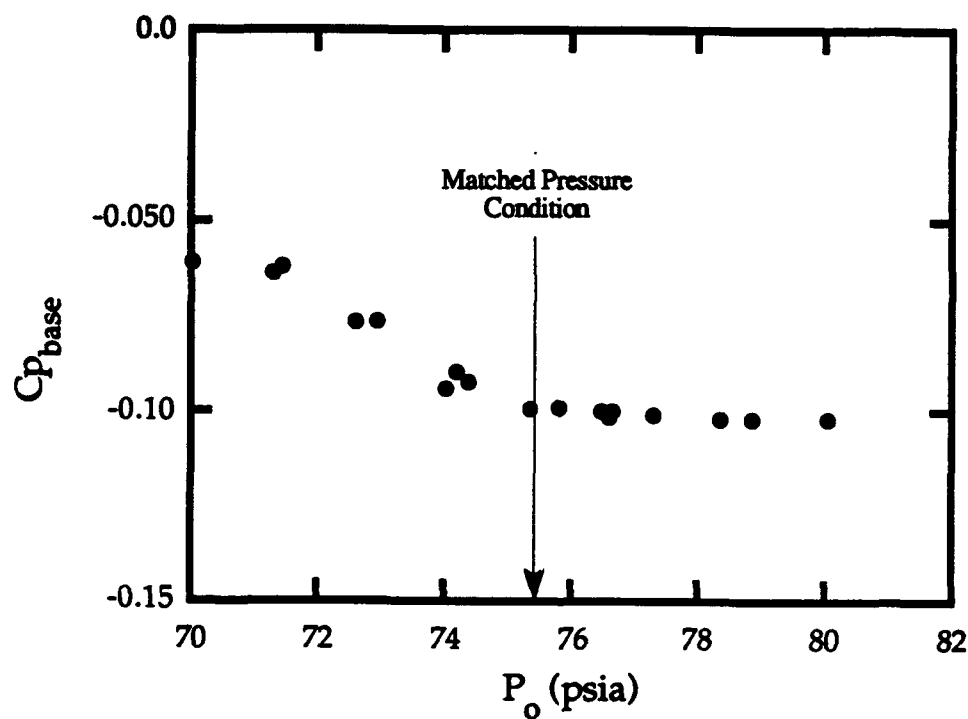
(a)

(b)

Figure 5 Schlieren Photographs of (a) underexpanded nozzle, (b) perfectly expanded nozzle, and (c) overexpanded nozzle
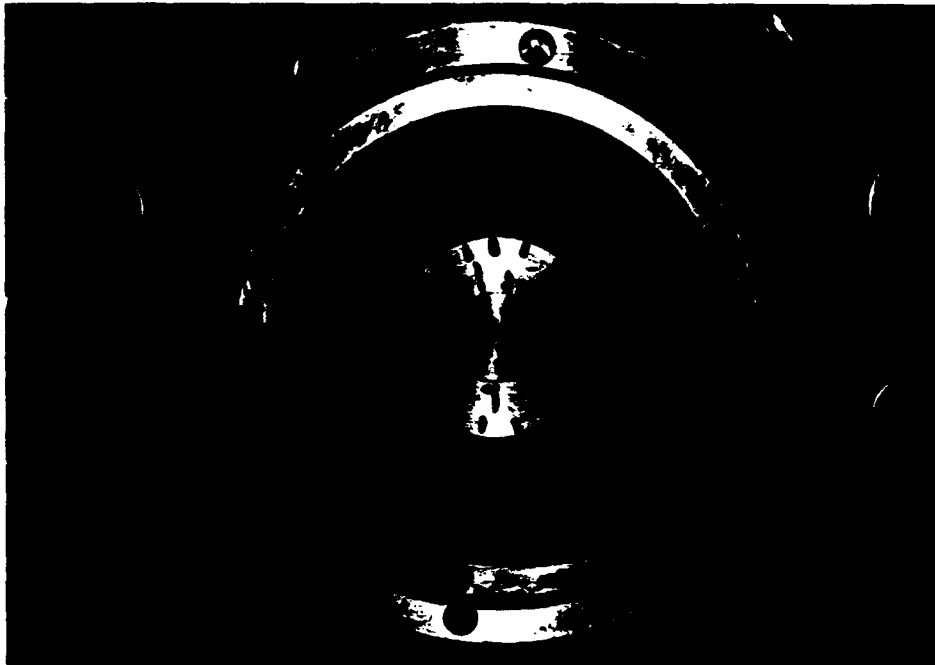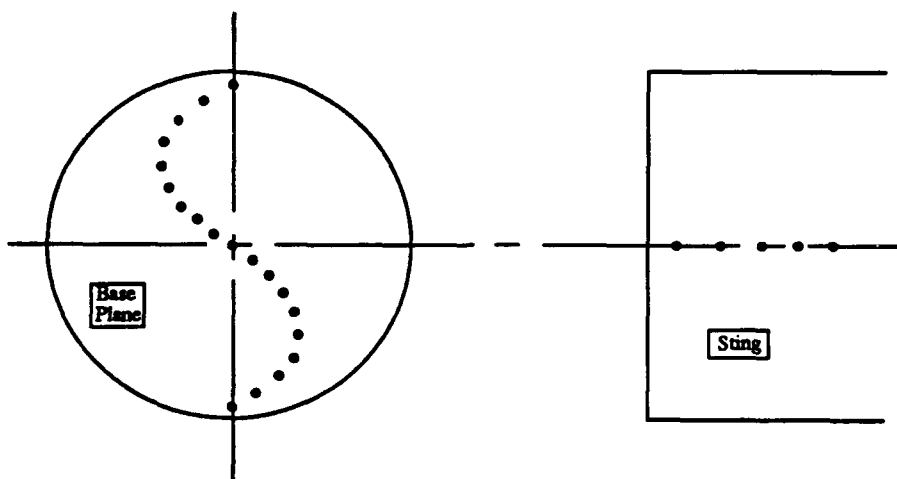
Figure 5 (c)   Overexpanded Nozzle

Figure 6   Average Base Pressure Coefficient at Different Stagnation Pressures

Figure 7 Photograph of Base Oil-Streak Visulization for "Best-Centered", Symmetric Flowfield

Figure 8 Location of Static Pressure Taps on Base and Sting Surfaces
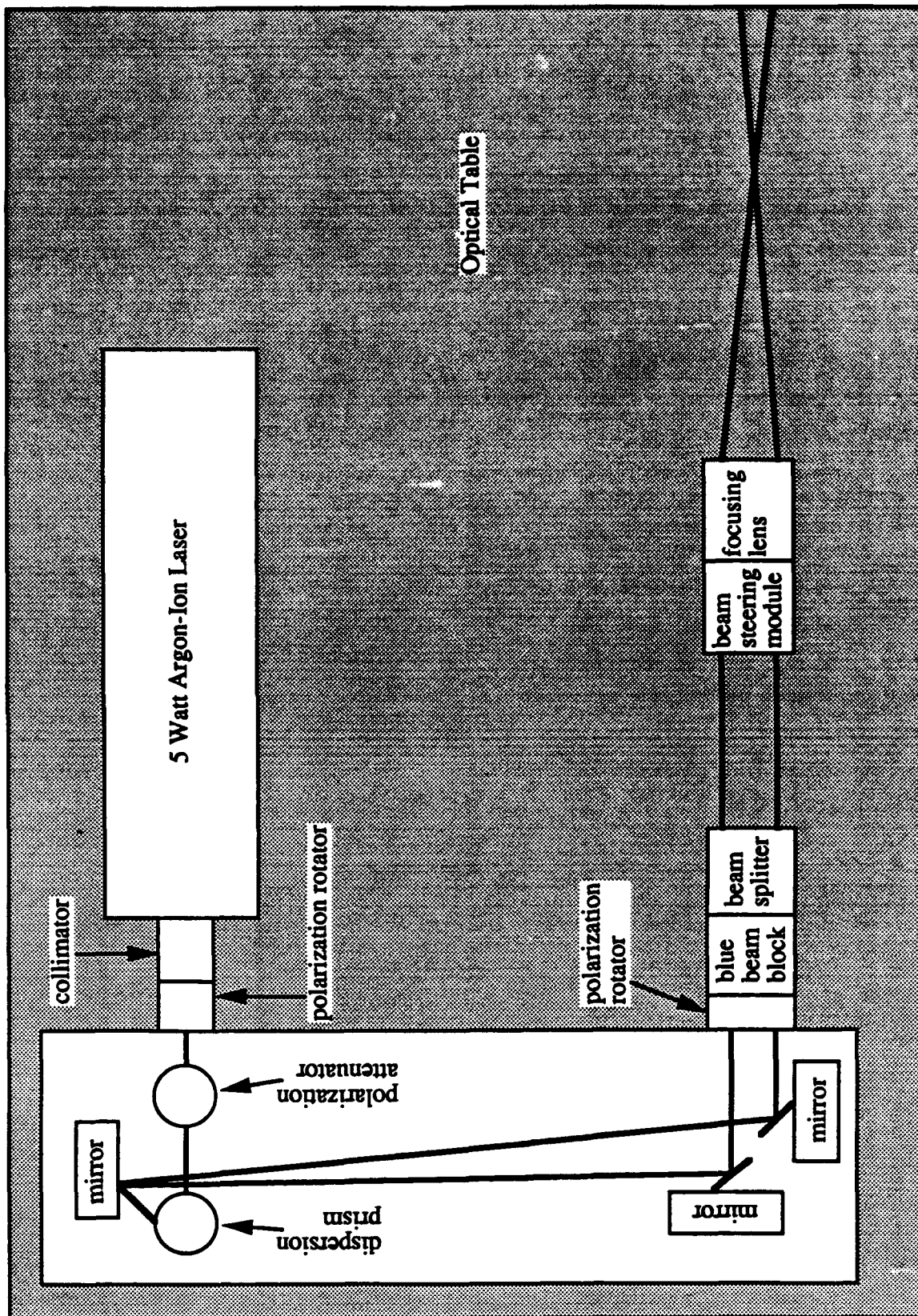
Figure 9   LDV Optical Arrangement (transmitting side only)
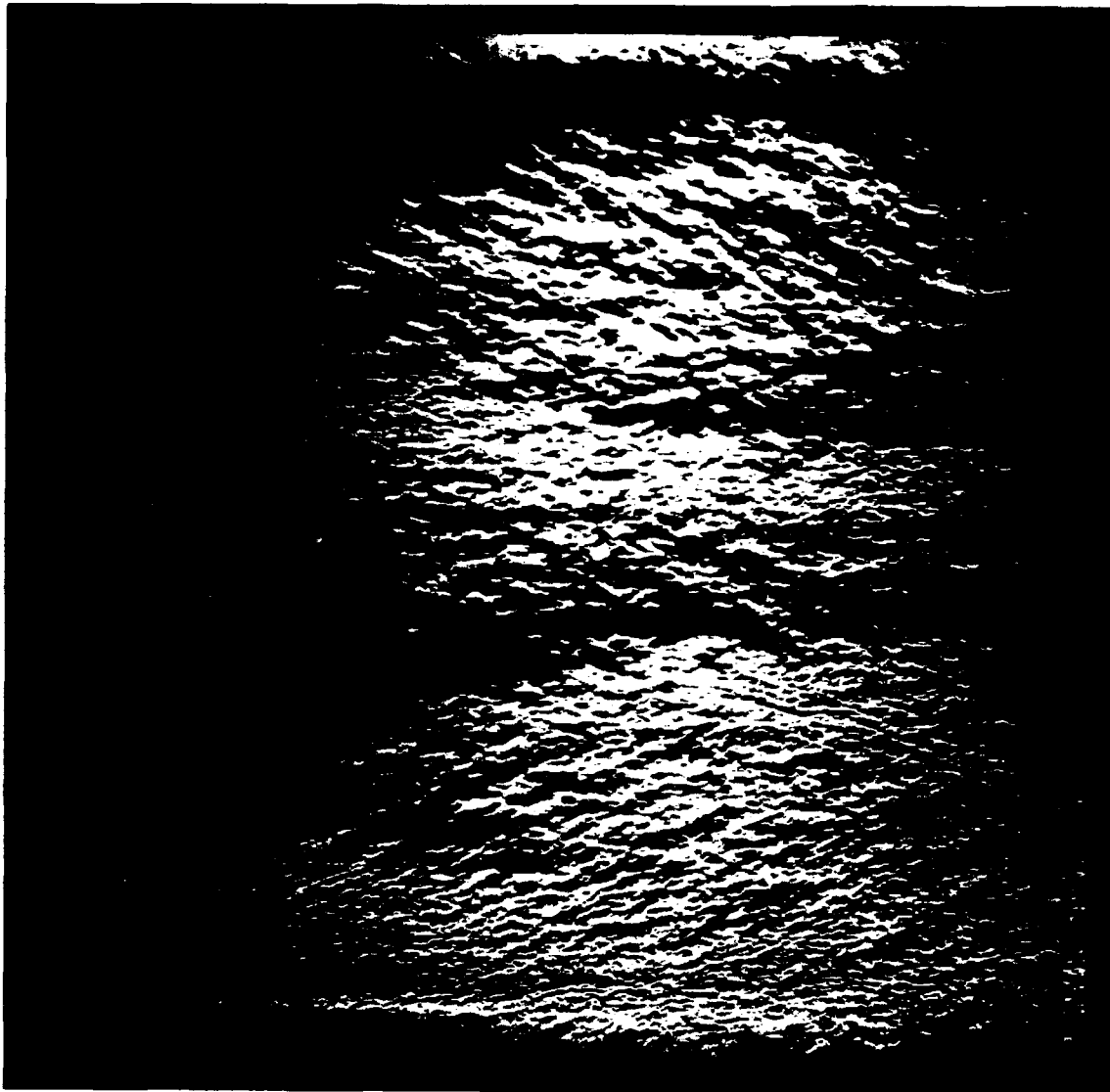
Figure 10 Spark-schlieren Photograph of Interference-free Base Flowfield for Wind Tunnel Operating in the Matched Pressure Condition
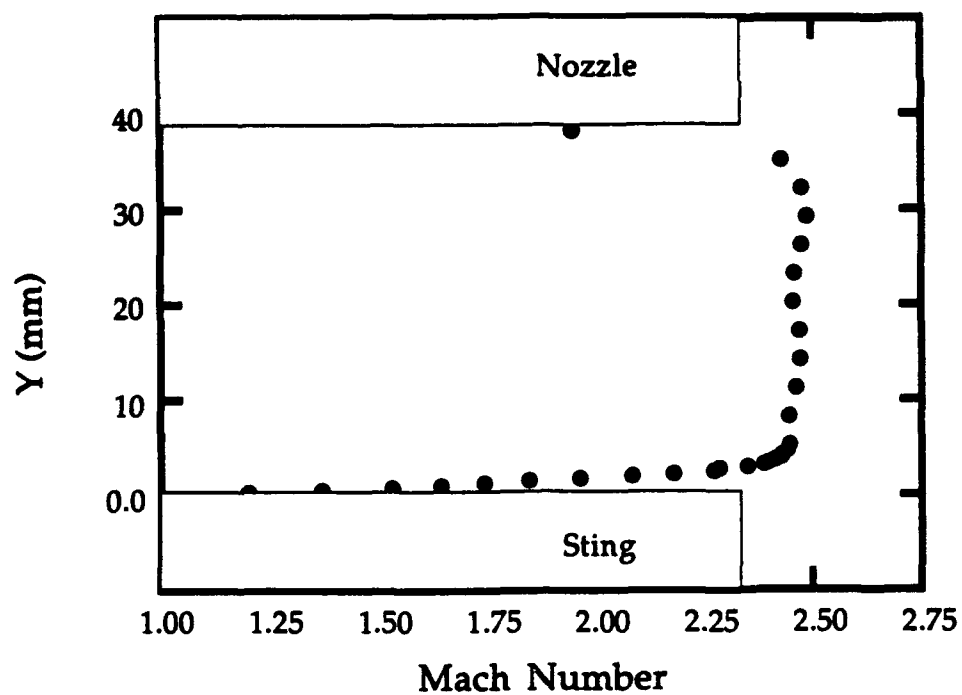
Figure 11   Mach Number Distribution Across the Nozzle Exit
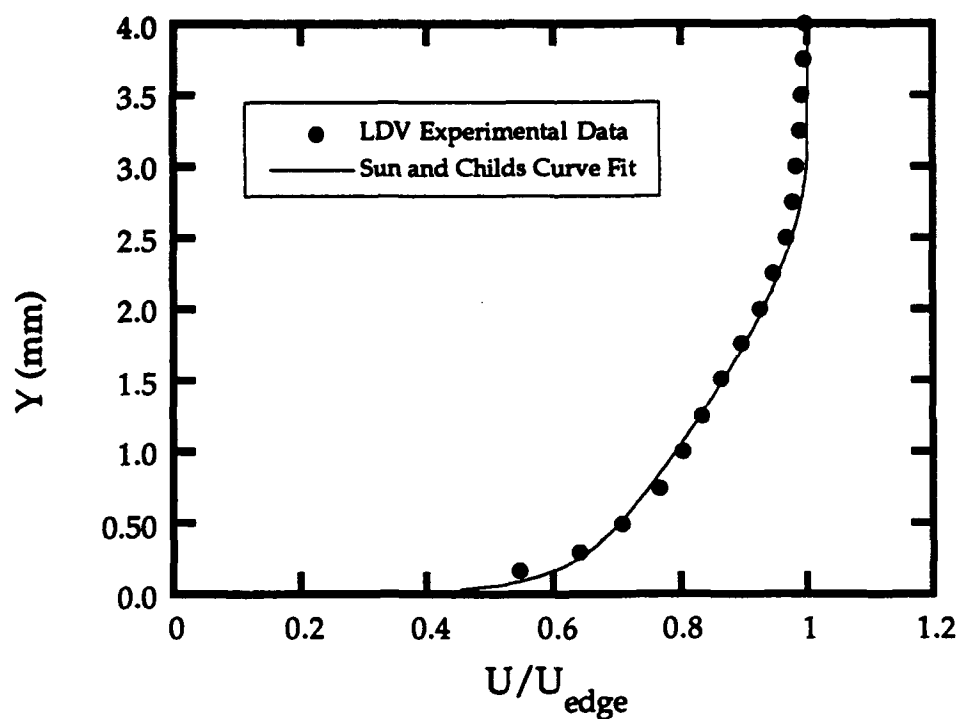
Figure 12   Sting Boundary Layer at X=8mm Along with Sun & Childs Compressible Boundary Layer Curve Fit [15]
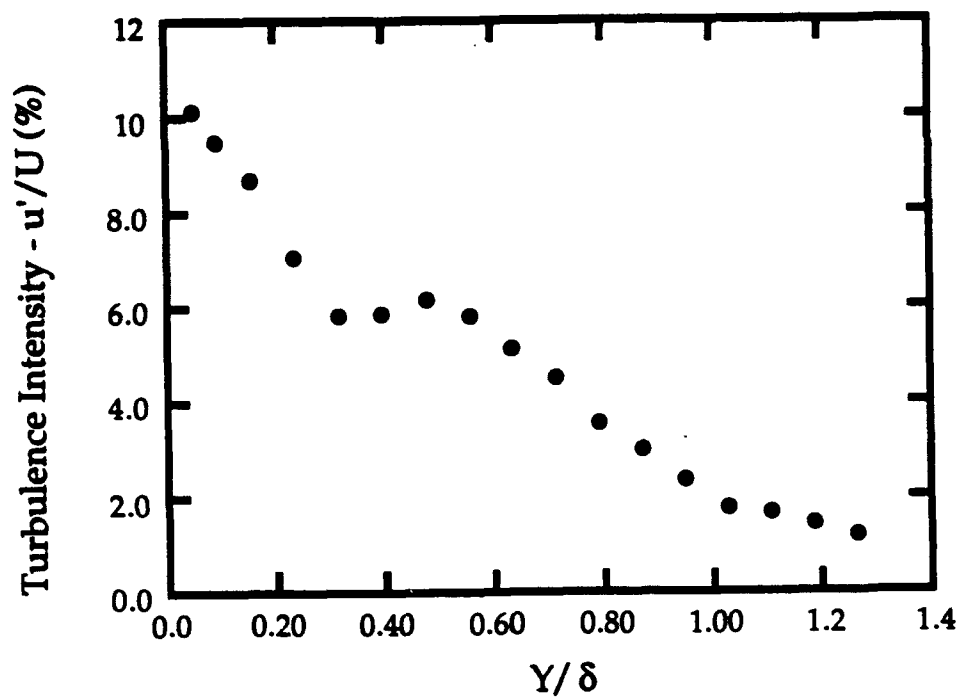
Figure 13 Turbulence Intensities Throughout Sting Boundary Layer, X=8mm
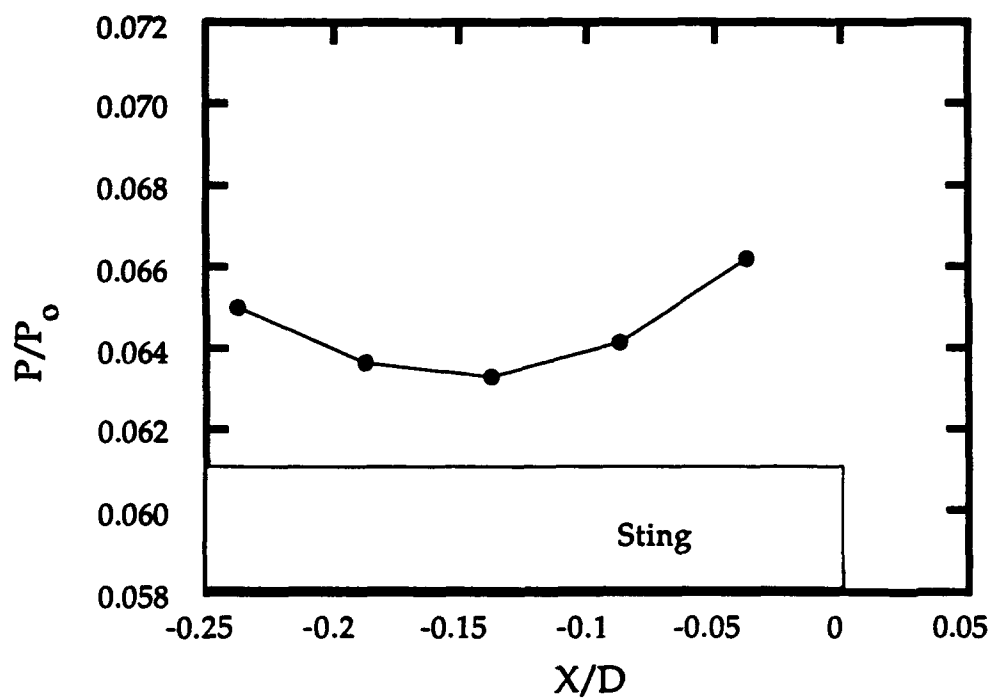
Figure 14 Static Pressure Distribution Along Sting Upstream of Base Plane
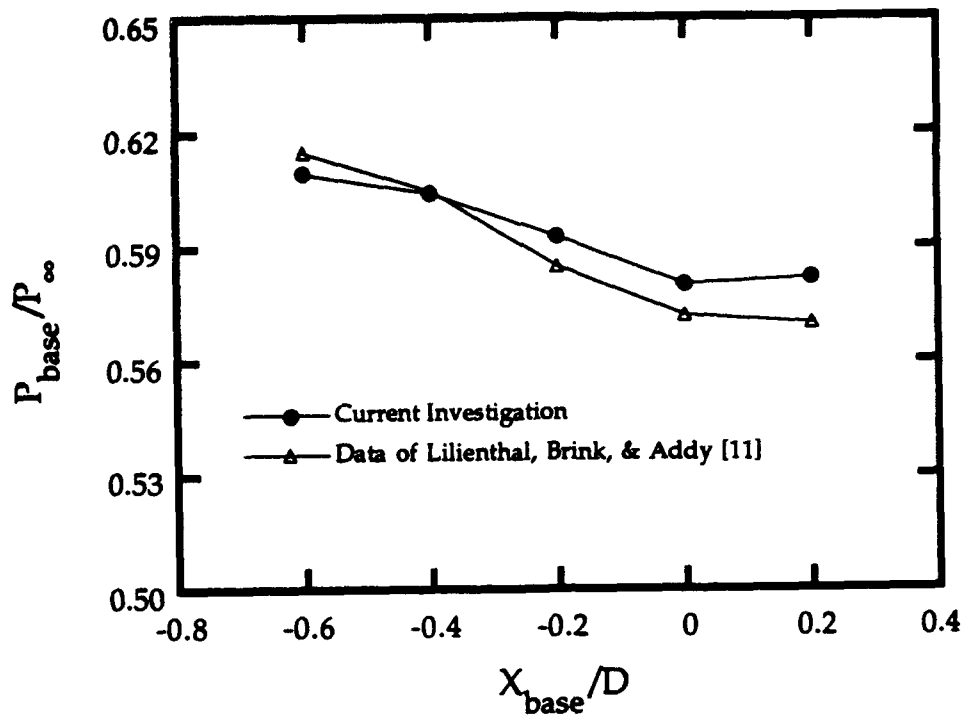
Figure 15   Base Pressure Variation with Axial Location of Sting
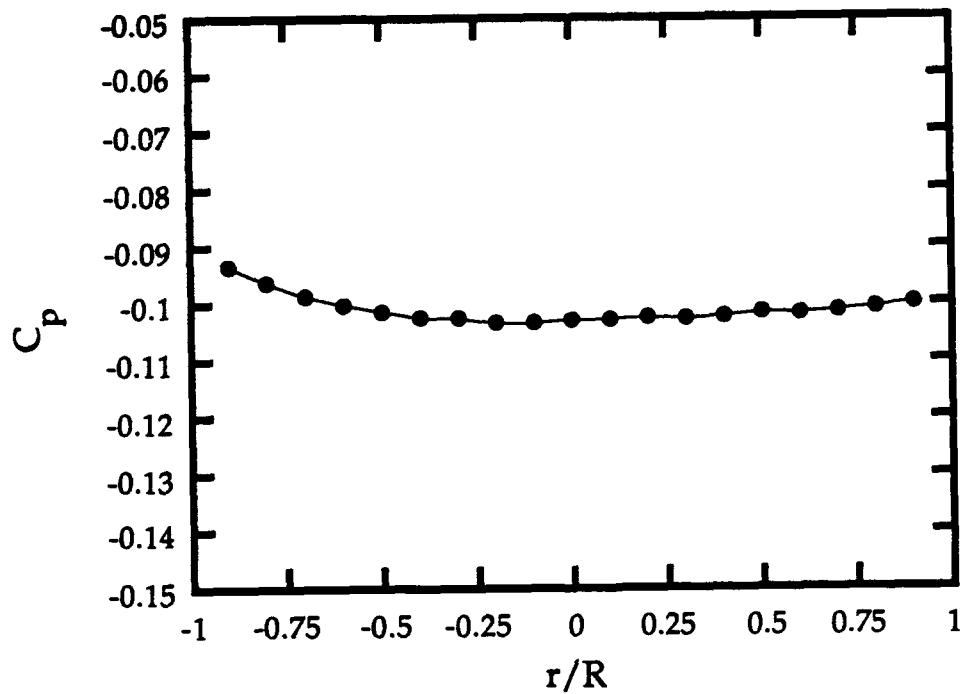
Figure 16   Dimensionless Base Pressure Profile

APPENDIX A.8

DESIGN OF A PARTICLE IMAGE VELOCIMETER FOR HIGH SPEED FLOWS

Paper Presented at the AIAA Student Regional Conference

Purdue University

West Lafayette, Indiana

March 1991

Also:

AIAA Paper No. 92-0259

Presented at the 30th AIAA Aerospace Sciences Meeting

Reno, Nevada

January 1992

by

R. A. Rosner

AIAA

AIAA-92-0259

Design of a Particle Image Velocimeter for High Speed Flows

R. A. Rosner
University of Illinois at Urbana-Champaign
Champaign, Il

30th Aerospace Sciences Meeting & Exhibit
January 6-9, 1992 / Reno, NV

DESIGN OF A PARTICLE IMAGE VELOCIMETER FOR HIGH SPEED FLOWS

R. A. Rosner[*]

Department of Mechanical and Industrial Engineering
University of Illinois at Urbana-Champaign

Abstract

A particle image velocimetry (PIV) system has been developed for use as a non-intrusive laser diagnostic tool to complement laser Doppler velocimetry (LDV) in high speed (transonic and supersonic) wind tunnel studies. The PIV system is capable of extracting instantaneous two-dimensional velocity maps within a flow by recording double images of seed particles on photographic film and then examining the local displacement of particle images to determine velocity vectors. The image acquisition system uses two high power pulsed Nd:YAG lasers focused into a thin light sheet to illuminate seed particles for recording on either 35 mm or 4" x 5" format film, with control of seeders, lasers, and the camera shutter performed by a Macintosh II computer. Interrogation of the double-exposed photographs to extract velocity information is done on an image processing system based on a 50 MHz Macintosh workstation, a HeNe laser for illumination, automated positioners to handle the film, and a CCD array camera. The design of the acquisition system, including special considerations for PIV in high speed flows, is discussed. The theory and design of the interrogation system are also described. Finally, results from the cases used to validate and demonstrate the PIV system are presented.

Introduction

Particle image velocimetry (PIV) is a non-intrusive laser diagnostic technique used to make instantaneous velocity measurements in a planar region of turbulent and separated flows. The technique involves two complementary yet independent processes; these processes are called acquisition and interrogation. In the current setup the acquisition system uses two pulsed lasers which are focused into a sheet of light to illuminate seed particles within a planar region of the flow. The particle images are then double-exposed onto photographic film by flashing the lasers at a set time interval (Figure 1). The double-exposed photograph, with a known magnification and time delay, can then be interrogated to determine particle separations and thus velocity vectors. This is done by successively illuminating small regions of the photo and digitizing and storing the images in a computer, where the average displacement of the particles in each interrogation region is found via image processing.

PIV has been determined to be a necessary and useful tool for fluid mechanics research because it can be used to quantitatively visualize highly unsteady, turbulent, and separated flowfields. Because it is non-intrusive, no probes or sensors need to be placed in the flow which could disturb or alter the flow regime which is under study. Unlike flow visualization, PIV determines accurate, quantitative velocity information. Because a map of an entire plane in the flow field is made with the process, PIV allows observation of important instantaneous spatial structures that cannot be determined with laser Doppler velocimetry (LDV), which evaluates mean velocities and other turbulence data on a point by point basis. LDV also requires much longer wind tunnel run times in order to map the entire flow field. PIV is not meant to be used to duplicate the important statistical turbulence data which can be obtained from LDV, but is instead intended to be used as a complement to LDV to determine instantaneous flow structures.

Acquisition System

Equipment

The image acquisition system uses two pulsed lasers focused into a thin sheet of light to illuminate seed particles in the wind tunnel. The sheet is 0.4 mm

[*] Currently Mechanical Engineer, B&V Waste Science and Technology Corporation, Kansas City, MO. Member AIAA.

thick and is adjustable from 66 to 108 mm wide. The light sheet is sent vertically through a window in the bottom of the tunnel and photographs of the illuminated particles are taken through a side window. In the acquisition process, two laser pulses are used to capture two images of each particle on a single photograph. The entire process is operated from a Macintosh II computer. The computer controls the operation of the seeder valves and camera shutter and specifies the time interval for the laser pulses. A schematic of the acquisition equipment is shown in Figure 2. The top section of the laser table is placed on anti-vibration mounts to avoid displacement of the optics and camera during a run, but can be traversed in the streamwise direction to take multiple photos in long test sections without moving the entire apparatus.

The design of the image acquisition system started with the choice of the illuminating laser for photographic double-exposure of seed particles suspended in the flow. The requirements for the laser included very short duration pulses to prevent blurring of particle images, high power in the visible spectrum to illuminate small seed particles used in high speed flows, and an accurate and tunable pulse separation to adjust for varied flow speeds. Two pulsed Nd:YAG lasers, frequency doubled to 532 nm (green), were chosen because of their combination of high power (550 mJ) and short pulse width (4-6 ns). Two lasers are required in order to obtain two pulses within the necessary time separation (approximately 200 ns for some supersonic applications). Adjustable pulse separation is accomplished by using a Stanford Research Systems Inc. digital delay pulse generator to trigger the lasers. The Stanford box, along with the 35 mm camera shutter and seeder valves, is controlled from the Macintosh by means of a National Instruments digital I/O board. The optical components chosen to form the light sheet are made from fused silica substrate with special coatings to withstand high energy pulses. The sheet forming optics are detailed in Figure 3.

A Canon 35 mm camera with an electronic shutter was chosen for the acquisition process. The 35 mm format is generally preferred over 4" x 5" film because it is relatively inexpensive and allows for automatic control of shuttering so that multiple photographs can be taken quickly and easily, reducing wind tunnel run time. The limitation of this choice is that 35 mm negatives produce larger particle images due to diffraction effects when enlarged and positive printed on 4" x 5" film for interrogation. The larger images in turn require larger interrogation spots which are undesirable for some flows with large spatial gradients. This PIV system can also be used with a 4" x 5" camera, but the procedure for obtaining particle image photographs with this camera has not been automated yet.

Directional Resolution

When the double-exposed PIV photograph is examined to determine a velocity vector field, the interrogation process assumes that the particle images have positive displacements. That is, it is assumed that the image of the particle at the time of the second laser flash is downstream of the first image. However, in a turbulent or recirculating flow field negative particle displacements are often encountered. This problem is referred to as directional ambiguity.

In general, directional ambiguity is resolved by assuring that the second images of the particles have positive displacements even if the particles themselves do not. This process, called image shifting, can be achieved mechanically by placing a rotating mirror in front of the acquisition camera lens or by displacing the whole camera between laser flashes. A mechanical method is not used in the system described here partly because of the increased complexity but primarily due to the restraints placed upon it by its application to high speed flows. A mechanical system simply cannot be used with the small laser time delay required to capture instantaneous structures in a high speed flow.

An electrooptical method of image shifting, described by Landreth and Adrian,[1] is employed in this PIV system. This method uses a calcite crystal plate (Figure 4) and takes advantage of the fact that light from one of the Nd:YAG lasers is vertically polarized, whereas the output from the other laser is horizontally polarized. The calcite plate has a uniaxial birefringent crystal structure with a different refractive index for each of the two directions of light propagation in the crystal. The calcite crystal is placed in front of the camera lens and passes the vertically polarized light from the first laser (o-ray) without disturbing its path. The light from the second laser,

with opposite polarization (e-ray), is refracted as it passes through the calcite crystal. The images from the second laser pulse are therefore shifted in a direction which is determined by the orientation of the calcite crystal and a distance which is proportional to the thickness of the calcite. This simple, flexible approach used to resolve directional ambiguity in separated flows can also be utilized in unseparated flows to increase small scale velocity resolution by shifting out the dominant streamwise velocity magnitude.

Parameters for Successful PIV

Keane and Adrian[2] have performed extensive numerical simulations to determine the important parameters for PIV systems and to show how these parameters can be optimized to assure accurate PIV measurements. Similar parameters were verified experimentally and presented by Lourenco and Krothapalli.[3] It is suggested that the image density on the photograph be large enough to provide 5 to 15 particle pairs for each interrogation region (typically on the order of 1 mm in diameter). Also, the displacement of the particle pairs should not exceed 30 percent of the diameter of the interrogation spot. By using a fixed light sheet thickness and choosing the size of the interrogation region, the equations given by Keane and Adrian[2] can be used to find an estimate of the laser pulse delay which will provide adequate results for the particular flow to be studied. For supersonic applications, the pulse delay, Δt, may be required to be as small as 200 ns. The equations can also be used to choose a Δt which is small enough to minimize errors caused by particles moving into and out of the plane of the light sheet but is large enough to provide adequate velocity resolution. When significant three-dimensional (out-of-plane) motion exists, particle images which are not paired with other images contribute to noise in the interrogation process, reducing the number of vectors which can be accurately computed.

Challenges for High Speed Flow

Along with the consideration of the criteria described above, the application of PIV to high speed (transonic and supersonic) flows requires special equipment and procedures that have not been needed for the low speed flow applications for which

PIV has been demonstrated in the past. Some of these details have also been addressed by Kompenhans and Hocker.[4] The challenges and issues facing PIV in high speed flows can be arranged into three categories: laser requirements, particle dynamics, and imaging requirements.

The acquisition laser is required to emit a powerful, visible pulse of light, so that small particles can be captured on photographic film. The pulse length must be small to prevent image blur in high speed flows, and the pulse separation must also be small, which requires the use of two separate laser units. If only one laser was used, its flashlamp would not be able to recharge and emit a consistent pulse of adequate power in such a short time. Also, for accurate velocity measurement in a high speed flow, the pulse timing must be precisely calibrated. These requirements for precision and timing lend themselves to digital control. For that reason, the current PIV acquisition system is operated from the previously described Macintosh II computer and the lasers are triggered with the Stanford box, which is calibrated to ± 5 ps.

With any laser diagnostic technique, proper flow seeding is critical for good results. The particles used in high speed flows must be very small (on the order of 1 μm or less) to accurately follow the flow. The particles are also required to scatter enough light for photography and to maintain the polarization of the light they scatter so that electrooptical image shifting can be used. Silicone oil droplets from a TSI six-jet atomizer, with an average diameter of about 0.8 μm, have been used successfully in this PIV system and have been shown to maintain light polarization due to their spherical shape.

Finally, the particle images that are recorded on photographic film for interrogation must meet two requirements. The images (which are larger than the actual particles due to diffraction) must be small enough to resolve small scale turbulence. There must also be an adequate image density so that there are enough particle image pairs within each interrogation region to provide accurate results. These problems are addressed by using a 4" x 5" camera when necessary and by using local seeding to increase seed density.

Interrogation System

Equipment

The interrogation system uses a double-exposed photograph from the acquisition process and examines the particle images to determine the velocity vector field. The photographic negative from the wind tunnel is positive printed on 4" x 5" portrait film such that the background is dark and the particle images are transparent. Special techniques, such as under-exposing the negative and over-developing the positive, are used to increase the contrast between the images and the background. The photographic positive is then sandwiched between two glass plates and mounted on a two-dimensional Aerotech positioner.

The entire interrogation process is controlled by a Macintosh II workstation (separate from the Macintosh II used to control the acquisition system). The interrogation computer, which is based on the 16 MHz Macintosh II design, has been modified to increase its speed, capabilities, and disk storage. The processor has been replaced with a unit which operates at 50 MHz. The other primary speed advantage comes from a Mercury array processor. This board, when installed in the computer, works as a second central processing unit (CPU), allowing parallel processing. While some operations are being controlled by the Macintosh CPU, the array processor can be simultaneously dedicated to other numerical tasks. The array processor operates at speeds up to 20 Mflops (million floating point operations per second) and is used for mathematical and scientific programming applications including large matrix operations and two-dimensional fast Fourier transforms (FFTs).

The image processing proceeds as follows (see Figure 5 for a schematic of the interrogation process). A Uniphase 5 mW Helium-Neon (HeNe) laser is used as a light source to illuminate a small portion of the particle image photograph (called the interrogation spot). The photograph is mounted on the two-dimensional positioner for movement to successive interrogation spots. The entire process is controlled by the computer, with each spot being imaged onto the CCD array camera and digitized for mathematical manipulation before moving to a new location. The camera used to record the illuminated interrogation region is a Sierra Scientific solid-state video camera. A Perceptics frame-grabber or video digitizer is used to transfer a single frame of video information to the computer. The video image is formatted by the frame-grabber into a two-dimensional array of 512 x 512 8-bit integers, with a value of zero corresponding to the darkest part of the image and a value of 255 for the brightest. The video camera records only black and white (grey-scale) images.

Young's Fringe Method

The single most important facet of the interrogation process is the manipulation which is done to the illuminated interrogation region optically (prior to input into the camera) and digitally (within the computer workstation and array processor). The Young's fringe method of analysis starts with the light source, which is required to be collimated for this method. The HeNe laser beam is passed through a neutral density filter and a spatial filter as shown in Figure 6. The neutral density filter consists of three polarizing filters whose orientation can be varied to control the intensity of the beam. The spatial filter consists of a pinhole and a microscope objective which are used to clean up the beam and create a more Gaussian intensity distribution. When a microscope objective is placed one focal length from the pinhole, the beam exiting the spatial filter is collimated, as is the original HeNe beam. Before the beam is passed through the photograph, a mask made of thin brass material (with holes varying from 0.4 to 1.5 mm in diameter) is used to adjust the size of the interrogation region.

When the collimated light source is passed through the particle image photograph, the light which is transmitted through the particle image pairs in the interrogation region creates a diffraction pattern in the far field. By placing the PIV photograph at the front focal point of the plano-convex lens and the CCD video camera at the rear focal point, the diffraction or fringe pattern is imaged into the computer via the video camera and frame-grabber. This interference pattern, called Young's fringes, represents the power spectral density (magnitude squared) of the two-dimensional Fourier transform of the particle images in the interrogation region.

Inside the computer, this digitized fringe pattern, now represented by an array of 512 x 512 unsigned

integers between 0 and 255, is downloaded into the array processor where a second two-dimensional Fourier transform is performed digitally. This second transform is called a fast Fourier transform (FFT). The FFT refers to an algorithm which more quickly and efficiently computes the discrete Fourier transform of a data sample set. When the power spectral density of this second transform is computed, the resulting array of numbers is referred to as the spatial correlation or autocorrelation plane. The Young's fringe method of image manipulation is shown in Figure 7. For the present application, the spatial correlation output includes a large central (autocorrelation) peak surrounded by two smaller signal peaks. The signal peaks are symmetrically located opposite the autocorrelation peak. The center peak represents the correlation of each particle image with respect to itself (zero displacement), whereas each signal peak represents the correlation of each particle image with respect to its image pair. The distance from the center peak to a side peak is directly proportional to the average displacement of the particle images in the interrogation spot and is inversely proportional to the spacing of the Young's fringes. The location of the side peak with respect to the center autocorrelation peak also represents the direction of displacement of the particle images. Since the average displacement of the particles, the magnification of the photograph, and the time delay of the acquisition laser pulse are now known, a velocity vector (magnitude and direction) can be computed for the interrogation spot.

It should be noted that the two symmetric signal peaks represent equal and opposite velocity vectors. This is the directional ambiguity problem that was discussed previously. When searching for the signal peak, it is assumed that the images have been shifted during the acquisition phase to assure positive image displacements. Then only the right half-plane of the spatial correlation is examined.

Autocorrelation Method

The second method used for interrogation is called the autocorrelation method. Instead of using the optical setup described in the previous section (Figure 6), the beam mask is not used and a diverging beam is passed through the photograph. A large portion of the photograph is then illuminated, and the spot size is set by adjusting the distance between the

CCD camera and photograph. Instead of using a plano-convex lens (as before), a microscope objective is placed between the photo and the camera. As a result, the particle images in the interrogation spot are imaged directly onto the camera and are passed into the computer/array processor, where two digital fast Fourier transforms are performed. The power spectral density of the first transform is found before computing the second FFT and represents the Young's fringe pattern which was previously found optically. The power spectral density of the second transform is the autocorrelation plane. The signal peak in the right half-plane of the spatial correlation can then be located and a velocity vector can be computed for the interrogation region, as with the Young's fringe technique.

The autocorrelation method differs from the Young's fringe method in two significant ways; the complexity of the interrogation optics is decreased but the computational time is increased. The optics are simplified primarily because the light source need not be collimated, as in the Young's fringe method. However, the time required to compute a velocity vector at each interrogation spot is increased with this method since a second FFT must be performed by the computer. As a result, the autocorrelation method presently takes approximately 4.0 seconds per interrogation spot, whereas the Young's fringe method requires only about 2.3 seconds per spot. For a field of 10,000 vectors (a 100 x 100 array), this represents a total interrogation time of 11.1 and 6.4 hours, respectively.

The main advantage of the autocorrelation method is in its flexibility. Because the particle images are focused directly onto the camera, the size of the interrogation region can be easily varied. Also, a very large interrogation spot can be imaged onto the camera and then sub-divided within the computer into smaller spots (but with reduced pixel resolution) as shown in Figure 8. With the Young's fringe method, on the other hand, the resolution is effectively fixed at the pixel resolution of the camera. Prasad, et al.[5] demonstrated that reduced pixel resolution does not significantly affect accuracy in all cases, so this windowing process can dramatically reduce interrogation time without significantly sacrificing the quality of the results.

Post-Processing

When a photograph is interrogated, the raw data must be post-processed to subtract any image shifting and to remove erroneous vectors. After the image shift is removed, the velocity vectors corresponding to the largest signal peak in the autocorrelation plane are computed. Then any bad vectors are found and replaced by the vector corresponding to the second largest signal peak or by interpolating from nearby vectors. A method using multiple linear regression, as suggested by Landreth and Adrian,[6] has been implemented for this interpolation process. Generally the data yield for the two largest signal peaks is greater than 90%. That is, less than 10% of the vectors are erroneous and need to be interpolated.

The data can also be smoothed by convoluting the vector field with an axisymmetric Gaussian kernel to remove any high frequency noise in the data. This smoothing process, which is also detailed in Reference 6, has been implemented in this system.

Results

Interrogation System Validation

A test photograph was created and used to check the repeatability and accuracy of the interrogation system. For the test, dots representing particle images were computer generated and laser printed to plain white paper. This paper was then imaged and exposed on 4" x 5" portrait film to create a PIV photograph with a dark background and transparent particle images. This method of producing test photographs was used in an attempt to accurately simulate the effects of the photographic process on the particle images. Those aspects missing in this method are the non-uniformity of the particle images and the diffraction effects caused when the acquisition lasers illuminate the seed particles.

The test photograph had particle pairs with constant displacements randomly placed throughout the photo. The resulting particle images were approximately 50-60 μm in diameter and were present on the photo in a density of about 10 pairs per mm^2. Four separate regions, each with constant displacements of 93, 140, 187, and 233 μm were present on the photo. The photo was interrogated several times with both the Young's fringe and

autocorrelation methods, and in all cases the largest signal peak for each interrogation region yielded at least 98% good vectors, as documented by Rosner.[7] The interrogations were repeated with the photograph oriented horizontally, vertically, and at a 45° angle to demonstrate that there was no directional bias present with either the Young's fringe or autocorrelation method of analysis. Once again, the data yield was at least 98% and the standard deviation of the determined displacement was less than 2.5% of the actual displacement.

It should also be noted that there is a slight error inherent in the test photograph itself. This is caused when the particle pairs are laser printed and when the laser printer output is reduced and printed on the 4" x 5" film. The particle displacements can vary as much as 10 μm from the intended (constant) displacement, thereby accounting for some of the variations determined in the interrogation process.

Free Jet Example

To demonstrate the PIV acquisition and interrogation systems, the low speed flow exiting from a tube was studied. This axisymmetric free jet example was used to study seeding and photographic techniques as well as to practice interrogation and post-processing procedures. A schematic of the free jet setup is shown in Figure 9. The flow exiting the 25.4 mm diameter tube has a maximum velocity of 2.1 m/s and was seeded with silicone oil droplets. To resolve directional ambiguity, the images of the particles at the second laser pulse were shifted vertically using the calcite crystal technique.

A plot of the raw velocity data with the image shift removed, but including bad vectors, is shown in Figure 10. A grid of 102 horizontal and 101 vertical data points (10302 total vectors) was interrogated with a position increment of $\Delta x = \Delta y = 0.5$ mm. The autocorrelation method was used with a square interrogation region of 1.1 by 1.1 mm. During post processing, examination of the two largest signal peaks yielded nearly 95% good vectors. The vector map resulting after the bad vectors were found, removed, and interpolated is presented in Figure 11. The vectors presented in Figure 11 were not smoothed during post-processing. Large scale structures can be seen at the edges of the jet, particularly at the top of the jet.

A shaded contour plot of the absolute velocity of the free jet is shown in Figure 12. The higher velocities experienced near the top of the jet can be attributed to a 90° bend in the tube before it enters the test section (see Figure 9), resulting in a non-uniform velocity distribution at the nozzle exit.

Conclusions

A particle image velocimetry system has been designed and constructed for use in wind tunnel flows with the extra requirements of high speed flow applications in mind. An acquisition system with directional resolution capability has been implemented and demonstrated on a low speed flow case using all of the components and techniques required for a high speed flow. The interrogation system equipment has been integrated into a successful image processing system for examining the double-exposed photographs from the acquisition phase and for post-processing the results. Both the Young's fringe and autocorrelation methods of interrogation have been validated with a computer generated test photograph.

Because the present PIV system was designed to be used in high speed flow applications, the next step is to demonstrate it on such flows. A transonic base flow facility has been modified for use with PIV by installing windows in the top and bottom walls of the test section and by installing a system for injecting silicone oil seed into the tunnel. It is intended that PIV results will be compared with previous experimental studies of this flowfield by Kruiswyk and Dutton[8] and also computational results by Rudy.[9]

Acknowledgments

References

1. Landreth, C. C., and Adrian, R. J., "Electrooptical Image Shifting for Particle Image Velocimetry," Applied Optics, Vol. 27, No. 20, 15 October 1988, pp. 4216-4220.

2. Keane, R. D., and Adrian, R. J., "Optimization of Particle Image Velocimeters," Measurement Science and Technology, Vol. 1, 1990, pp. 1202-1215.

3. Lourenco, L., and Krothapalli, A., "The Role of Photographic Parameters in Laser Speckle or Particle Image Displacement Velocimetry," Experiments in Fluids, Vol. 5, 1987, pp. 29-32.

4. Kompenhans, J., and Hocker, R., "Application of Particle Image Velocimetry to High Speed Flows," von Karman Institute for Fluid Dynamics, Lecture Series 1988-06: Particle Image Displacement Velocimetry, Brussels, March 21-25, 1988.

5. Prasad, A. K., Adrian, R. J., Landreth, C. C., and Offutt, P. W., "Effect of Resolution on the Speed and Accuracy of Particle Image Velocimetry Interrogations," Twelfth Biennial Symposium on Turbulence (University of Missouri-Rolla, 1990).

6. Landreth, C. C., and Adrian, R. J., "Measurement and Refinement of Velocity Data Using High Image Density Analysis in Particle Image Velocimetry," Fourth International Symposium on Applications of Laser Anemometry to Fluid Mechanics (Lisbon, Portugal, July 1988).

7. Rosner, R. A., "Design and Validation of an Interrogation System for Particle Image Velocimetry," M.S. Thesis, Department of Mechanical and Industrial Engineering, University of Illinois at Urbana-Champaign, May 1991.

8. Kruiswyk, R. W., and Dutton, J. C., "An Experimental Investigation of the Effects of a Base Cavity on the Near-Wake Flowfield of a Body at Subsonic and Transonic Speeds," AIAA-89-0210, 27th Aerospace Sciences Meeting (Reno, Nevada, January 1989).

9. Rudy, D. H., "A Numerical Study of Unsteady Two-Dimensional Subsonic Compressible Base Flow," Ph.D. Thesis, Department of Mechanical and Industrial Engineering, University of Illinois at Urbana-Champaign, May 1987.
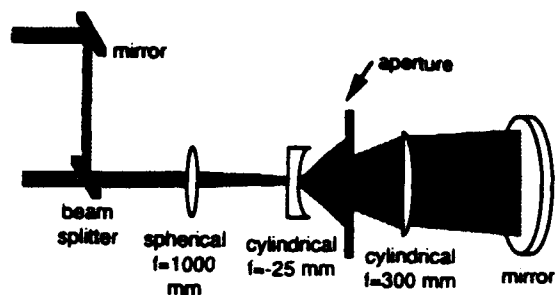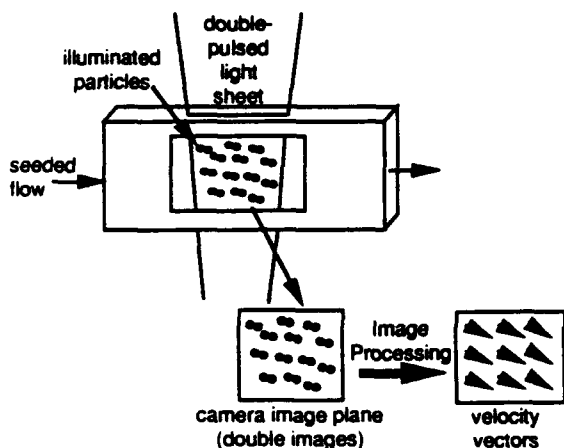
Figure 3: Light Sheet Forming Optics

Figure 1: Principle of PIV
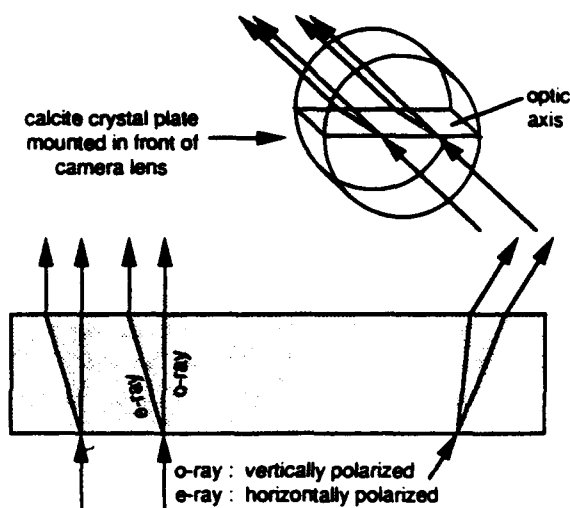

Figure 4: Calcite Crystal Image Shift
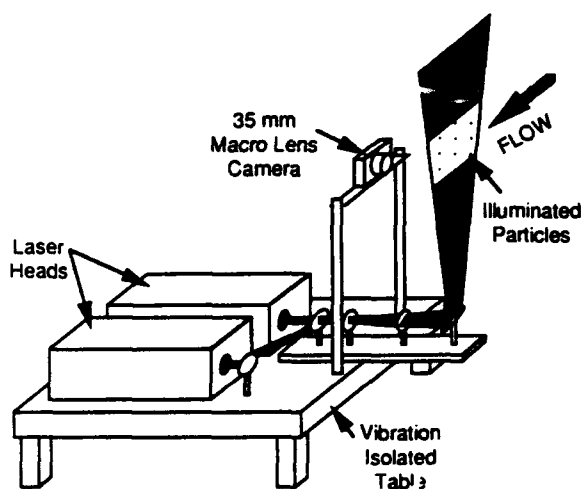
Figure 2: PIV Acquisition System
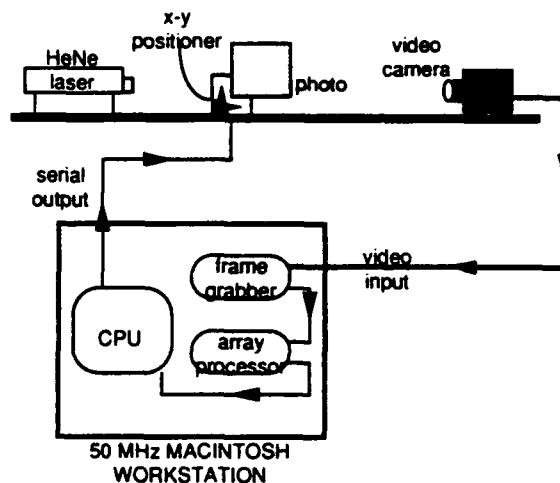
Figure 5: Interrogation System Schematic
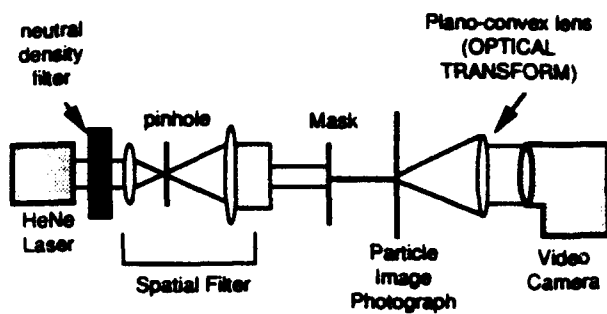
Figure 6: Interrogation Optics (Young's Fringe Method)

Figure 7: PIV Image Manipulation
(Young's Fringe Method)

Figure 8: Autocorrelation Method
with Reduced Resolution
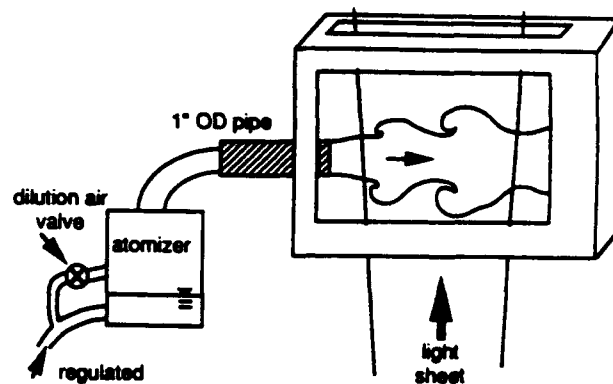
Figure 9: Free Jet Test Stand
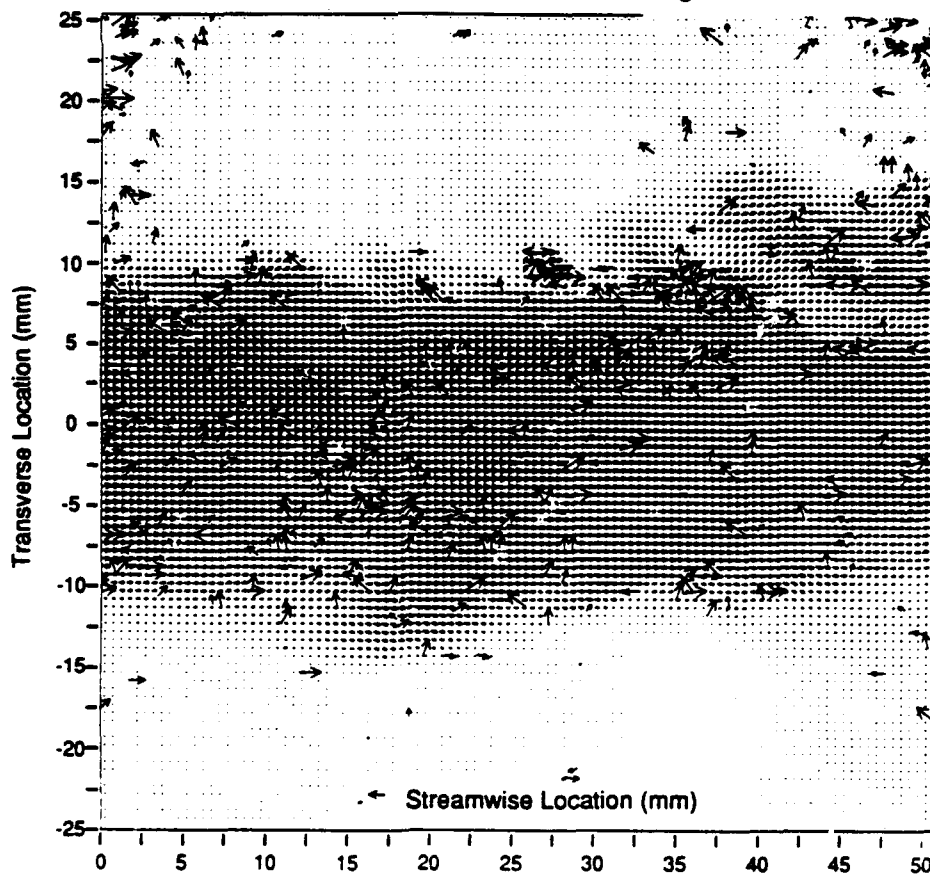
Figure 10: Free Jet Raw Velocity Data

-9-
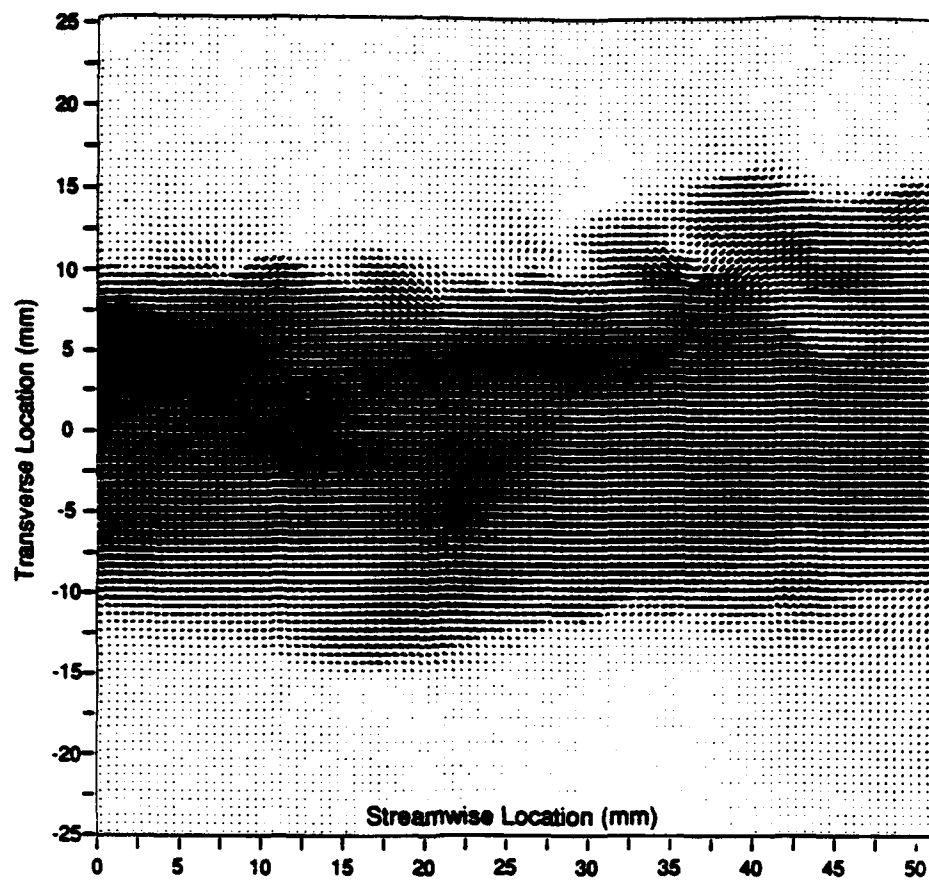
Figure 11: Free Jet Post-Processed Velocity Data
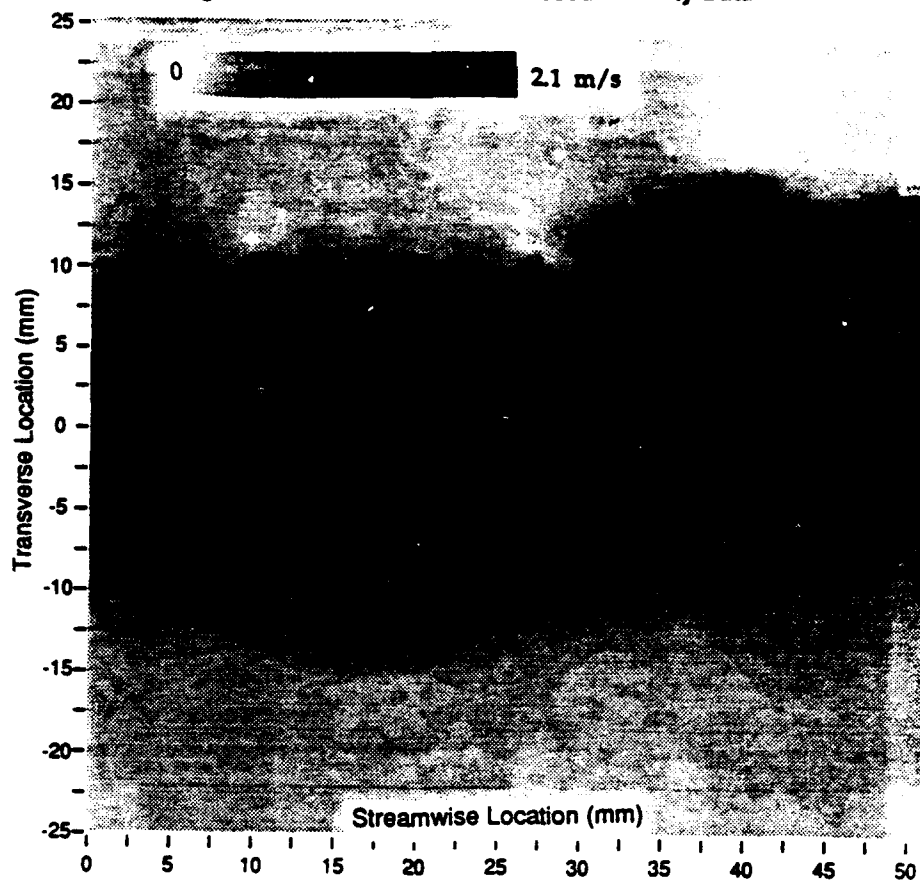
Figure 12: Free Jet Velocity Magnitude

APPENDIX A.9

DEVELOPMENT AND APPLICATION OF A PARTICLE IMAGE VELOCIMETER FOR HIGH SPEED FLOWS

AIAA Paper No. 92-0004

Presented at the 30th AIAA Aerospace Sciences Meeting

Reno, Nevada

January 1992

by

M. J. Molezzi and J. C. Dutton

AIAA 92-0004

Development and Application of a Particle Image Velocimeter for High-Speed Flows

M. J. Molezzi and J. C. Dutton
Dept. of Mechanical & Industrial Engineering
University of Illinois at Urbana-Champaign
Urbana, IL

30th Aerospace Sciences Meeting & Exhibit
January 6-9, 1992 / Reno, NV

DEVELOPMENT AND APPLICATION OF A PARTICLE IMAGE VELOCIMETER FOR HIGH-SPEED FLOWS

M. J. Molezzi[*] and J. C. Dutton[**]
Department of Mechanical and Industrial Engineering
University of Illinois at Urbana-Champaign
Urbana, IL 61801

Abstract

A particle image velocimetry (PIV) system has been developed for use in high-speed separated air flows. The image acquisition system uses two 550 mJ/pulse Nd:YAG lasers and is fully controlled by a host Macintosh computer. The interrogation system is also Macintosh-based and performs interrogations at approximately 2.3 sec/spot and 4.0 sec/spot when using the Young's fringe and autocorrelation methods, respectively. The system has been proven in preliminary experiments using known-displacement simulated PIV photographs and a simple axisymmetric jet flow. Further results have been obtained in a transonic wind tunnel operating at Mach 0.4 to 0.5 (135 m/s to 170 m/s). PIV experiments were done with an empty test section to provide uniform flow data for comparison with pressure and LDV data, then with a two-dimensional base model, revealing features of the von Karman vortex street wake and underlying small scale turbulence.

Introduction

Experimental investigation of turbulent and compressible flows has become increasingly sophisticated in recent years with the advent of laser-based measurement techniques. Among these tools is a relatively new technique called particle image velocimetry (PIV). PIV is performed by illuminating a seeded flowfield with a planar laser sheet which is pulsed at a known time interval, forming two or more images of each seed particle within the light sheet (Fig. 1). After recording these images on film or another medium, image separations and therefore velocities can be determined for the entire plane. Unlike pointwise techniques such as laser Doppler velocimetry (LDV) which provides statistical velocity data on a point-by-point basis, PIV has the ability to identify instantaneous flow structures which may be random in nature but important to the overall behavior of the flow. PIV also reveals planar views of three-dimensional flow structures which are smeared by volume integration inherent in techniques such as schlieren photography.

Other advantages include the ability to obtain PIV images quickly, allowing shorter run times, larger test sections, and higher Mach numbers.

PIV has only recently been extended to high-speed applications[1-3] due to many difficulties in the acquisition of usable PIV images. One of the most important considerations in high-speed applications is obtaining adequate seed density for successful interrogation at all locations. Since most high-speed wind tunnels are not recirculatory, high seed density can only be obtained by injecting a large mass of seed with the flow. Local seeding in areas of interest can be a solution, but injection may need to be done upstream of flow conditioning devices and nozzles which partially disperse the seed. Difficulty also arises in obtaining sufficient seeding in separated zones of the flow (behind bases, steps, etc.). Experience with both PIV and LDV shows that seed density in these areas is generally sparse, causing significant data dropout. Another concern is the choice of seed particles that are small enough to follow large velocity gradients while still scattering sufficient light to expose film. The seeding material is also restricted to spherical particles when electrooptical image shifting[4] is used to resolve the directional ambiguity of image displacements in high-speed separated flows. Image shifting involves shifting the second image of every particle by a known distance to assure that the direction of image displacement is known over the entire PIV photograph. Electrooptical image shifting is done by using vertically and horizontally polarized light for the two illumination pulses, then photographing the flowfield through a birefringent calcite crystal which shifts one polarization of light (and therefore one set of images) by a known distance. Maintenance of the polarization in sidescatter from seed particles requires spherical particles according to Mie scattering theory. After image displacements are determined from the photo, the "shift displacement" is subtracted off to return the actual flowfield displacements (and velocities).

Laser requirements are also a factor in the use of PIV for high-speed applications. In order to illuminate small seed particles, high power in the visible spectrum is a necessity. Kompenhans and Hocker[1,2] have used a

---

Nd:YAG system with 70 mJ/pulse for recording images on 35 mm film, but when necessary, resolution of small-scale velocity fluctuations in high-speed test sections requires the use of larger format film to reduce diffraction-limited image sizes and to avoid film grain limitations. The larger film area, in turn, requires much greater illumination. The high laser energy must also be combined with very short pulse durations to prevent image blur which reduces the res(..ution of velocity measurements. Typical supersonic flow speeds require pulse durations on the order of 10 ns or less.

Equipment

A diagram and accompanying control schematic of the PIV acquisition system are shown in Figs. 2 and 3. The acquisition system refers to the equipment used to obtain double-exposed particle image photographs of the flowfield of interest. This system uses two Continuum YG681C-10 lasers. Two separate units are required since a single laser cannot generate two distinct, equal energy pulses in the short time interval required for hⁱgh-speed flows. The YG681C-10 is a Nd:YAG laser equipped with a frequency doubling crystal to provide an output pulse energy of 550 mJ/pulse at a wavelength of 532 nm (green light) with a pulsewidth of only 4-6 ns. Although PIV has also been performed with pulsed ruby lasers, high-resolution black-and-white films are much more sensitive to the green wavelength output of Nd:YAG lasers than to the red wavelength output of ruby lasers. The high visibility of the green beam output also simplifies alignment of the two beams which is a critical factor in obtaining double exposures of particles in the flow. The horizontally and vertically polarized beams of the two lasers are combined by a polarized beam splitter, then shaped by spherical and cylindrical lenses to form a planar beam profile with a waist thickness of 0.4 mm and an adjustable width of 75 mm to 125 mm.

The photographic recording of particle images is done by a camera mounted on the same optical table as the lasers and beam shaping optics. This allows maintenance of the relative position of all optical components for consistent alignment and focus. This table is also mounted on vibration-isolated supports to avoid the effects of laboratory vibrations. The camera mount can be used with a 35 mm, 6 x 8 cm, or 4" x 5" camera. The 35 mm camera used is a Canon EOS 630 with autowind, electronic shutter, and a 100 mm macro lens. It is most useful for automated multiple photograph runs since it can be operated remotely and allows 36 photographs on a single film roll. A modified Fuji GX680 6 x 8 cm camera with the same features and a 300 mm copy lens can also be used. This camera uses 120 film which allows up to 9 frames/roll. The system has also been used with a modified 4" x 5" camera with a manual shutter and

120 mm lens, but since it can take only one frame before reloading, it is only useful when the highest possible resolution of particle images for determination of small scale turbulent motions is necessary.

Automation of the acquisition system is a key for short run-time test sections and/or multiple photographs for random capture of unsteady structures in various stages of development. Control of this system is done by a Macintosh II computer equipped with a digital I/O board and solid state module switches. Through software, the computer controls triggering of the Stanford Research pulse generator for operation of the lasers, the camera shutter, and seeder valve switches. When started, the operation proceeds by triggering the lasers for a user-specified warm-up period to allow start-up of the wind tunnel and thermal equilibration of the lasers. The seed valve is then opened and there is a user-specified delay time (with the lasers still operating) to allow seed to propagate to the test section. The camera shutter is then triggered for the specified number of photographs, followed by shutdown of the lasers, seeders, and camera.

Various seed types have been examined for tracking and optical performance, resulting in the choice of silicone oil seed generated by a TSI six-jet atomizer. The polydispersed atomized droplets have a mean diameter of 0.8 μm and show good response to the velocity gradient across an oblique shock wave[5]. Test photographs also show good performance for image exposure intensity and for electrooptical image shifting.

After the negatives are processed for high contrast (to increase signal-to-noise ratio) and contact printed onto film for photographic positives, the photographs are examined using an automated interrogation system controlled by a "Dash 30" modified Macintosh II computer operating at .:? MHz (Fig. 4). In high image density photographs, statistical methods must be employed to determine the average particle image displacement in each small region of the photograph. This is done by examining a small region of the photo (an interrogation spot) and deriving the spatial autocorrelation for that region. The location of the highest signal peak in the spatial autocorrelation corresponds to the most likely correlation distance (particle image displacement) in the interrogation spot. Simply explained, the spatial autocorrelation is derived by performing two 2-D Fourier transforms on the interrogation spot. This is most commonly done by either the "Young's fringe" method where the first transform is done optically and the second is done digitally by fast Fourier transform (FFT), or the "autocorrelation" method where the original interrogation spot image is digitized and both transforms are done by digital FFTs.

In this system, the PIV photograph is mounted between glass plates on a two-dimensional Aerotech positioner system to scan the photograph spot by spot

2

with a fixed 5 mW HeNe illumination beam and optics. The HeNe beam is first spatially filtered to eliminate high-frequency intensity variations which could add noise to the illuminated interrogation spot. The remainder of the optics are set to image either the actual particle images (autocorrelation method) or the far-field diffraction pattern (Young's fringe method).

The image is received by a Sierra Scientific CCD array camera equipped with a HeNe bandpass filter to eliminate room light interference. The image is digitized by a frame grabber board to a 512 x 512 element array with 8-bit grayscale (256 gray levels) and is passed to a Mercury MC3200-NU array processor which performs FFTs and other array operations to obtain the two-dimensional autocorrelation of the original image. The array processor then uses a centroidal peak-finding routine to locate the two strongest autocorrelation peaks. These peak locations are stored as the most likely image displacements for that interrogation spot and the process begins again for the next spot.

After the full vector field is determined, post processing must be done to refine the data. As a first pass, the vector field is checked by a routine that looks for bad vectors that are outside of user-specified absolute limits and replaces them with the second peak for that location if it is acceptable, or with a default value to indicate a bad measurement. The few remaining spurious velocity vectors are manually removed and replaced with the aforementioned default value. Another automated routine then searches for default values and replaces them with values interpolated from valid neighboring vectors using multiple linear regression. The vector field is then smoothed by convolution with a Gaussian kernel as described by Landreth and Adrian[6] to eliminate random noise in the vector field caused by image imperfections, video noise, and other factors. This is crucial when spatial differentiation is to be performed on the vector field to derive quantities such as vorticity since any high-frequency random error will be accentuated in the derivatives.

Results

Interrogation System Validation

Validation of the PIV system first involved testing of the interrogation system. As a first check on the accuracy of the autocorrelation output and the associated image processing software, an interrogation was performed on a known uniform dot pattern with a spacing of 133 dots/inch in both the horizontal and vertical directions. After analysis, peaks in the spatial autocorrelation output were compared to the original dot pattern. The peak spacing was found to match identically with the original dot pattern. This is expected for a uniform pattern since each dot correlates

perfectly with itself, the closest neighbor in each direction, the second closest neighbor, etc.

Tests were then done with known-displacement simulated PIV photographs. The most accurate simulation used two photographs of uniform displacement image pairs, each with a different displacement. The photographs were made by first printing a randomly spaced dot pattern on an 8-1/2" x 11" sheet. A photograph of the unpaired images was then made onto 4" x 5" Kodak Technical Pan 4415 film in an enlarger. This unpaired image positive (clear dots on a dark background) was then attached to a translation stage and placed over unexposed film for contact printing. Exposures were made in the initial position and with the positive displaced a given distance by the translation stage, assuring uniform image displacements. The resulting paired image negative was again contact printed onto film, resulting in the desired paired image positive. Two photographs were made with displacements of approximately 100 μm and 200 μm. The photographs were then examined under a 14X stereo microscope equipped with a measuring reticule marked in 5 μm increments to determine the actual displacements as shown in Table 1. Both photos had approximately 12.5 image pairs/mm^2 and the image diameters varied from 20 μm to 50 μm. This variation in image size and other photographic effects due to the multiple printing of the images creates a good simulation of real PIV photographs, except for the presence of unpaired images which occurs in real flowfields due to out-of-plane motion. Interrogations were made of each photograph at 10,000 locations with the results shown in Table 1. The statistics shown were calculated using only "good" data falling within ±17 μm of the mean displacement in each direction, which was over 90 % of the total for both photos. Bad vector replacement and smoothing were not done in order to preserve the true error in the interrogation. The photos were interrogated at approximately a 45° angle of inclination to examine interrogation measurement errors in both the x- and y-directions. The data reveal that the standard deviation of the interrogated displacements is approximately equal for both photos. This is an expected result since the random error in displacement should be proportional to the particle image diameter and not the magnitude of displacement[7]. For a mean particle diameter, d_p, of 35 μm, the random error is approximately 6 % of d_p. It should be noted that although photographic imperfections and other factors in real PIV photos may tend to increase this error ratio, the use of vector field smoothing will tend to reduce the random error significantly as mentioned in the preceding section. The mean interrogated displacement for Photo 2 is taken as exactly 187 μm since it was used as the reference for determining the pixel-to-μm scaling factor. The mean interrogated displacement for

3

Photo 1 matches the actual displacement to within 1 %, showing no evidence of mean bias error.

The interrogation system was also used to analyze an actual PIV photograph of turbulent channel flow with published results[8]. The result of the interrogation is not shown here due to space limitations, but it showed similar flow structure to the published results and had a similar success rate of approximately 95 % valid vectors found during interrogation.

Low-Speed Axisymmetric Jet

The full PIV system has been used to examine the flow from an axisymmetric free jet test stand consisting of a 6" long, 1" O.D. tube fed by a TSI six-jet atomizer with silicone oil seed and an adjustable dilution air supply as shown in Fig. 5. The jet flows into an 8" x 10" x 48" test section exhausted to atmosphere. Image shifted PIV photographs were taken on both 35 mm and 4" x 5" film. Although the jet velocity is relatively low, experiments done with this test stand utilize all of the same equipment and procedures that are used for high-speed flow experiments, including seeding, automated system operation, photographic equipment, high-resolution film, electrooptical image shifting optics, and small image separations for high spatial resolution of velocity measurements. The purpose of the experiments is to demonstrate the operation and data analysis capabilities of the system.

The particle image sizes (in the frame of reference of the test section) were measured from the best photographs for determination of spatial resolution limits. Average image diameters were approximately 55 μm for 35 mm photos and 35 μm for 4" x 5" photos. The dynamic range of PIV measurements is limited by the measurable image separations, giving

$$\text{Dynamic Range} = \frac{\Delta X_{max}}{\Delta X_{min}}$$

$$= \frac{0.3(\text{interrogation spot diameter})}{\text{image diameter}}$$

where the value for maximum image separation is recommended by Keane and Adrian[9]. The maximum spatial resolution (minimum interrogation spot size) for a given image diameter and desired dynamic range can then be found. A reasonable dynamic range estimate can be as low as five since the ability to resolve slight changes in average image separation is a fraction of a pixel (out of the 512 pixel dimension of the image array) when a centroidal peak finding routine is used for interrogation. The estimate of a dynamic range of five results in the following:

Film Type	35 mm	4" x 5"
Image Dia.	55 μm	35 μm
Min. Spot Size	0.92 mm	0.58 mm

An example PIV photograph of the free jet was then interrogated. This photo was taken on Kodak Technical Pan 4415 4" x 5" film with a 120 mm lens at f5.6. Other parameters for acquisition and interrogation are shown in Fig. 6.

Before a full interrogation was done, the repeatability of measurements was checked by interrogating a small region of the photo then resetting the positioner to its original position and re-interrogating. The results showed perfect agreement of both the first and second peak locations for the entire 4 x 4 grid of interrogation spots. This was also done by re-interrogating two 5 x 5 regions (total of 50 spots) after the full interrogation was completed, resulting in 28 matches of both the first and second highest autocorrelation peaks, 18 matches of the first peak only, and 4 non-matches. It should be noted that exact peak locations can vary due to positioner error over long travel distances and random electronic noise in video imaging.

Removal and interpolation of bad vectors for the full flowfield showed a success rate for valid vector determination of approximately 94 %, which is quite reasonable in comparison to other reported success rates. The final velocity plot after subtraction of image shift, interpolation, and smoothing is shown in Fig. 6. The photo was interrogated over a 50 mm x 50 mm area with 0.5 mm increments in each direction, resulting in 10,201 vectors (101 x 101). The full interrogation took 11 hours, 18 minutes or 4.0 sec/spot using the autocorrelation method. Interrogations using the Young's fringe method took 2.3 sec/spot.

The mean velocity at the tube exit is approximately 2.05 m/s. Examination of Fig. 6 shows typical vortex structures at the edges of the jet with a gradual decrease in the centerline velocity as the jet propagates downstream. A plot of the axially averaged streamwise velocity component at each transverse location is shown in Fig. 7. Although this spatial mean is not equivalent to a time average velocity profile due to spreading of the jet over the field of view, it does reveal a general non-uniformity of the flow, implying that the jet is not truly axisymmetric. The higher velocity at the top of the tube was induced by the flow around a bend in the flexible tubing just prior to the straight section at the jet exit. Although the test flow is not ideal, the ability to reveal such information is part of the purpose of this experiment.

Identification of flow structures can also be done by manipulating the acquired velocity data. The vortex structure in the upper right section of Fig. 6 is shown in Fig. 8(a) with a portion of the mean streamwise velocity subtracted and in Fig. 8(b) by deriving the out-of-plane vorticity $(\frac{\partial v}{\partial x} - \frac{\partial u}{\partial y})$ from finite differences of the original velocity data. Both reveal the expected dominant positive (CCW) vorticity at the upper edge of

4

the jet and some resulting negative (CW) vorticity between the shed vortices. Such analysis allows quantification of the flow structure such as vortex strength and position. Similar analysis can be done by finding rate-of-strain, volumetric flux, and other derivative and integral quantities important in a particular flowfield to provide information about the nature of complex high-speed flows. Low-pass and high-pass spatial filtering can also be done[10] to reveal both large- and small-scale structures.

Transonic Base Flow

Two-dimensional finite thickness bases in subsonic and transonic flows form a separated flowfield very rich in turbulent structure due to the presence of the well-known von Karman vortex street wake. The motivation for studying this flow with PIV stems from both the fact that it exhibits a well-defined instantaneous structure and that the mechanism of the observed base drag reduction in the presence of a base cavity is not completely understood. Several studies of this topic have proposed various reasons for the drag reduction, including vortex trapping[11], loss of vortex strength due to cavity wall interference[12], and loss of vorticity due to fluid mixing at the cavity boundary[13]. Although numerical simulations[14,15] have shown agreement with experiments in the trend of drag reduction up to maximum cavity depth of approximately 0.3 to 0.5 base heights, they show discrepancies with experiments in the trends of both vortex shedding frequency and vortex formation location with increasing cavity depth.

In order to resolve these discrepancies and better define the mechanisms of base cavity drag reduction, PIV experiments are being done to match conditions used in both experimental work by Kruiswyk and Dutton[13] and computational work by Rudy[14]. Examples from Ref. 14 of numerical velocity and vorticity data for this flowfield are shown in Fig. 9.

Modifications have been made to an existing transonic wind tunnel for the use of PIV on two-dimensional base flows (Fig. 10). The previously fabricated tunnel has a 4" x 4" test section with solid side walls and slotted upper and lower inner walls to relieve the blockage effect of models in the transonic speed range. Six-inch diameter round windows are mounted in both sidewalls to allow visualization past the aft end of base models. The base models consist of interchangeable afterbodies mounted on a 15.24 mm thick wedge-shaped forebody. The afterbodies include a solid base, a rectangular cavity base with a depth of half the base height, and a rectangular cavity base with a depth of one full base height.

Slot-shaped upper and lower windows have been fabricated and installed in the outer walls for access with a vertically propagating planar laser sheet for PIV. The sheet passes through the lower window and through one of the streamwise slots of the inner wall to enter the

base flow test section. The seed delivery is done by two TSI six-jet atomizers feeding a single 3/4" O.D. tube which enters the stagnation chamber. This tube leads to a manifold tube which feeds 8 smaller tubes directed downstream and oriented in a transverse (vertical) plane aligned with the illuminating laser sheet. The flow then passes through 2" long, 3/16" cell honeycomb and a 44 x 44 mesh screen with 57 % open area to reduce turbulent fluctuations in the supply flow. It should be noted that the screen is cut out in the areas where the seed tubes feed through the honeycomb. This is due to the fact that experience with LDV in this laboratory has shown that silicone oil droplets tend to build up on any surfaces perpendicular to the flow direction, causing large drops to form and burst off, which bias velocity measurements. Flow seeding behind the base is sufficient due to the motion of the alternating von Karman vortex street carrying seed into the wake. This is seen in other flow visualization studies of subsonic two-dimensional base flows where seeded vortices are visible directly behind the base.

The first experiments in this facility were done without a base model to compare PIV velocity measurements to data obtained with both LDV and static pressure taps. To facilitate comparison to the time-integrated pressure and LDV measurements of velocity, PIV velocity data from a single photograph were summed along the row at each transverse location to obtain mean velocity components and standard deviations to determine turbulence intensities. Given that the flowfield is not evolving in the streamwise direction in this tunnel-empty case, equating spatial statistics to temporal statistics is adequate for a first approximation, although the number of samples available from a single PIV photograph is not sufficient for highly accurate statistics. It should be noted at this point that there were not yet any flow conditioning devices in the wind tunnel when these experiments were done, the effects of which will be discussed in the following paragraphs.

The results for mean velocity from a run at Mach 0.5 are shown in Fig. 11(a) with the relevant PIV parameters listed below. The PIV data are compared to the mean velocity calculated with pressure data from taps measuring P in the test section and P_o in the stagnation chamber. Although there are at most only 81 PIV measurements per data point in this plot, the mean velocity at each transverse location varies only slightly from the overall mean of 173.4 m/s which is within 2 % of the mean velocity determined from the pressure measurements.

A more stringent test of the accuracy of PIV lies in the ability to measure velocity fluctuations. To this end, LDV measurements of streamwise and transverse turbulence intensity were made for comparison to PIV data (Fig. 11(b)). Due to the spatial constraint of avoiding contact between the LDV laser and the lower

wall of the wind tunnel, LDV measurements could only be made up to a transverse location of -12.5 mm measured from the test section centerline. Again, a maximum of only 81 PIV measurements was used for the data at each transverse location, but it can be seen from the plot that both the LDV and PIV data vary from 5 % to 8 % turbulence intensity. Although this data lends some confidence in the accuracy of the PIV data, it revealed undesirable freestream turbulence in the test section without flow conditioning. The aforementioned honeycomb and screen were subsequently added. PIV measurements of turbulence intensity with the flow conditioning devices included have shown turbulence intensities of 3 % to 5 % which, while improved, are still relatively high. Although LDV measurements with flow conditioning have not yet been made due to restrictions on the availability of the LDV system, the high turbulence intensity measured by PIV is quite likely due to turbulence generated downstream of the honeycomb and screen by the velocity gradients between the freestream and the lower velocity seeded jets.

Experiments have most recently been done with a solid base model in a Mach 0.4 freestream. The Mach 0.4 freestream condition is determined by running the test section at a stagnation pressure which results in a Mach 0.4 flow when no model is present. The interpolated and smoothed velocity vector plot for a region approximately 1.3 to 2.3 base heights downstream of the base edge (see Fig. 10) is shown in Fig. 12(a). Seed density immediately behind the base was sufficient, but unpaired images due to out-of-plane motion and laser sheet thickness variations at the base reduced the successful interrogation rate in this region to approximately 40 %; results from this region were therefore not included in Fig. 12. Although the rotational flow around two of the vortices in the wake is somewhat evident in Fig. 12(a), the structure is accentuated by subtraction of a fraction of the mean streamwise velocity from the vector field in Fig. 12(b) which is plotted over a grayscale representation of the vorticity. Only every other vector is plotted in the interest of clarity. The vorticity plot reveals the fragmentation of the main vortices and the presence of lower vorticity small scale turbulent structures on the order of 3 mm diameter throughout the flowfield. The source of these structures is unknown, but may be due to the freestream turbulence levels or possibly is a secondary feature of this vortex street wake flow.

Conclusion

An operational PIV system has been developed for application in separated high-speed flows. The entire system has been successfully demonstrated both in validation experiments and in low- and high-speed air flows. Capabilities have also been demonstrated for detailed analysis of instantaneous flowfield velocity data to identify and quantify flow structures.

Current work has recently advanced to transonic base flows. Future work in this area will concentrate on reduction of freestream turbulence, adjustment of the acquisition system (increase in sheet thickness, laser tuning, etc.) to obtain higher data rates in the area immediately behind the base, and improvement of seeding uniformity, which has been the most challenging problem to this point.

The resulting velocity data for two-dimensional solid and cavity bases at various freestream velocities will be used for better definition of the source of structure within the flow including the small scale turbulence mentioned above, for quantitative analysis of the mechanisms of base cavity drag reduction, and for comparison to previous numerical and experimental data for the same flow.

References

1. Kompenhans, J., Hocker, R., "Application of Particle Image Velocimetry to High Speed Flows," *Von Karman Institute Lecture Series 1988-06, Brussels, March 21-25, 1988, pp. 67-83.*

2. Hocker, R., Kompenhans, J., "Application of Particle Image Velocimetry to Transonic Flows," *Proceedings, Fifth International Symposium on Applications of Laser Anemometry to Fluid Mechanics, Lisbon, Portugal, 1990, Paper 15.1.*

3. Post, M.E., Goss, L.P., Brainard, L.F., "Two-Color Particle-Imaging Velocimetry in a Turbine Cascade," *AIAA 29th Aerospace Sciences Meeting, Reno, Nevada, Jan. 1-7, 1991, Paper 91-0274.*

4. Landreth, C.C., Adrian, R.J., "Electrooptical Image Shifting for Particle Image Velocimetry," *Applied Optics, V.27, No.20, 1988, pp. 4216-4220.*

5. Bloomberg, J.E., "An Investigation of Particle Dynamics Effects Related to LDV Measurements in Compressible Flows," *M.S. Thesis, Univ. of Illinois at Urbana-Champaign, May 1989.*

6. Landreth, C.C., Adrian, R.J., "Measurement and Refinement of Velocity Data Using High Image Density Analysis in Particle Image Velocimetry," *Proceedings, Fourth International Symposium on Applications of Laser Anemometry to Fluid Mechanics, Lisbon, Portugal, 1988, pp. 485-497.*

7. Adrian, R.J., "Particle-Imaging Techniques for Experimental Fluid Mechanics," *Annu. Rev. Fluid Mech., V.23, 1991, pp. 261-304.*

8. Adrian, R.J., Offutt, P.W., Landreth, C.C., Liu, Z., Hanratty, T.J., "Studies of Liquid Turbulence Using Double-Pulsed Particle Correlation," *Proceedings, Fifth International Symposium on Applications of Laser Anemometry to Fluid Mechanics, Lisbon, Portugal, 1990, Paper 15.4.*

9. Keane, R.D., Adrian, R.J., "Optimization of Particle Image Velocimeters. Part I: Double Pulsed Systems," *Meas. Sci. Technology, V.1, No.11, 1990, pp. 1202-1215.*

10. Reuss, D.L., Adrian, R.J., Landreth, C.C., French, D.T., Fansler, T.D., "Instantaneous Planar Measurements of Velocity and Large-Scale Vorticity and Strain Rate in an Engine Using Particle-Image Velocimetry," *SAE International Congress and Exposition, Detroit, MI, 1989, Paper 890616.*

11. Pollock, N., "Some Effects of Base Geometry on Two-Dimensional Base Drag at Subsonic and Transonic Speeds," *Australian ARL, Aerodynamics Note 316, Oct. 1969.*

12. Nash, J.F., Quincey, V.G., Callinan, J., "Experiments on Two-Dimensional Base Flow at Subsonic and Transonic Speeds," *ARC R&M No. 3427, Jan. 1963.*

13. Kruiswyk, R.W., Dutton, J.C., "Effects of a Base Cavity on Subsonic Near-Wake Flow," *AIAA Journal, V.28, No.11, 1990, pp. 1885-1893.*

14. Rudy, D.H., "A Numerical Study of Unsteady Two-Dimensional Subsonic Compressible Base Flow," *Ph.D. Thesis, Univ. of Illinois at Urbana-Champaign, April 1987.*

15. Clements, R.R., "Computer Models of Separated Flows Behind Two-Dimensional Bluff Bodies," *Ph.D. Dissertation, Cambridge University, July 1973.*

TABLE 1

Uniform displacement photograph interrogation results.

	Photo 1	Photo 2
$\overline{\Delta x}$ (μm)	63.515	131.299
$\overline{\Delta y}$ (μm)	58.523	133.153
$\sigma_{\Delta x}$ (μm)	2.001	2.166
$\sigma_{\Delta y}$ (μm)	1.929	2.153
$\sigma_{\Delta x}/d_p$	5.72 %	6.19 %
$\sigma_{\Delta y}/d_p$	5.51 %	6.15 %
$\overline{|\Delta X|}$ (μm)	86.366	187.000
$\overline{|\Delta X|}_{actual}$ (μm)	87.000	187.000

Interrogation Spot	0.8 x 0.8 mm
Increment	0.4 mm
Total Spots/Photo	10,000
Image Pairs/Spot	~8
Mean Image Dia. d_p	~35 μm

$\overline{\Delta x}$ = mean interrogated x-displacement

$\overline{\Delta y}$ = mean interrogated y-displacement

$\overline{|\Delta X|}$ = $((\overline{\Delta x})^2 + (\overline{\Delta y})^2)^{1/2}$
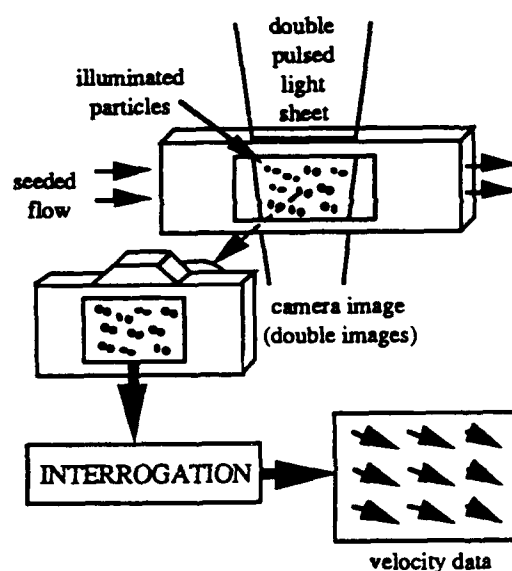
FIGURE 1 Principle of PIV
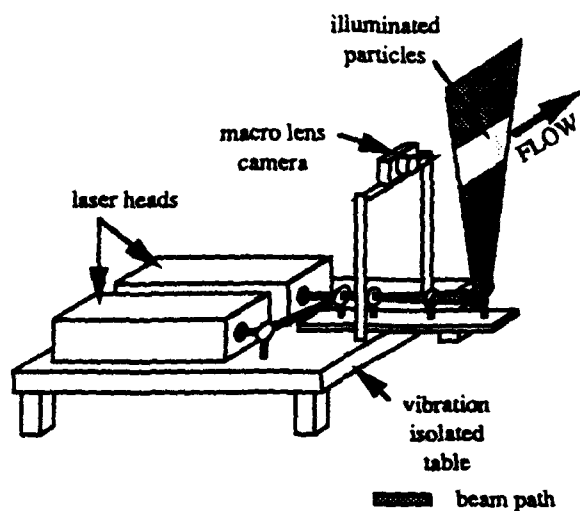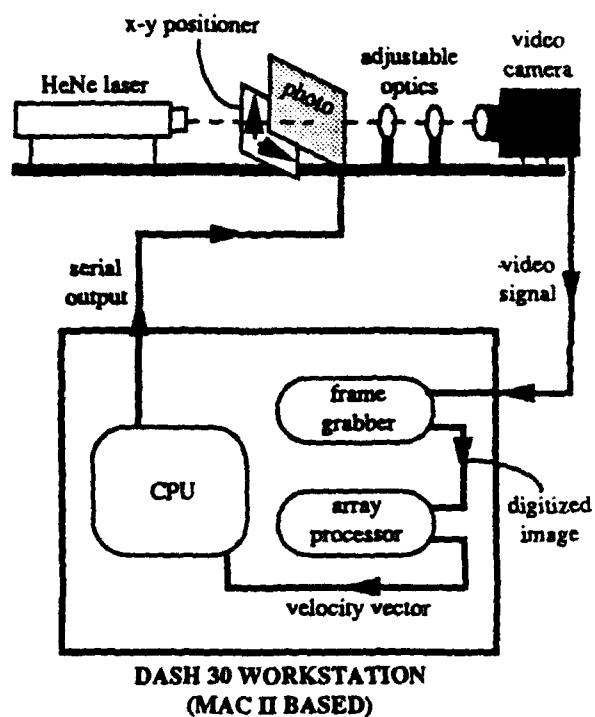
FIGURE 2 Acquisition System

**DASH 30 WORKSTATION
(MAC II BASED)**

FIGURE 4 Interrogation System Schematic
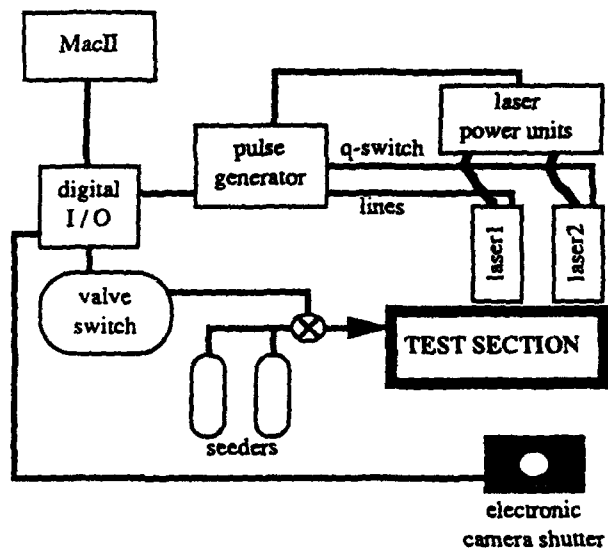
FIGURE 3 Acquisition System Control Schematic
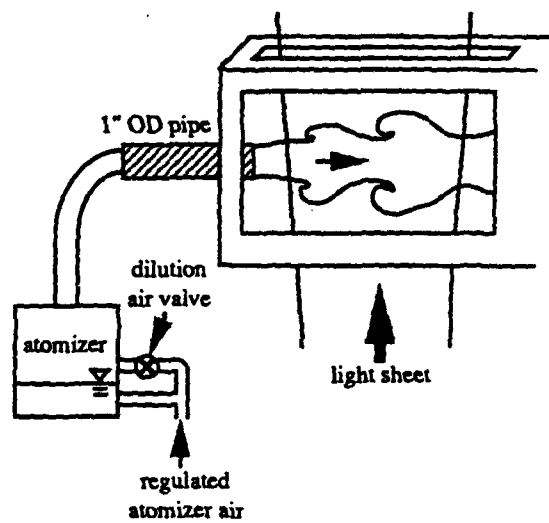
FIGURE 5 Axisymmetric Jet Test Stand

8
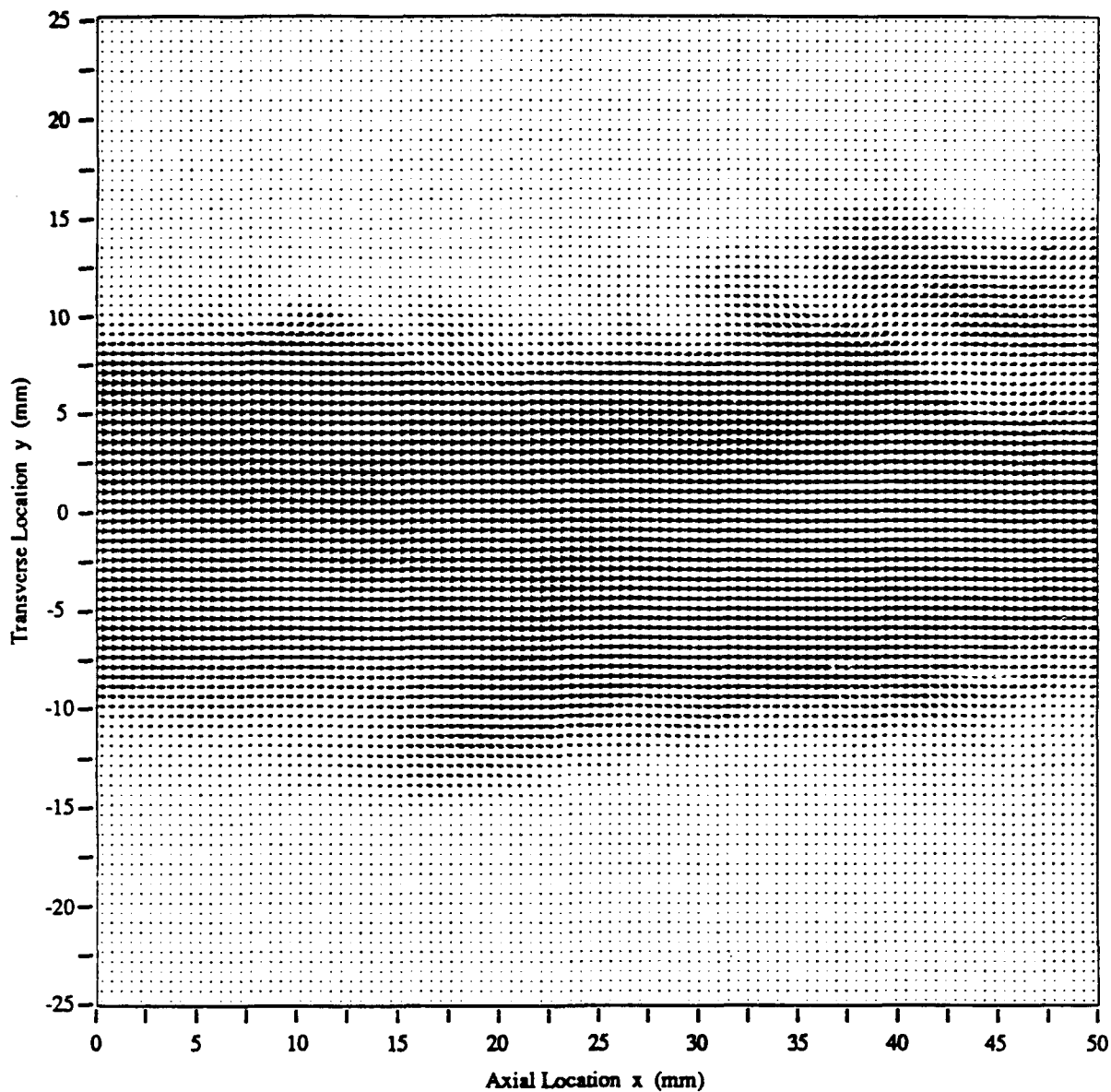
→ 2.0 m/s

PIV PARAMETERS

Mean Jet Exit Velocity	2.05 m/s	Interrogation Method	autocorrelation
Jet Diameter	18 mm	Spot Size (in flowfield)	1.08 mm x 1.08 mm
Laser Energy	500 mJ/pulse	Increment	0.5 mm
Laser Sheet Thickness	0.5 mm	Avg. Image Pairs/Spot	approx. 8
Pulse Separation	150 μs	Interrogation Time	11 hrs. 18 min.
Image Shift	100 μm (transverse)		(10,201 spots @ 4.0 sec/spot)
Magnification	1.08	Success Rate	approx. 94 %

FIGURE 6 Axisymmetric Jet Velocity Field

9
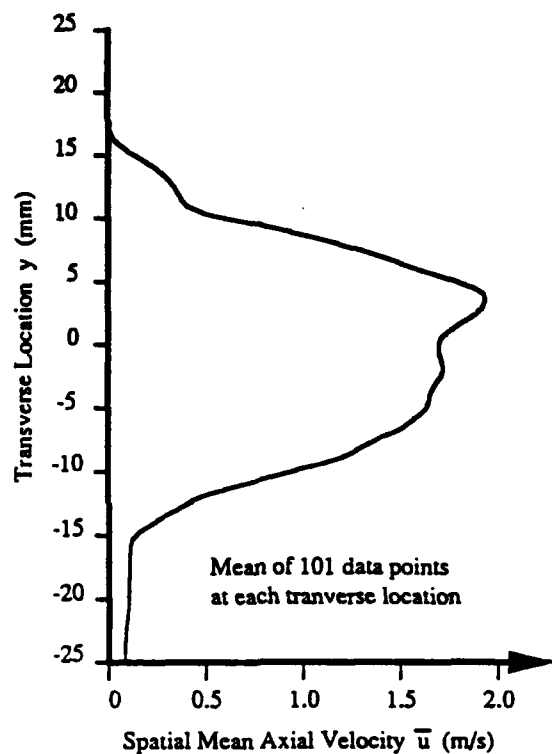
FIGURE 7 Axisymmetric Jet Spatial Mean Velocity

→ 1.5 m/s

(a)

-1400 sec⁻¹   1400 sec⁻¹

(b)
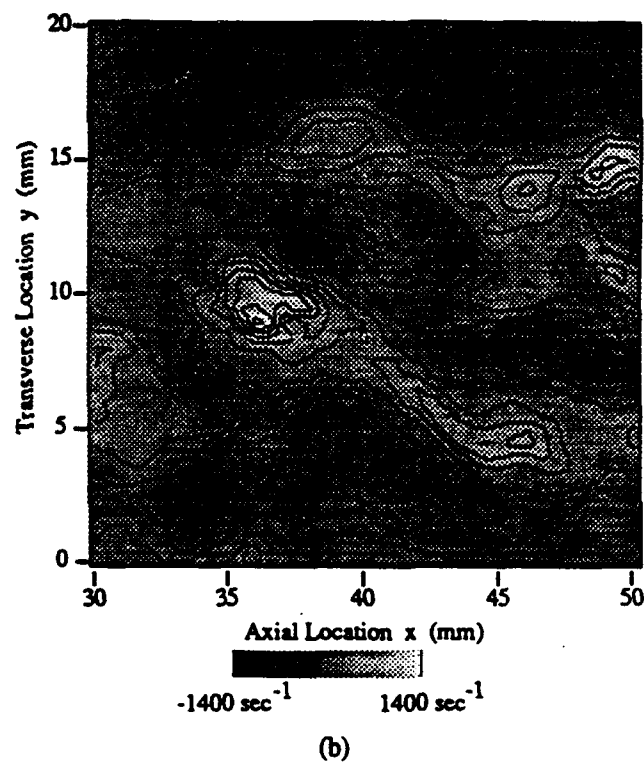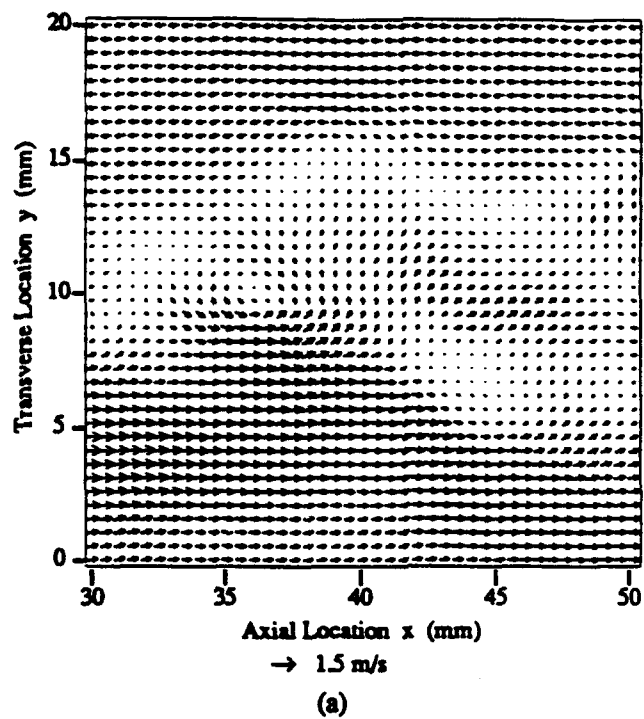
FIGURE 8 Enlarged Section of Axisymmetric Jet
(a) Velocity field with 1/3 of mean jet velocity subtracted
(b) Vorticity

(a)   (b)
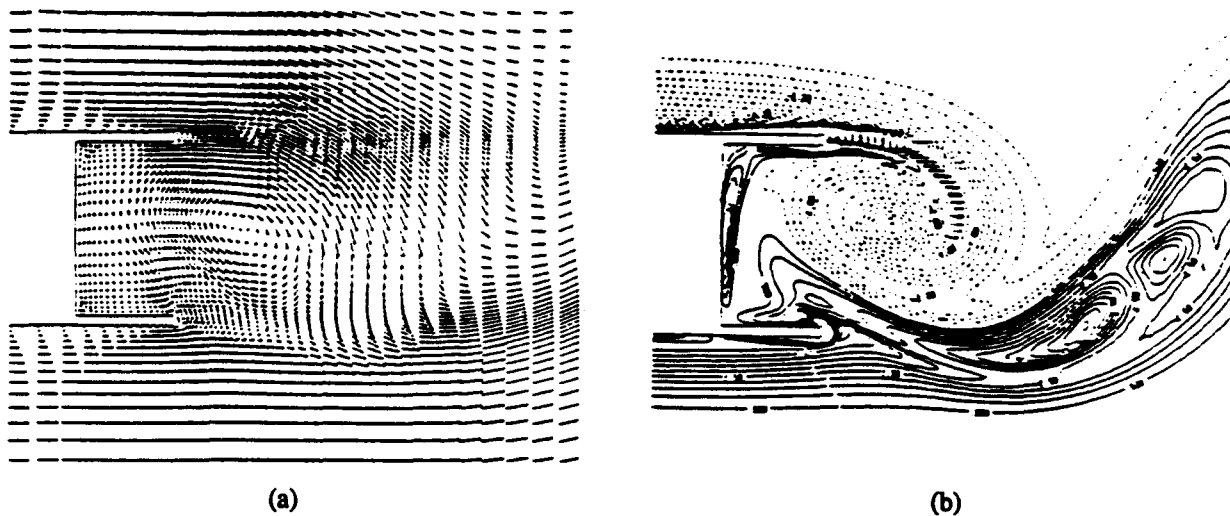
FIGURE 9 Base Flow Numerical Simulations (from Ref. 14)
(a)   Velocity field for half-height cavity, $M_\infty = 0.6$
(b)   Constant vorticity contours for half-height cavity, $M_\infty = 0.6$
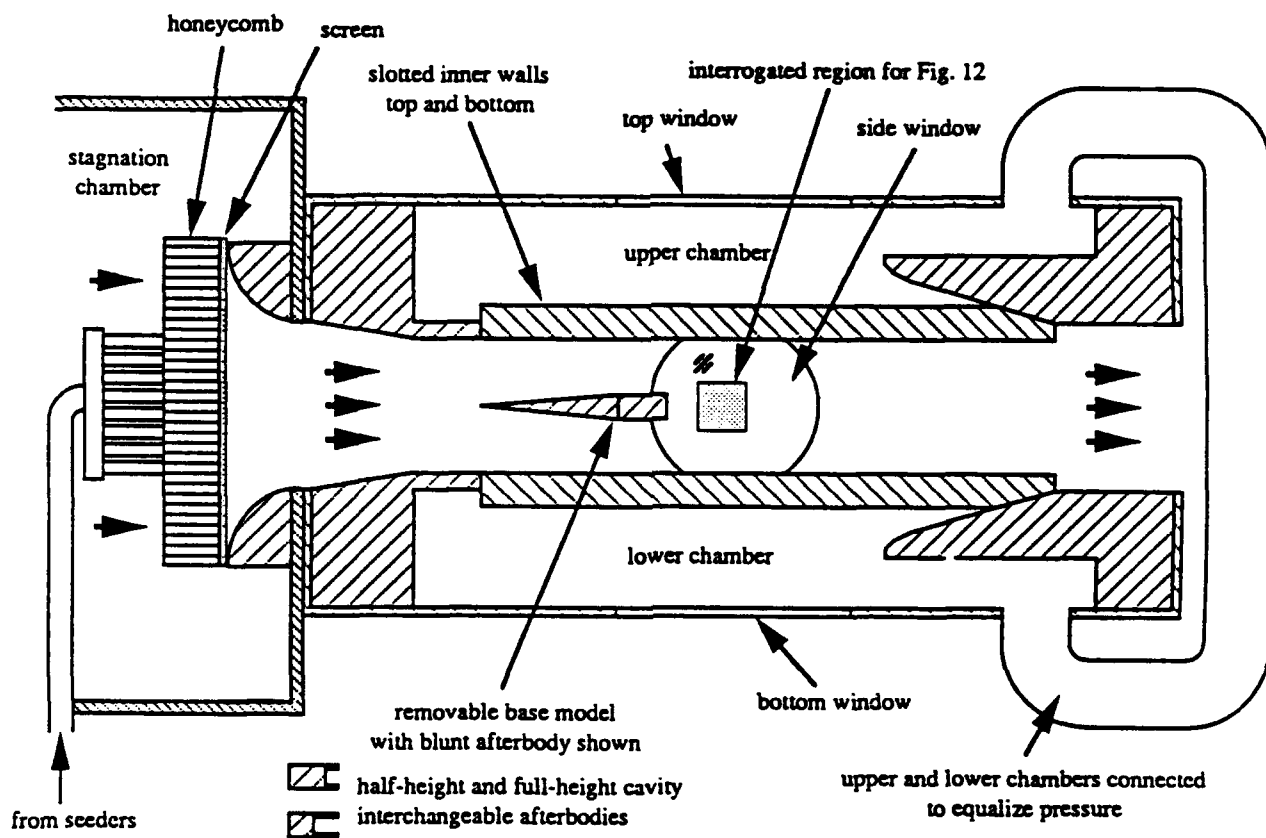
FIGURE 10 Transonic Base Flow Test Section

11

(a)

→ 180 m/s

(a)

(b)

→ 120 m/s

-65000 sec^{-1} 65000 sec^{-1}

(b)
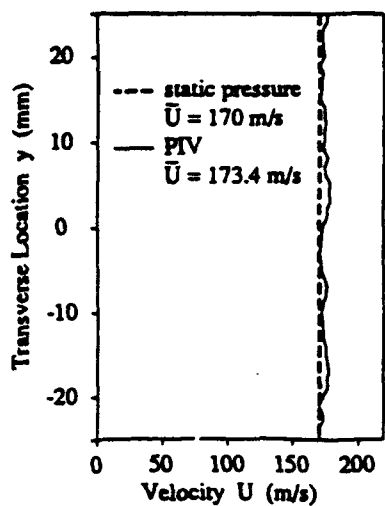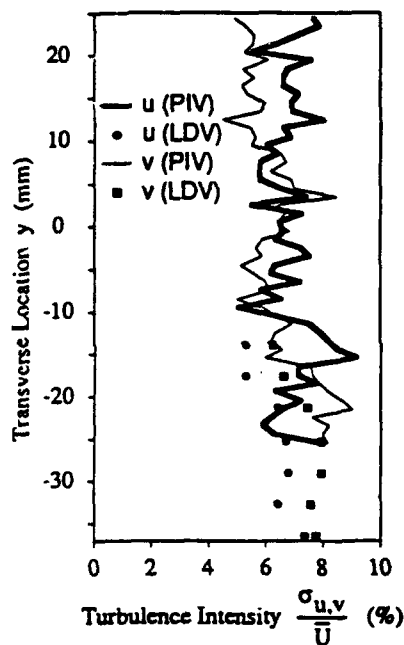
PIV PARAMETERS

Laser Energy	450 mJ/pulse
Laser Sheet Thickness	0.5 mm
Film type	35 mm
Magnification	0.3
Image Shift	none
Interrogation Method	autocorrelation
Spot Size (in flowfield)	1.1 mm x 1.1 mm
Increment	1 mm

PIV PARAMETERS

Laser Energy	450 mJ/pulse
Laser Sheet Thickness	0.8 mm
Film type	35 mm
Magnification	0.31
Image Shift	100 μm horizontal
Interrogation Method	autocorrelation
Spot Size (in flowfield)	1.2 mm x 1.2 mm
Increment	.6 mm

FIGURE 11 Mach 0.5 Tunnel-Empty Results
(a) PIV spatial mean velocity vs. temporal mean velocity
    from pressure data
(b) Turbulence intensity: PIV spatial data vs. LDV
    temporal data

FIGURE 12 Transonic Base Flow
(a) Velocity field
(b) Vorticity and velocity field with 100 m/s subtracted

12

APPENDIX A.10

A PLUME-INDUCED BOUNDARY LAYER SEPARATION EXPERIMENT

by

R. J. Shaw and J. C. Dutton

A PLUME-INDUCED BOUNDARY LAYER
SEPARATION EXPERIMENT

Russell J. Shaw, Graduate Research Assistant

and

J. Craig Dutton, Professor

Department of Mechanical and Industrial Engineering

University of Illinois at Urbana-Champaign

Urbana, Illinois 61801

INTRODUCTION

This paper describes an ongoing experimental investigation of plume-induced, turbulent boundary layer separation as it occurs in supersonic flight. Plume-induced boundary layer separation (PIBLS) is a phenomenon that can occur on a wide range of aerodynamic vehicles during some portion of the flight regime. Examples include single-stage tactical missiles, multiple-stage missiles and rockets, high-performance fighter aircraft, and atmospheric reentry vehicles to name but a few. Figure 1 depicts PIBLS occurring on a generic two-stage missile. The existence of PIBLS in the flowfield can detrimentally influence the static stability of the vehicle, degrade the effectiveness of control surfaces, and significantly contribute to base and afterbody heating. Since these effects can severely endanger the structural integrity of the aerodynamic vehicle, PIBLS is a subject worthy of the scientific community's attention because, not only is it an important topic for basic fluid dynamics research, but a better understanding of this phenomenon can also benefit the flight performance of aerodynamic vehicles.

In addition to being dependent upon the vehicle geometry, the occurrence of this phenomenon is also dependent upon the external airstream and nozzle flow properties. The exhaust gases from a propulsive unit, either a jet engine or a rocket motor, will expand to form a plume with a diameter larger than the engine nacelle or vehicle body diameter when the static pressure at the nozzle exit plane is substantially larger than the static pressure of the surrounding airstream. The presence of this underexpanded exhaust plume deflects the freestream flow and thereby imposes an adverse pressure gradient upon the afterbody boundary layer. If the momentum of the fluid in the boundary layer is not sufficient to overcome this adverse pressure gradient, the boundary layer will separate upstream of the physical corner of the base. The upstream movement of the boundary layer separation point, resulting from the interaction of the exhaust plume with the external airstream, is called plume-induced boundary layer separation.

With the development of jet aircraft and ballistic missiles in the 1950's, PIBLS began to be recognized as a potential problem affecting the flight performance of atmospheric vehicles. The early experimental investigations of this flowfield phenomenon were conducted in the 1960's and involved laminar boundary layers. Laminar boundary layers were used because the region of the flight envelopes which encountered the most severe cases of PIBLS occurred at high altitudes where the extremely large jet-to-freestream static pressure ratios resulted in extensive regions of separation and, consequently, the laminar boundary layer did not have a sufficient development distance for transitioning to a turbulent state prior to separation. These early studies were conducted on both single nozzle [e.g., 1,2] and multiple nozzle [e.g., 3,4] base configurations, and focused primarily on understanding the impact that PIBLS had on the static stability of aerodynamic vehicles by examining both the overall physical characteristics of the separated flow region (separation pattern, separation length, angle of separation, etc.) and the resultant aerodynamic loads as a function of various flow properties (jet static pressure ratio, freestream Mach number, freestream Reynolds number, etc.), base and afterbody geometries (nozzle divergence angle, afterbody flare or boattail angle, nozzle-to-base diameter ratio, etc.), and angle of attack. These studies relied strongly upon schlieren photography, surface oil flow visualization, measurements of the resultant aerodynamic forces and moments, and, to a lesser extent, surface static pressure measurements to examine the effects caused by PIBLS.

As a result of the design evolution of propulsion units to produce higher thrust, the region of the flight envelope encountering PIBLS expanded [5] and the plume-induced separation of turbulent boundary layers became important. Experimental studies involving the plume-induced separation of turbulent boundary layers were conducted on wind tunnel models beginning in the 1970's. With one exception [6], these experiments were primarily conducted at the Aeronautical Research Institute of Sweden (FFA) [e.g., 7,8] and the University of Alabama [9-11], and have tended to focus on obtaining insight into the fundamental nature of PIBLS flowfields. While the

University of Alabama experiments involved surface pressure fluctuation measurements beneath the unsteady separation shock wave, the FFA experiments, specifically the pressure probe measurements of Agrell [12] and the one-component laser Doppler velocimeter (LDV) measurements reported by Agrell [13] and Pira and Agrell [14], attempted to make flowfield property measurements throughout the separated flow region of a PIBLS flowfield. Although for different reasons, neither the LDV technique [13,14] nor the pressure probe technique [12] were sufficiently accurate to allow a quantitative determination of the velocity field within a PIBLS region.

Beginning in the 1950's and continuing on into the 1960's, two analytical techniques were developed for calculating the flow properties behind a blunt base immersed in a supersonic flow. The two techniques were the integral or moment method [15] and the Chapman-Korst component or multicomponent method [16,17]. Although the integral method was extended to deal with a zero thickness base geometry undergoing PIBLS [18], this technique has proven to be more difficult and less versatile than the component method [19]. Aided in part by the development of computer programs by Addy [e.g., 20], the component method emerged in the 1970's as the method of choice for computing PIBLS flowfields because of its flexibility in modeling a wide range of base geometries and flow proper..es. The component method has been used to calculate PIBLS flowfields on aerodynamic bodies at both zero and nonzero angles of attack [e.g., 21,22]. On axisymmetric models at zero angle of attack, the component method, in general, underpredicts the extent of separation at lower jet static pressure ratios and overpredicts the extent of separation at higher jet static pressure ratios. Although the quantitative prediction of the base pressure distributions and the separation lengths are not, generally speaking, in good agreement with the experimental measurements, the qualitative trends induced by the jet static pressure ratio and the nozzle half-angle are predicted reasonably well by the component method for both symmetric and asymmetric PIBLS flowfields.

With the advent of supercomputers and better numerical algorithms, the numerical modeling of PIBLS flowfields using Navier-Stokes (N-S) methods has developed over the past decade and stands today as an area of major interest. The Navier-Stokes investigations which have calculated PIBLS flowfields [e.g., 23,24], in general, underpredict the extent of separation, underpredict the separation angle, and underpredict the base and afterbody pressure distributions. Even when one of these studies was successful at quantitatively predicting one or more of these four features, the remaining features were not in agreement with the experimental data. Although the quantitative prediction of these features, in general, is in poor agreement with the experimental measurements, the parametric trends induced by the jet static pressure ratio and the nozzle half-angle are predicted reasonably well by the N-S methods.

A majority of the N-S studies [e.g., 25,26] have emphasized the need for better turbulence modeling throughout the plume-induced, separated region of the flowfield in order to achieve a more accurate prediction of the flow. As just discussed, the extent of the separation zone, the angle of separation, and the surface static pressure distributions over the base and afterbody have formed the basis for comparing N-S calculations with experimental data. Although these features allow a determination to be made of the general accuracy of a N-S prediction, they do not permit a direct evaluation of a turbulence model's ability to predict the turbulence structure throughout a plume-induced, separated flowfield. Accurate measurements of mean velocity and turbulence quantities obtained throughout a PIBLS flowfield are necessary in order to evaluate the accuracy of a turbulence model. This is exactly the information that the present work is directed at obtaining.

The experimental investigation described herein will provide a better understanding of the mechanisms and interactions present in a PIBLS flowfield primarily by measuring the mean and fluctuating components of velocity with an LDV system. Schlieren photographs and shadowgraph pictures, surface flow visualization, and mean and fluctuating wall static pressure measurements have also been made of the PIBLS flowfield. By gaining a better understanding of the fluid

2

dynamic processes present in a PIBLS flowfield, it is felt that the existence of this phenomenon can more accurately be predicted and thus technological improvements can be made to aerodynamic vehicles which will delay, control, or totally eliminate either PIBLS or the adverse effects associated with its occurrence.

FLOW FACILITY AND WIND TUNNEL DESCRIPTION

The experiments conducted in this study are performed using the flow facility located in the Gas Dynamics Laboratory. The flow facility consists of a tank farm with a storage capacity of approximately 146 m³ and two air compressors: an Ingersoll-Rand compressor which produces 0.68 kg/s at 960 kPa and a Gardner-Denver compressor which delivers 0.33 kg/s at 760 kPa.

A two-stream, supersonic wind tunnel was specifically designed to produce plume-induced, turbulent boundary layer separation in the test section. The small-scale wind tunnel incorporates a two-dimensional planar geometry and operates in the blowdown mode. The geometry of the wind tunnel is shown in Figures 2 and 3. Figure 2 is a cross sectional view of the wind tunnel test section. Figure 3 is a photograph of the actual PIBLS wind tunnel with one side wall removed. In order to minimize pressure losses, the cross sectional area of each stream was scaled so that the Mach number of the flow would not exceed 0.2 at any location upstream of the nozzle blocks. The region of supersonic flow in each stream is produced with a fixed nozzle block whose diverging contour was calculated using the method of characteristics nozzle design program NOZCS. The height of the base is 1.27 cm and the angle between the two streams is 40 degrees (see Figure 2). The width of each stream is 5.08 cm, except at the inlet of the tunnel where each stream is 7.62 cm wide. Optical access to the test section is provided by a removable glass window assembly mounted in each of the two side walls of the tunnel.

As just stated, the angle between the two streams is 40 degrees. A brief discussion of the method used to arrive at this value is in order since choosing this parameter was the most critical aspect in the design of the wind tunnel. In essence, the concept was to choose an angle between the two streams which would be sufficient to deflect the discriminating streamline present in the shear layer emanating from the separation point (assumed to be at the corner of the base) in the upper stream at an angle of about 15 degrees (discussed below) with respect to the freestream flow direction. The location of the discriminating streamline was calculated using the restricted model of the multicomponent method [27,28] modified to include the reattachment criterion of Addy [29] with a reattachment coefficient of 0.9. All of the computations were done for a single operating condition: an upper stream stagnation pressure of 517 kPa and a lower stream stagnation pressure of 345 kPa. By summarizing data taken from experiments on turbulent boundary layer separation ahead of forward-facing steps for Mach numbers ranging from 1.0 to 6.0 and step heights of at least one boundary layer thickness, Zukoski [30] found that the inner surface of the shear layer bounding the separation zone formed an angle of 13 degrees with respect to the freestream flow direction and the outer surface formed an angle of 16.5 degrees. Since separation in the forward-facing step experiments is produced by a solid geometric boundary and separation in the PIBLS study is caused by a compliant aerodynamic boundary, there is an intrinsic difference between the two flowfields [31] and therefore it was deemed unnecessary to know the precise location of the discriminating streamline in the forward-facing step experiments. The decision was made to simply equate the angle of the discriminating streamline in the PIBLS study to a value slightly above (approximately 15 degrees) the average of the angles between the upper and lower surfaces of the shear layer from the forward-facing step data of Zukoski. The angle of the discriminating streamline in the upper shear layer of the PIBLS investigation was computed to be 14.7 degrees for an angle between the two streams of 39 degrees, and 15.5 degrees for an angle of 40 degrees. The decision was made to opt for the 40 degree angle, and, in so doing, it was hoped that there would exist sufficient latitude in throttling or unthrottling the lower stream away from the 345 kPa stagnation pressure design point so as to achieve PIBLS.

3

Preliminary investigations of the flowfield using schlieren photographs, shadowgraph pictures, and surface oil flow visualization have shown that plume-induced, boundary layer separation can be produced in the wind tunnel designed for this investigation (see Figures 4 and 5). Acceptable PIBLS flowfields can be produced by varying the stagnation pressure of the lower stream over the approximate range of 255 kPa to 186 kPa while maintaining a stagnation pressure of 517 kPa in the upper stream. This corresponds to jet static pressure ratios of approximately 2.4 to 1.7. In these flowfields, a boundary layer develops on the bottom wall of the upper stream and forms a free shear layer after undergoing separation somewhere upstream of the upper base corner. It is interesting to note that an angle of approximately 15 degrees (i.e., the value used in the design) results from averaging the angles made by the inner and outer surfaces of this shear layer. The separation point is nominally located 1.9 cm (about $6\delta_0$) forward of the upper base corner (as determined by surface oil flow experiments) at a lower stream stagnation pressure of 255 kPa ($p_j/p_\infty=2.4$). (The surface flow technique determines the downstream boundary of the region over which the unsteady shock wave oscillates [32].) The nominal location of the separation point can be reduced to approximately 0.64 cm (about $2\delta_0$) forward of the upper base corner if the stagnation pressure in the lower stream is throttled to about 186 kPa ($p_j/p_\infty=1.7$). The only two regions having a spanwise variation in the streamwise location of the separation line, as delineated by the surface oil flow experiments, are located adjacent to each wind tunnel side wall and extend for 0.97 cm from each side wall. Since the separation line is straight and perpendicular to the freestream flow direction over the inner 3.18 cm of the tunnel width, the flowfield appears to be reasonably two-dimensional over this inner region.

From the review of experimental work on the plume-induced separation of turbulent boundary layers, the separation process has been shown to be unsteady on wind tunnel models. Separation shock wave unsteadiness has also been reported on actual flight vehicles undergoing PIBLS [33, 34], although it is unknown whether the mechanism causing the unsteadiness on the wind tunnel models is the same mechanism causing the unsteadiness on flight vehicles. The PIBLS flowfield produced in the wind tunnel of this investigation also exhibits an unsteady separation process. The streamwise extent of the unsteadiness (as indicated by separation shock motion) has been estimated from schlieren observations to be on the order of several boundary layer thicknesses. The detailed motion of the unsteady separation shock wave also appears under schlieren observation to be very similar to the unsteadiness described in the PIBLS experiments of Boggess [9] and Doughty [10,11], i.e. a quasi-random, aperiodic movement of the shock. This unsteadiness clearly poses a problem when making LDV measurements because it is impossible to distinguish between velocity fluctuations caused by turbulent eddies and velocity fluctuations caused by the gross translational movement of the separation region. The conditional sampling approach to be used to address this LDV measurement problem is described in the following section.

RESULTS

Although a range of PIBLS flowfields can be produced in the wind tunnel designed and built for this investigation, only one such flowfield has been chosen in which to conduct the detailed LDV measurements. The flowfield chosen for the preliminary measurements presented in this paper is produced by setting the upper and lower stream stagnation pressures at approximately 517 kPa and 255 kPa, respectively. The foot of the separation shock wave is then nominally located 1.9 cm (about $6\delta_0$) upstream of the base corner and thus, based upon previous experimental results [7], the separation process should be a free-interaction at this location.

Schlieren/Shadowgraph Visualizations

Visualization of the near-wake flowfield has been documented using shadowgraph pictures and schlieren photographs. Both systems were configured with components in the standard "Z"-shaped arrangement where the light source and receiving optics were positioned as close as possible to the collimated light beam passing through the wind tunnel test section. The schlieren system uses a Xenon Model 457 Micropulser light source having a spark duration of approximately 1.4 microseconds when operated in the single pulse mode. The shadowgraph system uses a Xenon Model 437B Nanopulser light source having a spark duration of approximately 25 nanoseconds in the single pulse mode. The collimated light was created using two, 30.48 cm diameter, 243.8 cm focal-length mirrors. The receiving optics in the schlieren setup consisted of a horizontally mounted knife-edge, and a "smoked" glass collection plate for viewing the image or a Polaroid film holder for obtaining a permanent photograph. The receiving optics in the shadowgraph setup consisted of a Nikon Model F2 35 mm camera. Figure 4 shows a typical schlieren photograph of the PIBLS flowfield while Figure 5 shows a typical shadowgraph picture. When comparing the two prints, it is quite evident that the shadowgraph system, with the 25 nanosecond light pulse, resolves much smaller turbulence scales throughout the flowfield than does the schlieren system.

Mean Static Pressure Measurements

Mean wall static pressure measurements have been obtained from static pressure taps mounted in the top, bottom, and base surfaces of the center partition, as well as from a side wall assembly that has been extensively instrumented with static pressure taps. The top surface of the center partition has twenty-nine pressure taps installed at a spanwise station located 0.475 cm off the wind tunnel centerline. (The taps could not be placed on the centerline because two miniaturized, high-frequency response, piezoresistive pressure transducers are mounted along the centerline.) Beginning 0.318 cm upstream of the base plane and extending to 3.81 cm upstream of the base plane, the taps are located every 0.159 cm; the taps are uniformly spaced every 0.635 cm starting at 3.81 cm upstream of the base plane and continuing to 7.62 cm upstream of the base plane. The bottom surface of the center partition has four pressure taps mounted along the same spanwise station as the top surface. The location of these taps begins 0.318 cm upstream (measured local to the Mach 1.5 flow direction) of the base plane and continues to 1.27 cm upstream of the base plane in intervals of 0.318 cm. The base plane of the center partition has four pressure taps mounted along a spanwise station 0.556 cm off the wind tunnel centerline. Beginning 0.419 cm from the top surface of the center partition, the taps are located every 0.203 cm.

The side wall static pressure measurement assembly is a rectangular aluminum insert which is used for conducting mean static pressure measurements over the entire PIBLS flowfield. In order to do so, one of the window assemblies is removed from the tunnel side wall and the pressure measurement assembly is installed in its place. This assembly contains 425 static pressure taps uniformly distributed, 0.229 cm between centers, over the main region of interest in the flowfield. The region of interest was established from schlieren photographs and is shown in Figure 6.

Pressure measurements from the pressure taps in the center partition, the side wall insert, and the pitot probes at the nozzle entrances are acquired by connecting the pressure taps to a Pressure Systems Incorporated Model DPT 6400 digital pressure transmitter using clear flexible vinyl tubing. The pressure transducers of the DPT 6400 were calibrated with a Bell & Howell dead weight tester. Figure 7 shows a two-dimensional surface plot of the mean static pressure field taken from the side wall insert. The general trends of a constant pressure in the base region and a pressure increase in the initial portion of the wake redevelopment region downstream of the

point of confluence between the two shear layers is evident in the data. However, the strong pressure gradients across the separation shock wave and the recompression shock waves emanating from the point of confluence between the two shear layers are significantly smeared over a sizeable area due to the unsteadiness of the separation process. These mean static pressure measurements, along with those shown in Figure 8, provide strong motivation for conducting conditional sampling of the LDV data. Figure 8 shows the mean static pressure measurements taken from the pressure taps in the top surface of the center partition and the mean static pressure measurements taken from a horizontal row of pressure taps, 0.114 cm above the top surface of the center partition, in the side wall insert. The two rows of measurements differ over the intermittent region of the separation shock motion and over the separated region confined between the intermittent region and the base plane.

Conditionally Sampled LDV Measurement Approach

The mean and fluctuating velocity components will be measured with the LDV over the entire region of interest in the PIBLS flowfield. Also, measurements in the turbulent boundary layer and the adjacent inviscid flow for both streams forward of the separation location will be made. In order to obtain LDV measurements throughout an unsteady PIBLS flowfield, a means must be found to overcome the problems posed by the unsteady separation shock motion. There are essentially two options: either a method must be found to stabilize the separation shock or a conditional sampling technique must be developed for acquiring the data. There are several passive techniques available which have been used to stabilize shock wave motion on airfoils in transonic flow [e.g., 35]. Unfortunately, it is not at all obvious that these techniques will apply to a supersonic two-stream interaction. In addition, applying blowing or suction to the boundary layer, or any other approach that would produce the same effect, will perturb the flow in the separated region and hence is unacceptable. Previous work by Doughty [11] has shown that the length scale of the unsteadiness can be reduced by approximately 80% in a PIBLS flowfield by positioning a small wire protuberance of circular cross section near the separation point. This method was implemented in the wind tunnel designed for the present PIBLS study and the resulting flowfields were examined qualitatively using schlieren photography. Although a reduction in the length scale of the unsteady separation shock wave motion was observed, this approach was deemed inappropriate for the present PIBLS study because the presence of the small wire protuberances appeared to alter the turbulence structure in the resulting separated shear layer. Therefore, a conditional sampling technique for acquiring and analyzing the LDV data is under development.

The approach of conditionally sampling LDV data using surface pressure measurements as a means for locating the separation shock wave has been reported in the experiments of Kussoy, et al. [36]. In this study, six fast-response pressure transducers were used to conditionally sample LDV measurements taken from two unsteady separated flowfields produced by a cylinder-flare body. The axis of the 30 degree flare was canted at an angle relative to the axis of the cylinder in order to produce a region of three-dimensional separation. Flowfields for canted angles of 5 degrees and 23 degrees were examined by simultaneously measuring and recording the pressure sensed at all six pressure transducers with every LDV measurement. However, the authors reported only one rather simple approach for conditionally sampling the data. This approach basically consisted of dividing the transducer array region into two sections using the pressure sensed at the transducer located beneath the average shock position. This transducer, called the center transducer, was identified by observing shadowgraph movies of the shock unsteadiness. For each LDV measurement location, the ensemble-averaged mean and standard deviation of the pressure (P_w and σ_{pw}) were computed using the pressure data recorded from the center transducer. Then, for each LDV measurement location, all LDV realizations having an associated pressure level greater than $P_w + \sigma_{pw}$ were collected and labeled as the "shock forward" data set. Likewise, all LDV realizations having an associated pressure level less than $P_w - 0.5\sigma_{pw}$ were collected and labeled as the "shock back" data set. Using this conditional sampling technique on the data from both flowfields, Kussoy, et al. [36] reported the mean streamlines constructed from the ensemble-

averaged velocity components, contours of the mean streamwise velocity, and the streamwise distribution of the maximum turbulent kinetic energy (k_{max}) for all three data sets: the "shock forward" data set, the "shock back" data set, and the data set constructed from ensemble-averaging all of the measurements. The authors pointed out that, although the recirculating core within the separated region does move streamwise along the cylinder, there is little change in the appearance of the mean velocity field as the shock wave fluctuates between its upstream and downstream positions. The streamwise distributions of the maximum turbulent kinetic energy for both flowfields show that the largest difference between the three data sets occurs in the intermittent region over which the shock wave oscillates.

The conditional sampling technique, more accurately described as a conditional analysis technique, used in the current work is being implemented in the following manner. Two Kulite Model XCS-062-15G pressure transducers have been mounted flush to the surface of the lower wall of the Mach 2.5 stream as shown in Figure 9. The transducers are located 1.91 cm and 1.65 cm upstream of the base plane, and are both within the intermittent region of the separation shock wave motion. The flowfield to be studied will be selected by adjusting the stagnation pressure of the lower stream such that the two pressure transducers are positioned on either side of the average separation shock location. The two time history traces, one trace created from each of the two pressure transducers during the course of a tunnel run, will be used to define the instantaneous location of the separation shock wave by implementing a two-threshold algorithm [37,38] designed to determine whether the shock wave is upstream or downstream of each transducer. There are three regions in which the shock could be located at any instant in time: the region upstream of both pressure transducers, the region in between the two transducers, and the region downstream of both transducers. LDV data acquisition from a TSI Model IFA 750 digital Doppler signal processor is controlled using FIND software running on a Gateway 2000 personal computer, which is an IBM-compatible 486 machine. By initializing acquisition of the LDV data simultaneously with the acquisition of data from the pressure transducers, the location of the separation shock wave relative to the two pressure transducers can be determined for each LDV realization because each velocity measurement also has an absolute time stamp, accurate to within one microsecond, recorded at the time of acquisition. Thus, during data analysis, each LDV measurement will be sorted according to the region in which the shock was located when the LDV measurement was acquired. By comparing the ensemble-averaged flowfield quantities derived from the LDV measurements taken while the separation shock was in the region between the two transducers with the ensemble-averaged flowfield quantities computed from all of the LDV measurements, the effect of the unsteady separation shock wave motion on the mean velocity and turbulent statistical data can be determined.

The data acquisition system for the pressure transducers is based around a Macintosh IIfx computer equipped with 32 MBytes of RAM, a 160 MByte internal hard disk drive, a National Instruments Model NB-A2000 Analog-to-Digital (A/D) converter, and a MicroNet Technology Model SB-1000 external hard disk drive having a storage capacity of approximately 1 GByte. Data acquisition via the A/D converter is controlled by a National Instruments Model NB-DMA2800 Direct Memory Access Interface Board. LabVIEW 2, an icon-based computer language written by National Instruments, is used exclusively to acquire and analyze the pressure data. This data acquisition system is capable of simultaneously sampling two channels at a rate of 166,667 samples/sec per channel for 8.5 minutes (longer than the blowdown time of the tunnel) before overwriting the allocated memory buffer. Currently, LabVIEW programs based upon the two-threshold algorithm [37,38] are being written to analyze the pressure data.

The conditional analysis technique outlined above will work in principle because the frequency spectrum of the unsteady separation shock wave motion, although being broadband, is centered around 1 kHz or less as shown in the power spectral density estimate of Figure 10. The data used to create Figure 10 were taken with the pressure data acquisition system by sampling one

7

of the flush-mounted pressure transducers located in the intermittent region at a rate of 416,667 samples/sec. The resulting time history was then digitally low-pass filtered at 100 kHz and FFT calculations using the split-radix algorithm were performed on each of 183 records, where each record consists of 16,384 data points. The power spectral density estimate is plotted as $f \cdot G(f)$ versus f on linear-log axes [39] as shown in Figure 10.

Once the LabVIEW conditional analysis programs have been completed, acquisition of the two-component conditionally sampled LDV data will commence. Results of these measurements will be reported in detail in future publications.

CONCLUSIONS

The current paper describes an experimental investigation of a PIBLS flowfield produced by the interaction between two nonparallel, supersonic streams in the presence of a finite thickness base. The purpose of the study is to gain a better understanding of the extent to which the fluid dynamic mechanisms and interactions present in the PIBLS flowfield influence the turbulence properties of the flow. A two-stream, supersonic wind tunnel, incorporating a two-dimensional planar geometry and operating in the blowdown mode, was specifically designed to produce a PIBLS flowfield. Preliminary experiments have demonstrated that the wind tunnel is capable of producing a wide range of PIBLS flowfields by simply regulating the stagnation pressure of the lower stream (jet flow) relative to the upper stream (freestream flow). One PIBLS flowfield has been chosen in which to conduct a detailed set of measurements. This flowfield has its separation point located about $6\delta_0$ upstream of the base corner. A detailed study of this PIBLS flowfield is underway using schlieren photography and shadowgraph pictures, surface streakline visualization, surface static pressure measurements, and two-component, coincident LDV measurements.

Unfortunately, the separation shock wave associated with the PIBLS flowfields is unsteady. The streamwise extent of the unsteadiness was estimated from schlieren observation to be on the order of several boundary layer thicknesses. This unsteadiness poses a problem when making LDV measurements because it is impossible to distinguish between velocity fluctuations caused by the turbulent eddies and velocity fluctuations caused by the gross movement of the separated region. Fortunately, this problem is not insurmountable. A conditional sampling technique for acquiring and analyzing the LDV data is currently under development using surface static pressure measurements taken from fast-response pressure transducers as a means of tracking the separation shock wave motion. This technique effectively reduces the length scale of the unsteadiness by eliminating from the data analysis any LDV measurements that are recorded when the shock wave is outside the region confined between the two pressure transducers.

ACKNOWLEDGMENTS

REFERENCES

1. Salmi, R. J., "Effects of Jet Billowing on Stability of Missile-Type Bodies at Mach 3.85," NASA TN D-284, June 1960.

2. Hinson, W. F. and Falanga, R. A., "Effect of Jet Pluming on the Static Stability of Cone-Cylinder-Flare Configurations at a Mach Number of 9.65," NASA TN D-1352, September 1962.

3. Goethert, B. H., "Base Flow Characteristics of Missiles with Cluster-Rocket Exhausts," Aerospace Engineering, Vol. 20, No. 3, March 1961, pp. 28-29, 108-117.

4. Alpinieri, L. J. and Adams, R. H., "Flow Separation Due to Jet Pluming," AIAA Journal, Vol. 4, No. 10, October 1966, pp. 1865-1866.

5. Deep, R. A., Henderson, J. H., and Brazzel, C. E., "Thrust on Missile Aerodynamics," Report No. RD-TR-71-9, U.S. Army Missile Command, Redstone Arsenal, Alabama, May 1971.

6. James, C. R., "Aerodynamics of Rocket Plume Interactions at Supersonic Speeds," AIAA Paper No. 81-1905, AIAA Atmospheric Flight Mechanics Conference, Albuquerque, New Mexico, August 1981.

7. Agrell, J. and White, R. A., "An Experimental Investigation of Supersonic Axisymmetric Flow Over Boattails Containing a Centered Propulsive Jet," Technical Note AU-913, The Aeronautical Research Institute of Sweden (FFA), December 1974.

8. White, R. A. and Agrell, J., "Boattail and Base Pressure Prediction Including Flow Separation for Afterbodies with a Centered Propulsive Jet and Supersonic External Flow at Small Angles of Attack," AIAA Paper No. 77-958, AIAA/SAE 13th Propulsion Conference, Orlando, Florida, July 1977.

9. Boggess, A. L., "An Investigation of the Unsteady Flow Associated with Plume-Induced Flow Separation," Bureau of Engineering Research Report No. 149-02, University of Alabama, July 1972; also available as NASA CR-112218.

10. Doughty, J. O., "Effects of Periodic Plume Pulsing on the Flow Field Generated by Plume Induced Flow Separation," Bureau of Engineering Research Report No. 164-02, University of Alabama, December 1973.

11. Doughty, J. O., "A Study of a Plume Induced Separation Shock Wave, Including Effects of Periodic Plume Unsteadiness," Bureau of Engineering Research Report No. 207-02, University of Alabama, October 1976; also available as NASA CR-150170.

12. Agrell, J., "An Experimental Survey of a Separated Region on a Conical Afterbody in a Supersonic Free Stream," Report No. TN-AU-1187, The Aeronautical Research Institute of Sweden (FFA), October 1978.

13. Agrell, J., "Wind Tunnel Investigation of Separated Flow Over an Afterbody in Supersonic Axisymmetric Stream Utilizing One-Component Laser-Doppler-Velocimetry," Technical Note 1983-10, The Aeronautical Research Institute of Sweden (FFA), 1983.

14. Pira, K. and Agrell, J., "LDV Measurements in the Separated Region Bounded by Supersonic Flows at a Rocket Afterbody," In: International Congress on Instrumentation in Aerospace Simulation Facilities (ICIASF), Saint-Louis, France, September 1983.

15. Alber, I. E. and Lees, L., "Integral Theory for Supersonic Turbulent Base Flows," AIAA Journal, Vol. 6, No. 7, July 1968, pp. 1343-1351.

16. Chapman, D. R., "An Analysis of Base Pressure at Supersonic Velocities and Comparison with Experiment," NACA TN 2137, July 1950.

17. Korst, H. H., Page, R. H., and Childs, M. E., "A Theory for Base Pressures in Transonic and Supersonic Flow," ME Technical Note 392-2, Mechanical Engineering Department, University of Illinois, March 1955.

18. Klineberg, J. M., Kubota, T., and Lees, L., "Theory of Exhaust-Plume / Boundary-Layer Interactions at Supersonic Speeds," AIAA Journal, Vol. 10, No. 5, May 1972, pp. 581-588.

19. Fox, J. H. and Bauer, R. C., "Analytical Prediction of the Base Pressure Resulting from Hot, Axisymmetric Jet Interaction in Supersonic Flow," AIAA Paper No. 81-1898, AIAA 8th Atmospheric Flight Mechanics Conference, Albuquerque, New Mexico, August 1981.

20. Addy, A. L., "Plume-Induced Free-Stream Separation During Powered Supersonic Flight: A Computer Program and Representative Results," Report No. RD-72-20, U.S. Army Missile Command, Redstone Arsenal, Alabama, December 1972.

21. Addy, A. L., Korst, H. H., White, R. A., and Walker, B. J., "A Study of Flow Separation in the Base Region and Its Effects During Powered Flight," AGARD Conference on Aerodynamic Drag, CP-124, April 1973.

22. Wagner, B., "Jet-Afterbody Interference on Missiles in Supersonic Flow," AGARD Conference on Ramjets and Ramrockets for Military Applications, CP-307, October 1981.

23. Diewert, G. S., "Supersonic Axisymmetric Flow Over Boattails Containing a Centered Propulsive Jet," AIAA Journal, Vol. 22, No. 10, October 1984, pp. 1358-1365.

24. Fox, J. H., "Predicting Plume-Induced Separation on Bluff-Base Bodies," AIAA Paper No. 84-0315, AIAA 22nd Aerospace Sciences Meeting, Reno, Nevada, January 1984.

25. Deiwert, G. S., Andrews, A. E., and Nakahashi, K., "Theoretical Analysis of Aircraft Afterbody Flows," AIAA Paper No. 84-1524, AIAA 17th Fluid Dynamics, Plasma Dynamics, and Lasers Conference, Snowmass, Colorado, June 1984.

26. Sahu, J., "Computations of Supersonic Flow Over a Missile Afterbody Containing an Exhaust Jet," Journal of Spacecraft and Rockets, Vol. 24. No. 5, September-October 1987, pp. 403-410.

27. Korst, H. H. and Tripp, W., "The Pressure on a Blunt Trailing Edge Separating Two Supersonic Two-Dimensional Air Streams of Different Mach Number and Stagnation Pressure but Identical Stagnation Temperature," Proceedings of the Fifth Midwestern Conference on Fluid Mechanics, 1957, pp. 187-199.

28. Tripp, W., "The Base Pressure Behind a Blunt Trailing Edge for Supersonic Two-Dimensional Flow; Approaching Streams Having the Same Stagnation Temperature but

Dissimilar Mach Numbers and Stagnation Pressures," Ph.D. Thesis, University of Illinois, Urbana, Illinois, 1956.

29. Addy, A. L., "Experimental-Theoretical Correlation of Supersonic Jet-on Base Pressure for Cylindrical Afterbodies," Journal of Aircraft, Vol. 7, No. 5, September-October 1970, pp. 474-477.

30. Zukoski, E. E., "Turbulent Boundary-Layer Separation in Front of a Forward-Facing Step," AIAA Journal, Vol. 5, No. 10, October 1967, pp. 1746-1753.

31. Buchanan, T. D., "Study of Flow Separation on Missile by Jet Plume," M.S. Thesis, University of Tennessee, Tullahoma, Tennessee, August 1967.

32. Gramann, R. A. and Dolling, D. S., "Interpretation of Separation Lines from Surface Tracers in a Shock-Induced Turbulent Flow," AIAA Journal, Vol. 25, No. 12, December 1987, pp. 1545-1546.

33. Jones, J. H., "Acoustic Environment Characteristics of the Space Shuttle," NASA TM-X-52876, Space Transportation System Technology Symposium, Volume 2: Dynamics and Aeroelasticity, July 1970, pp. 285-300.

34. Wilkinson, C. L., "Heat Transfer Within Plume-Induced Flow Separation Region of Saturn 5," Paper No. ASME-69-WA/HT-18, ASME Winter Annual Meeting, Los Angeles, California, November 1969.

35. Raghunathan, S., Hall, D., and Mabey, D., "Alleviation of Shock Oscillations in Transonic Flow by Passive Controls," AIAA Paper No. 90-0046, AIAA 28th Aerospace Sciences Meeting, Reno, Nevada, January 1990.

36. Kussoy, M. I., Brown, J. D., Brown, J. L., Lockman, W. K., and Horstman, C. C., "Fluctuations and Massive Separation in Three-Dimensional Shock-Wave / Boundary-Layer Interactions," Second International Symposium on Transport Phenomena in Turbulent Flows, Tokyo, Japan, October 1987.

37. Dolling, D. S. and Brusniak, L., "Separation Shock Motion in Fin, Cylinder and Compression Ramp-Induced Turbulent Interactions," AIAA Journal, Vol. 27, No. 6, June 1989, pp. 734-742.

38. Brusniak, L., "Evaluation of Conditional Sampling Methods for Analyzing Separation Shock Motion," AIAA Paper 88-0091, AIAA 26th Aerospace Sciences Meeting, Reno, Nevada, January 1988.

39. Dolling, D. S. and Smith, D. R., "Unsteady Shock-Induced Turbulent Separation in Mach 5 Cylinder Interactions," AIAA Paper No. 88-0305, AIAA 26th Aerospace Sciences Meeting, Reno, Nevada, January 1988.
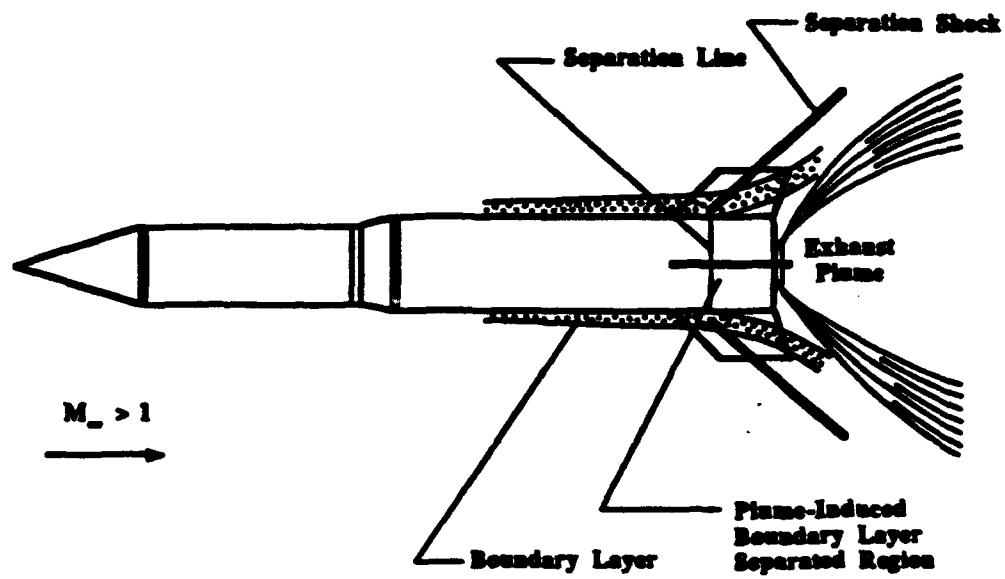
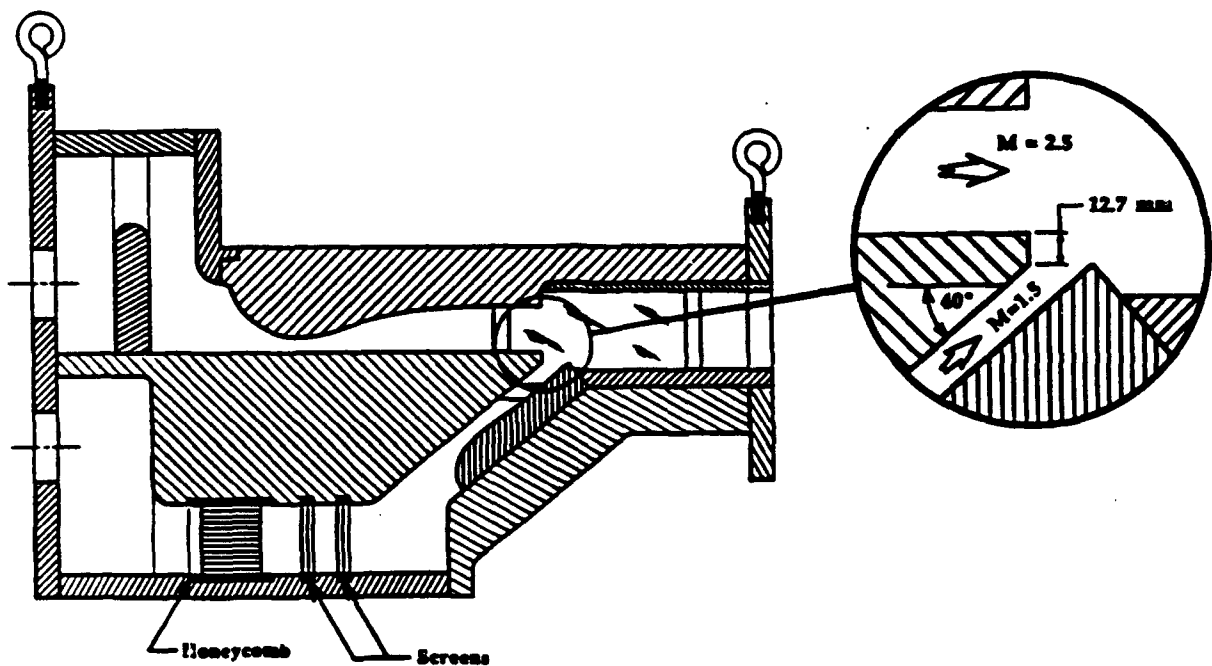Figure 1. Typical PIBLS Phenomenon Occurring on a Missile

Figure 2. Cross Sectional View of the PIBLS Wind Tunnel

12

Figure 3. Photograph of the PIBLS Wind Tunnel

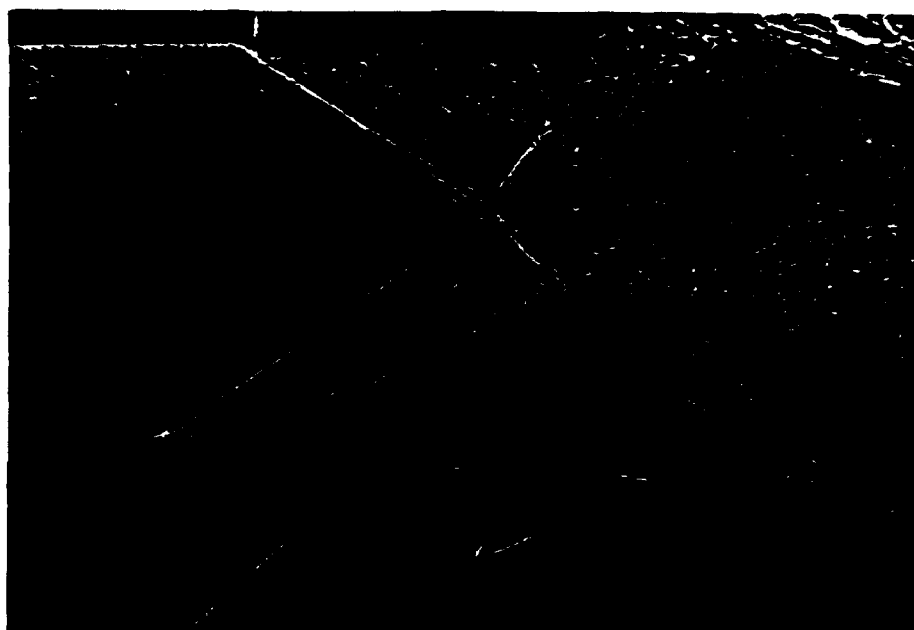Figure 4. Typical Schlieren Photograph of PIBLS Flowfield

13

Figure 5. Typical Shadowgraph of PIBLS Flowfield
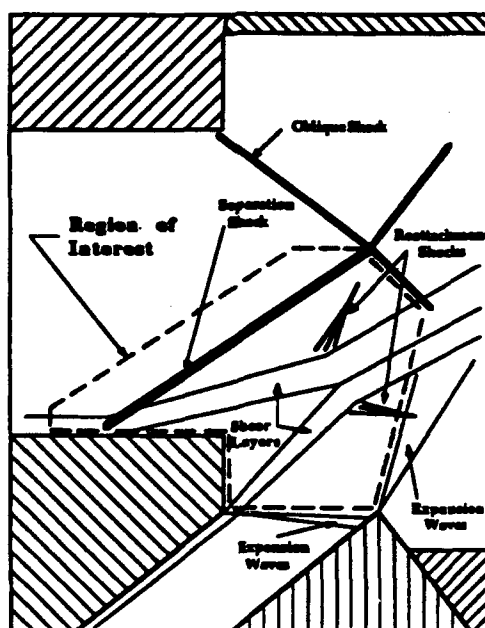

Figure 6. Region of Interest in PIBLS Flowfield

14
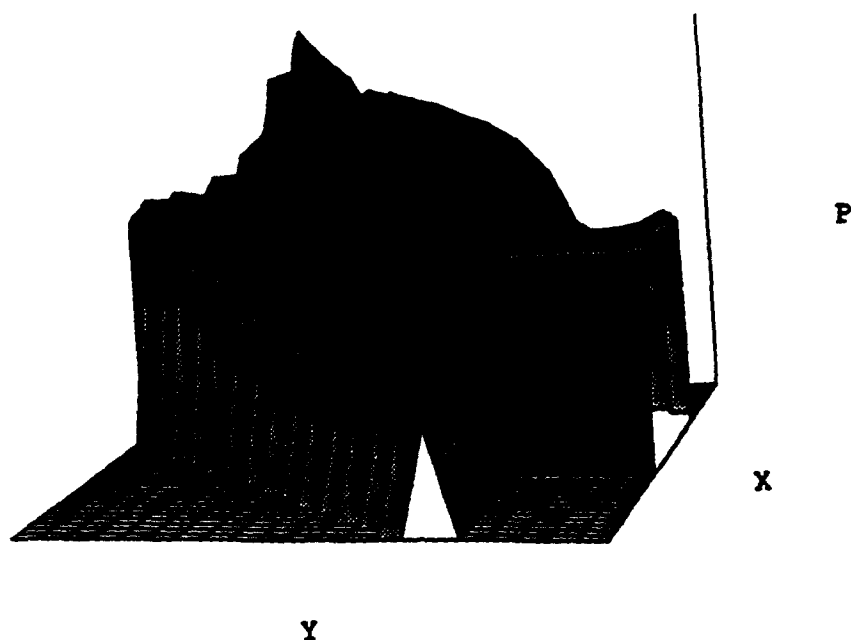
Figure 7. Surface Contour Plot of the Mean Static Pressure Field
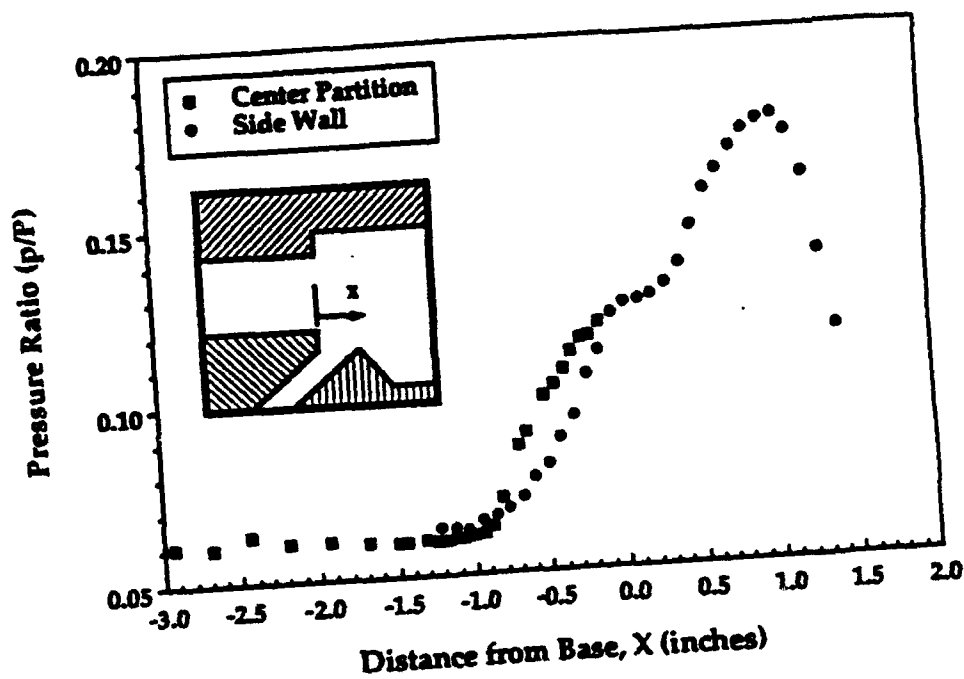
Figure 8. Streamwise Distribution of the Mean Static Pressure Along/Near the Center Partition

15
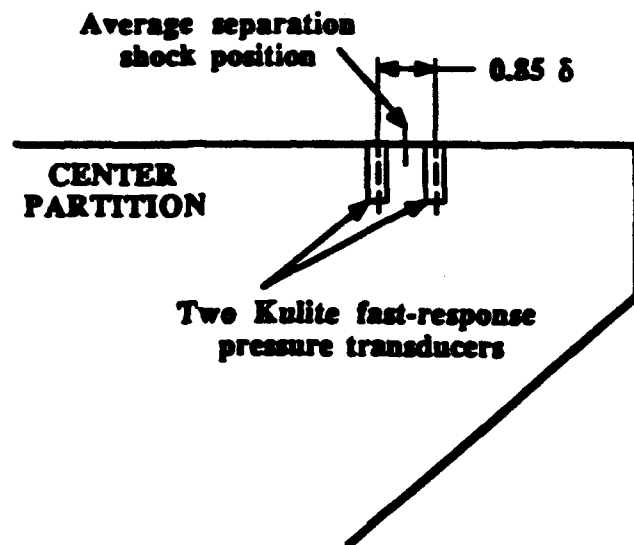
Figure 9. Fast-Response Pressure Transducer Mounting Locations
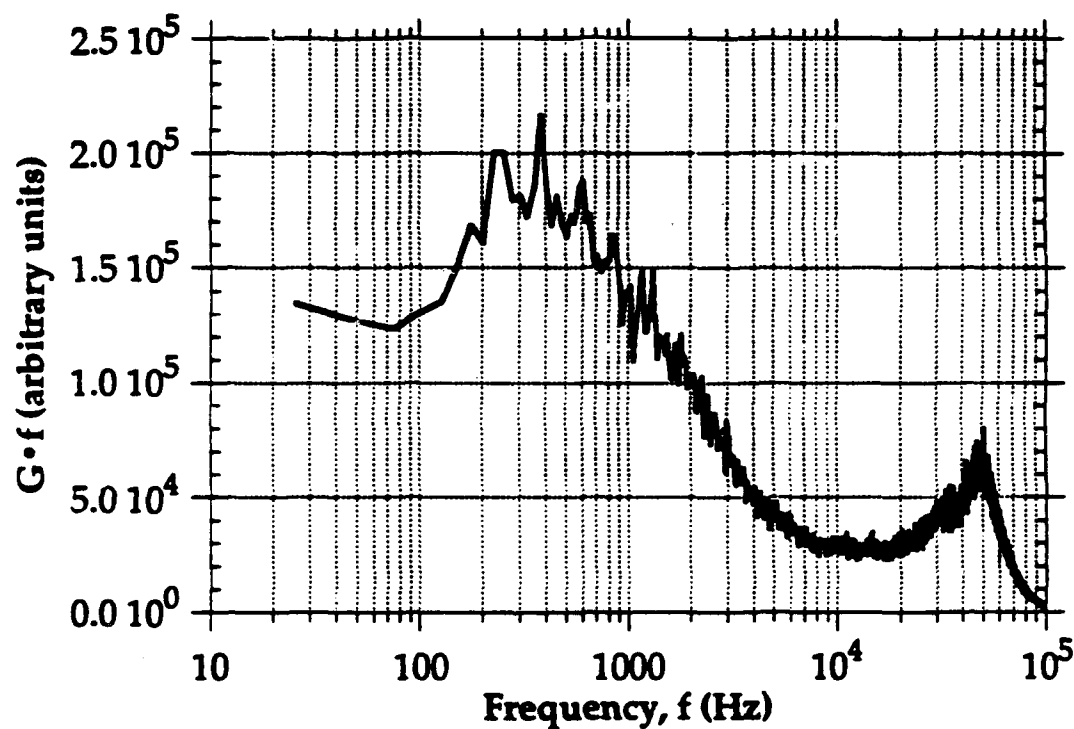
Figure 10. Power Spectral Density Estimate of the Pressure Signal in the Intermittent Region

16

APPENDIX A.11

STUDY OF THE NEAR-WAKE STRUCTURE OF A SUBSONIC BASE CAVITY FLOWFIELD USING PIV

AIAA Paper No. 93-3040

Presented at the <u>24th AIAA Fluid Dynamics Meeting</u>

Orlando, Florida

July 1993

by

M. J. Molezzi and J. C. Dutton

AIAA 93-3040
Study of the Near-Wake Structure of a Subsonic Base Cavity Flowfield Using PIV

M. J. Molezzi and J. C. Dutton
Dept. of Mechanical & Industrial Engineering
University of Illinois at Urbana-Champaign
Urbana, IL

AIAA 24th
Fluid Dynamics Conference
July 6-9, 1993 / Orlando, FL

STUDY OF THE NEAR-WAKE STRUCTURE OF A SUBSONIC BASE CAVITY FLOWFIELD USING PIV

M. J. Molezzi[*] and J. C. Dutton[**]
Department of Mechanical and Industrial Engineering
University of Illinois at Urbana-Champaign
Urbana, IL 61801

Abstract

A new particle image velocimetry (PIV) system has been used to study the near-wake structure of a two-dimensional base in subsonic flow in order to determine the fluid dynamic mechanisms of observed base drag reduction in the presence of a base cavity. Experiments were done over a range of freestream Mach numbers up to 0.8, including local flowfield velocities over 300 m/s. Effects of the base cavity on the von Kármán vortex street wake were found to be related to the expansion and diffusion of vortices near the cavity, although the effects are of small magnitude and no significant change in the vortex formation location or path was observed. The base cavity effects are also less significant at higher freestream velocities due to the formation of vortices further downstream from the base. The base cavity drag reduction was found to be mainly due to the displacement of the base surface to a location upstream of the low-pressure wake vortices, with only a slight modification in the vortex street itself.

Introduction

The separated flow past a two-dimensional body at subsonic speed and large Reynolds number forms a wake structure made up of alternately shed vortices known as the von Kármán vortex street. This commonly occurring structure has been the subject of numerous studies beginning with von Kármán's first theoretical analysis of vortex streets[1]. A significant feature of this flowfield is the interaction of the low pressure vortices in the near-wake with the downstream surface or base of the body, inducing a net streamwise pressure force on the body known as base drag. The base drag is typically a significant component of total drag, even for slender bodies with a finite thickness base. For this reason, drag reduction methods based on the modification of the vortex street have received much attention.

One effective drag reduction method is the use of a base cavity, which is the subject of this study. It has been shown experimentally that the presence of a solid-walled cavity in the base of a slender two-dimensional body (see Fig. 1) increases the base pressure, resulting in base drag reduction of up to 30%[2-5]. Other effects of a base cavity that have been experimentally observed include an increase in vortex shedding frequency or Strouhal number as compared to a blunt base[4,5] and limited base drag reduction for a cavity depth beyond approximately half the base height.

The mechanism of drag reduction due to base cavities is as yet unclear, although several theories have been proposed, all of which imply some modification of vortex formation location and reduction in vortex strength. The earliest published base cavity experiments were done by Nash et al.[2] They proposed that, although a vortex or eddy may not be completely trapped by the cavity, the cavity does have a stabilizing effect on standing eddies near the base, implying that the vortices form at least partially within the cavity where they are affected by the cavity walls. Pollock[3] performed experiments based on theoretical work by Ringleb[6] who suggested that a stable vortex may be trapped in a cavity, causing the wake to revert to a steady flow. Pollock used a special asymmetric cusp-shaped cavity which showed no advantage in drag reduction over a rectangular cavity, in effect disproving Ringleb's theory. In a study of resonance effects on vortex shedding, Wood[7] showed that resonance of the base at the vortex shedding frequency causes vortex formation within the cavity, while formation normally occurs outside the cavity. He concluded that the drag reduction observed for base cavities must be due to some resonance or vibration in the flowfield, moving the vortices into the cavity where the solid walls restrict vortex growth and inhibit the strength of successive vortices.

A study of axisymmetric base cavities by Compton[8] suggested that recirculation within the cavity forms a co-flowing stream at the cavity edge which interacts with the separated freestream, reducing the vorticity of the separated shear layer. In a subsequent

---

* Currently employed at General Electric CR&D, P.O. Box 8, K1-ESB-121, Schenectady, NY 12301. Member AIAA.

** Professor. Associate Fellow AIAA.

1

study of axisymmetric base cavities, Morel[9] suggested that the co-flowing stream could be an important effect in two-dimensional geometries as well. More recently, Kruiswyk and Dutton[4] used a combination of pressure measurements and flow visualization techniques to conclude that, although vortex motion does not extend into the cavity, oscillating air flow at the cavity boundary increases fluid mixing in the near-wake, thereby reducing vortex strength. Their results concerning the change in base pressure and vortex shedding frequency due to a base cavity are shown in Table 1. The base cavity configuration was a rectangular cavity with a streamwise depth equal to half the base height. A base cavity with a depth of one full base height was also used, but the results were similar to the half base height cavity. The experimental conditions used in the present study match those used by Kruiswyk and Dutton[4] to facilitate comparison of data. The results in Table 1 show an increase of 10 to 14% in the base pressure coefficient which is non-dimensionalized by reference conditions in the flow just prior to separation near the downstream edge of the base. The relative increase in the Strouhal number (vortex shedding frequency) is less, although still significant. Another evident feature is that both effects are largest at the lowest freestream Mach number.

Two notable computational simulations of two-dimensional base cavity flows have also been done. Rudy[10] obtained laminar finite difference Navier-Stokes solutions using base configurations and freestream Mach numbers of 0.4 and 0.6 that matched those of Kruiswyk and Dutton[4], although Rudy's simulations used freestream Reynolds numbers (based on base height) of 700 and 962 (significantly lower than the experimental values). Clements and Maull[5] used an inviscid discrete vortex method for simulations of their experimental results. Rudy's results more accurately predicted the experimentally measured base pressure increase due to a cavity, but both simulations showed vortex formation within the cavity and a *decrease* in shedding frequency due to the cavity, which disagrees with experimental results. Rudy concluded that the observed increase in base pressure with a cavity was mainly due to the physical displacement of the base surface away from the low pressure vortices.

The work presented here will take advantage of both the new results available from PIV and the extensive experimental and computational data available from Kruiswyk and Dutton[4] and Rudy[10], respectively. The ability to directly compare results from several techniques for similar base geometries and flow conditions will allow a thorough analysis of the effects of a base cavity on the structure and properties of the

flowfield, leading to a better understanding of the mechanisms of drag reduction.

Equipment

Test Section

Experiments for this study were performed in a previously fabricated transonic wind tunnel (Fig. 2) based on a design described by Little and Cubbage[11]. The tunnel has a 4" x 4" (101.6 mm x 101.6 mm) test section with solid side walls and slotted upper and lower inner walls to relieve the blockage effect of models in the subsonic to transonic speed range. Six-inch diameter round windows are mounted in both sidewalls to allow visualization of the downstream end and near-wake of a base model. The tunnel is a blowdown type supplied with compressed dry air from a 140 m[3] tank farm at 120 psia. The base model (Fig. 3) consists of an interchangeable afterbody mounted on a wedge-shaped forebody. Trip wires are mounted on the top and bottom surfaces near the upstream edge to assure an equilibrium turbulent boundary layer at separation. When mounted in the test section, the upstream edge is located approximately 17" (432 mm) downstream of the wind tunnel entrance with approximately 0.75" (19 mm) of the downstream end of the model visible through the side windows. The afterbodies used are a blunt base and a rectangular base cavity with a depth of half the base height. The wind tunnel and base models are the same as those used by Kruiswyk and Dutton[4].

Modifications have been made to the original wind tunnel for the flow seeding and optical access necessary for this study. Slot-shaped upper and lower windows have been fabricated and installed in the outer tunnel walls for access with a vertically propagating planar laser sheet. The sheet passes through the lower window and through one of the streamwise slots of the inner wall to enter the test section. The arrangement of the wall slots requires the position of the sheet to be 10 mm off the tunnel centerline in the spanwise direction, but surface flow visualization on the base model[4] and laser Doppler velocimetry (LDV) data in the near-wake[12] indicate no significant variation of the flow from centerline conditions. Delivery of silicone oil seed for PIV is done by two TSI six-jet atomizers feeding a single 3/4" O.D. tube that enters the stagnation chamber. Flow from the stagnation chamber passes through a pair of screens (44 x 44 mesh screen with 57% open area) and enters an enclosure at the nozzle entrance to reduce turbulence. The silicone oil seed is then injected by a manifold tube with a series of holes directed downstream and oriented in a transverse (vertical) plane aligned with the illuminating laser sheet. The flow then passes through a 2" long section

2

of honeycomb with a 3/16" cell diameter to further reduce turbulent fluctuations. The seed injection is done downstream of the screens due to experience with LDV indicating that silicone oil droplets tend to build up on screens, causing large drops to form and burst off which bias velocity measurements. LDV data from the final tunnel configuration indicate tunnel-empty turbulence intensities of less than 1% at the freestream conditions used in this study.

PIV System

To meet the objectives set forth for this study, data were obtained with a non-intrusive velocity measurement technique called particle image velocimetry (PIV). PIV is performed by illuminating a seeded flowfield with a planar laser sheet that is pulsed at a known time interval, forming two or more sequential images of each seed particle within the light sheet (Fig. 4). The particle images are captured on film or another medium, then the local image separations and, therefore, velocities can be determined for the entire plane. Unlike pointwise techniques such as LDV, which provides statistical velocity data on a point-by-point basis, PIV can quantitatively identify instantaneous flow structures that may be random in nature but important to the overall behavior of the flow. PIV also reveals planar views of three-dimensional flow structures that are smeared by volume integration inherent in techniques such as schlieren photography. A detailed discussion of the design, development, and validation of the PIV system used in this study can be found in References 12 and 13; therefore, only a brief discussion is given below.

The acquisition system refers to the equipment used to obtain raw particle images from the test section flowfield (see Fig. 5). This system captures double images of each particle within the illuminated laser sheet by using two Continuum YG681C-10 Nd:YAG lasers equipped with frequency doubling crystals to provide a maximum output energy of 550 mJ/pulse at a wavelength of 532 nm (green light) with a pulsewidth of 4-6 ns. High-resolution black-and-white films are very sensitive to green wavelengths and the high visibility of the green light also simplifies alignment of the two beams which is a critical factor in obtaining double images of particles in the flow. Two separate lasers are required since a single laser cannot generate two distinct, equal energy pulses in the short time interval required for high-speed flows (typically less than 1 μs). The horizontally and vertically polarized beams of the two lasers are combined by a polarized beam splitter, then shaped by spherical and cylindrical lenses to form a planar beam profile. Beam thickness and width at the test section can be controlled by

adjustment of the beam shaping optics. The current study used a beam thickness of 1.2 mm and width of 64 mm at the test section.

The photographic recording of particle images is done by a 35 mm camera mounted on the same optical table as the lasers and beam shaping optics. This allows maintenance of the relative position of all optical components for consistent alignment and focus. This table is also mounted on vibration-isolated supports to avoid the effects of laboratory vibrations. The camera has a flat field 100 mm macro lens with auto film wind and an electronic shutter for automated operation. Other features of the acquisition system include automated operation of the lasers, camera, and test section seeding by means of an Apple Macintosh II computer.

Derivation of velocity at each location in the flowfield is done through a digital analysis of the PIV photograph in a spot by spot fashion in an automated process performed by an interrogation system. The analysis technique used in the present PIV system is called the "autocorrelation method". Each velocity vector is determined from a small region of the flowfield photograph containing multiple particle image pairs, called an interrogation spot. Each spot is illuminated, magnified, and viewed by a video camera. The video image is then digitized into a two-dimensional array and passed to an array processor on a host computer. Two FFTs and other array operations are then performed to obtain the two-dimensional autocorrelation function of the original spot. The distance from the origin to a peak in the autocorrelation function corresponds to the separation distance of particle image pairs in the original spot, which in turn is proportional to the local particle velocity. The array processor uses a centroidal peak-finding routine to locate the three highest peaks in the autocorrelation array. Multiple peaks are found since the peak due to actual particle velocity is sometimes not the highest, but can be determined by later comparison of results with neighboring velocity data. The three peak locations are stored and the process is repeated for the next spot.

The size of the spot used for each individual velocity vector determines the spatial resolution, i.e., the in-plane dimensions of the effective probe volume. The data shown here were obtained using a uniform spot size of 1 mm x 1 mm in the frame of reference of the test section. The probe volume is therefore 1 mm by 1 mm (spot size) by 1.2 mm (laser sheet thickness) or 1.2 mm^3. Velocity vectors were found on a grid with an increment of 0.5 mm in each direction (overlapping spots) to prevent biasing due to small scale motions in the flowfield.

3

Validation experiments have been performed with this PIV system using both simulations and high-speed flow experiments, indicating a maximum total error in raw PIV velocity measurements of less than 3%[12]. Random error makes up a significant portion of the total, and is reduced by post-processing operations performed on the data as described in the following section.

both the streamwise and transverse directions. By defining the coordinate system as positive x in the streamwise direction and positive y in the transverse direction with the origin at the center of the downstream base edge, each realization covers the wake from x = 1 mm to 50 mm and from y = −17 mm to 17 mm. This region extends 3.3 base heights downstream of the aft edge of the base.

Results and Discussion

Experimental Conditions

Experiments were initially performed with two base configurations at three freestream velocity conditions, resulting in six cases. Flow conditions for each case were determined by running the test section without the base model. The test section flow velocity was measured as a function of wind tunnel stagnation pressure, allowing the appropriate stagnation pressure to be determined for each desired freestream velocity condition. This stagnation pressure was maintained for the corresponding experiments with the base model. A summary of the flow conditions and base configurations used in this study is shown in Table 2, including the freestream Reynolds number based on freestream velocity and base height and shorthand notations for each case. As mentioned previously, these cases match those used by Kruiswyk and Dutton[4] and the Mach 0.4 and 0.6 freestream conditions used by Rudy[10] with similar base configurations.

As expected from inviscid flow theory, the measured velocity just outside the boundary layer at the downstream edge of the base (reference Mach number in Table 2) is greater than the associated freestream velocity due to local compression of streamlines near the body. The mean measured reference Mach numbers for each case were found to match the reference Mach numbers quoted by Kruiswyk and Dutton[4] for the associated freestream conditions. The velocity data from individual flowfield realizations showed some variation from the desired reference velocities (maximum 9%) due to the lack of tunnel control valve resolution at the small stagnation pressures required and due to changes in the stagnation temperature of the supply air from run to run. A simple scaling factor was therefore applied to the velocity data from each flowfield realization to account for these variations.

Fifteen flowfield realizations were obtained for each of the Mach 0.4 and Mach 0.6 cases listed. Realizations were also obtained for each of the Mach 0.8 cases, but difficulties with seeding density in the vortex street prevents the use of those cases in the quantitative analysis presented here[12]. Each individual realization consists of an array of 6831 (99 x 69) instantaneous velocity vectors with 0.5 mm spacing in

Individual Flowfield Realizations

An example raw velocity vector plot from a single Mach 0.6 blunt base (M6b) realization is shown in Fig. 6. As noted in the figure, only every other vector from the actual data set is plotted for the sake of clarity. The raw PIV data shown have a limited number of invalid vectors which have been removed. This is necessary in the application of PIV since photographic imperfections, lack of particle images at a particular location, and other random factors cause a small percentage of invalid measurements which must be corrected during processing. This is done automatically in software which scans the raw velocity field and uses an algorithm requiring satisfaction of both absolute velocity limits and velocity gradient limits in the flowfield for acceptance of data. The raw velocity realizations used in this study had anywhere from 92% to 98% valid data which is comparable to reported PIV data validation rates in the literature. The missing data are then filled in from neighboring data by a two-dimensional linear interpolation method[14]. Finally, the vector field is smoothed by convolution with a Gaussian kernel[14] to eliminate random noise caused by image imperfections, video noise, and other factors. The kernel convolution is the analog of a low-pass digital filter, only in two dimensions. The resulting smoothed velocity vector field corresponding to Fig. 6 is shown in Fig. 7. This step is crucial when spatial differentiation is to be performed on the vector field to derive quantities such as vorticity, since any high frequency random error will be accentuated by differentiation.

In order to analyze vortex location and strength, the out-of-plane vorticity

$$\omega_z = \left(\frac{\partial v}{\partial x} - \frac{\partial u}{\partial y} \right)$$

was computed for each flowfield realization. This was done by central differencing of the original velocity data. A color plot of vorticity with overlaid velocity vectors corresponding to Figs. 6 and 7 is shown in Fig. 8. These data present a new capability for quantitatively analyzing separated compressible flow structure which has to this point been impossible. One of the notable features in Fig. 8, which holds for all realizations at all experimental conditions, is the significant

4

fragmentation of the vortices as they shed from the separated shear layers at the aft edge of the base. This is indicative of the high level of boundary layer turbulence prior to separation and its effect on the turbulent structure of the wake. This is confirmed by boundary layer turbulence intensity measurements of up to 5% using LDV[12], and fast response pressure measurements made in the wake by Kruiswyk and Dutton[4] which showed a broad range of spectral density peaks along with the strongest peak at the vortex shedding frequency, indicating the superposition of the vortex street on a random turbulent flowfield. Turbulence energy is therefore transferred in the wake from the large scale vortices to smaller scales, causing the gradual breakdown of distinct vortices as they travel downstream.

Vorticity Statistics

As mentioned earlier, previous theories regarding the mechanism of base cavity drag reduction all hinge on some modification of vortex strength and/or position. For this reason, it is desirable to use the vorticity data now available to examine vortex path and strength, both with and without base cavities. Due to the turbulent nature of the flowfield and the resulting vortex fragmentation discussed previously, it is rather difficult to select a particular location for each vortex in an instantaneous realization. Therefore, a statistical method was adopted to estimate vortex path and strength. Due to the alternate shedding of the wake vortices, successive vortices have peak vorticity values, ω_z, of alternating sign, causing the mean vorticity to go to zero where the opposing vortex paths overlap. Since only the vorticity magnitude is necessary for the determination of vortex strength and path, it was decided to derive the root mean square (RMS) vorticity for each experimental case, which is defined at each flowfield location (x, y) by

$$\omega_{RMS}(x,y) = \left[\frac{\sum\limits_{i=1}^{N} \left[\omega_z(x,y) \right]_i^2}{N} \right]^{\frac{1}{2}}$$

where the index i represents each individual realization for the experimental case of interest and N is the total number of realizations, or 15.

The results for the M4b, M4c, M6b, and M6c cases are shown in Fig. 9. These plots show the region within approximately one base height of the aft edge to concentrate on the notable features. Although some data scatter is present due to the turbulence level and limited ensemble size, these plots do reveal useful

information about cavity effects. One of the first noticeable features is the presence of the free shear layers at each separation point and their extension into the wake. At a point less than half of a base height downstream, they rapidly lose strength, indicating the mean location at which free vortices break off into the wake, or the vortex formation location. Lines have been included on the plots to identify the mean shear layer location, shape, and length. Each line was determined by a curve fit to the peak vorticity values in the shear layer, with the line terminating at the point where the vorticity drops below 67% of the maximum scale, or 67,000 s^{-1} for the M4b and M4c cases, and 100,000 s^{-1} for the M6b and M6c cases. This allows a relative comparison of the shear layer lengths between all four cases.

Table 3 shows the average shear layer length and the transverse separation distance of the shear layer endpoints for each case shown in Fig. 9. Although the average shear layer length is 0.6 mm shorter for the M6c case than the M6b case, the difference of 0.1 mm is not significant for the Mach 0.4 cases. The asymmetry in the shear layers propagating from the upper and lower base corners for a given case also prevents drawing any firm conclusion of a change in vortex formation location due to the cavity, although wake static pressure data were used by Kruiswyk and Dutton[4] to conclude that vortex formation occurs further downstream due to the cavity for a Mach 0.4 freestream velocity.

Figure 9 does, however, reveal that the angle of convergence of the shear layers toward the transverse centerline appears steeper for the base cavity cases than for the blunt base. There may also be a slight increase in shear layer curvature, although it is difficult to determine conclusively. Increased shear layer curvature would indicate a larger pressure gradient across the shear layer, which would, in turn, imply that the cavity causes lower mean static pressure in the region just inside the shear layer and just past the separation point. However, this must be only a *local* effect confined near the shear layer, since the cavity has been shown in previous research to *increase* the mean pressure at the base surface, which is upstream of the shear layers inside the cavity.

Convergence of the shear layers causes the transverse separation distance between the two shear layers to be reduced at their endpoints (see Table 3), explaining the increase in shedding frequency observed by Kruiswyk and Dutton[4] for the base cavity (see Table 1). As stated by Fage and Johansen[15], the shedding frequency in a vortex street is inversely proportional to the separation distance of the shear layers in the wake. When the shear layer separation is reduced in the base

cavity wake due to convergence, it follows that the shedding frequency increases.

In examining the vortex path just downstream of the shear layers, reduced vortex strength due to the base cavity can be seen in Fig. 9 for both freestream Mach numbers. In an effort to quantify this result, the spatially averaged RMS vorticity was calculated for each case in Fig. 9 over a region extending between the two shear layer endpoints (in the transverse direction) and extending from the longest shear layer endpoint to 7.5 mm downstream of that endpoint (in the streamwise direction). This region was chosen to uniformly cover the initial vortex path for each case. The results are shown in Table 4. Although the data scatter in Fig. 9 makes small differences difficult to determine visually, the data in Table 4 show that the average RMS vorticity level is indeed reduced by the cavity for both freestream Mach numbers, implying a small decrease in vortex strength.

Finally, any effect of the base cavity on mean vortex path is not clear from Fig. 9, although it is evident that turbulence causes the vortex path to be somewhat random, since the RMS vorticity magnitude peaks are widely scattered in the wake for all cases.

The effects of increasing Mach number on the shear layers include a small increase in shear layer separation (see Table 3) which seems to be caused by a reduction in both the initial convergence angle and the curvature of the shear layers, and can be attributed to increased streamwise momentum in the fluid stream outside the wake. The shear layers are also extended by approximately 1 mm for the Mach 0.6 freestream cases versus Mach 0.4, causing the vortex formation to occur further downstream of the base edge. However, any change in vortex path downstream of the shear layers due to the increase in freestream velocity is not evident from these data. Displacement of the vortex formation location further downstream of the base would serve to explain the reduced effectiveness of the cavity at higher Mach number as shown by Kruiswyk and Dutton[4] (see Table 1). As the vortices form further away from the base at higher Mach number, their effect on the pressure at the base surface is reduced, causing any modification of the vortex street due to the cavity to have less relative effect on the base pressure.

Instantaneous Wake Structure

Further information on base cavity wake effects can be obtained by comparing the instantaneous wake structure for the blunt base and base cavity at a similar point in the vortex shedding cycle. For each freestream velocity condition, realizations were selected from the two base configurations with closely matching vortex locations in the near-wake. Velocity vector plots for

the best match from the M4b and M4c cases are shown in Fig. 10, with plots from the M6b and M6c cases shown in Fig. 11. As in Figs. 6-8, these velocity vector plots show only every other vector in each direction for the sake of clarity. It is evident from Figs. 10 and 11 that for each pair of realizations, the center stagnation point of the first vortex downstream of the base matches to within 1 mm in each direction.

Each of these realizations, along with others not shown here, indicates that the circulating region around a fully formed vortex entering the wake covers most of the base height, which is confirmed by the results of Kruiswyk and Dutton[4]. However, in both Figs. 10 and 11, a significant difference in the vortices due to the cavity is evident. In the presence of the base cavity, the circulating region around the fully formed vortex is more extended in all directions, diffusing the vortex motion over a larger region. Although velocity data are available only to within 1 mm of the base boundary, the vortex seems to extend partially into the cavity boundary (see first column of vectors at x = 1 mm and y = -7.5 mm to 7.5 mm in Figs. 10 (b) and 11 (b)), but the relatively small magnitude of this motion and the distance of the vortex center from the cavity precludes the vortex from being seriously inhibited by the cavity walls. The extension of the vortices partially into the cavity is confirmed by tuft visualization experiments done by Kruiswyk and Dutton[4], which showed that short strands of lightweight thread hung at the cavity boundary oscillated back and forth into the cavity in the streamwise direction, with small oscillations in the spanwise direction. However, surface flow visualization experiments performed to determine the interaction of the vortices with the inner walls of the cavity indicated very little fluid motion on the walls (i.e., very small cavity wall shear stress), even near the cavity boundary. The RMS vorticity data obtained here also show no evidence of vortex formation near the cavity boundary (see Fig. 9), so it is not likely that the vortices extend far enough into the cavity to be seriously inhibited by the cavity walls.

Another feature of the vortex expansion shown in Figs. 10 and 11 is that, with the base cavity, the vortices extend far enough across the wake to affect the opposing shear layer. For example, in Fig. 11 (b), the fully formed vortex shed from the lower separation point clearly interacts more strongly with the upper shear layer than is the case for the blunt base in Fig. 11 (a).

To examine this interaction, the instantaneous vorticity is plotted in Figs. 12 and 13 for each of the four realizations shown in Figs. 10 and 11. From these plots, the shear layer position can be determined, and is indicated by a line in the same manner as in Fig. 9.

6

The fluid motion near the shear layers due to vortex expansion across the wake is also shown with curved arrows. One effect from interaction of the diffused vortices with the opposing shear layers is a folding of the shear layer region toward the transverse centerline. For example, in Fig. 13 (b), the upper shear layer gains transverse momentum toward the centerline at locations upstream of the vortex center. The subsequent increase in shear layer curvature and convergence angle in the area upstream of the vortex center is clearly evident from both base cavity plots (lower shear layer in Fig. 12 (b) and upper shear layer in Fig. 13 (b)). Evidence of the vortex interaction with remnants of the shear layer *downstream* of the vortex center is also apparent with the corresponding motion *away* from the transverse centerline.

Another effect of diffused vortex motion is that increased vorticity in the area just inside of the shear layers and just downstream of the separation point can reduce the local pressure, thereby increasing the curvature of the shear layer, an effect which was discussed previously. However, increases in vorticity magnitude near the shear layers which would be associated with reduced pressure are not readily apparent in Figs. 12 (b) and 13 (b).

The instantaneous flow structure data can also be used for comparison to the numerical simulation of this flowfield done by Rudy[10]. This study used a time-accurate simulation of the Navier-Stokes equations to compute the laminar flow past base models similar to those used in the present experiments, with the only difference being in the transverse cavity height, which is equal to 90% of the total base height in the simulations and 80% of the base height in the present experiments. As previously mentioned, the simulations were done for freestream Mach numbers of 0.4 and 0.6 and at relatively low freestream Reynolds numbers (based on freestream velocity and base height) of 700 and 962 for Mach 0.4 and Mach 0.6, respectively.

Instantaneous vorticity plots have been selected from the Mach 0.6 simulations that most closely match the stage of vortex development indicated by the experimental results shown in Fig. 13. The simulations corresponding to the M6b and M6c experimental cases are shown in Figs. 14 (a) and (b). In comparing these plots to Figs. 13 (a) and (b), it can be seen that there are some significant differences in the vortex structure. The lack of turbulence in the simulations and the resultant discrepancy from the experimental wake structure (lack of small-scale turbulence and vortex fragmentation) are evident. The simulations also show that the vortices are elongated for both the blunt and cavity configurations, especially for the base cavity where the vortex stretches in the

streamwise direction as it expands into the cavity, causing vortex motion far into the cavity. Additional data from Rudy[10] also show distinct vortices forming near the cavity boundary at the transverse center of the wake. Although the PIV data do not extend into the cavity, the scale of the fluid motion at the boundary and the vortex formation location indicated by the experiments do not support these results. Rudy recognized the limitations of his computations and suggested future studies to include both higher Reynolds numbers and turbulence modeling to more accurately predict experimental results under typical Reynolds number conditions.

Conclusions and Summary

Analysis of the time-resolved flowfield structure in the turbulent separated wake of a base cavity has been made possible by implementation of a new particle image velocimetry (PIV) system. The data obtained have shed light on the effects of the base cavity and on the mechanism by which it reduces base drag.

The evidence presented indicates that the most prominent effects of a base cavity on the vortex street wake are the increased convergence of the separated shear layers from each base corner toward the transverse wake centerline and the diffusion of vortex motion due to the expansion of individual vortices partially into the cavity and across the near-wake. The diffusion of the vortices, in turn, reduces their strength by approximately 4% to 6%, although the vortices do not form further upstream due to the cavity and are not significantly inhibited by the cavity walls. These effects are seen at both freestream conditions examined here. It is also evident that the effects are less significant at higher freestream velocities due to the extension of the separated shear layers and the movement of the vortex formation location further downstream of the aft edge of the base, thereby reducing the effect of the cavity on the vortices. These specific wake structure effects provide the information necessary for determination of the drag reduction mechanisms of base cavities.

The apparent mechanism of the observed base cavity wake modifications depends on the replacement of the solid boundary of the blunt base with the compliant fluid boundary of the base cavity. This compliant boundary allows greater expansion of vortex motion and a resulting small increase in shear layer convergence toward the transverse centerline due to the interaction of each vortex on the upstream part of the opposite shear layer. However, the vortex formation location does not occur any closer to the aft edge of the base for the cavity case. These results refute the theories of Nash et al.[2], Pollock[3], Ringleb[6], and Wood[7], all of which assume that the vortices are

7

somehow trapped or stabilized by interaction with the inner walls of the cavity. The suggestion by Compton[8] and Morel[9] that a co-flowing stream sheds from the cavity wall is partially valid in that there is some momentary outflow from one edge of the cavity when vortex motion partially extends into the cavity, but the magnitude of the motion seems to be generally very small and too short-lived to affect the general vorticity level in the shear layer prior to vortex formation. This conclusion is confirmed by the surface flow experiments of Kruiswyk and Dutton[4] which indicate little or no fluid motion on the inner walls of the cavity. The proposal by Kruiswyk and Dutton[4] that periodic fluid mixing at the cavity boundary is responsible for a reduction in vortex strength is closest to being in agreement with the present results, since some mixing must occur as each vortex partly extends into the cavity, although the reduction in vortex strength is small.

Aside from the mechanisms of wake modification, one must consider the mechanism of the base pressure increase and subsequent drag reduction due to base cavities. It is true that the effects described above modify and slightly weaken the vortex street, which, in turn, should slightly increase the pressure in the vicinity of the vortices in the near-wake. However, the wake structure changes are relatively small and the vortex formation location and path are not significantly modified. Without a significant change in the strength or location of the vortices in the near-wake due to the base cavity, it seems that the most significant factor affecting the base pressure is the physical displacement of the base surface within the cavity to a position upstream of the wake, where it does not interact with the low pressure vortices. This is the conclusion drawn by Rudy[10], although his numerical simulations showed the vortices extending far into the cavity with corresponding effects on the wake structure.

In summary, the drag reduction mechanism of a base cavity in subsonic flow is the physical displacement of the base surface away from the vortex street wake, which is only slightly modified by the presence of the cavity.

Acknowledgments

References

1. von Kármán, T., "Über den Mechanismus des Widerstandes, den ein bewegter Körper in einer Flüssigkeit erfährt," *Nachrichten von der Königlichen Gesellschaft der Wissenschaften zu Göttingen. Mathematisch-Physikalische Klasse*, 1911, pp. 509-517.

2. Nash, J.F., Quincey, V.G., Callinan, J., "Experiments on Two-Dimensional Base Flow at Subsonic and Transonic Speeds," ARC R&M No. 3427, 1963.

3. Pollock, N., "Some Effects of Base Geometry on Two-Dimensional Base Drag at Subsonic and Transonic Speeds," Australian A.R.L., Aerodynamics Note 316, 1969.

4. Kruiswyk, R.W., Dutton, J.C., "Effects of a Base Cavity on Subsonic Near-Wake Flow," *AIAA Journal*, Vol. 28, No. 11, 1990, pp. 1885-1893.

5. Clements, R.R., Maull, D.J., "The Representation of Sheets of Vorticity by Discrete Vortices," *Progress in Aerospace Sciences*, Vol. 16, No. 2, 1975, pp. 129-146.

6. Ringleb, F.O., "Separation Control by Trapped Vortices," *Boundary Layer and Flow Control*, G. V. Lachmann, ed., Pergamon Press, 1961, pp. 265-294.

7. Wood, C.J., "The Effect of Lateral Vibrations on Vortex Shedding from Blunt-Based Aerofoils," *Journal of Sound and Vibration*, Vol. 14, No. 1, 1971, pp. 91-102.

8. Compton, W.B., "Effect on Base Drag of Recessing the Bases of Conical Afterbodies at Subsonic and Transonic Speeds," NASA Technical Note D-4821, 1968.

9. Morel, T., "Effect of Base Cavities on the Aerodynamic Drag of an Axisymmetric Cylinder," *Aeronautical Quarterly*, Vol. 30, Part 2, 1979, pp. 400-412.

10. Rudy, D.H., "A Numerical Study of Unsteady Two-Dimensional Subsonic Compressible Base Flow," Ph.D. Thesis, University of Illinois at Urbana-Champaign, 1987.

11. Little, B.H., Jr., Cubbage, J.M., Jr., "The Development of an 8-inch by 8-inch Slotted Tunnel for Mach Numbers up to 1.28," NASA Technical Note D-908, 1961.

12. Molezzi, M.J., "Development and Application of Particle Image Velocimetry in High-Speed Separated Flow: Two-Dimensional Base Cavities," Ph.D. Thesis, University of Illinois at Urbana-Champaign, 1993.

13. Molezzi, M.J., Dutton, J.C., "Application of Particle Image Velocimetry in High-Speed Separated Flows," *AIAA Journal*, Vol. 31, No. 3, 1993, pp. 438-446.

14. Landreth, C.C., Adrian, R.J., "Measurement and Refinement of Velocity Data Using High Image Density Analysis in Particle Image Velocimetry," *Proceedings, Fourth International Symposium on Applications of Laser Anemometry to Fluid Mechanics*, Lisbon, Portugal, July 1988, pp. 485-497.

15. Fage, A., Johansen, F.C., "The Structure of Vortex Sheets," ARC R&M No. 1143, 1927.

Table 1 Base pressure and shedding frequency effects due to base cavity
(taken from Kruiswyk and Dutton[4])

Freestream Mach No. (M_∞)	Freestream Reynolds No. (Re_∞)	Base Pressure Coefficient (C_p) Increase, %	Strouhal No. (St) Increase, %
0.4	1.36×10^5	14.1	6.53
0.6	1.82×10^5	9.8	3.65
0.8	2.09×10^5	10.3	2.57

Table 2 Experimental conditions

Freestream Mach No. (M_∞)	Reference Mach No. (M_{ref})	Base Configuration	Freestream Reynolds No. (Re_∞)	Notation
0.4	0.49	blunt	1.36×10^5	M4b
0.4	0.49	half-height cavity	1.36×10^5	M4c
0.6	0.74	blunt	1.82×10^5	M6b
0.6	0.74	half-height cavity	1.82×10^5	M6c
0.8	0.88	blunt	2.09×10^5	M8b
0.8	0.88	half-height cavity	2.09×10^5	M8c

Table 3 Base flow shear layer length and separation

Experimental Case	Average Shear Layer Streamwise Length (mm)	Cavity % Change	Shear Layer Endpoint Transverse Separation (mm)	Cavity % Change
M4b	6.9	—	13.0	—
M4c	6.8	-1.4	12.5	-3.8
M6b	8.0	—	13.5	—
M6c	7.4	-7.5	12.8	-5.2

Table 4 Base flow near-wake vortex strength

Experimental Case	Spatially Averaged RMS Vorticity s^{-1}	Cavity % Change
M4b	42590	—
M4c	40890	-4.0
M6b	66120	—
M6c	62490	-5.5

Fig. 1   Typical two-dimensional base cavity and subsonic vortex street wake
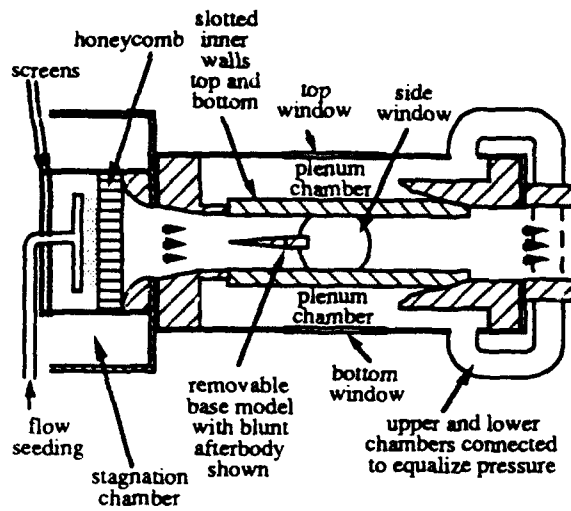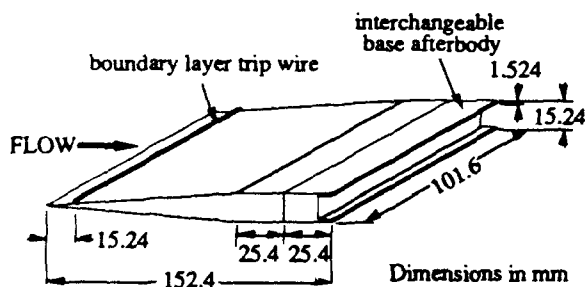

Fig. 2   Base flow test section
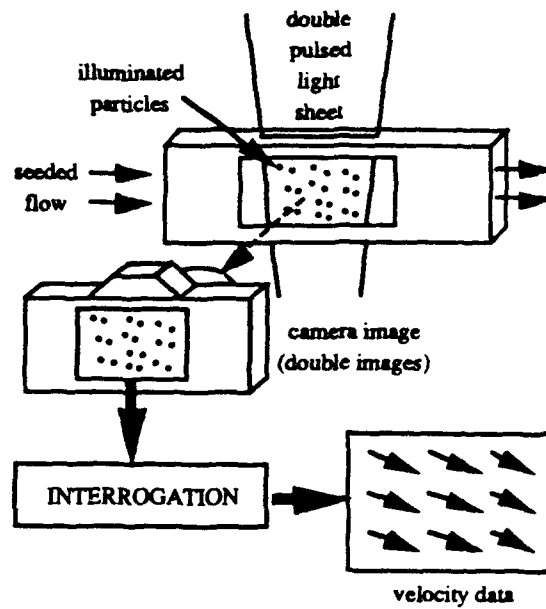

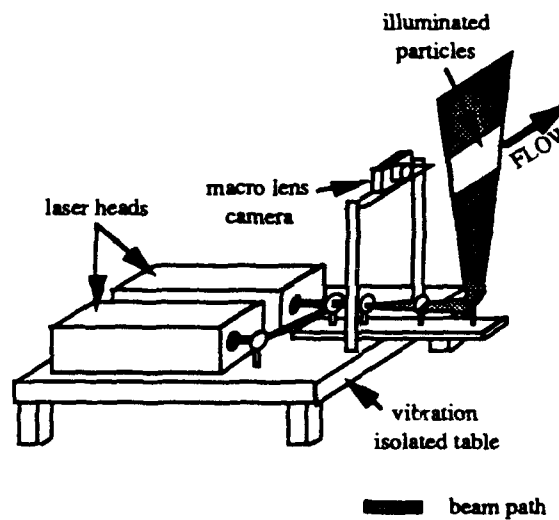
Fig. 3   Base cavity model

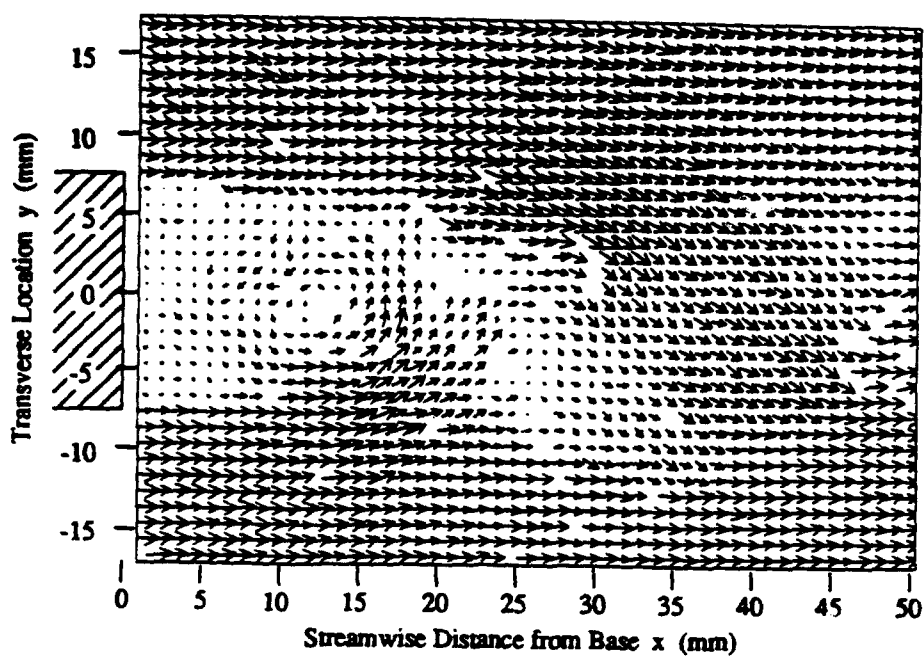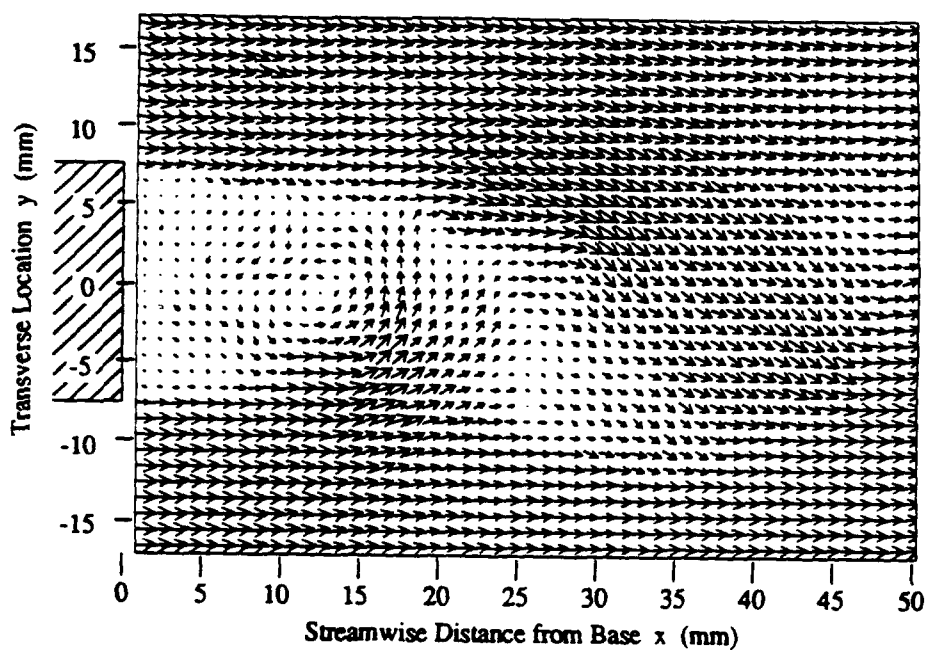Fig. 4   Principle of PIV

Fig. 5   PIV acquisition system

10

Actual data includes array of 99 x 69
vectors
(49 x 35 shown)

$\rightarrow$ 275 m/s

Fig. 6   M6b raw velocity vectors

Actual data includes array of 99 x 69
vectors
(49 x 35 shown)

$\rightarrow$ 275 m/s

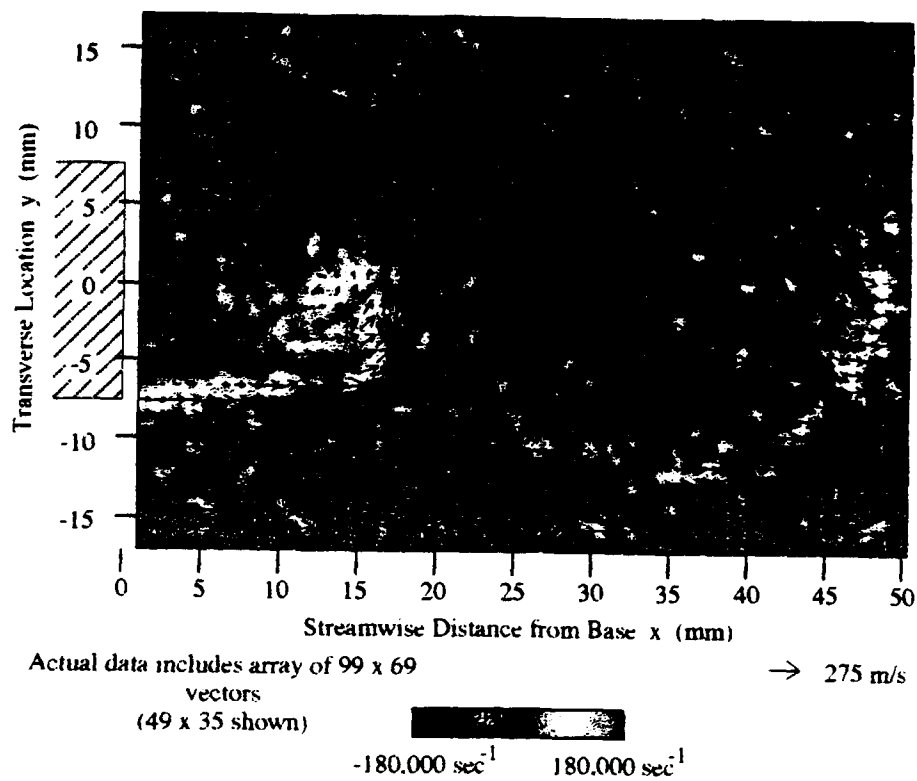**Fig. 7   M6b interpolated and smoothed velocity vectors**

Fig. 8 M6b color vorticity plot with velocity vector overlay

Actual data includes array of 99 x 69 vectors (49 x 35 shown)

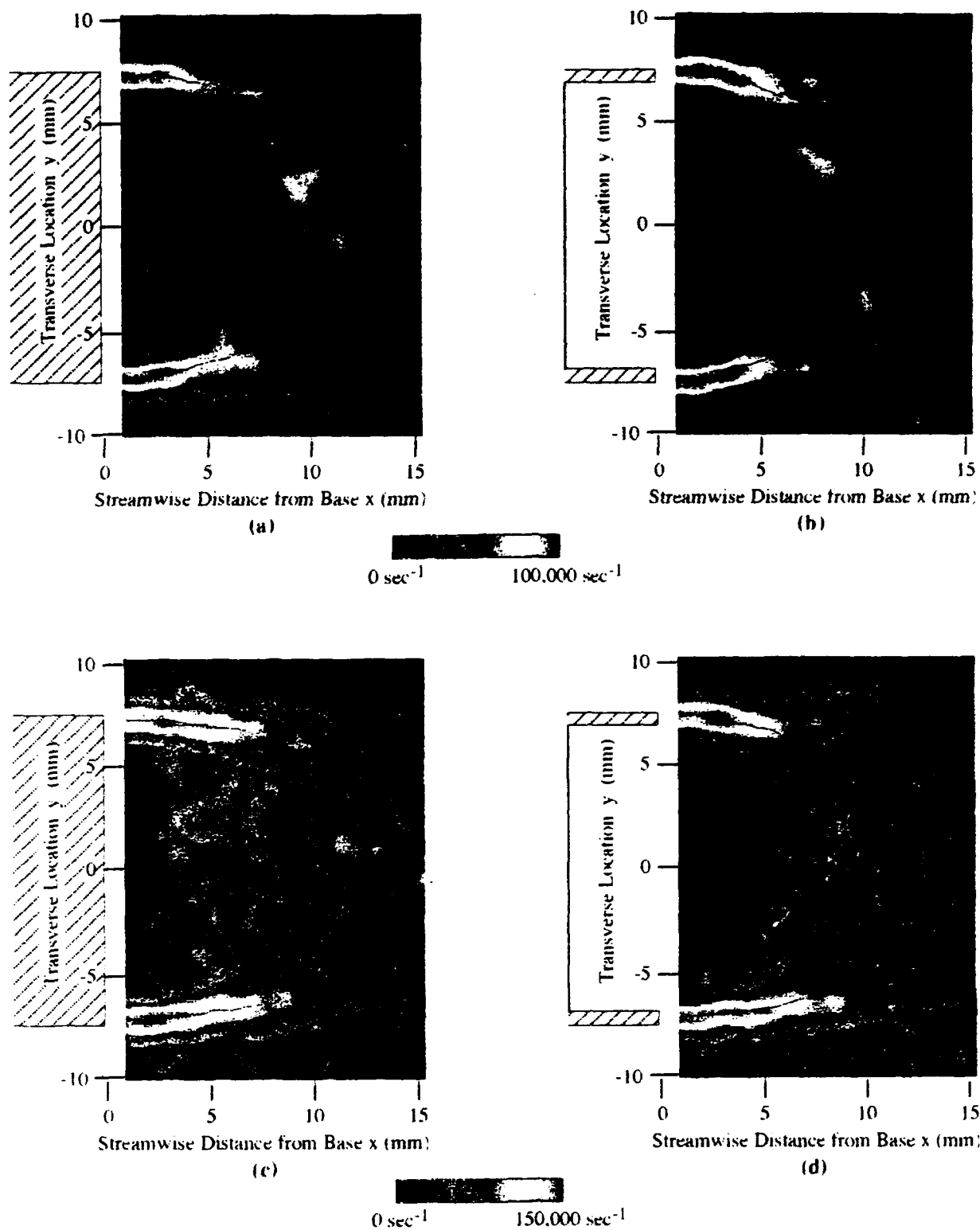→ 275 m/s

-180.000 sec^{-1} 180.000 sec^{-1}

Fig. 9 Enlarged color RMS vorticity plots indicating shear layers
(a) M4b (b) M4c (c) M6b (d) M6c

13

Fig. 10 Instantaneous flow structure comparison: $M_\infty=0.4$ velocity vectors
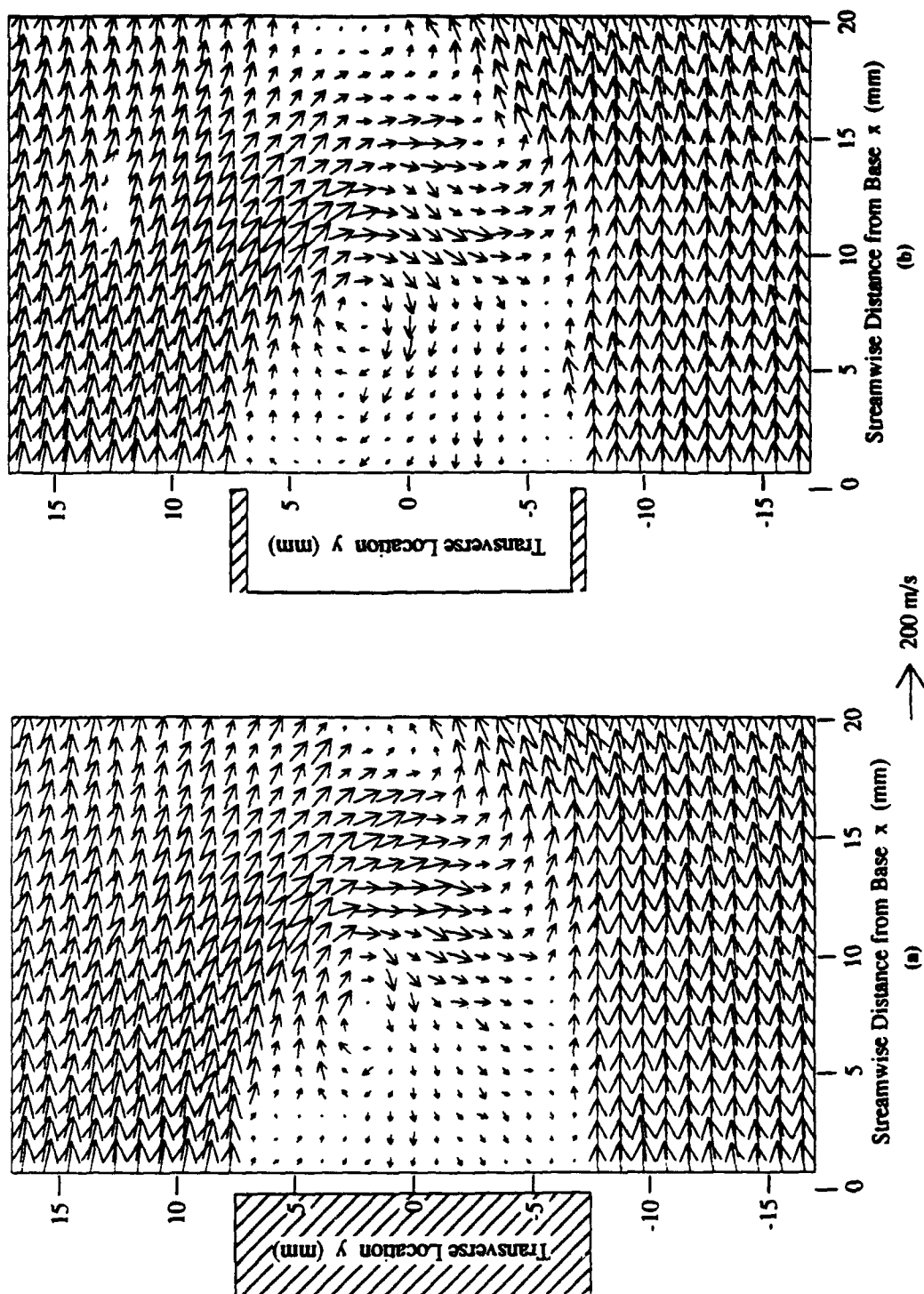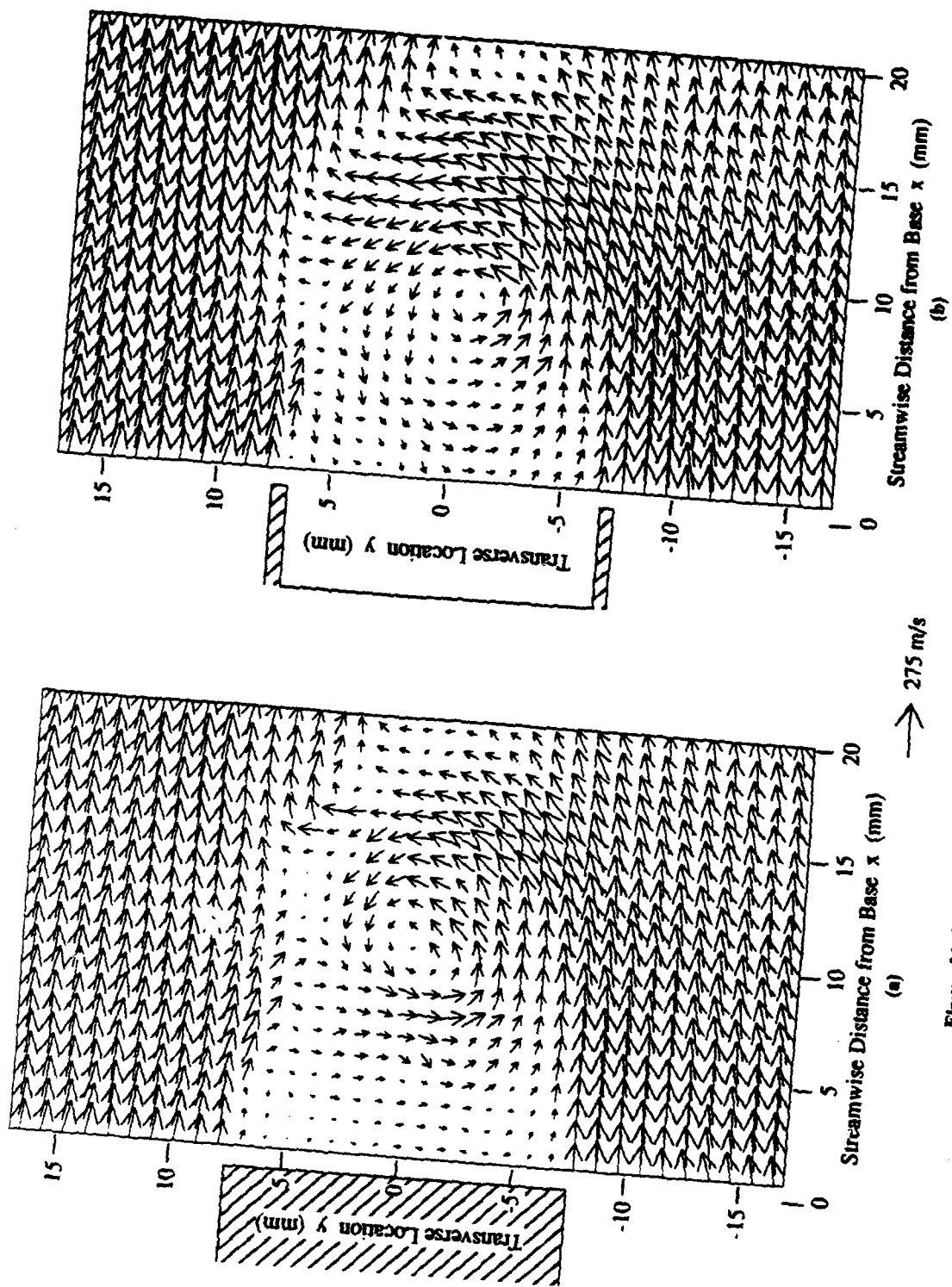(a) M4b (b) M4c

$\longrightarrow$ 200 m/s

14

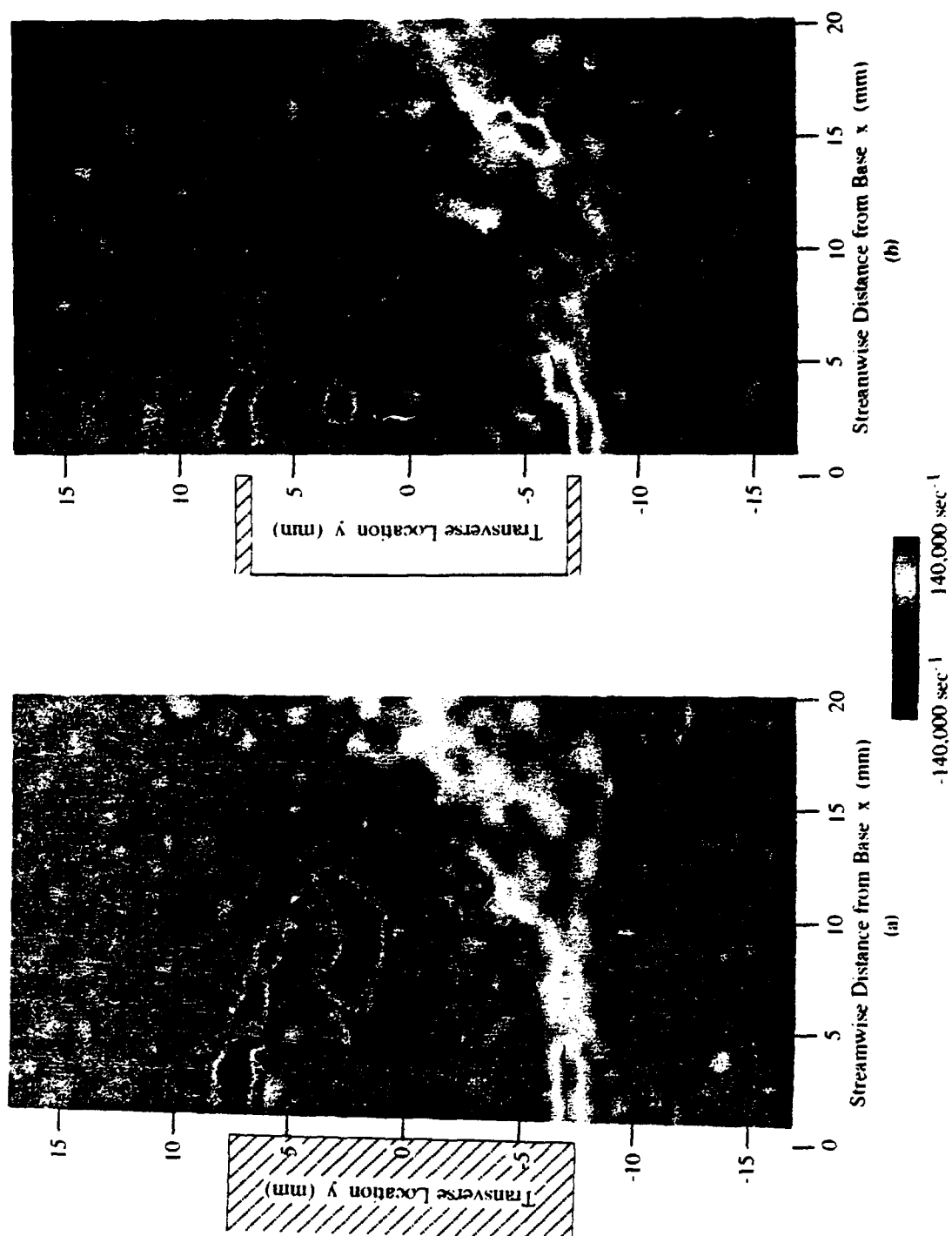Figure 11 Instantaneous flow structure comparison: M_{∞}=0.6 velocity vectors
(a) M6b (b) M6c

15

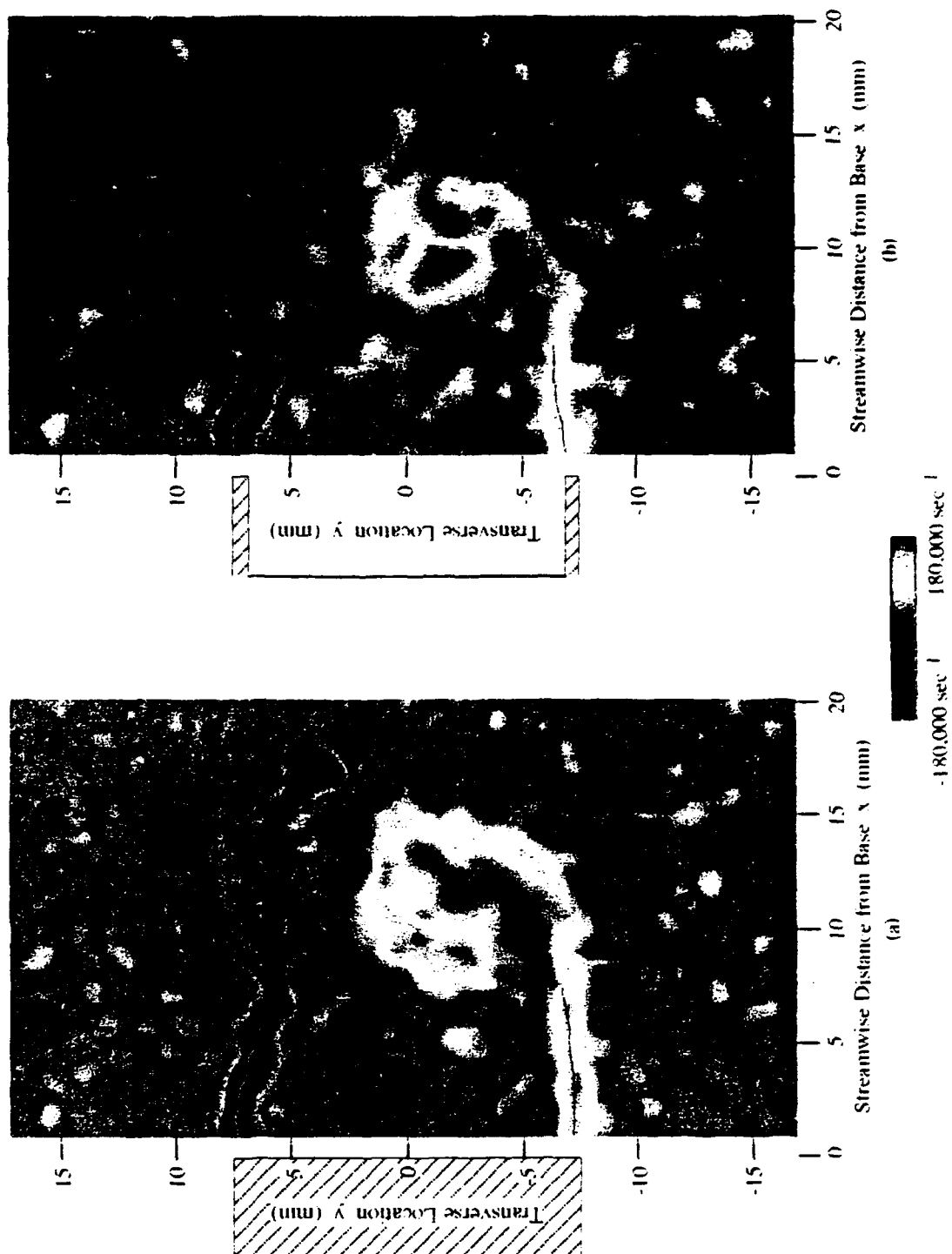Figure 12 Instantaneous flow structure comparison: $M_x = 0.4$ color vorticity plots
(a) M4b (b) M4c

16

Figure 13 Instantaneous flow structure comparison: $M_\infty = 0.6$ color vorticity plots
(a) M6b (b) M6c

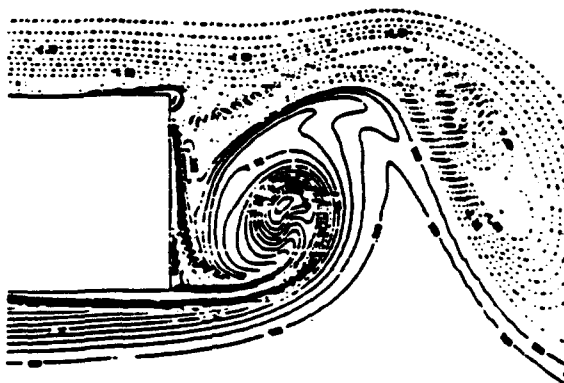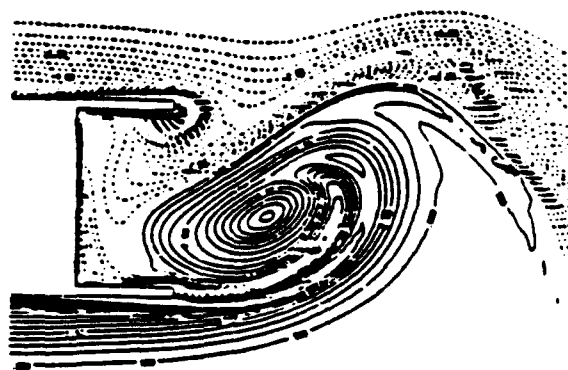$-180,000 \text{ sec}^{-1}$ $180,000 \text{ sec}^{-1}$

17

(a)   (b)

Fig. 14   Navier-Stokes numerical solution vorticity contours, taken from Rudy[10]
(a) M6b   (b) M6c

18

APPENDIX A.12

**AN EXPERIMENTAL INVESTIGATION OF THE SUPERSONIC
AXISYMMETRIC BASE FLOW BEHIND A
CYLINDRICAL AFTERBODY**

M.S. Thesis

Department of Mechanical and Industrial Engineering

University of Illinois at Urbana-Champaign

May 1991

by

J. L. Herrin

AN EXPERIMENTAL INVESTIGATION OF THE SUPERSONIC AXISYMMETRIC BASE FLOW BEHIND A CYLINDRICAL AFTERBODY

J. L. Herrin, M.S. Thesis
Department of Mechanical and Industrial Engineering
University of Illinois at Urbana-Champaign

ABSTRACT

An experimental investigation has been conducted to study the flowfield behind a blunt-based circular cylinder aligned with a supersonic freestream. The experiments have been conducted in a newly designed axisymmetric wind tunnel facility at a nominal approach Mach number of 2.5. A cylindrical sting aligned with the axis of the wind tunnel provided the physical support for the bases and afterbodies. Qualitative flowfield information was obtained with spark-schlieren photography and surface oil visualization. Mean wall static pressure measurements were made across the base and along the sting parallel to the wind tunnel axis. A two-component laser Doppler velocimeter (LDV) system was used to document the mean and turbulent velocity fields near the shear layer reattachment point. In addition, the nozzle approach flowfield including the sting boundary layer profile was measured with a one-component LDV configuration. The base pressure measurements indicated only a small dependence on radial location with an average base pressure coefficient of -0.102. Interference waves generated at the junction of the nozzle exit and test section were found to have a large effect on the base pressure profile at certain operating conditions but could be eliminated by proper operation of the tunnel. The shear layer reattachment point was found to lie 1.4 base diameters downstream of the base plane. The entire region surrounding the reattachment point was characterized by large turbulence intensities and steep radial velocity gradients.

APPENDIX A.13

**DESIGN AND VALIDATION OF AN INTERROGATION SYSTEM FOR
PARTICLE IMAGE VELOCIMETRY**

M.S. Thesis

Department of Mechanical and Industrial Engineering

University of Illinois at Urbana-Champaign

May 1991

by

R. A. Rosner

DESIGN AND VALIDATION OF AN INTERROGATION SYSTEM FOR PARTICLE IMAGE VELOCIMETRY

R. A. Rosner, M.S. Thesis
Department of Mechanical and Industrial Engineering
University of Illinois at Urbana-Champaign

ABSTRACT

A particle image velocimetry (PIV) system has been developed for use as a non-intrusive laser diagnostic tool to complement laser Doppler velocimetry (LDV) in high speed (transonic and supersonic) wind tunnel studies. The PIV system is capable of extracting instantaneous two-dimensional velocity maps within a flow by recording double images of seed particles on photographic film and then examining the local displacement of particle images to determine velocity vectors. The image acquisition system uses two high power pulsed Nd:YAG lasers focused into a thin light sheet to illuminate seed particles for recording on either 35 mm or 4" x 5" format film, with control of seeders, lasers, and the camera shutter performed by a Macintosh II computer. Interrogation of the double-exposed photographs to extract velocity information is done on an image processing system based on a 50 MHz Macintosh workstation, a HeNe laser film illumination source, automated positioners to handle the film, and a CCD array camera. The design of the acquisition system, including special considerations for PIV in high speed flows, is discussed. The theory and design of the interrogation system is described in detail. Finally, results from the cases used to validate and demonstrate the PIV system are presented.

APPENDIX A.14

DEVELOPMENT AND APPLICATION OF PARTICLE IMAGE VELOCIMETRY IN HIGH-SPEED SEPARATED FLOW: TWO-DIMENSIONAL BASE CAVITIES

Ph.D. Thesis

Department of Mechanical and Industrial Engineering

University of Illinois at Urbana-Champaign

April 1993

by

M. J. Molezzi

DEVELOPMENT AND APPLICATION OF PARTICLE IMAGE VELOCIMETRY IN HIGH-SPEED SEPARATED FLOW: TWO-DIMENSIONAL BASE CAVITIES

M. J. Molezzi, Ph.D. Thesis
Department of Mechanical and Industrial Engineering
University of Illinois at Urbana-Champaign

ABSTRACT

A new particle image velocimetry (PIV) system has been developed to obtain two-dimensional instantaneous velocity data over a planar region in high-speed separated flows for the quantitative analysis of turbulent and unsteady flow structures. This PIV system is the first of its type to incorporate sub-micron seed particles and birefringent image shifting for the resolution of flow velocity in separated regions. The system was also developed with improved in-plane spatial resolution over previous high-speed flow PIV applications by using a 1.0 mm^2 interrogation region (in flowfield dimensions) for each independent velocity measurement. The system has been proven in preliminary experiments using a simple low-speed round jet flow and has been validated for accuracy with both known-displacement simulated PIV photographs and uniform flow experiments at Mach 0.5 (170 m/s) for comparison to pressure and laser Doppler velocimeter (LDV) data.

The PIV system was also used in a study of the near-wake structure of a two-dimensional base in subsonic flow. This application was chosen in order to determine the fluid dynamic mechanism of the observed base drag reduction in the presence of a base cavity. Experiments were done over a range of freestream Mach numbers up to 0.8, including local flowfield velocities up to 300 m/s. Effects of the base cavity on the von Kármán vortex street wake were found to be related to the expansion and diffusion of vortices near the cavity, although the effects are of small magnitude and no significant change of the vortex formation location or path was observed. The base cavity effects are also less significant at higher freestream velocities due to the formation of vortices further downstream from the base. The base cavity drag reduction was found to be mainly due to the displacement of the base surface to a location upstream of the low-pressure wake vortices, with only a slight modification in the vortex street itself.

APPENDIX A.15

AN EXPERIMENTAL INVESTIGATION OF SUPERSONIC AXISYMMETRIC
BASE FLOWS INCLUDING THE EFFECTS OF AFTERBODY BOATTAILING

Ph.D. Thesis

Department of Mechanical and Industrial Engineering

University of Illinois at Urbana-Champaign

July 1993

by

J. L. Herrin

AN EXPERIMENTAL INVESTIGATION OF SUPERSONIC AXISYMMETRIC BASE FLOWS INCLUDING THE EFFECTS OF AFTERBODY BOATTAILING

J. L. Herrin, Ph.D. Thesis
Department of Mechanical and Industrial Engineering
University of Illinois at Urbana-Champaign

ABSTRACT

An experimental investigation of the near-wake flowfield downstream of blunt-based axisymmetric bodies in supersonic flow has been conducted. Using a blowdown-type wind tunnel designed specifically for this purpose, experiments were conducted at a nominal approach Mach number of 2.5 and a unit Reynolds number of 51 (10^6) per meter. Two different axisymmetric afterbodies were examined in the study: a circular cylinder was used as a baseline configuration, and a conical boattailed afterbody with a boattail angle of five degrees and a boattail length of one afterbody radius was used to investigate the effects of afterbody boattailing on the fluid dynamic processes in the near-wake. Neither afterbody contained a central jet so that the base flowfield in unpowered, supersonic flight was simulated. The primary objective of the research program was to enhance the understanding of the fluid dynamic processes inherent to axisymmetric base flows by obtaining and analyzing detailed, non-intrusive experimental data including flow visualization photographs, static pressure measurements, and mean velocity and turbulence data throughout the near-wake. Of special significance in the current research is the detailed turbulence information obtained with laser Doppler velocimetry (LDV) since these data are virtually nonexistent in supersonic base flows and provide new insight into the physics of these complex flows. In addition, the present data form a substantial data base which can be used to advance and improve theoretical and numerical base flow modeling techniques.

The static pressure measurements on the base and afterbody of each model indicate a relatively constant pressure across the base with the addition of the boattail resulting in a decrease in the base drag coefficient of 16% from the baseline cylindrical afterbody. The net afterbody drag coefficient (boattail + base contributions) was reduced by 21% which shows the usefulness of afterbody boattailing as a practical method to reduce afterbody drag in supersonic, axisymmetric flow. The mean velocity and turbulence fields in the near-wake of each afterbody were

investigated with LDV. In general, the near-wake flowfield can be characterized by large turbulence levels in the separated shear layer, relatively large reverse velocities in the recirculation region, and gradual recompression/realignment processes as the shear layer converges on the axis of symmetry. The shear layer development was found to be dependent on the conditions immediately downstream of the base corner separation point (upstream history effect). Furthermore, the centered expansion at the base corner reduced the turbulence levels in the outer region of the shear layer relative to the approach boundary layer but enhanced the mixing and entrainment along the fluid-fluid interface between the shear layer and the recirculating region which results in large turbulence levels along the inner edge of the shear layer. The shear layer growth rate is initially large due to substantial mass entrainment from the recirculation region near the inner edge, but further downstream, a self-similar state is reached where growth rates are significantly reduced. In general, the effects of afterbody boattailing on the near-wake flowfield include a weaker expansion at the base corner separation point (less distortion of the shear layer and reduced turbulence production near the inner edge), reduced turbulence intensity and Reynolds shear stress levels throughout the near-wake (reduced mass entrainment along the length of the shear layer resulting in a higher base pressure), and a mean velocity field which is qualitatively similar to that of the cylindrical afterbody.